Simulation quantique de modèles de spins avec des grandes matrices d'atomes de Rydberg

Pascal Scholl

HAL Id: tel-03523082
https://pastel.hal.science/tel-03523082

Submitted on 12 Jan 2022

université
PARIS-SACLAY

Quantum simulation of spin models using large arrays of Rydberg atoms

Simulation quantique de modèles de spins avec des grandes matrices d'atomes de Rydberg

Thèse de doctorat de l'université Paris-Saclay

École doctorale n° 572 : ondes et matière (EDOM)
Spécialité de doctorat : Physique
Graduate School : Physique Référent : Institut d'Optique

Thèse préparée dans le **Laboratoire Charles Fabry** (Université Paris-Saclay, Institut d'Optique Graduate School, CNRS), sous la direction de **Antoine BROWAEYS**, directeur de recherche, et le co-encadrement de **Thierry LAHAYE**, chargé de recherche

Thèse soutenue à Paris-Saclay, le 06 décembre 2021, par

Pascal SCHOLL

Composition du Jury

Jacqueline BLOCH Directrice de recherche, CNRS-C2N	Présidente
Monika AIDELSBURGER Professor, LMU München	Rapporteure
Igor DOTSENKO Maître de conférence, LKB	Rapporteur
Tommaso ROSCILDE Maître de conférence, ENS Lyon	Examinateur
Antoine BROWAEYS Directeur de recherche, CNRS-LCF	Directeur de thèse

Remerciements

Si on m'avait dit il y a cinq ans que j'écrirai un document de 260 pages comprenant 95 figures et traitant de simulation quantique, je ne pense pas que j'y aurai crû. Et pourtant, on y est, après près de quatre ans de travail. J'ai passé les quatres années les plus intenses, intéressantes et motivantes de ma vie. Tout cela n'aurait pas été possible sans les personnes que je souhaite remercier sur ces quelques pages.

Tout d'abord, je souhaite remercier les membres de mon jury de thèse, Jacqueline Bloch, Monika Aidelsburger, Igor Dotsenko et Tommaso Roscilde qui ont lu avec attention mon manuscrit. Je vous remercie pour vos rapports très positifs et vos questions intéressantes, qui pour certaines continuent à me faire réfléchir aujourd'hui.

Ensuite, je tiens à remercier la direction du Laboratoire Charles Fabry pour nous avoir permis de retourner au laboratoire en jauge réduite rapidement après le début de la pandémie, tout en nous fournissant masques et solution hydroalcoolique. Grâce à vous, nous avons pu reprendre nos travaux très rapidement et je suis persuadé que les résultats présentés dans ce manuscrit n'auraient pas été les mêmes sans vos efforts.

Mes remerciements vont également à la start-up Pasqal, qui a toujours été très positive avec nous, et nous a sauvé maintes fois en nous prêtant du matériel à des moments particulièrement critiques.

Je souhaite en particulier remercier chaudement Antoine Browaeys et Thierry Lahaye, mes deux directeurs de thèse. Lorsque je suis arrivé au laboratoire en Mars 2018 et que vous m'avez présenté le sujet de thèse, je n'en comprenais pas un seul mot. Si aujourd'hui je donne l'impression de maîtriser le sujet, c'est grâce à nos innombrables discussions, à la fois sur les aspects techniques des divers appareils que nous utilisons, mais aussi sur tous les concepts fondamentaux que nous étudions. Après avoir passé plus de 3 ans dans ton bureau Antoine, je pense pouvoir dire sans me tromper que tu es une personne incroyable, autant sur le plan humain que scientifique. Je ne peux compter le nombre d'heures que tu as passé avec moi dans le bureau pour m'expliquer tous les concepts les plus simples de nos recherches, et je me demande parfois comment tu as fais pour ne pas perdre patience. C'est extrêmement agréable de travailler avec toi: tu es toujours à l'écoute de nos idées, de nos feelings, même lorsque tu sais que nous ne maîtrisons pas ce dont nous sommes en train de parler. Je ne suis pas sûr que beaucoup de leader de groupe réagissent comme toi face à un étudiant en thèse qui ne sait pas dériver les équations du modèle de l'électron

élastiquement lié. Et pourtant, je pense que c'est ce point particulier qui fait en partie le succès de ta carrière: tu sais faire ressortir le meilleur des gens qui t'entourent, et je te serai éternellement reconnaissant pour ça.

Je vous suis aussi éternellement reconnaissant pour m'avoir permis de travailler sur cette expérience magnifique qu'est CHADOQ. Je tiens ici à la remercier. Après avoir passé quatre ans 10 heures par jour à la chouchouter, la réparer, la rendre meilleure ou encore parfois m'énerver dessus, on développe forcément une certaine affection. C'est fou de voir à quelle point cette manip' est généreuse: à force de travail et d'acharnement, elle m'a toujours rendu un résultat positif. Lors des simulations quantiques à très grand nombre d'atomes signifiant que nous ne pouvions plus vérifier nos résultats avec des simulations classiques, ce fut avec un immense plaisir que je découvris ce qu'est la simulation quantique à mes yeux: c'est ma machine qui détient la vérité, et mon but est de lui poser les bonnes questions pour la découvrir. Grâce à CHADOQ, la simulation quantique est devenue pour moi quelque chose de tangible.

Tout ceci n'aurait été possible sans mes prédécesseurs qui ont construit CHADOQ. En particulier, je tiens à remercier les personnes qui étaient présentes lorsque je suis arrivé sur la manip': la tornade Sylvain de Léséleuc, la force tranquille Vincent Lienhard et le magic postdoc Daniel Barredo. Vous étiez la "Dream Team" qui fait un Science ou un Nature tous les quatre matins, des gars hyper talentueux et super sympas. Vous êtes clairement des modèles de réussite pour moi. Intégrer cette équipe au tout début ne fut pas simple. Je me souviens d'être resté debout de longues heures derrière vous dans la salle de manip' à vous regarder changer à la vitesse de l'éclair 1000 câbles et tourner 1000 boutons sans jamais en être fatigués. Mais à force de persévérance et de quelques blagues, j'ai fini par entrer dans l'équipe.

J'ai commencé ma thèse en travaillant en particulier avec Vincent qui m'a beaucoup appris sur la manip'. Nous avons passé de super moments ensembles, qu'est-ce qu'on a bougé nos corps devant CHADOQ! C'était vraiment incroyable. Je crois que je n'ai jamais autant écouté de styles de musique différents qu'à ce moment là. Quand je repense à ces moments, alors que tu étais très proche de la fin de ta thèse et tout le stress qui va avec, tu étais exceptionnellement patient et attentif à mes questionnements, je te remercie pour le temps que tu as pris pour moi. Ton intuition et ta compréhension profonde de tous les phénomènes très complexes que nous étudions est vraiment impressionnante et inspirante. Je te remercie aussi de m'avoir permis d'écrire ces remerciements.

Je tiens ensuite à remercier Hannah Williams. Quand je vois ce que nous avons réussi à accomplir ensemble en deux ans, je pense que nous pouvons être fiers de

4

nous! Ce ne fut pas facile, en particulier au vu de la rude compétition en face. Et pourtant, tu es toujours restée très calme et posée, à l'écoute et prête à suivre le thésard qui courait dans tous les sens. Merci beaucoup de m'avoir toujours soutenu et fait confiance, cela m'inspire pour les années à venir!

Pendant ces quatres années, j'ai eu l'immense chance et l'honneur de travailler avec Daniel Barredo. Tu es à mes yeux le meilleur expérimentateur que j'ai rencontré. C'est toi qui m'as appris à obtenir le meilleur de CHADOQ, à optimiser au maximum tous les paramètres et à ne jamais lâcher le morceau. Tu as un don pour résoudre rapidement les divers problèmes que nous rencontrons tous les jours au labo. Tu es une sorte de héros, lorsqu'il y a un problème qui semble insolvable et que nous perdons espoir, tu arrives à la rescousse pour tous nous sauver! Une autre de tes grandes qualités que j'apprécie est ta capacité à poser les bonnes questions, c'est-à-dire celles qui ouvrent de nouveaux horisons ou permettent de voir les choses sous un autre angle.

J'ai aussi eu l'occasion de travailler avec Kai-Niklas Schymik à quelques occasions pendant toute la durée de ma thèse. Ton impact fut majeur pour les résultats présentés dans ce manuscrit, merci beaucoup! Il y eut quelques moments mémorables tout au long de nos thèses, notamment avec Daniel.

Et puis finalement il y a la nouvelle équipe de CHADOQ: Guillaume Bornet, Gabriel Emperauger et Cheng Chen. J'espère vous avoir transmis la joie de travailler sur cette expérience, mais aussi l'envie de toujours obtenir les meilleurs résultats. En particulier Guillaume avec qui j'ai le plus travaillé: l'esprit de CHADOQ est en toi, je me fais donc aucun soucis pour l'avenir!

Il y a aussi des personnes extérieures au labo qui m'ont permis indirectement de rédiger ce manuscrit. Il y a tout d'abord mes amis, qui ont toujours crû en ma capacité à faire une thèse... Ou pas. Je remercie en particulier Natacha Vivier qui a tenté de m'aider à comprendre ce mystère qu'est Adobe Illustrator. Et puis la famille aussi, notamment mes parents et mon frère qui m'ont toujours poussé dans les études et tout fait pour me valoriser au maximum. Ca y est, je suis moi aussi docteur, les chats ne font pas des chiens.

J'ai gardé le meilleur pour la fin. J'écris mes plus grands remerciements pour celle qui me suit déjà depuis 9 ans dans toutes mes aventures, depuis mes concours pour intégrer l'ENS Cachan, puis l'agrégation, jusqu'à ce manuscrit. Le dénominateur commun à tous ces succès, c'est toi, et c'est sûrement pas une coïncidence. Tu as toujours été un soutient incroyable, prête à tout pour moi. Je te remercie pour tous les moments de bonheur quotidien que nous passons ensemble, cela m'a toujours permis de donner le meilleur de moi-même. J'espère que nos aventures dureront éternellement.

Contents

Introduction

Quantum physics is now a well-established theory and over the recent decades, the field has evolved towards using its laws for more applied studies. This evolution was triggered by our technical ability to isolate and control individual quantum objects, such as charged particles [Dehmelt, 1990; Paul, 1990] or photons [Haroche, 2013], and also the isolation of neutral atoms from laser-cooled gas [Phillips, 1998]. It allowed experimentalists to verify the fundamental concepts enunciated by the founders of quantum physics, amongst which the most counter-intuitive example might be entanglement: if we consider two entangled quantum objects, measuring the properties of the first object instantaneously affects the property measured on the second object. This gives rise to intriguing properties such as the non-locality of quantum physics. Entanglement was measured for the first time by Aspect, Grangier, and Roger [1982] with correlated pairs of photons, and revisited later with various quantum objects such as two interacting ions [Schmidt-Kaler *et al.*, 2003].

These pioneering experiments triggered a huge interest into the use of these fundamental laws for practical applications. For instance, at the single-particle level, the coherent manipulation of the isolated quantum objects allows for the local probing of external fields, leading to the development of quantum sensors [Kitching, Knappe, and Donley, 2011]. In particular, the use of atomic clocks improved the precision of global navigation satellite systems. In the field of quantum computing, state superposition and entanglement could be used to enable operations impossible with classical algorithms, which would speed up the calculations leading to a quantum advantage with respect to classical computers. Over the last few years, huge efforts towards demonstrating such an advantage have been deployed [Arute *et al.*, 2019].

Although the fundamental laws of quantum physics are now settled, there remain many open questions regarding their impact on a wide variety of strongly-correlated systems, ranging from high-energy physics to magnetic materials. In the latter case, these laws play an important role in high-temperature superconducting materials [Keimer *et al.*, 2015], or topological insulators governed by the quantum Hall effect [Klitzing, Dorda, and Pepper, 1980]. The modeling and simulation of these materials are difficult

to perform due to entanglement. In practice, the number of parameters which needs to be taken into account to exactly simulate the system grows exponentially with the number of particles, making it intractable when the number of particles is higher than ~ 40.

Another approach to understand and model these phenomena is to use a quantum simulator. This concept, originally introduced by Richard Feynman [Feynman, 1982], consists of using an artificial quantum system to understand the behavior of a real material. This approach recently became possible with state-of-the-art experimental apparatuses [Georgescu, Ashhab, and Nori, 2014]. Their growing level of control and the versatility in the type of interactions they can implement (including purely mathematically-conceived interactions which would not exist in nature) allows physicists to use these simulators "as if" they were performing simulations on a classical computer.

In this thesis, I describe our quantum simulator, and report the quantum simulation experiments realized during my PhD. They were performed on a platform based on neutral ^{87}Rb atoms, trapped in configurable arrays of micrometer-sized optical tweezers, and interacting via highly-excited states known as Rydberg states. In this introduction, I first briefly motivate quantum simulation in the frame of condensed-matter physics, then give an overview of the various synthetic platforms. I finally focus on our Rydberg quantum simulator, and give the outline of this thesis.

1.1 Quantum simulation using synthetic platforms

In order to motivate the interest for quantum simulation, let us take the example of quantum magnetism in condensed-matter physics, which is relevant for our platform (see below). To understand the intriguing features of condensed-matter systems such as superconductivity, one would ideally like to be able to vary the system's parameters in order to assess their contribution to the observed features. However, condensed-matter systems are usually limited in the number of tunable parameters. For example, one cannot vary the spin of the electrons in the material. A usual approach to try to understand the macroscopic properties of these materials is to model them from a microscopic perspective, and numerically study the emergent properties of these models. In order to simplify the problem, we consider that a material can be described as an ensemble of electrons with spin degrees of freedom $\sigma = \downarrow, \uparrow$ localized at the nodes of a crystalline structure. The simplest way to model the behavior of those electrons [Hubbard and Flowers, 1963] is to consider that they can hop between nearby nodes with a strength $-t$, with an energy cost U for two electrons to be on the same

node. This simple model leads to the Fermi-Hubbard Hamiltonian written as:

$$\hat{H} = -t \sum_{(i,j),\sigma} \left(\hat{c}_{i,\sigma} \hat{c}_{j,\sigma}^{\dagger} + \hat{c}_{i,\sigma}^{\dagger} \hat{c}_{j,\sigma} \right) + U \sum_{i} \hat{n}_{i,\uparrow} \hat{n}_{i,\downarrow}. \qquad (1.1)$$

where the first sum runs over neighboring lattice sites (i, j), $\hat{c}_{\sigma}$ and $\hat{c}_{\sigma}^{\dagger}$ are the fermionic annihilation and creation operators, and $\hat{n}_{\sigma} = c_{\sigma}^{\dagger} c_{\sigma}$. Although this model is a crude approximation of real materials, it is nonetheless extremely hard to solve. There is therefore no point in proposing more elaborate models, if this one is already not solved. For example, one does not know whether the ground state of the model exhibits superconductivity when the number of spins $\uparrow$ and $\downarrow$ is not equal.

It turns out however that this Hamiltonian can be readily implemented using a gas of ultracold fermionic atoms placed in optical lattices (see below). Hence, by measuring the ground state of this *synthetic atomic* system, one can hope to answer the question of the existence of superconductivity for the Fermi-Hubbard model. Furthermore, the values of t and U can be varied over a wide range of parameters, allowing investigations into their effect on the system. Synthetic platforms can even replace fermions by bosons and probe the effect of the fermionic nature of the electrons on superconductivity by comparing the results obtained for bosons and fermions.

In this thesis, I will perform the quantum simulation of spin-1/2 models. These models are relevant to describe, for example, insulating magnetic materials, for which the energy cost of having two electrons on the same node of the crystalline structure is large, which translates, in our simple model, to the condition $t \ll U$. Under this assumption, the above model can be rewritten as:

$$\hat{H} = \sum_{(i,j)} J_x(\sigma_i^x \sigma_j^x + \sigma_i^y \sigma_j^y) + J_z \sigma_i^z \sigma_j^z \text{ with } J_{x,z} \propto \frac{t^2}{U}, \qquad (1.2)$$

where $\sigma^{x,y,z}$ are the usual Pauli matrices acting on the spin-1/2 particles. These spin models have various names depending on J_x and J_z: for $J_x \neq J_z$, this Hamiltonian is referred to as the anisotropic Heisenberg model, and for $J_x = 0$, the model is known as the Ising model.

1.2   A wide variety of synthetic platforms

In order to be a useful quantum simulator, a synthetic platform has to fulfill several constraints. First, it needs to handle an ensemble of particles in a controlled geometrical

configuration, mimicking the structure of the studied material. Second, the interactions of those particles with their environment and between themselves must be controllable. Third, the experimentalists must have the ability to initialize the system in specific states, and also measure the relevant quantity describing its evolution. A wide variety of platforms fulfill those three points to a certain extent, which I briefly present now.

Ultracold quantum gases of atoms and molecules. As mentioned above, one synthetic platform which implements various Hamiltonians of interest for condensed-matter physics relies on degenerate quantum gases of atoms. To get the particles in a controlled spatial configuration, experimentalists mostly use periodic trapping potentials, coming from standing waves of off-resonant light, known as optical lattices [Bloch, 2005]. The lattice is filled by making the degenerate gas undergo a phase transition from a superfluid to a Mott insulator [Greiner *et al.*, 2012]. This platform has the ability to measure the system's state at the single-atom level using a "quantum gas microscope" [Bakr *et al.*, 2010]. The hopping of the atoms from one lattice site to another one naturally implements the model described in Equation 1.1. The parameters of the Hamiltonian are tuned by varying the lattice depth, and the geometry is tuned (to a certain extend) by playing on the relative phase and amplitude of the beams generating the optical lattice. Many models have been explored with this platform, which has allowed for the study of e.g. topology [Atala *et al.*, 2013], band structures [Tarruell *et al.*, 2012], or antiferromagnetism [Simon *et al.*, 2011; Mazurenko *et al.*, 2017].

This approach has also been demonstrated with polar molecules, where the dipole-dipole interaction implements spin models [Zhou, Ortner, and Rabl, 2011; Yan *et al.*, 2013].

Trapped ions. Most trapped ion-based platforms rely on the trapping of individual ions into linear Paul traps [Raizen *et al.*, 1992]. These implement spin Hamiltonians, in which the spin-spin interactions are engineered using a laser coupling between the internal states of the ions and the collective vibrational modes of the ionic crystals [Cirac and Zoller, 1995]. The platform exhibits very high fidelity in single- or two-qubit operations [Blatt and Wineland, 2008], which allows for the engineering of arbitrary spin Hamiltonians [Lanyon *et al.*, 2011; Kokail *et al.*, 2019].

Superconducting circuits. The platforms presented above use "real" objects, i.e. atoms, molecules or ions, to perform quantum simulation. Here, the quantum object

is materialized by a Josephson junction, which can be engineered to behave as an "artificial atom" [Nakamura, Pashkin, and Tsai, 1999]. The spin-spin interactions are engineered using either the exchange of microwave photons in a cavity [Wallraff *et al.*, 2004], or by coupling circuits for example by mutual inductances [Chen *et al.*, 2014]. An interesting asset of this platform is the fact that the interactions do not rely on geometrical arrangement, but on inter-connecting wiring. Their potential integrability and on-chip compactness makes them promising candidates for the future of quantum information [Devoret and Schoelkopf, 2013]. As for the trapped ions, this platform exhibits very high fidelity in single- and two-qubit operations, and can engineer arbitrary spin Hamiltonians [Salathé *et al.*, 2015].

Other types of platforms engineering "artificial atoms", such as polaritons in micro-cavities [Carusotto and Ciuti, 2013] or electron spins in quantum dots [Vandersypen *et al.*, 2017], are also promising candidates towards the study of many-body physics.

Challenges. All of these platforms (including ours) face two key challenges. First, quantum simulation becomes interesting when the number of interacting particles becomes intractable to numerical simulations. Nowadays, the limit in the (approximate) simulation of a system's dynamics is a few hundreds of particles. Second, the output of the simulators has to be ascertainable. These conditions means that these platforms need (i) high-quality control over the parameters governing the interactions of, at least, $\sim 100 - 1000$ particles, and (ii) a way to assess the quality of the results. The solutions to these challenges are different for each platform, as they rely on various technologies.

1.3   Rydberg quantum simulators

I now turn to Rydberg quantum simulators. The first proposals suggesting Rydberg atoms for quantum gates [Jaksch *et al.*, 2000; Lukin *et al.*, 2001] relied on a mechanism known as *Rydberg blockade*, discussed in Chapter 5, which prevents the simultaneous excitation of several nearby atoms to the Rydberg states. This was first demonstrated in 2004 in dilute cold gases [Löw *et al.*, 2012]. In order to implement the Rydberg blockade in a more controlled environment, our team at the Institut d'Optique combined this idea with the individual trapping of neutral atoms in micrometer-sized optical dipole traps, also known as *optical tweezers*. This technology was pioneered by Philippe Grangier [Schlosser *et al.*, 2001]. It led to the observation of the Rydberg blockade between two atoms [Gaëtan *et al.*, 2009], jointly with the group of Mark Saffman in a

similar setup [Urban *et al.*, 2009]. These two teams then demonstrated the generation of entangled states [Wilk *et al.*, 2010], and the realization of the two-qubit C-NOT gate [Isenhower *et al.*, 2010].

Evolution of the platform. Since these first experimental demonstrations, arrays of Rydberg atoms evolved towards a promising platform for quantum simulation experiments [Weimer *et al.*, 2010]. The versatility of geometries of optical tweezers arrays [Nogrette *et al.*, 2014] combined with the first implementations of the van der Waals and resonant dipole-dipole interactions, and Förster resonances [Browaeys, Barredo, and Lahaye, 2016] between a few atoms showed that various Hamiltonians could be implemented using a Rydberg simulator.

Initially, tweezers platforms suffered from the stochastic loading of the optical tweezers by single atoms, with filling fraction 1/2. An important breakthrough was the development of techniques to assemble chosen patterns [Barredo *et al.*, 2016]. This allowed the group to perform quantum simulation with up to ~ 40 atoms [de Léséleuc *et al.*, 2018b; Lienhard *et al.*, 2018]. They observed, for example, the emergence of antiferromagnetism in the quantum Ising model, although this was limited by the system's coherence. When comparing the results to classical computing, this limited coherence combined with the relatively low number of atoms meant that the system's evolution could still be simulated numerically. In parallel, the group of Mikhail Lukin also started a Rydberg quantum simulator, and studied the quantum Ising model in 1D with impressive results.

This was the status when I arrived in the lab, in March 2018. During the three years of my PhD, we pushed the platform to ~ 200 atoms, and increased the system's coherence by one order of magnitude. Thanks to those upgrades, we were able to investigate the quantum Ising model in a regime for which classical simulations are extremely difficult to perform, bringing the platform one step closer to its original purpose. We also showed the implementation of (i) the Heisenberg model with tunable anisotropy and (ii) complexed-value interactions on few-body systems, thus further increasing the class of models we can simulate.

Improving the simulator's performances. Another important aspect we achieved was to improve the reliability of the setup, and to extend the automation of the various experimental procedures. These improvements allow the simulator to acquire data in a quasi-continuous way. We now realize ~ 1 million experiments each month when we perform quantum simulation, see Figure 1.1 a). This improvement, combined with the
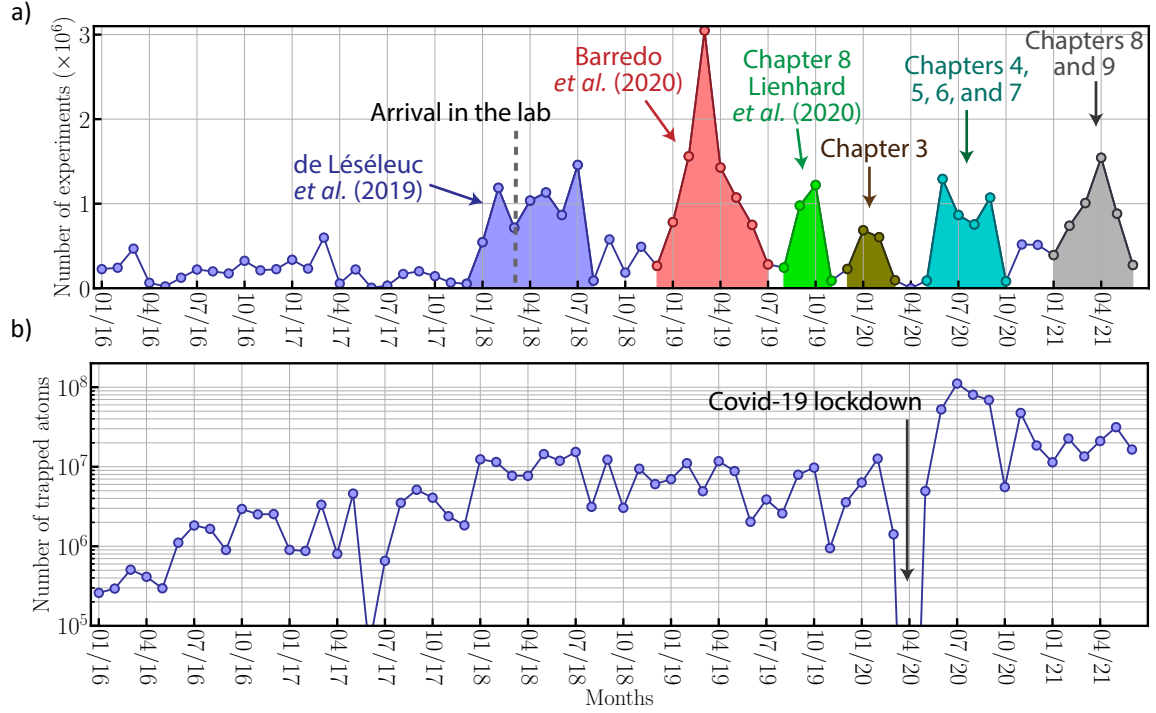
Figure 1.1: Evolution of our Rydberg quantum simulator over the last years. Temporal evolution per month of a) the number of experiments and b) the corresponding number of involved single atoms. We now realize ~ 1 million experiment per month when we perform quantum simulation. The number of manipulated atoms increased by ~ 3 orders of magnitude in five years.

capability to work with a constantly increasing number of atoms, led to an increase by ~ 3 orders of magnitude in the number of manipulated single atoms (per month) over the last five years, see Figure 1.1 b). In particular, during the period which corresponds to the large-scale quantum simulation of the Ising model, we manipulated ~ 100 million atoms per month. During the three years of my PhD, we performed ~ 30 million experiments which involved the individual trapping and the manipulation of ~ 800 million atoms.

Thesis outline. I start this manuscript with an overview of the technical improvements we achieved during my PhD (Part I). After describing the various manipulations we can perform on the individually trapped atoms (Chapter 2), I focus on the technical improvements which allowed us to increase the system's coherence (Chapter 3), and the number of atoms we can manipulate (Chapter 4). These improvements led to the large scale quantum simulation of antiferromagnetism in the quantum Ising model, reported in Part II. I first detail how this model is implemented using the van der

Waals interaction by focusing on the example of a 1D chain (Chapter 5). I then probe the model in square lattices (Chapter 6) and triangular lattices (Chapter 7) by exploring the model's phase diagram and the corresponding phase transitions. In Part III, I report on the implementation of new types of Hamiltonians using the resonant dipole-dipole interaction between Rydberg atoms. I start with the engineering of complex-valued interactions (Chapter 8), then present the engineering of Heisenberg Hamiltonians with tunable anisotropy (Chapter 9).

Part I.

Improved experimental apparatus

Overview of the experimental apparatus

Contents

This chapter gives an overview of the experimental apparatus and describes the main techniques we routinely use to manipulate the atoms. The chapter is structured as follows:

- I start with a brief explanation on how we create arrays of single atoms in optical tweezers. I will detail how we produce large arrays in Chapter 4.

- I then present the various manipulations we can perform on the atoms. I will describe in detail the Rydberg excitation in Chapter 3.

- Finally, I present the way we control the electromagnetic environment experienced by the atoms.

Many of the techniques which I present here were already implemented when I arrived in the lab. However, we managed to improve some of them either by increasing the speed at which we can perform them, or by improving their efficiency. I will thus detail the improvements made during my PhD.

2.1 Arrays of single atoms in optical tweezers

In this section, I will give a brief description of how, starting with one gram of solid rubidium (Rb), we end up with hundreds of single ^{87}Rb atoms held in optical tweezers separated by tens of micrometers in arbitrary 2D geometries. More detail can be found is the theses of Lucas Béguin [2013] and Sylvain de Léséleuc [2018].

2.1.1 Trapping and observing a single atom in an optical tweezers

In order to trap and observe a single atom, the first step is to produce a cold cloud of Rb atoms which is used as a reservoir to load the optical tweezers. Creating a cold cloud of Rb atoms requires an ultra high vacuum system to isolate the Rb atoms from their environment. The experimental setup is continually pumped with ion pumps, reaching pressures as low as a few 10^{-11} millibars. The setup is divided into three parts (see Figure 2.1):

- **The rubidium oven.** A heating belt is used to heat the rubidium to a typical temperature of 60°C to create a vapour. The design of the oven is made such that only the atoms which are quasi-collimated along the y direction flow out of the oven.

- **The Zeeman slower.** At the output of the oven, the atoms are slowed down using a Zeeman slower to a speed of $\sim 10\,\mathrm{m/s}$.

- **The science chamber.** After the Zeeman slower, the atoms enter the main chamber in which we perform the experiments. They are first trapped in a Magneto-Optical Trap (MOT), then in the tweezers arrays created by an Aspherical Lens (AL) with large numerical apperture. A second AL is used to collimate the light after the tweezers arrays, used to perform various optics alignments.
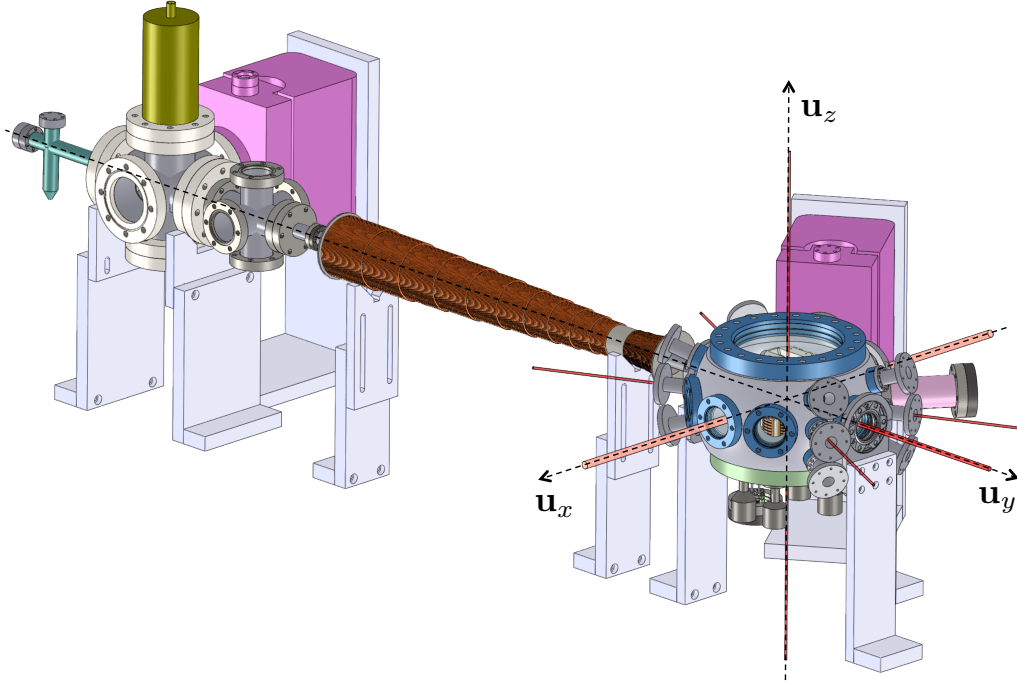
Figure 2.1: Overview of the experimental apparatus. Adapted from the thesis of Lucas Béguin [2013]. The apparatus consists of three parts: the oven (left) producing the rubidium vapor, the Zeeman slower (center) slowing down the atoms, and the science chamber (right) in which they are trapped.

Characteristics of the MOT. The MOT is created using six independent counter-propagating beams. The ALs are placed inside the vacuum chamber at a distance of 10 millimeters from the atoms position, which leads to a geometrical constraint on the generation of the MOT: the beams in the (x, y) equatorial plane cross with an angle of $\sim 60°$. The MOT beams are detuned from the $(5S_{1/2}, F = 2) \to (5P_{3/2}, F' = 3)$ by $\sim -5\Gamma_{5P} = -2\pi \times 30\,\mathrm{MHz}$ (see Figure 2.2 a)), with Γ_{5P} the lifetime of the $5P_{3/2}$ level. The presence of the nearby $F' = 2$ level imposes the need of a repumper, resonant with the transition $(5S_{1/2}, F = 1) \to (5P_{3/2}, F' = 2)$. Each MOT beam has a power $\sim 0.7\,\mathrm{mW}$ with a typical waist of ~ 2 mm, which gives a saturation of the transition of ~ 3. We use a pair of coils mounted on the lens holders to generate the magnetic quadrupole. We obtain an atomic cloud with a typical size of hundreds of micrometer, containing $\sim 10^7$ atoms. The temperature of the atoms in the MOT is $\sim 120\,\mu\mathrm{K}$. These atoms will be used as a reservoir to fill the optical tweezers traps.

Optical tweezers. An optical tweezers is a laser beam tightly focused down to a waist of $\sim 1\,\mu\mathrm{m}$, which is done using the AL, with a numerical aperture of 0.5 and
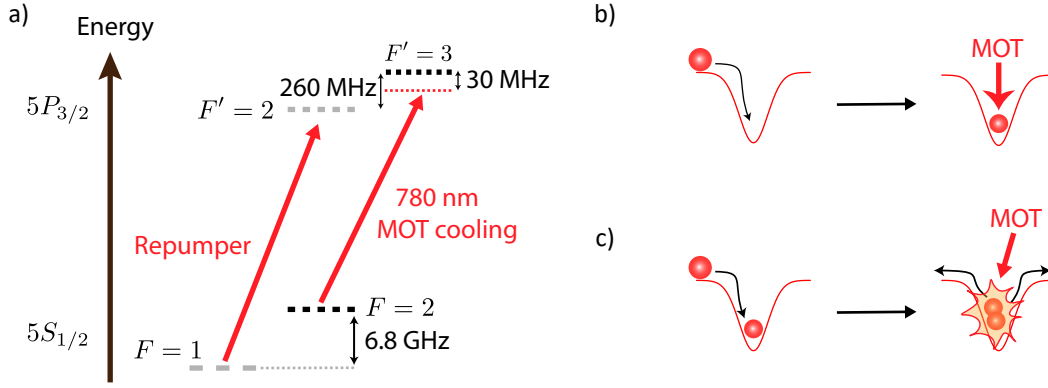
Figure 2.2: Trapping a single atom. a) Sketch of the levels involved in the trapping and cooling. b) When an atom enters the optical tweezers, the friction force exerted by the MOT results in the atom being trapped inside the tweezers. c) Sketch of the collisional blockade: when a second atom enters the tweezers, a light-assisted collision expels both atoms from the tweezers.

a focal length $f = 10\,\mathrm{mm}$. The intensity profile I of the tweezers follows, to a good approximation, a Gaussian profile:

$$I(r, z) = \frac{I_0}{1 + \frac{z^2}{z_r^2}} e^{-2\frac{r^2}{w_0(1 + z^2/z_r^2)}}, \tag{2.1}$$

with $w_0 = 1.1\,\mu\mathrm{m}$ the waist of the tweezers, $z_r = \frac{\pi w_0^2}{\lambda} = 4.4\,\mu\mathrm{m}$ its Rayleigh range for $\lambda = 850\,\mathrm{nm}$ and $I_0 = \frac{2P}{\pi w_0^2}$ the peak intensity. The power P of the optical tweezers is a few milliwatts. The optical tweezers is linearly polarized and red-detuned from the $5S - 5P$ transitions. The ground-state levels of an atom entering the tweezers are thus light-shifted towards lower energies, by the same amount for all the Zeeman sublevels m_F. The atom feels a potential U, expressed as [Grimm, Weidemüller, and Ovchinnikov, 2000]:

$$U(r, z, F) = \frac{U_0(F)}{1 + \frac{z^2}{z_r^2}} e^{-2\frac{r^2}{w_0(1 + z^2/z_r^2)}}. \tag{2.2}$$

In the limit where the tweezers' detuning is large compared to the ground-state hyperfine splitting and assuming the $5P_{1/2}$ and $5P_{3/2}$ levels to have the same linewidth, the expression of U_0 reads:

$$U_0(F) = \frac{\hbar \Gamma_{5P}^2 I_0}{8 I_{\mathrm{sat}}} \left(\frac{1}{3\Delta_{1/2}(F)} + \frac{2}{3\Delta_{3/2}(F)} \right), \tag{2.3}$$
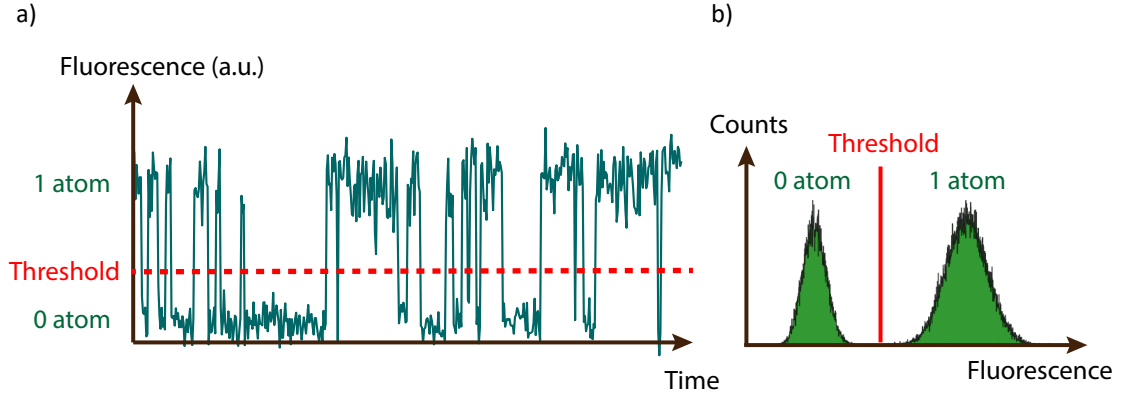
Figure 2.3: Observing the fluorescence of a single atom. a) Trace of the collected fluorescence from the tweezers region recorded on the EMCCD camera. We see two regimes which correspond to having one or zero atoms in the tweezers. We never encounter double step events that would indicate the presence of two atoms. b) Typical histogram of the fluorescence collected from the tweezers position.

with Δ the tweezers' detuning and I_{sat} the saturation intensity. The typical value of the trap depth is $U_0 \simeq h \times 20\,\mathrm{MHz} \simeq k_B \times 1\,\mathrm{mK}$. The atoms in the MOT thus have a temperature which is typically ~ 10 times smaller than the depth of the tweezers. The tweezers potential being conservative, we need a friction force to keep the atom inside the tweezers: it is provided by the MOT lasers, sketched in Figure 2.2 b) and detailed for example in the thesis of Benoît Darquié [2005].

Collisional blockade. One specificity of the tweezers is the fact that it contains at most one atom, due to the collisional blockade [Schlosser *et al.*, 2001; Schlosser, Reymond, and Grangier, 2002], sketched in Figure 2.2 c). If an atom enters in an already filled tweezers, the two atoms are close enough to create a loosely-bound molecule via photo-association induced by the MOT light. The rapid decay of the molecule releases a large amount of kinetic energy to the two atoms which ejects both of them from the trapping region. The arrival of an atom in a tweezers therefore either fills (if the tweezers is empty) or empties (if the tweezers is filled) the trap. The filling fraction of the tweezers is thus $1/2$.

Observing a single atom. To observe the atom trapped in the tweezers, we collect the scattered light induced by the MOT lasers using the same AL that creates the tweezers. A dichroic mirror separates the scattered light at 780 nm from the tweezers light at 850 nm. An optical setup images the focal plane of the AL onto an EMCCD

camera with a typical averaging time of 20 ms. When looking at the fluorescence coming from the position of the tweezers, we obtain traces as shown in Figure 2.3 a) in which we observe two fluorescence levels: (i) a low level which corresponds to an empty tweezers, and (ii) a high level which corresponds to having one atom in the tweezers.

The presence of an atom in the tweezers is detected using an automatically adjustable threshold level in between the two regimes, which accounts for long-term fluctuations of both the background light and the scattered light. A typical histogram of the fluorescence is shown in Figure 2.3 b). The two levels are separated enough to avoid any substantial detection errors.

2.1.2 Arrays of single atoms

Having given an overview of how we trap and observe a single atom in a tweezers, I now present the way we produce fully-loaded arrays of single atoms. As discussed above, the filling fraction of a given trap is 1/2 due to the collisional blockade. To circumvent this, we use a rearrangement technique which allows us to deterministically load the tweezers with single atoms. I start by explaining how we produce arrays of optical tweezers, then present the assembling technique.

Tweezers arrays. The production of tweezers arrays have been demonstrated using various techniques:

- Instead of using a single lens which focuses the tweezers beam, one can use an array of microlenses [Schäffner *et al.*, 2020]. Each microlens focuses a small portion of the light, thus resulting in an array of tweezers. The limitation of this method is its flexibility: changing the geometry of the tweezers array requires changing the microlens array.

- The use of multiple beams generated by a acousto-optic deflectors [Endres *et al.*, 2016] driven by multiple radiofrequency tones.

- The use of holographic techniques to modify the phase of the tweezers beam [Bergamini *et al.*, 2004]. The light pattern in the focal plane of the lens is given by the Fourier transform of the tweezers beam, making it possible to create an array of tweezers by imprinting the correct phase pattern on the beam. This approach was developed by our group at Institut d'Optique and is thus the one used on the experiment.
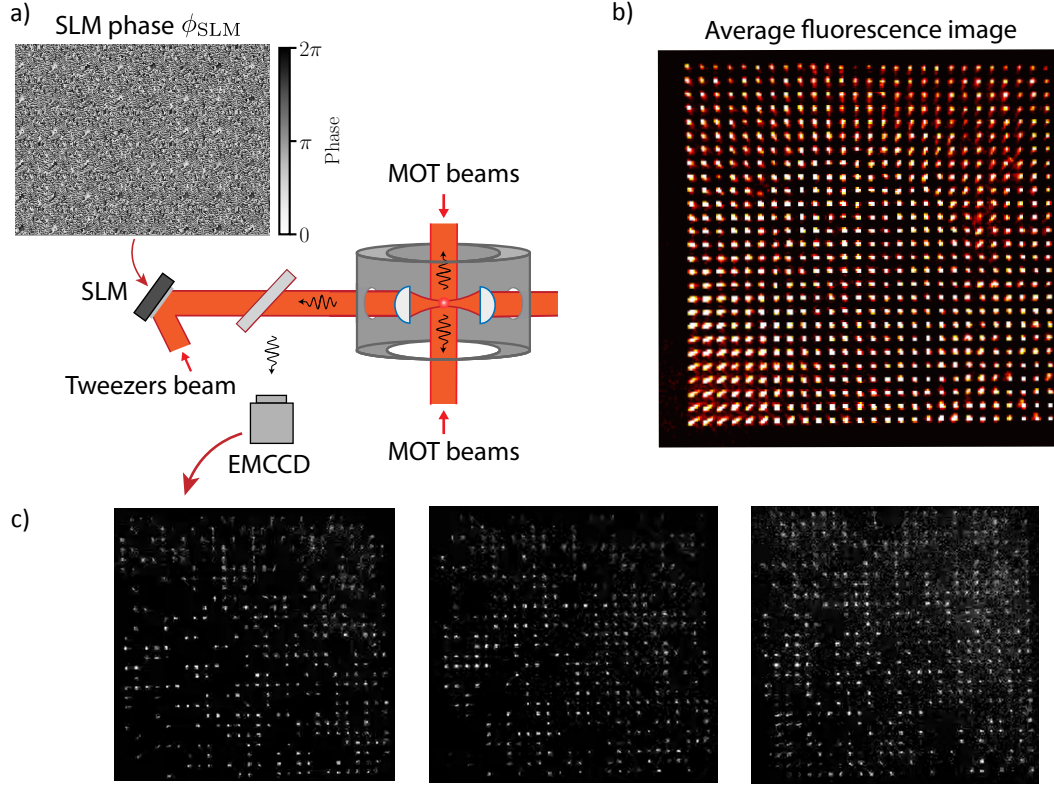
Figure 2.4: Observing the fluorescence of a 27×27 **array.** a) Sketch of the setup used to observe the fluorescence of the atoms, illustrated here on a $27 \times 27 = 729$ tweezers array. b) Average fluorescence image of the atoms in the tweezers array. c) Fluorescence images of the atoms using the EMCCD camera.

We use a Spatial Light Modulator (SLM) to modify the phase of the light. As the light pattern in the focal plane of the AL is the Fourier transform of both the phase and the amplitude of the light, it is impossible to *rigourously* produce arbitrary intensity patterns by only modifying the phase. To circumvent this issue, we use an optimization process based on the Gerchberg-Saxton (GS) algorithm [Gerchberg and Saxton, 1972], described in Section 4.1.1, to create the arrays.

Arrays of single atoms. Combining the use of the SLM and the GS algorithm [Nogrette *et al.*, 2014], we are able to create arrays of up to ~ 1000 traps. We use the EMCCD camera to observe the fluorescence of the atoms in the tweezers (see the setup sketch in Figure 2.4 a)), illustrated here on the example of a target 27×27 array, see Figure 2.4 b). Each bright dot is a single atom loaded in a tweezers. We show an average fluorescence image in order to see all the atoms on a single image.

We also show three examples of images recorded with the EMCCD camera, see

Figure 2.4 c). As the filling fraction of the tweezers is 1/2, we observe that: (i) approximately half of the tweezers are filled, and (ii) the position of the atoms in the array is random. The latter property is detrimental for the many-body experiment we perform, as we wish to work with fixed interactions between the atoms, hence with a fixed atomic configuration. The simplest solution is to wait until the array is fully filled. The probability p_N to have an array of N traps fully filled scales as $p_N \sim 0.5^N$, which is a possible solution only for small number of atoms. Two ways to overcome this problem have been explored: (i) by increasing the tweezers' filling fraction by manipulating the light-assisted collisions between pairs of trapped atoms [Brown *et al.*, 2019; Grünzweig *et al.*, 2010], and (ii) by re-arranging the atoms in the array to work with a fixed configuration. We use the latter solution, which I now describe.

Assembling atoms in tweezers arrays. Once the atoms are in the tweezers, we reorder them into a targeted configuration, a process which we call the atom-by-atom assembly. As half of the traps are filled with atoms due to the collisional blockade mechanism (see Section 2.1.1), we need to generate $2N$ traps in order to assemble an array of N atoms. Different techniques exist to rearrange atoms in tweezers arrays:

- By loading the atoms into the SLM traps and dynamically changing the SLM pattern to reach the desired configuration. The assembling of up to 21 atoms in 3D has been demonstrated [Song *et al.*, 2021].

- Using an Acousto-Optic Deflector (AOD) driven by multitones to generate multiple tweezers and dynamically changing the frequencies. The assembling of up to 51 atoms has been demonstrated [Bernien *et al.*, 2017].

- Using a SLM to create the tweezers and a single moveable tweezers (MT) driven by two AODs. The MT rearranges the atoms between the tweezers. This is the technique we use, for which the assembly of up to 209 atoms has been achieved, detailed in Section 4.2.

- Using a SLM and a 1D array of MTs generated by two AODs (actually a variant of the previous method). The atoms are assembled row by row. The assembly of up to 256 atoms has been demonstrated by the group of M. Lukin [Ebadi *et al.*, 2021].

To assemble the atoms into a targeted configuration, we add, onto the static traps generated by the SLM, a moveable tweezers (MT) generated by two orthogonal AODs. A sketch of the setup is shown in Figure 2.5 a). The power and position of the MT is
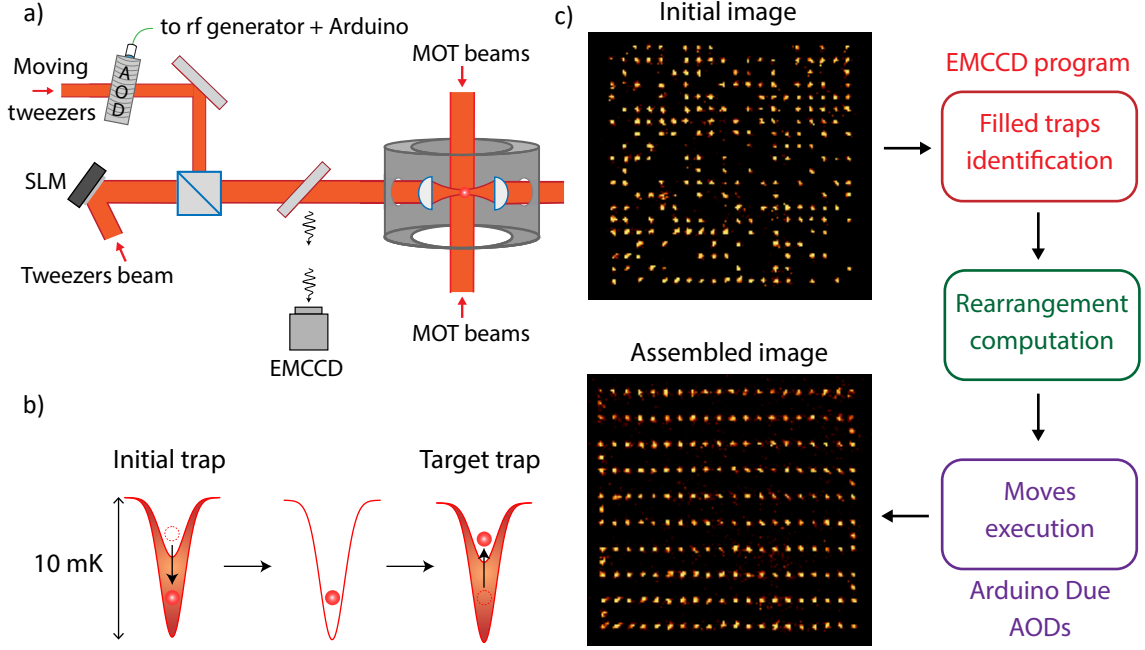
Figure 2.5: Assembling arrays of tweezers. a) Sketch of the setup. b) Procedure used to transfer an atom from an initial trap to a target trap. We shine the MT with a depth of $\sim 10\,\mathrm{mK}$, move the MT from the initial to the target trap, and swith off the MT. c) Overview of the assembling process, illustrated on an assembled 209-atom array. We take a first image of the initial configuration, compute and execute the rearrangement using the MT, and record an image of the atoms after assembling.

set by the radiofrequency (rf) power and frequency used to drive the AODs. The rf is set by two Arduino Due micro-controllers. To move an atom from an initial trap to a target trap, we use the following procedure, summarized in Figure 2.5 b):

- We start by focusing the MT onto the initial trap with low power. We then ramp up the MT power to a trap depth of $\sim 10\,\mathrm{mK}$ in $300 - 500\,\mu\mathrm{s}$, which is 10 times higher than the trap depth of the SLM traps. The atom is thus transferred into the MT.

- We then move the MT from the initial trap to the target trap at a speed of $100\,\mathrm{nm}/\mu\mathrm{s}$.

- We ramp down the MT power to zero in $300-500\,\mu\mathrm{s}$. The atom is thus transferred into the target trap.

The duration of each step is set to optimize the efficiency of the process, and is larger than the typical oscillation period of the atom in the tweezers. The typical efficiency
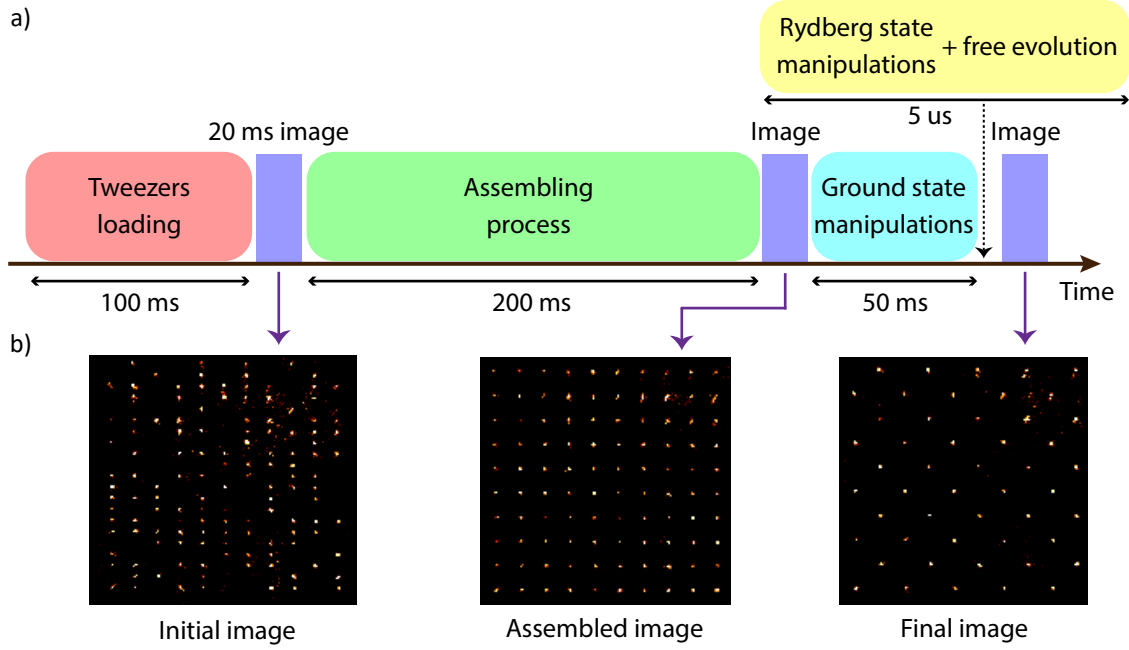
Figure 2.6: A typical experimental sequence. a) Overview of a typical experimental sequence. The duration of each operation is indicative and depends on the conducted experiment. b) Fluorescence images of the initial (left), assembled (centre) and final (right) configurations of an experiment conducted in the study of the transverse field Ising model (see Chapter 6).

of this process is $\sim 99\%$ [Barredo *et al.*, 2016], allowing for the assembly of hundreds of atoms with high fidelity.

At each repetition of the experiment, the initial position of the atoms is different. We thus need to calculate in real time the moves required to assemble the targeted configuration. To do so, we (i) take an image of the initial configuration, (ii) measure the atoms position and (iii) calculate the moves to reach the targeted configuration. We devised an algorithm (see Section 4.2.2) which optimizes the number of moves and the travelling distance of the MT, whilst keeping a relatively short calculation time. We take another image of the atoms after the assembling process allowing us to post-select the experiments for which the assembling process worked without producing any defect. The process is summarized in Figure 2.5 c) with the example of a 209-atom assembled array.

2.1.3 A typical experimental sequence

The typical experimental steps, described in Figure 2.6 a), are the following:

- **Loading the tweezers array.** We start by loading the tweezers from the MOT and take an image of the initial configuration. We then rearrange the atoms and take an image of the new position of the atoms. This step duration is $\sim 300\,\text{ms}$. The example of a 10×10 array is shown in Figure 2.6 b).

- **Ground-state atom manipulation.** We cool the atoms and prepare them into a specific internal ground-state by optical pumping in $\sim 50\,\text{ms}$, see Section 2.2.

- **Many-body experiment.** We transfer the atoms into specific Rydberg states (see Section 2.3) and let them interact under the dipole-dipole interaction. Thanks to the strong interactions between Rydberg atoms which govern the evolution of the system, this step takes typically $5\,\mu\text{s}$, much shorter than the other steps.

- **Final image.** We take a last image to measure the presence and absence of the atoms, which is directly linked to their internal states at the end of the previous step, as detailed in Section 2.3.2.

The duration of a complete experiment is thus typically $\leq 500\,\text{ms}$, which allows for fast repetition rates, above 2 Hz. The step durations given here are indicative and depend on the conducted experiment. Every measured quantity is related to the presence or the absence of the atom in the final image (see more detail in Section 2.3.2). To reconstruct the probability of presence of the atom in the tweezers p_{atom}, we repeat the same sequence $100 - 1000$ times.

2.2 Ground-state atom manipulations

This section presents the various manipulations we routinely perform on the individually-trapped ground-state atoms. These operations have two main goals: (i) reducing the atomic temperature which allows us to perform experiments on longer timescales (see Section 2.3), and (ii) to optically pump the atoms into a specific ground state in view of transferring the atoms into their Rydberg states (see Section 2.3.1).
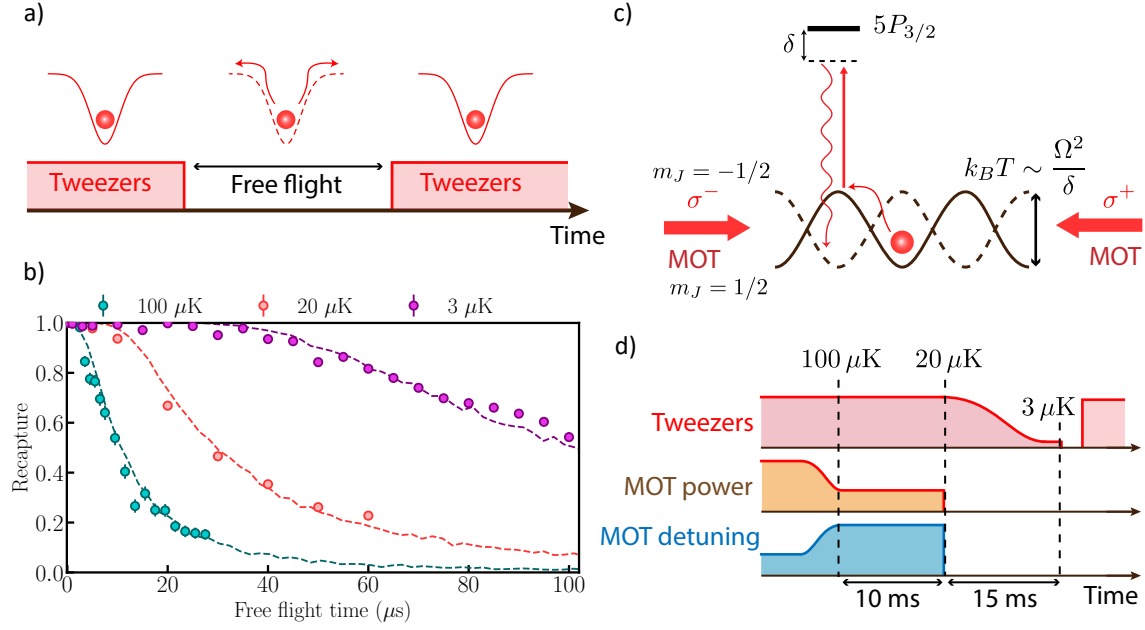
Figure 2.7: Cooling atoms in the tweezers. a) Sketch of the release-and-recapture experiment: we switch off the tweezers for a variable amount of time. The recapture probability depends on the atom temperature in the tweezers. b) Experimental results for three different temperatures, obtained after the different cooling steps described below. c) Sketch of the polarization gradient cooling created by the MOT beams with opposite polarization. The final temperature of the atoms is set by the amplitude of the potential, which gives $k_B T \sim \Omega^2/\delta$. d) Summary of the manipulations used to cool the atoms, with the corresponding temperatures.

2.2.1 Cooling the atoms in the tweezers

Due to the repulsive ponderomotive potential described in Section 2.3.2 which is applied by the tweezers on the Rydberg atoms, the tweezers are off during the many-body experiments. As the atom have a finite temperature hence a finite velocity, there is a probability that the atom leaves the trapping region during the many-body experiment, and is thus lost. In this subsection, I describe the techniques we use to cool the atoms in order to extend the time during which we can perform experiments without losing the atoms.

The release-and-recapture experiment. The standard technique to measure the temperature of an atom trapped in an optical tweezers is to do a release-and-recapture experiment: we first load an atom in the optical tweezers, switch it off (typically for a

few microseconds) and then switch it on again. When switching off the tweezers, the atom moves and eventually gets out of the trapping region, and is thus not recaptured. We repeat this experiment for different release times and obtain the curves shown in Figure 2.7 b) for three different temperatures of the atoms, obtained after the different cooling steps which are described below. Knowing the trapping volume and performing simulations of the release-and-recapture experiment for different temperatures (dashed lines) [Tuchendler *et al.*, 2008], we extract the atom temperature. The curve shown for $T = 100\,\mu\text{K}$ corresponds to the initial temperature of the atoms in the tweezers.

As can be seen in Figure 2.7 b), the recapture probability stays at ~ 1 for a few microseconds, and then start to decrease. This feature corresponds to the early times in which the atom explores the tweezers region. The losses become important after $\sim 2\,\mu\text{s}$ for $T = 100\,\mu\text{K}$, whereas they remain negligible for more than $20\,\mu\text{s}$ when $T = 3\,\mu\text{K}$, showing the importance of cooling the atoms. We use two techniques to cool the atoms: Sisyphus cooling and ramping down of the tweezers trap depth.

Sisyphus cooling using the MOT light. The Sisyphus cooling is a technique which allows atoms to reach sub-Doppler temperature. Its principle, based on polarization gradient [Wineland, Dalibard, and Cohen-Tannoudji, 1992], is sketched in Figure 2.7 c). We perform the Sisyphus cooling for a typical duration of 10 ms. The temperature of the atoms after Sisyphus cooling is $k_B T \sim \Omega^2/\delta$, with Ω the Rabi frequency of the MOT beams and δ their detuning from the $(5S, F = 2) \rightarrow (5P, F' = 3)$ transition. We increase the detuning and decrease the power in the MOT laser during this step to further lower the temperature. A limitation of the technique is the presence of a residual magnetic field. Before I started my PhD, the cooling was limited to temperatures of $\sim 40\,\mu\text{K}$. A careful compensation of the magnetic field (see Section 2.4.1) allowed us to reach a temperature of $20\,\mu\text{K}$.

Adiabatic ramping down of the tweezers trap depth. To further reduce the temperature, we add a second stage of cooling consisting of adiabatically ramping down the tweezers trap depth. We can decrease the trap depth without losing the atoms, as its initial value is $\sim 1\,\text{mK}$ and the temperature of the atoms after Sisyphus cooling is $\sim 20\,\mu\text{K}$. The probability P_l for the atom to be in the tweezers level $|l\rangle$ follows the Boltzmann law $P_l \sim e^{-E_l/kT}$, with $E_l = l\hbar\omega$, ω being the oscillation frequency of the atom in the tweezers. By adiabatically ramping down the trap depth, the probability P_l, and hence the ratio ω/T, remains constant. As ω decreases, T must also decrease and the atoms are cooled. In practice, we decrease the trap depth to $\sim 20\,\mu\text{K}$ in 15 ms,

which is slow compared to the inverse of the lowest oscillation frequency $\omega_\parallel = 20\,\text{kHz}$, leading to a temperature of the atoms $T = 3\,\mu\text{K}$.

A summary of the methods detailed in this subsection is presented in Figure 2.7 d). Starting with atoms at $T = 100\,\mu\text{K}$, we first decrease the MOT light power and increase its detuning to optimise the Sisyphus cooling. We then adiabatically ramp down the power in the tweezers, reaching a temperature of $T = 3\,\mu\text{K}$. To further reduce the atom temperature, we are in the process of implementing Raman sideband cooling [Kaufman, Lester, and Regal, 2012] in order to transfer the atoms into the tweezers motional ground state.

2.2.2 Internal states manipulations

The atoms in the MOT are distributed among the Zeeman sublevels of the $F = 2$ state. However, we need to prepare them into a specific ground state to efficiently transfer them into their Rydberg states (see Section 2.3.1). We use optical pumping to initialize the atoms in $|g\rangle = \left|5S_{1/2}, F = 2, m_F = 2\right\rangle$.

Hyperfine-level selective push-out beam. In order to measure the optical pumping efficiency, we use a detection method which allows us to discriminate between $F = 1$ and $F = 2$ of the $5S_{1/2}$ manifold, which I present now. The push-out beam is derived from a 780 nm laser, σ^+ polarized, and set on resonance on the closed transition $F = 2 \rightarrow F' = 3$. When the push-out beam is applied, atoms in $F = 2$ are heated and eventually expelled from the tweezers, whereas atoms in $F = 1$ are not affected and thus remain in the tweezers. The push-out beam duration is typically hundreds of microseconds. Its efficiency is higher than 99% and limited by non-resonant coupling to the $F' = 2$ state.

Optical pumping. We prepare the atoms in $|g\rangle$ by optical pumping. The optical pumping beam comes from a 795 nm laser on resonance with the $F = 2 \rightarrow F' = 2$ transition. Its σ^+ polarization ensures that $|g\rangle$ is a dark state, as shown in Figure 2.8 a). As the atoms may also decay to $F = 1$, we use a repumper to bring them back into the $F = 2$ manifold. The quality of the σ^+ polarization of the optical pumping is critical. If the polarization is not perfect, $|g\rangle$ is not a true dark state leading to a finite probability η that the atoms do not end up in $|g\rangle$ after the optical pumping procedure. Before my PhD, the finite optical pumping efficiency implied that $\eta \sim 1 - 5\%$. In order to reduce η, we implemented a more precise method to set the polarization,
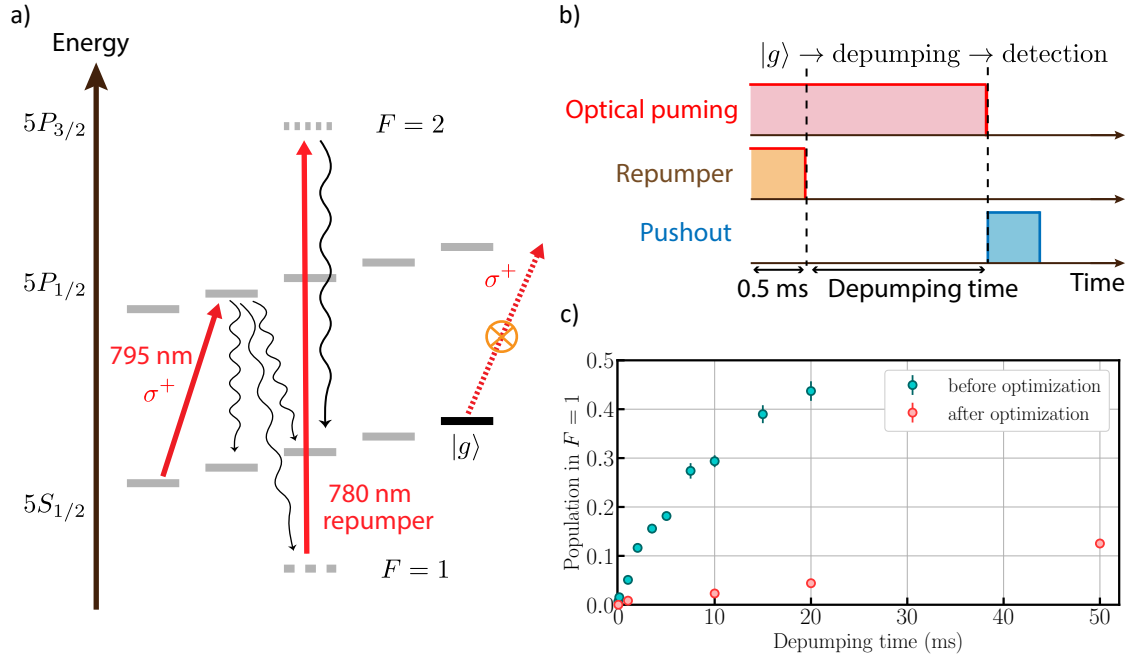
Figure 2.8: Optical pumping optimization. a) Principle of the optical pumping technique. Using a pure σ^+ beam at 795 nm combined with a repumper, the system is pumped into the $|g\rangle = \left|5S_{1/2}, F = 2, m_F = 2\right\rangle$ state. b) Sketch of the experiment used to optimize the optical pumping polarization. After pumping the atoms in $|g\rangle$, we let the optical pumping beam alone for variable depumping times. If the optical pumping is not perfectly polarized, the atoms eventually decay to the $F = 1$ state and are detected using the push-out beam. c) Experimental results of the above experiment before (green) and after (orange) optimizing the optical pumping polarization.

described in the Thesis of Adam Kaufman [2015] and presented in Figure 2.8 b):

- We apply optical pumping and the repumper to reach the targeted state $|g\rangle = \left|5S_{1/2}, F = 2, m_F = 2\right\rangle$. This requires that the optical pumping beam is already well polarized.

- Once the atoms are in $|g\rangle$, we shine for a varying duration the optical pumping beam without the repumper. If the beam is not perfectly polarized, the atoms are eventually depumped into $F = 1$.

- We switch off the optical pumping and measure the population in $F = 1$ using the push-out beam.

An imperfect optical pumping polarization results in a finite population in $F = 1$. We therefore minimize the population in $F = 1$ by precisely controlling the angle of

a)

b)

c)
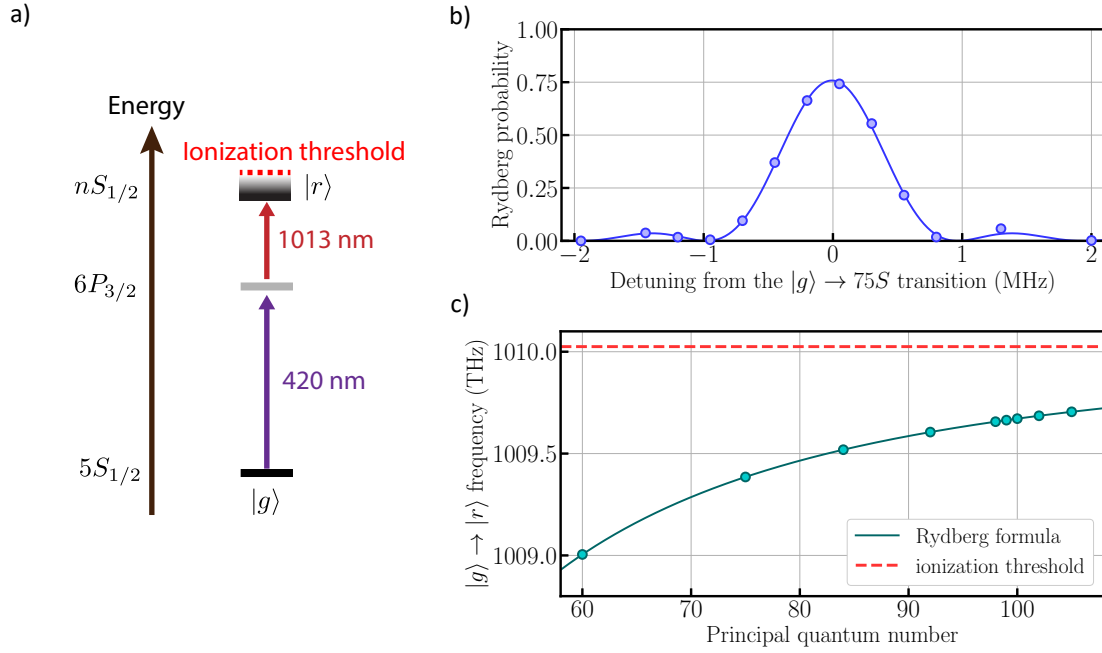
Figure 2.9: Ground-Rydberg spectroscopy using a two-photon transition. a) Sketch of the Rydberg excitation scheme. We use a two photon scheme with $6P_{3/2}$ as intermediate state to reach the Rydberg manifold. b) Typical spectrum of the $|g\rangle \to \left|75S_{1/2}, m_J = 1/2\right\rangle$ transition. We measure the probability to excite the atoms into the Rydberg state P_r as a function of the laser detuning from the transition. The solid curve is a fit using the Rabi formula. c) Ground-Rydberg transition frequency as a function of n for the nS series. The solid line is a fit using the Rydberg formula.

the waveplates. Figure 2.8 c) shows the result of this experiment before (green) and after (orange) optimization using the present technique. We derive the value of η by extrapolating the results for the typical optical pumping time of $500\,\mu$s and extract $\eta \simeq 0.5\%$. This remaining finite value of η is believed to come from an imperfect alignment of the optical pumping beam with respect to the magnetic field.

2.3 Excitation and manipulation of atoms in their Rydberg states

We now move on to the various manipulations related to the Rydberg states. I will start by giving an overview of how we excite the atoms to their Rydberg states, then explain how we detect and trap the Rydberg atoms, and finally describe the basic tools we use to manipulate the states of the atoms in the Rydberg manifold.

2.3.1 Excitation to the Rydberg states

Once the atoms are initialized in $|g\rangle$, we use two lasers with different wavelengths to transfer them into a chosen Rydberg state $|r\rangle$. We use two schemes: a two-photon transition driving a Rabi oscillation, or a STImulated Raman Adiabatic Passage (STIRAP). The driving of ground-Rydberg Rabi oscillations is detailed in Chapter 3.

Two-photon scheme. The transition wavelength between $|g\rangle$ and $|r\rangle$ is 297 nm, which is challenging to achieve in an efficient way using a single laser (see Section 3.1). Instead, we use a two-photon scheme to reach the Rydberg state (see Figure 2.9 a)) involving two lasers at 420 nm and 1013 nm, detuned with respect to the $6P_{3/2}$ state (see Section 3.2). We use M-Squared Titanium:Sapphire lasers with wavelengths 420 nm and 1013 nm, described in detail in Section 3.2.1 and Section 3.2.2.

The selection rules on dipole matrix elements imply that the reachable Rydberg states are nS or nD, n being the principal quantum number. A typical spectrum of the $|g\rangle \to \left|75S_{1/2}, m_J = 1/2\right\rangle$ transition is presented in Figure 2.9 b). The solid curve is a fit to the data using the Rabi formula. We repeat this experiment for the typical nS Rydberg states we use, ranging from 60 to 100 and measure the ground-Rydberg transition frequency, see Figure 2.9 c). The solid line is a fit to the data using the Rydberg formula:

$$E_{n,S} = E_\mathrm{I} - \frac{13.6\,\mathrm{eV}}{(n - \delta_S)^2}, \tag{2.4}$$

with $\delta_S \simeq 3.13$ the quantum defect for nS states and E_I the ionization threshold. We set E_I as a free parameter and measure $E_\mathrm{I} = h \times 1010.022(7)\,\mathrm{THz}$, in good agreement with accurate measurements $E_\mathrm{I} = h \times 1010.024\,\mathrm{THz}$ [Lee *et al.*, 1978].

STIRAP excitation. The STIRAP technique [Vitanov *et al.*, 2017] is an adiabatic transfer of the atoms from the ground state to the Rydberg state without populating the intermediate state, thus limiting the influence of spontaneous emission from the intermediate state (see Section 3.3.2). Here, the two lasers are resonant with the $6P_{3/2}$ state. The temporal pulse sequence is presented in Figure 2.10 a): we shine both lasers using a Gaussian shape, starting with the 1013 nm laser. To minimize the excitation time, we remove the parts during which only one laser is on (grey area). With the typical durations we use, the atoms are excited in $\sim 800\,\mathrm{ns}$.

The main advantage of the STIRAP lies in its insensitivity to many parameters, illustrated here in Figure 2.10 b) by measuring the Rydberg excitation probability P_{75S} as a function of the lasers detuning from the $|g\rangle \to \left|75S_{1/2}, m_J = 1/2\right\rangle$ transition. We
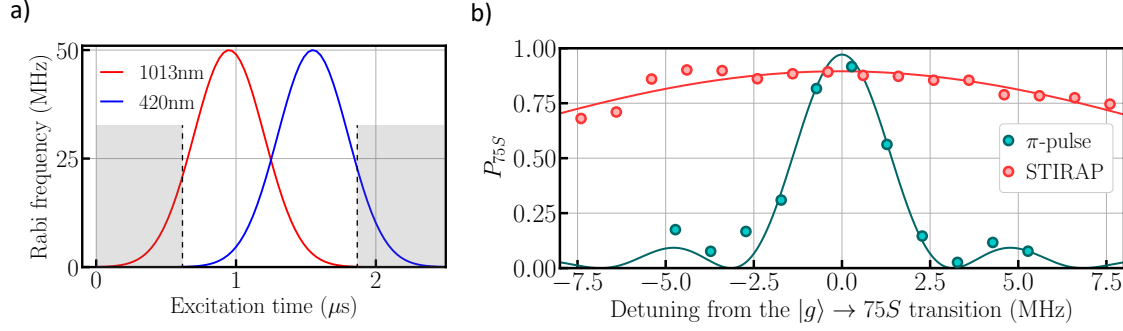
Figure 2.10: STIRAP excitation. a) Time profile of the laser pulses. We first shine the 1013 nm laser coupling the intermediate state to the Rydberg state, and then shine the 420 nm laser. b) Rydberg excitation probability P_{75S} as a function of the detuning, with a π-pulse (green) and the STIRAP (orange). Although the π-pulse is more efficient, the STIRAP efficiency is much broader which makes it very convenient on a daily use.

compare the results for the STIRAP (orange), and the 2-photon excitation scheme (green) using the same Rabi frequencies. The solid lines are: (i) a Gaussian fit for the STIRAP, and (ii) the fitted Rabi formula for the π-pulse. As the STIRAP is an adiabatic process, its efficiency is constant over a range of detuning of $5 - 10\,\mathrm{MHz}$.

Another appealing feature lies in its large insensitivity to the exact value of the lasers Rabi frequencies. The STIRAP remains efficient even though the Rabi frequencies fluctuate on a daily basis. We use the STIRAP insensitivity to homogeneously excite arrays with sizes comparable to the excitation lasers waists [de Léséleuc, 2018].

De-excitation to the ground state. For the many-body experiment presented in Part III in which we use several Rydberg states, we use the ability to selectively de-excite a specific Rydberg state back to the ground state. We take advantage of the short lifetime of the $6P_{3/2}$ level to de-excite the atoms in nS by simply shining the 1013 nm laser on resonance (see Figure 2.11 a)). We drive a Rabi oscillation with $\Omega_{1013} \gg \Gamma_{6P}$, leading to a decay rate $\propto \Gamma_{6P}/2$. To assess the speed at which the de-excitation occurs, we measure the probability P_r to find the atom in $|r\rangle = |60S_{1/2}, m_J = 1/2\rangle$ (the detection method is detailed below) as a function of the de-excitation time t_{deexc}, as shown in Figure 2.11 b). The solid line is a fit to the data by a damped sine of the form $A\cos^2(\Omega_{1013}t_{\mathrm{deexc}}/2)e^{-t_{\mathrm{deexc}}/\tau_{\mathrm{eff}}}$, with Rabi frequency $\Omega_{1013} = 40\,\mathrm{MHz}$ and effective lifetime $\tau_{\mathrm{eff}} = 35(1)\mathrm{ns}$. The effective lifetime is compatible with the $6P_{3/2}$ lifetime considering the multiple decay channels through the $6P_{3/2}$ state. The de-excitation process is nearly over after $\sim 100\,\mathrm{ns}$. We set a duration $t_{\mathrm{deexc}} = 300\,\mathrm{ns}$ to make sure the atoms decayed back to the ground state.
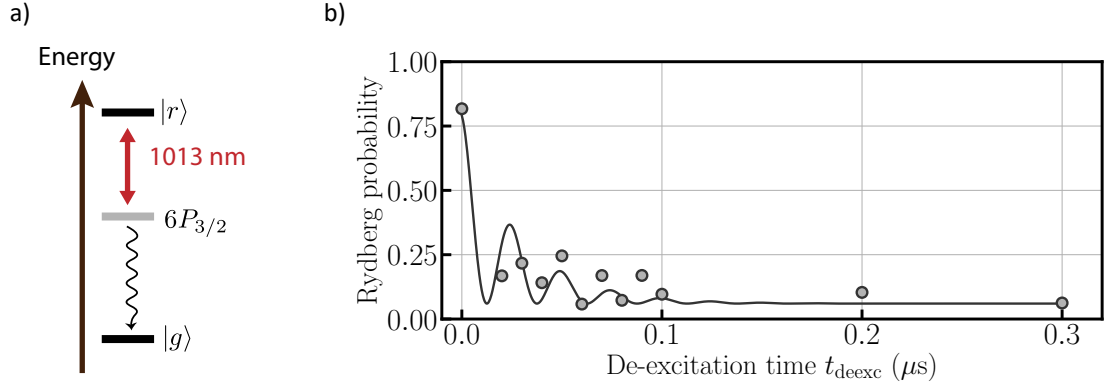
Figure 2.11: De-excitation of the Rydberg atoms. a) Sketch of the involved levels. We shine the 1013 nm laser on resonance with the $|r\rangle \to 6P_{3/2}$ transition. The atoms quickly decay back to the ground state due to the short lifetime of the $6P_{3/2}$ state. b) Probability P_r to measure the atom in $|r\rangle = \left|60S_{1/2}, m_J = 1/2\right\rangle$ as a function of the de-excitation time t_{deexc}. The solid line is a fit to the data by a damped sine of the form $A\cos^2(\Omega_{1013}t_{\text{deexc}}/2)e^{-t_{\text{deexc}}/\tau_{\text{eff}}}$, with Rabi frequency $\Omega_{1013} = 40\,\text{MHz}$ and effective lifetime $\tau_{\text{eff}} = 35(1)\,\text{ns}$.

2.3.2 Ponderomotive potential for Rydberg detection and Rydberg trapping

Due to the (repulsive) ponderomotive potential exerted by the tweezers onto the Rydberg atoms, the atoms are not trapped during the quantum simulation experiments. As the atoms have a finite temperature (see Section 2.2.1), the Rydberg experiments' duration is limited to $\sim 10 - 20\,\mu\text{s}$ before the atoms start to leave the trapping region, and are thus lost. A solution to extend the experiments' duration is to trap the Rydberg atoms. In this subsection, I detail the effect of the tweezers' ponderomotive potential on the Rydberg atoms, and explain how we trap them. The results presented here are published in Barredo *et al.* [2020].

Ponderomotive potential and Rydberg state detection. We consider the Rydberg atom as an approximately free electron around the ionic core. A free electron placed in an oscillating electric field $\vec{E}$ of frequency ω feels a ponderomotive potential [Younge *et al.*, 2010] U_{p} expressed as:

$$U_{\text{p}} = \frac{e^2}{4m\omega^2}E^2,\qquad(2.5)$$

with m and e the mass and the charge of the electron. As this potential is repulsive, the Rydberg atoms are expelled from the tweezers. We use the ponderomotive potential as an asset for the detection: when we switch back on the tweezers, the Rydberg
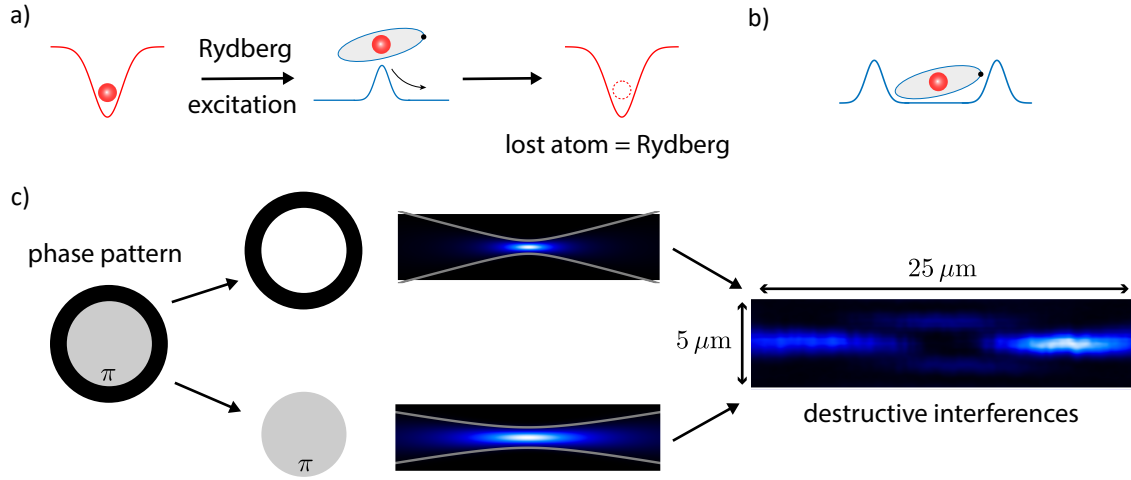
Figure 2.12: Trapping Rydberg atoms using bottle beam traps. a) Effect of the ponderomotive poential. When the atom is in a Rydberg state, the tweezers is repulsive and the atom leaves the trapping region. b) To trap the Rydberg atoms, we place them in a dark region surrounded by light. c) The SLM phase pattern is divided into two regions, π-phase shifted one from each other. Each region create tweezers which interferes destructively, giving rise to a dark region surrounded by light. The last image shows the measured intensity profile of the BoB trap.

atoms are expelled and lost (see Figure 2.12 a)), whilst the ground-state atoms are recaptured. This method allows for detection efficiencies above 95% (see Section 3.3.1).

Rydberg trapping using a bottle-beam trap. In order to trap the Rydberg atoms, we place them into hollow traps, i.e., dark spots surrounded by light (see Figure 2.12 b)). Thanks to the ponderomotive potential, the Rydberg atoms stay in the dark spots and are thus trapped.

To produce the hollow traps, we use a second SLM and create 'Bottle-Beam traps' (BoB traps) [Ozeri, Khaykovich, and Davidson, 1999; Xu *et al.*, 2010]. The phase pattern of the second SLM is the same as the tweezers SLM, with an extra π phase added to half of the phase pattern, as shown in Figure 2.12 c). At the focal point of the lens, the field diffracted by the two parts interfere destructively, thus producing a dark spot instead of a maxima of light. The image on the right of Figure 2.12 c) is the real, measured intensity profile, which looks like a bottle with caps on both sides, hence its name of "bottle-beam trap".
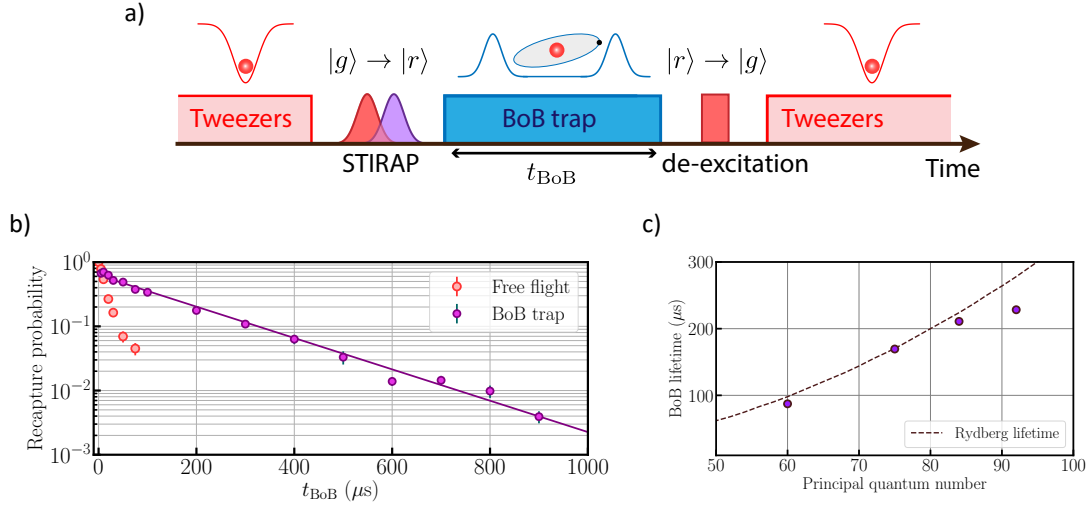
Figure 2.13: Demonstration of Rydberg trapping. a) Experimental procedure. We switch off the tweezers, excite the atom to the Rydberg state $|r\rangle$, and switch on the BoB trap for various durations t_{BoB}. We then de-excite the atom back to the ground state and trap it back in the regular tweezers. b) Recapture probability as a function of the BoB trap duration (purple) and in free-flight (red), with $|r\rangle = \left|75S_{1/2}, m_J = 1/2\right\rangle$. The Rydberg atoms are kept for longer times in the BoB trap, demonstrating Rydberg trapping. The solid line is an exponential fit to the data, from which we extract the $75S$ lifetime. c) We repeat the experiment for various nS Rydberg states and report their lifetime in the BoB trap. for $n \sim 60 - 90$, the BoB lifetime matches the Rydberg lifetime.

Measurement of Rydberg lifetime.   To demonstrate the trapping of Rydberg atoms using the BoB trap, we perform the following experiment, described in Figure 2.13 a):

- We initialize the atom into the $|g\rangle$ state, switch off the tweezers, and shine the Rydberg excitation lasers to reach the $|r\rangle$ state.

- We apply the BoB trap for varying durations t_{BoB}.

- We switch off the BoB trap, de-excite the atoms to the ground state, switch the tweezers on again and measure the recapture probability.

The results of an experiment involving the $75S_{1/2}$ state are shown in Figure 2.13 b). We perform the experiment with (purple) and without (red) the BoB trap. We observe that at long times, the recapture probability is higher using the BoB trap, demonstrating Rydberg trapping. The decay of the recapture probability decreases exponentially (solid line) with t_{BoB}, which is expected due to the finite Rydberg lifetime: when the atom naturally decays to another Rydberg state, we don't bring it
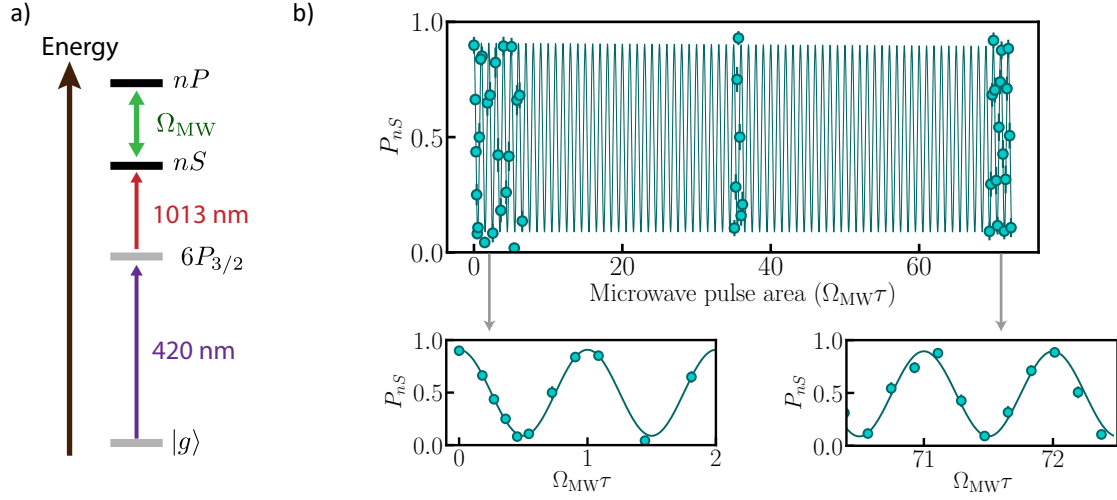
Figure 2.14: Rabi oscillations between Rydberg states. a) Sketch of the levels. We first initialize the atoms into nS, then use microwave field to couple to a nP Rydberg state. b) Rabi oscillations between the two Rydberg states $60S$ and $60P$. After 72 cycles we observe no appreciable damping, demonstrating the long coherence time of the system. A magnification of the beginning and the end of the oscillation is shown.

back to the ground state with the de-excitation pulse and the atom is thus lost. We extract from the fit the lifetime of the Rydberg atom in the BoB trap. We perform this experiment for various nS states and measure the lifetime of the atoms in the BoB trap, shown in Figure Figure 2.13 c). The dashed line represents the theoretical values of the lifetimes at 300 K [Beterov *et al.*, 2009]. We observe a good agreement with the theory for $n \sim 60 - 90$, which shows that the trapping lifetime is limited by the Rydberg lifetime. For $n \geq 90$, the lifetime of the atoms in the BoB is lower than the Rydberg lifetime. This lower lifetime is analyzed in detail in the thesis of Vincent Lienhard [2019], and is mainly due to the size of the Rydberg atom which is comparable to the trapping volume.

The Rydberg trapping could be used to study many-body physics for extended duration. However, the gain in time is not drastic as the system is still limited by the Rydberg lifetime. This technique is of high interest for longer Rydberg lifetime, e.g. in cryogenic environment [Schymik *et al.*, 2021], or using circular Rydberg states for which 2D confinement has been demonstrated [Cortiñas *et al.*, 2020].

2.3.3 Microwave manipulation of Rydberg states

Once the atoms are in a specific nS state, we use a microwave field to transfer them towards nearby nP states. This ability will be of great importance when using the resonant dipole-dipole interaction between Rydberg states, as discussed in Part III.

Microwave transitions between Rydberg states. For the range of principal quantum numbers n we use, the $nS \to nP$ transition frequency is in the $1 - 20\,\text{GHz}$ range, which is accessible with common microwave synthesizers. The synthesizer is connected to an antenna placed on top of the experimental chamber, which produces a microwave field with Rabi frequency Ω_{MW} and frequency f_{MW}, (see Figure 2.14 a)). The microwave transitions between Rydberg states have two assets:

- The strong dipole coupling between Rydberg states allows for Rabi frequencies up to 20 MHz with microwave power in the range $\sim 1 - 100\,\text{mW}$.

- The low intrinsic noise of microwave synthetisers combined with the extended lifetime of the Rydberg states allow for coherence of the Rabi oscillations over long timescales.

An example of a Rabi oscillation is presented in Figure 2.14 b). We use the Rydberg states $\left|60S_{1/2}, m_J = 1/2\right\rangle$ and $\left|60P_{3/2}, m_J = 3/2\right\rangle$, with $\Omega_{\text{MW}} = 2\pi \times 18\,\text{MHz}$ and $f_{\text{MW}} = 17176\,\text{MHz}$. We measure the probability P_{60S} for the atom to be in the $60S_{1/2}$ state (using the de-excitation technique presented above) as a function of the microwave pulse area. We observe no appreciable damping of the oscillation after 72 cycles, showing the long coherence time of the system. The solid line is a fit to the data by a sine function. To appreciate the matching of the fit, we show a magnification of the beginning and the end of the Rabi oscillation.

Although the system is highly coherent, the use of microwaves has several shortcomings:

- The control over the polarization of the microwave is challenging. Even though the polarization at the output of the antenna is linear, the multiple reflections from the metallic vacuum chamber scrambles the polarization at the position of the atoms.

- The microwave wavelength is $\sim 1\,\text{cm}$, which implies that the excitation is global. To excite specific atoms in the array, we combine the microwaves with an addressing beam.
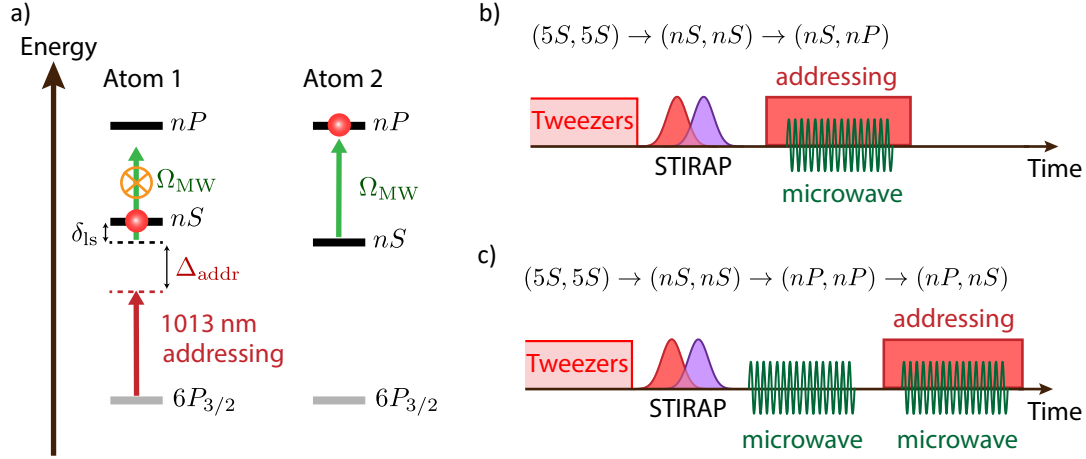
Figure 2.15: Selective excitation using an addressing beam. a) Sketch of the levels. We consider two atoms. The first one is addressed by a 1013 nm beam which light-shifts by δ_{ls} the nS level. The microwave field is thus not resonant with this atom. b) Sketch of the experimental sequence using the light-shift to prepare the two-atom state (nS, nP). c) Sketch of the experimental sequence using the Autler-Townes effect to prepare the two atom state (nP, nS).

We use a second antenna placed along the Zeeman axis to have some flexibility on the polarization: as the polarization balance of the antennas are different, we use the one whose polarization favors the targeted transition. A solution to set the polarization could be to use both microwave antennas at the same time and adjust the relative phase of the driving field.

Selective excitation using single-site addressing. We combine the global microwave field with a local addressing laser field to transfer specific atoms from the nS state to the nP state. The single-site addressing is a 1013 nm laser focused down on the atoms by the aspherical lens, which allows us to shift the $nS \rightarrow nP$ transition frequency of a specific atom. We explored two ways of proceeding:

- By setting the 1013 nm laser far-detuned from the $6P_{3/2} \rightarrow nS$ transition by Δ_{addr} and using a Rabi frequency $\Omega_{\text{addr}} \ll \Delta_{\text{addr}}$, we light-shift the nS state of one atom by $\delta_{\text{ls}} = \Omega_{\text{addr}}^2 / 4\Delta_{\text{addr}}$ (see Figure 2.15 a)) [de Léséleuc *et al.*, 2017]. The microwave field is thus out of resonance for the addressed atom. The experimental preparation is sketched in Figure 2.15 b).

- By setting the 1013 nm laser on resonance with the $6P_{3/2} \rightarrow nS$, we split the
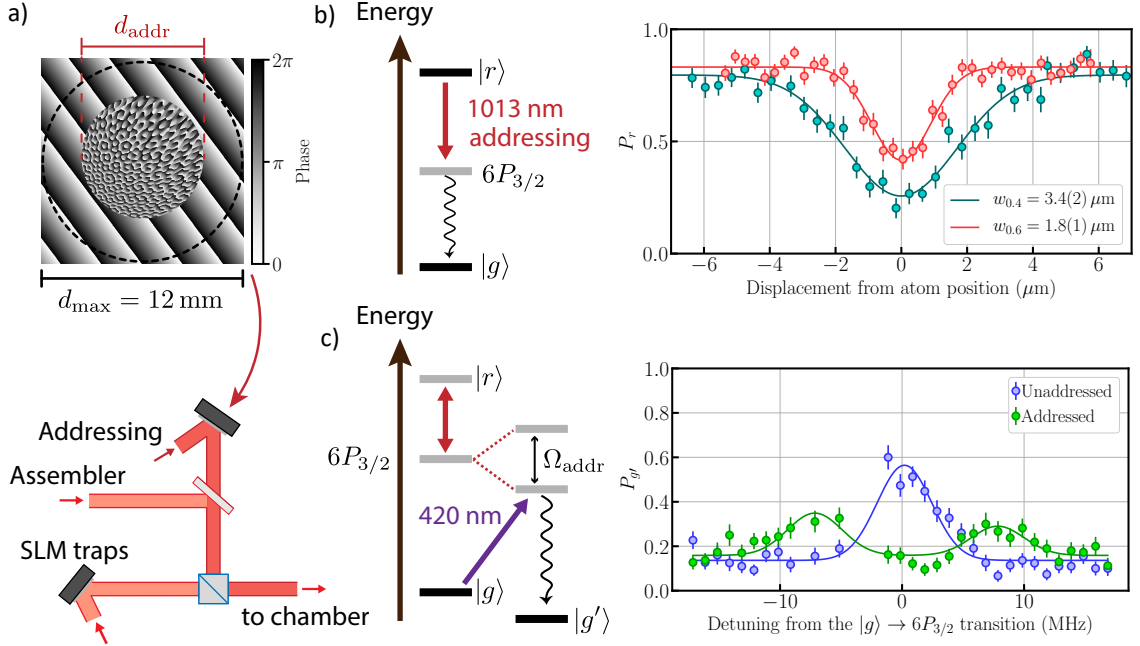
Figure 2.16: Characterization of the addressing. a) Sketch of the optical setup. We use a dichroic mirror to combine the addressing beam with the assembler. We put an iris of diameter $\eta = d_{\mathsf{addr}}/d_{\mathsf{max}}$ on the SLM phase pattern to increase the waist of the addressing tweezers. b) Measurement of the addressing tweezers waist w_η using the de-excitation technique. We show the results for two irises: $\eta = 0.4$ (green) and $\eta = 0.6$ (red). c) Measurement of the addressing Rabi frequency using the Autler-Townes effect described in Section 3.2.2. We measure the probability $P_{g'}$ to find the atom depumped in $F = 1$, gathered under the notation $|g'\rangle$. The experiment is performed with (green) and without (blue) the addressing.

nS level using the Autler-Townes effect described in Section 3.2.2. To avoid de-excitation of the atoms, we first transfer both atoms into the nP state, then transfer them back in presence of the addressing beam, as sketched in Figure 2.15 c). The microwave field is out of resonance for the addressed atom.

Arbitrary addressing using a SLM. During my PhD, we extended the use of these techniques to an arbitrary number of addressed atoms. To do so, we use a second SLM to generate an array of addressing tweezers at 1013 nm, combined with the optical path of the moving tweezers using a dichroic mirror (see Figure 2.16 a)). The phase pattern of the addressing SLM is calculated using the GS algorithm, described in Section 4.1.1. To reduce position mismatch between the addressing array and the atom array, the waist w_η of the addressing tweezers is enlarged by applying an iris of

diameter d_{addr} onto the SLM. We define the normalized diameter $\eta = d_{\text{addr}}/d_{\text{max}}$, with d_{max} the diameter of the 1013 nm laser. I briefly describe now how we determined the waist and the Rabi frequency of the addressing tweezers array.

To measure the waist of the addressing laser beams, we initially prepare the atoms in $|r\rangle = \left|75S_{1/2}, m_J = 1/2\right\rangle$ and apply the addressing on resonance with the $|r\rangle \rightarrow 6P_{3/2}$ transition for a duration t_{deexc} to de-excite the atoms. The Rabi frequency is set such that $\Omega_{\text{addr}} \leq \Gamma_{6P}$. Under these conditions, the probability P_r to find the atom in the Rydberg state evolves as $P_r \propto e^{-\Omega_{\text{addr}}^2 t_{\text{deexc}}/\Gamma_{6P}}$. We set $\Omega_{\text{addr}} t_{\text{deexc}} \ll 1$ such that the de-exciting rate can be considered as $\propto \Omega_{\text{addr}}^2/\Gamma_{6P}$. We measure P_r as a function of the tweezers position. As the signal is $\propto \Omega^2$, we directly measure the intensity profile of the addressing tweezers. The results are presented in Figure 2.16 b) for two diameters of the iris $\eta = 0.4$ (green), which gives $w_{0.4} = 3.4(2)\,\mu\text{m}$ and $\eta = 0.6$ (red), which gives $w_{0.6} = 1.8(1)\,\mu\text{m}$. In the following, we fix the iris diameter to be $\eta = 0.6$, such that the waist is about twice the one of the tweezers.

To measure the Rabi frequency of the addressing beam, we perform an experiment based on the Autler-Townes effect described in Section 3.2.2. We probe the $|g\rangle \rightarrow 6P_{3/2}$ transition using the 420 nm laser, and measure the splitting of the $6P_{3/2}$ level due to the addressing beam by a quantity $\hbar\Omega_{\text{addr}}$, as presented in Figure 2.16 c). We perform the experiment with two atoms: one with (green) and one without (red) the addressing beam, allowing to probe the free-space transition and the line split by the Autler-Townes effect. We extract a Rabi frequency $\Omega_{\text{addr}} = 2\pi \times 15(1)\,\text{MHz}$ when using a power of 9 mW and a waist of 1.8 μm.

2.4 Control of the electromagnetic environment

The Rydberg atoms are sensitive to both magnetic and electric fields. It is thus essential to control the electromagnetic environment in order to manipulate them accurately.

2.4.1 Magnetic field

We use two types of coils to control the magnetic field: the compensation coils which cancel the ambient magnetic field, and the quantization coils which define the quantization axis. The quantization coils are placed inside the vacuum chamber, on the lenses holder. When performing an experiment, we switch from an anti-
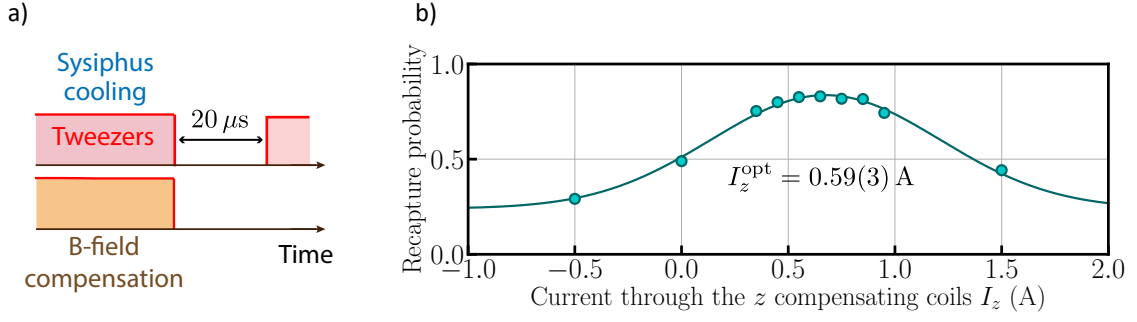
Figure 2.17: Magnetic field compensation using Sisyphus cooling. a) Sketch of the experiment. We vary the magnetic field compensation value during the Sisyphus cooling, then release the atoms for $20\,\mu$s and measure the recapture probability. b) Evolution of the recapture probability as a function of the current through the z compensation coils. The solid line is a Gaussian fit to the data from which we extract $I_z^{\mathrm{opt}} = 0.59(3)\,$A.

helmholtz configuration to generate the quadrupole field for the MOT, to a Helmholtz configuration producing a magnetic field in the range $B_z \sim 0 - 50\,$G along the z direction contained in the atomic plane.

Magnetic field compensation. We use three pairs of coils placed outside of the vacuum chamber to cancel the magnetic fields in the three directions of space. Various techniques allow us to compensate the magnetic fields. Before I started my PhD, they relied on spectroscopy. These methods are time consuming, as numerous spectra have to be recorded to reach cancellation of the magnetic field. During my PhD, we were able to accelerate the process by using the temperature of the atoms as an observable. As briefly explained in Section 2.2.1, the Sisyphus cooling is more efficient if all the Zeeman sublevels are degenerate, meaning that the magnetic field is canceled. The experiment, sketched in Figure 2.17 a), is the following: we vary the current going through the compensation coils during the Sisyphus cooling and measure the recapture probability after opening the tweezers for $20\,\mu$s: the lower the temperature, the higher the recapture probability is. The results for the compensation coils along z are shown in Figure 2.17 b). The solid line is a fit to the data by a Gaussian function, from which we extract the current which minimizes the atom temperature.

A new quantization axis. As will be discussed in Chapter 8, the interactions between two Rydberg atoms depend on the relative orientation of the magnetic field with respect to the inter-nuclear axis. Depending on the many-body experiment we perform, we either use a magnetic field in (z direction), or perpendicular to (x direction) the

a)

b)

c)
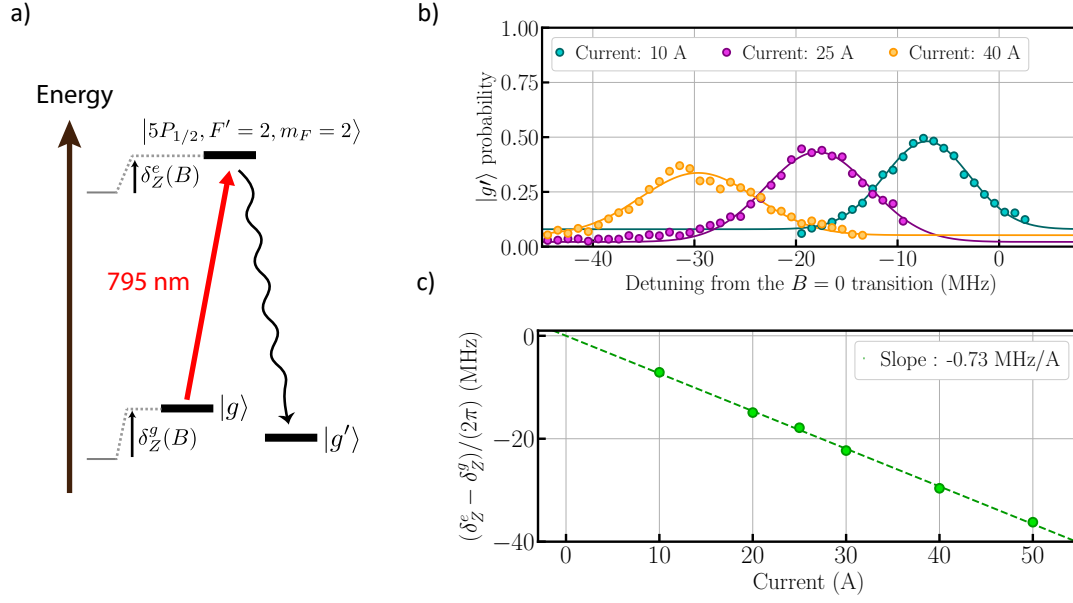
Figure 2.18: Characterization of the quantization coils along the x axis. a) Sketch of the levels. b) Spectra of the $|g\rangle \rightarrow \left|5P_{1/2}, F = 2, m_F = 2\right\rangle$ transition for different values of the current through the coils. c) Measurement of the differential Zeeman shift as a function of the current. The dashed line is a fit to the data with a slope of $-0.73\,\mathrm{MHz/A}$ from which we derive $\alpha = 0.78\,\mathrm{G/A}$.

atomic plane. The latter was implemented during my PhD. We added an extra pair of coils outside the vacuum chamber along the aspherical lenses axis. The ratio α between the value of the magnetic field and the intensity going through the coils $B_x = \alpha I_x$, which can be calculated using the Biot-Savart law, is measured via the spectroscopy of the $|g\rangle \rightarrow \left|5P_{1/2}, F = 2, m_F = 2\right\rangle$, sketched in Figure 2.18 a). Initializing the atoms in $|g\rangle$, we shine the 795 nm laser and measure the probability $P_{g'}$ to find the atom in depumped in the $F = 1$ states, gathered under the notation $|g'\rangle$, using the push-out beam. Typical spectra for various currents are shown in Figure 2.18 b). The transition frequency changes by $\delta_Z^e - \delta_Z^g$ due to the Zeeman effect which shifts the levels by $\delta_Z^g/(2\pi) = 1.4 \times B_x$ for $|g\rangle$ and $\delta_Z^e/(2\pi) = 0.46 \times B_x$ for $\left|5P_{1/2}, F = 2, m_F = 2\right\rangle$. We measure $(\delta_Z^e - \delta_Z^g)/(2\pi) = -0.94 \times B_x$ for different values of the current, see Figure 2.18 c). The dashed line is a linear fit to the data with a slope of $-0.75\,\mathrm{MHz/A}$, from which we derive $\alpha = 0.78\,\mathrm{G/A}$. These coils allow for magnetic field values in the range $B_x \sim 0 - 50\,\mathrm{G}$.

Rotation of the quantization axis. To perform quantum simulation with a quantization axis perpendicular to the atom array, along x, we need to pump the atom
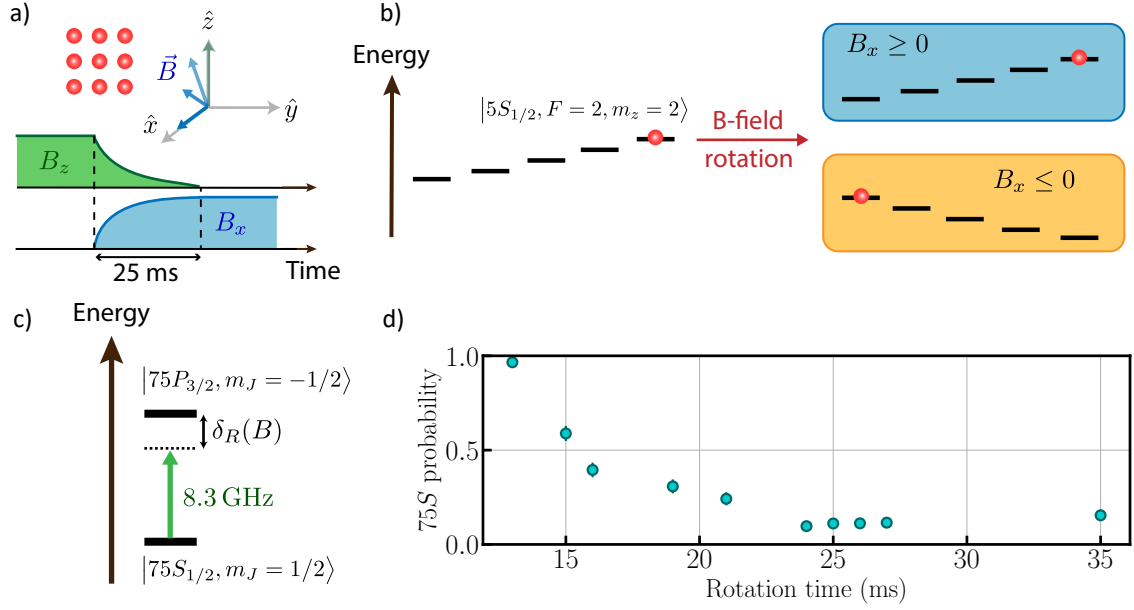
Figure 2.19: Rotation of the quantization axis. a) Starting with the magnetic field in the atomic plane along z, we rotate it perpendicular to the array, along x, in 25 ms. b) Initializing the atoms in $\left|5S_{1/2}, F = 2, m_z = 2\right\rangle$, we flip the magnetic field along $\hat{x}$. The atoms remain in the highest energy state, i.e., in $m_x = 2$ if $B_x \geq 0$, or $m_x = -2$ if $B_x \leq 0$. c) Sketch of the levels involved in the Ramsey experiment. We apply two microwave $\pi/2$-pulses separated by $0.5\,\mu$s, with a detuning $\delta_R(B)$. d) P_{75S} as a function of the rotation time. The probability evolves due to the dependence of δ_R on the value of the magnetic field. After ~ 25 ms, the magnetic field is stabilized.

into the $\left|g\right\rangle = \left|5S_{1/2}, F = 2, m_x = 2\right\rangle$ state. However, as the optical pumping beam propagates along z, we cannot use it when the magnetic field is along x. To solve this issue, we start by pumping the atoms into $\left|5S_{1/2}, F = 2, m_z = 2\right\rangle$ with the magnetic field along z. We then rotate the magnetic field by switching on B_x while switching off B_z, as sketched in Figure 2.19 a). As the atoms are initialized into the highest energy state, they follow the rotation of the magnetic field by remaining in the highest energy state, i.e, $\left|5S_{1/2}, F = 2, m_x = 2\right\rangle$ if $B_x > 0$ and $\left|5S_{1/2}, F = 2, m_x = -2\right\rangle$ if $B_x < 0$ (see Figure 2.19 b)). The same reasoning applies if the atoms are initialized in the lowest energy state by inverting the direction of B_z. Using this method, we can reach both stretched states in both magnetic field directions without the need to change the polarization of the optical pumping laser. This feature will be used in Section 8.3.

The duration of the magnetic field rotation is limited by eddy currents in the copper gaskets used to seal the vacuum window. We measure their influence using Ramsey interferometry on the $\left|75S_{1/2}, m_J = 1/2\right\rangle \rightarrow \left|75P_{3/2}, m_J = -1/2\right\rangle$ transition at a

a)

$V_1 = -V_x/2 + V_y/2 + V_z/2$
$V_2 = -V_x/2 - V_y/2 + V_z/2$

$V_5 = V_x/2 + V_y/2 + V_z/2$
$V_6 = V_x/2 - V_y/2 + V_z/2$

b)

$V_3 = -V_x/2 + V_y/2 - V_z/2$
$V_4 = -V_x/2 - V_y/2 - V_z/2$

$V_7 = V_x/2 + V_y/2 - V_z/2$
$V_8 = V_x/2 - V_y/2 - V_z/2$

$V_z/2$

$-\dfrac{V_x}{2}$ $\dfrac{V_x}{2}$

$-V_z/2$
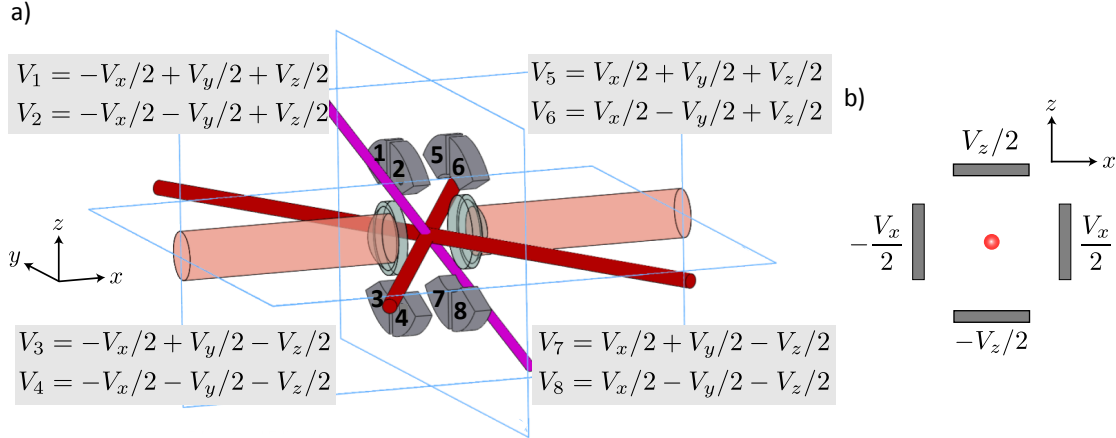
Figure 2.20: Electrodes configuration. Adapted from the Thesis of Lucas Béguin [2013] a) Sketch of the electrodes mounted on the aspherical lens holders. We use eight electrodes to control the electric field in the three directions of space. b) The system can be seen as a pair of electrodes along each direction with the applied voltage $\pm V_i/2$ along the three directions $i \in [x, y, z]$.

microwave frequency $8.3\,\mathrm{GHz}$, as depicted in Figure 2.19 c). Setting the microwave-field detuning at a value δ_R from the transition, we fix the delay between the microwave $\pi/2$ pulses to be $0.5\,\mu\mathrm{s}$ and vary the time at which we start the Ramsey experiment, see Figure 2.19 d). The probability P_{75S} to find the atom in $\left|75S_{1/2}, m_J = 1/2\right\rangle$ evolves with the time at which we perform the Ramsey experiment due to the dependence of δ_R on the magnetic field. The results show that the magnetic field has stabilized after a rotation time of $25\,\mathrm{ms}$.

2.4.2 Electric field

The electric field is controlled using eight electrodes placed on the lens holders inside the vacuum chamber (see Figure 2.20 a)). The system is equivalent to a pair of electrodes along each direction of space, see Figure 2.20 b). The relation between the applied voltage and the produced electric field (set by the effective distance between the electrodes) can be found in previous theses [Béguin, 2013; Ravets, 2014]. To produce an electric field E_i in the direction $i \in [x, y, z]$, we apply voltages $(-V_i/2; V_i/2)$ on the respective pair of electrodes. Doing so, the electric field is more homogeneous over the atomic array than applying the voltages $(0; V_i)$ (more detail can be found in the Thesis of Vincent Lienhard [2019]).
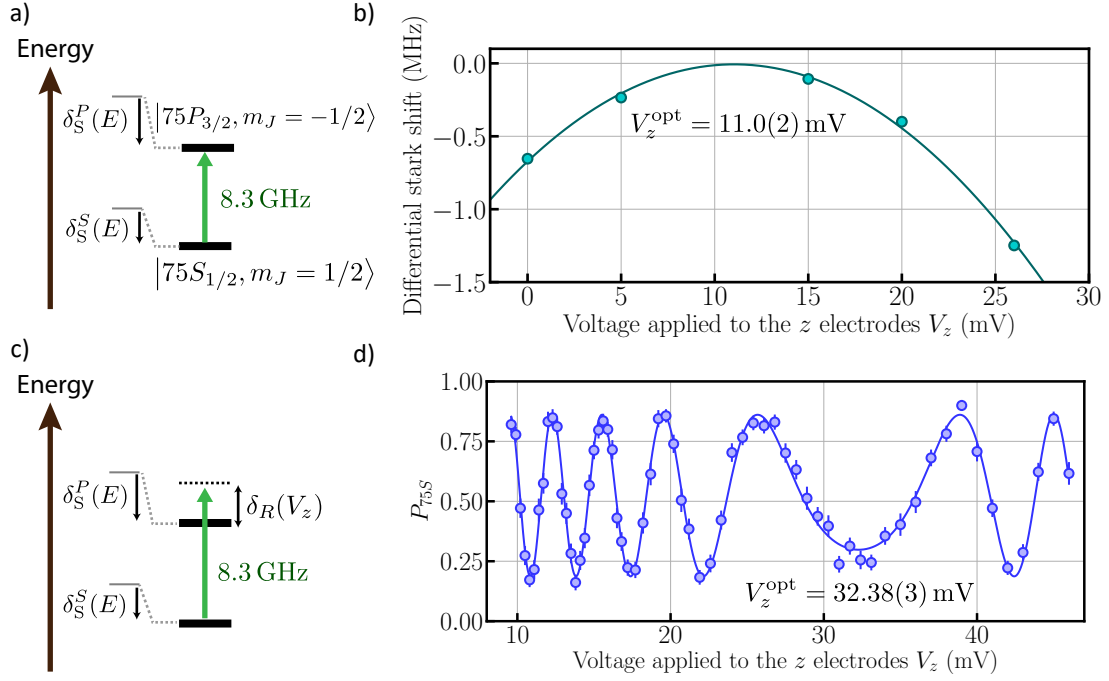
Figure 2.21: Cancellation of the electric field. a) Levels involved in the electric field cancellation experiment. b) We record the transition frequency for different potentials applied to the z electrodes V_z. The solid line is a fit to the data by a parabolic function from which we extract the electric field compensation value $V_z^{\text{opt}} = 11.0(2)$ mV. c) Sketch of the Ramsey experiment. We apply two microwave $\pi/2$-pulses separated by $t_R = 0.5\,\mu$s, with a detuning $\delta_R = \delta_0 + (\delta_{\text{S}}^P - \delta_{\text{S}}^S)$. d) P_{75S} probability as a function of V_z. The solid line is a fit to the data with a function of the form $A\cos(2\pi t_R \delta_R)$, from which we extract $V_z^{\text{opt}} = 32.38(3)$ mV.

Cancellation of the electric field.   The main purpose of the electrodes is to cancel the electric field E, as it mixes Rydberg states of different parity and prevents us from defining a pure two-level system. We cancel E by varying the voltage applied to the electrodes and measuring the corresponding Stark shift. We perform the experiment using microwaves between two Rydberg states, here between the $\left|75S_{1/2}, m_J = 1/2\right\rangle$ and the $\left|75P_{3/2}, m_J = -1/2\right\rangle$ states. The electric field produces a Stark shift on the transition frequency which evolves as $\delta_{\text{S}}^P - \delta_{\text{S}}^S = -(\alpha^P - \alpha^S)E^2$, with $\delta_{\text{S}}^i = -\alpha^i E^2$ where α^i is the polarizability of state $i = \{S, P\}$ (see Figure 2.21 a)). Before I started my PhD, the cancellation was performed via spectroscopy. A typical evolution of the transition frequency with the z potential V_z is presented in Figure 2.21 b). The solid line is a fit to the data by a parabolic function, from which we extract the cancellation voltage $V_z^{\text{opt}} = 11.0(2)$ mV. This experiment is time consuming as each data point is a
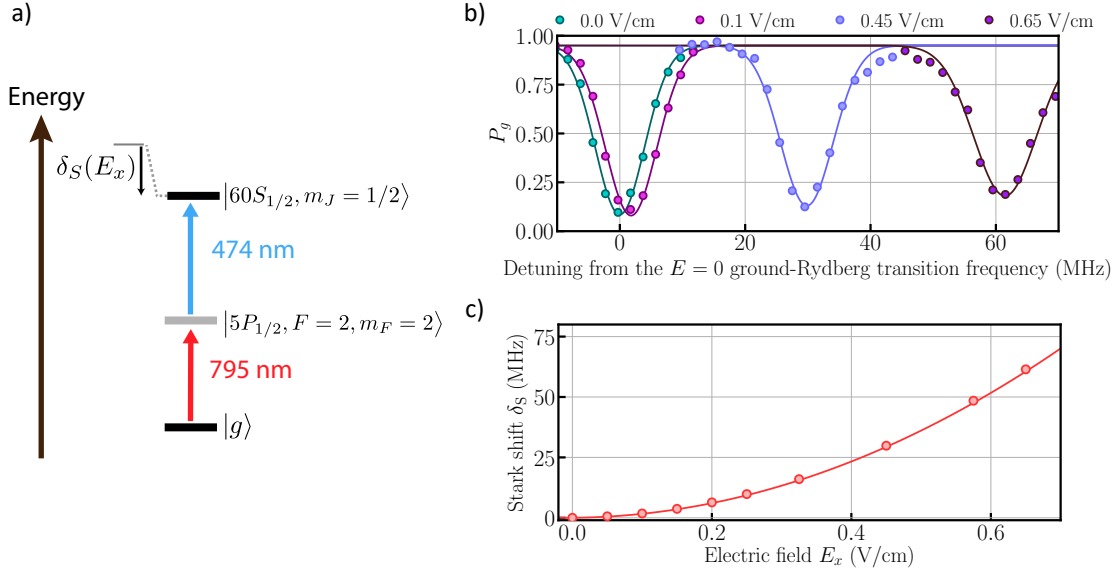
Figure 2.22: Application of a controlled Stark shift. a) Levels involved in the experiment. b) Typical spectra of the ground-Rydberg transition obtained for various values of E_x. We measure the probability P_g to find the atom in $|g\rangle$. The solid lines are Gaussian fits to the data. c) Evolution of the Stark shift δ_S as a function of E_x. The solid line is a fit to the data using a parabolic function, from which we extract the $60S_{1/2}$ polarizability $\alpha^{60S} = 140\,\mathrm{MHz}/(\mathrm{V/cm})^2$.

full spectrum. The precision on V_z^{opt} is limited by power broadening of the microwave field, giving typical uncertainties in residual electric field $\sim 130\,\mu\mathrm{V/cm}$.

We improved the electric field cancellation technique during my PhD. We now use a Ramsey interferometry experiment by applying two microwave $\pi/2$ pulses separated by $t_R = 0.5\,\mu\mathrm{s}$. We set a detuning $\delta_R = \delta_0 + \delta_S^P - \delta_S^S$ with $\delta_0 = 1\,\mathrm{MHz}$ (see Figure 2.21 c)). We vary the voltage applied to the electrodes and measure P_{75S} at the end of the Ramsey experiment, as presented in Figure 2.21 d) for V_z, which evolves as:

$$P_{75S} = A\cos\left(2\pi t_R(\delta_0 - (\alpha^P - \alpha^S)E^2)\right) + B. \tag{2.6}$$

The solid line is a fit to the data using the above function with $E = V_z - V_z^{\mathrm{opt}}$, from which we extract $V_z^{\mathrm{opt}} = 32.38(3)\,\mathrm{mV}$. This method is more precise as the measurement is not affected by power broadening, giving typical uncertainties in residual electric field $\sim 20\,\mu\mathrm{V/cm}$. The two experiments presented in Figure 2.21 were performed with one month interval, which is the typical duration between two cancellation calibrations, thus explaining the different values obtained for the electric field cancellation.

High electric field. The electrodes are also used to apply a controlled Stark shift to the Rydberg states, which will be used in Section 8.3. We demonstrate its implementation on the spectroscopy of the $|g\rangle \rightarrow \left|60S_{1/2}, m_J = 1/2\right\rangle$ transition (sketched in Figure 2.22 a)) for various values of E_x, see Figure 2.22 b). We show in Figure 2.22 c) the evolution of δ_S as a function of E_x. The solid line is a fit to the data using a parabolic function (as expected for the Stark effect $\delta_S = \alpha^{60S} E_x^2$), from which we extract $\alpha^{60S} = 140\,\mathrm{MHz}/(\mathrm{V/cm})^2$.

We observe in Figure 2.22 b) that the Rydberg excitation probability decreases when E_x increases, which is due to:

- The mixing of the targeted S state with the nearby P states.

- The sensitivity to fluctuations in the electric field value, which scale linearly with E_x.

For these reasons, we limit ourselves to Stark shifts $\delta_S \leq 25\,\mathrm{MHz}$, i.e. $E_x \sim 0.4\,\mathrm{V/cm}$ here, as we observe that the loss in Rydberg excitation efficiency is negligible.

2.5 Conclusion

In this chapter, I have presented an overview of the various operations we perform on the atoms, starting with a hot vapour of Rubidium until the Rydberg excitation of individually trapped atoms. In particular, I focused on the improvements made during my PhD. These improvements allow us (i) to perform the various calibrations faster and (ii) to improve the fidelity of the various operations. Combined, these induce a higher quality of the results when performing quantum simulation. In the next two chapters, I will come back to the detail of the major improvements I had on the apparatus: improving the coherence of the Rydberg excitation (Chapter 3) and extending the number of atoms (Chapter 4).

Improved excitation to Rydberg states

Contents

Exciting the atoms into their Rydberg states is key step, as it is the tool which allows us to implement interactions between the atoms, hence studying many-body physics. One of the important contributions to the setup I made during my PhD was to improve the Rydberg excitation by changing the way we excite the atoms, both on the atomic physics side and on the technical side with the use of a new laser technology. The change was triggered by the analysis of the previous setup imperfections carried out by de Léséleuc *et al.* [2018a], and the successful implementation of the new setup in the group of M. Lukin. The change of setup was done in the middle of my PhD. I thus worked on the platform with both setups for the same amount of time.

A way to assess the quality of both the efficiency and the coherence of the Rydberg excitation is to perform Rabi oscillations between the ground state and a Rydberg state. In this chapter, I will first present the main concepts related to the Rydberg excitation. I will then explain the changes I made on the setup, and finally study the limitations of the new system.

3.1 Excitation to Rydberg states

The wavelength of the transition from the ground state to the Rydberg states is 297 nm [Thoumany *et al.*, 2009]. A laser source operating at this wavelength has to fulfill two requirements:

- Due to the limited lifetime of the Rydberg states ($\sim 100\,\mu$s), the targeted Rabi frequencies are $\gtrsim 1\,$MHz to avoid decoherence effects.

- Considering the size of our 2D atomic arrays, the laser waists we are aiming for is $\sim 100\,\mu$m.

The required laser power is thus in the range of $\gtrsim 1\,$W to fulfill these conditions. However, single-mode highly coherent lasers delivering such power are not common, even though its implementation has been demonstrated in optical lattices [Zeiher *et al.*, 2016]. The solution to avoid using this wavelength is to use a two-photon transition to reach the Rydberg states.

3.1.1 Two-photon transition

We use a two-photon scheme to reach the Rydberg states. In our first implementation of the Rydberg excitation laser system, we used the $5P_{1/2}$ as an intermediate state, which involved diode lasers with wavelengths 795 nm and 474 nm. This setup is described in detail in the previous theses of the group. In order to improve our ability to drive the ground-Rydberg transition, we decided to modify our excitation scheme. We performed two changes: a different choice of the intermediate level and a change of the laser technology. These allowed us to increase the coherence and the efficiency of the Rydberg excitation, which is discussed below. We chose the $\left|6P_{3/2}, F = 3, m_F = 3\right\rangle$ as an intermediate level (see Figure 3.1 a)), with lasers at 420 nm and 1013 nm. The two lasers are counter-propagating and parallel to the magnetic field. Using these lasers, we can excite the atoms into the Rydberg states $\left|nS_{1/2}, m_J = 1/2\right\rangle$ or $\left|nD_{5/2}, m_J = 5/2\right\rangle$.

Limitations of two-photon transitions. There are two drawbacks associated to the use of two-photon transitions compared to single-photon transitions:

- The two lasers have to be locked in phase in order to coherently drive the Rydberg excitation.
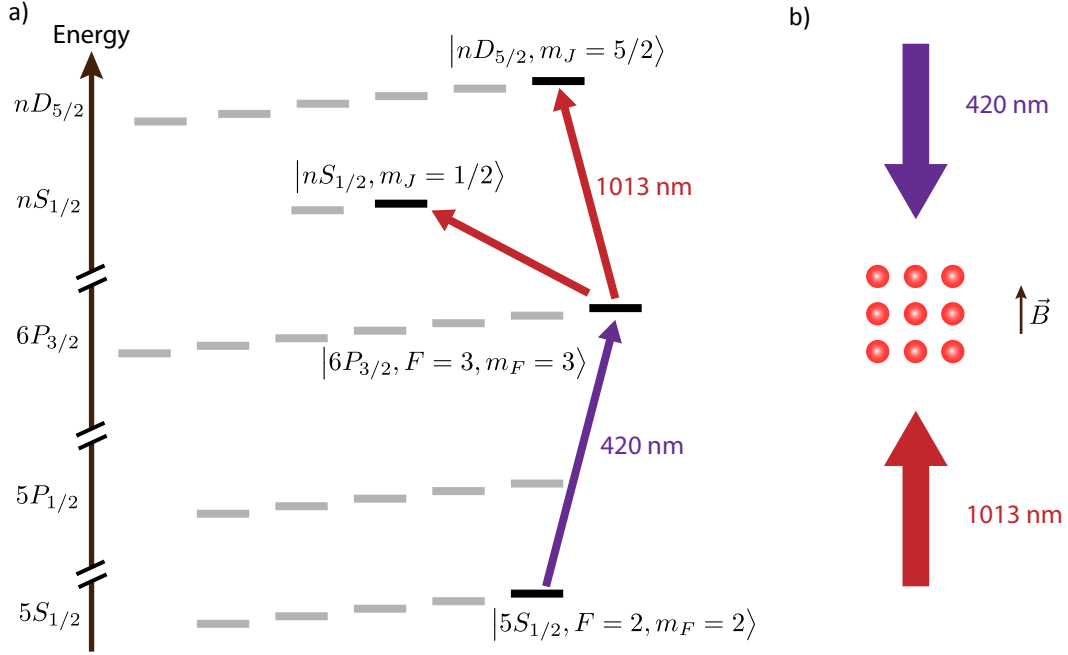
Figure 3.1: The "new" excitation scheme. a) Levels involved in the Rydberg excitation scheme, with $\left|6P_{3/2}, F = 3, m_F = 3\right\rangle$ as intermediate state. Using two lasers with wavelengths 420 nm and 1013 nm, we reach the Rydberg states $nS_{1/2}$ and $nD_{5/2}$. b) Optical setup sketch.

- As the intermediate state has a shorter lifetime than the typical Rabi oscillation duration, the atom decays to the ground state with a finite probability instead of going in the Rydberg state. The lifetime of the intermediate level is $\tau_{6P} = 113\,\mathrm{ns}$, corresponding to a linewidth $\Gamma_{6P} = 2\pi \times 1.2\,\mathrm{MHz}$.

We explored two ways to avoid the intermediate state population: (i) driving Rabi oscillations with a large detuning from the intermediate state, and (ii) using stimulated Raman adiabatic passage, described in Section 2.3.1. I will focus on the first method in this Chapter.

3.1.2 Rabi oscillations with large single-photon detuning

The most common approach to reach a Rydberg state $|r\rangle$ starting with atoms in $|g\rangle$ is to perform two-photon transitions with a large single-photon detuning Δ from the intermediate state $|p\rangle$. The relevant Hamiltonian describing the system is

$$H = \frac{\Omega_{gp}}{2}(|g\rangle \langle p| + |p\rangle \langle g|) + \frac{\Omega_{pr}}{2}(|p\rangle \langle r| + |r\rangle \langle p|) - \Delta |p\rangle \langle p| - \delta_0 |r\rangle \langle r|, \qquad (3.1)$$

57
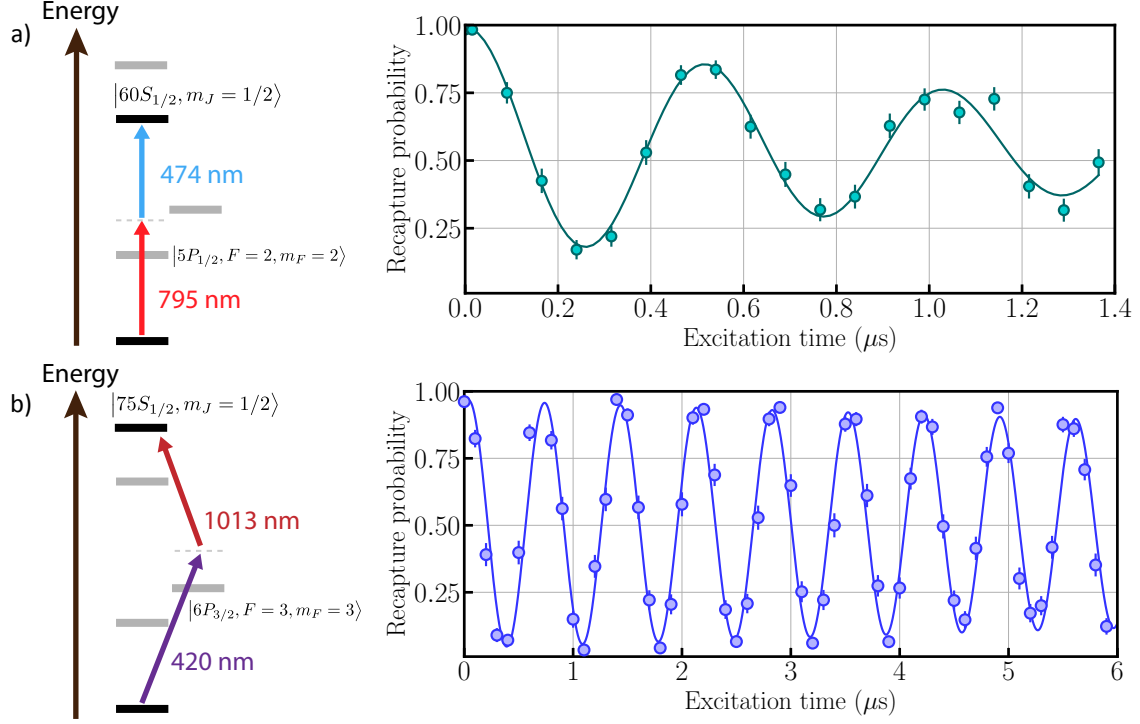
Figure 3.2: Comparison of the Rabi oscillations obtained with the previous and the new laser setups. We show a sketch of the involved levels and the corresponding typical Rabi oscillation obtained for a) $|r\rangle = |60S_{1/2}, m_J = 1/2\rangle$ using the previous scheme, and b) $|r\rangle = |75S_{1/2}, m_J = 1/2\rangle$ using the new setup. We observe that both the contrast and the damping are significantly improved. Solid lines are fits to the data with damped sines.

with Ω_{gp}, Ω_{pr} the single-photon Rabi frequencies of the $|g\rangle \rightarrow |p\rangle$ and $|p\rangle \rightarrow |r\rangle$ transitions, and δ_0 the two-photon detuning from the Rydberg state. In the regime where $\Delta \gg \Omega_{gp}, \Omega_{pr}, \Gamma_{6P}$, we can adiabatically eliminate the intermediate level and the problem reduces to a two-level system. The system is well described by the effective Hamiltonian

$$H_{\text{eff}} = \frac{\hbar\Omega}{2}(|r\rangle\langle g| + |g\rangle\langle r|) + \hbar\delta|r\rangle\langle r|, \tag{3.2}$$

where we define the effective Rabi frequency and detuning by:

$$\Omega = \frac{\Omega_{gp}\Omega_{pr}}{2\Delta} \quad \text{and} \quad \delta = \delta_0 + \frac{\Omega_{gp}^2 - \Omega_{pr}^2}{4\Delta}. \tag{3.3}$$

The second term in δ comes from the light shift induced by the two lasers. As mentioned above, we want to drive the excitation with $\Omega/(2\pi) \sim 1\,\text{MHz}$ to avoid decoherence. In order to fulfill this condition and $\Delta \gg \Omega_{gp}, \Omega_{pr}, \Gamma_{6P}$, we typically use $\Omega_{gp}/(2\pi) \sim 50 - 100\,\text{MHz}$, $\Omega_{pr}/(2\pi) \sim 25 - 50\,\text{MHz}$, and $\Delta/(2\pi) \sim 500 - 1000\,\text{MHz}$.

Experimental realization. We initialize all the atoms in the ground state $|g\rangle = |5S_{1/2}, F = 2, m_F = 2\rangle$ using the optical pumping technique described in Section 2.2.2. We then switch off the tweezers, shine the two lasers for a few microseconds and switch back on the tweezers. Atoms in the ground state are recaptured, whereas atoms in the Rydberg states are expelled from the tweezers region and lost (see Section 2.3.2). After 20 ms, we switch on the MOT lasers to observe the scattered light from the atoms. If the atom is present at the end of the experiment, we infer that the atom was in the ground state after the Rydberg excitation. If the atom is absent at the end of the experiment, we infer that the atom was in the Rydberg state. The various mechanisms leading to detection errors are discussed below.

Figure 3.2 presents two typical Rabi oscillations using a) the previous excitation scheme with $|r\rangle = |60S_{1/2}, m_J = 1/2\rangle$ and b) the new excitation scheme with $|r\rangle = |75S_{1/2}, m_J = 1/2\rangle$. The parameters are $\Delta/(2\pi) = 700\,\text{MHz}$, $\Omega_{pr}/(2\pi) = 50\,\text{MHz}$ and a) $\Omega_{gp}/(2\pi) = 90\,\text{MHz}$, b) $\Omega_{pr}/(2\pi) = 50\,\text{MHz}$. The solid line is a fit to the data using a damped sine. For a frequency of $\sim 2\,\text{MHz}$, we went from a $1/e$ coherence time of $\sim 1\,\mu\text{s}$ to a coherence time $\sim 25\,\mu\text{s}$[1]. The contrast is also improved. I now describe in detail the implementation of the new laser system.

3.2 Changing the excitation scheme to the Rydberg states

In this section, I first briefly motivate our choice for the new excitation scheme, then present the new setup. As discussed above, we now use lasers with wavelengths 420 nm and 1013 nm, going through the $6P_{3/2}$ level. This change in laser wavelengths is motivated by the intermediate state lifetime: the $6P_{3/2}$ lifetime is 113 ns, whereas it is 28 ns for the $5P_{1/2}$. We thus gain a factor four in lifetime, which thus reduces the effect of spontaneous emission from the intermediate state by a factor four (see Section 3.3.2). We also changed the laser technology in order to solve the laser phase noise issue [de Léséleuc *et al.*, 2018a], which I now briefly discuss.

Reduction of the lasers phase noise. In the previous setup, we used Toptica Diode Lasers with typical natural linewidths $\sim 1\,\text{MHz}$ [Henry, 1982] stabilized onto an ultrastable cavity. The feedback loop which stabilizes the laser's frequency produces a noise at a typical frequency of $\sim 1\,\text{MHz}$, a so-called "servo bump", which corresponds to the typical ground-Rydberg Rabi frequency. This "servo bump" induces decoherence

---

[1] This coherence time, extracted using the fit to the data, is too large to be observable due to the fact that the atom drifts away, as not trapped in the tweezers.

in the Rabi oscillations (detailed in the thesis of Sylvain de Léséleuc [2018]). Two ways of circumventing this phase noise have been explored on other platforms: (i) using an extra filtering cavity [Levine *et al.*, 2018] and (ii) using Rabi frequencies in the $\sim 10\,\text{MHz}$ range [Madjarov *et al.*, 2020], which is hard to achieve for large arrays due to limited power.

The approach we chose is to directly solve the issue at its source by using a laser technology which has a low phase noise at $\sim 1\,\text{MHz}$: Titanium Sapphire lasers (TiSaph). The natural linewidth of these lasers is $\ll 1\,\text{MHz}$, which allows us, in principle, to drive the transition without the need of actively stabilizing the laser's frequency. We however stabilize it (using an ultrastable cavity) to avoid long term frequency drifts. The stabilization is performed in a mechanical way using piezos with a bandwidth of $\sim 10\,\text{kHz}$, preventing any "servo bumps".

A sketch of the 420 nm and 1013 nm lasers optical setup is presented in Figure 3.3, which I now detail.

3.2.1 420 nm excitation laser

Optical setup.   We start from a M-Squared SolTis TiSaph laser emitting light at 840 nm, pumped by an M-Squared Equinox (532 nm). A small portion of the light is injected in a ultra low expansion (ULE) cavity to stabilize the laser in frequency. The cavity is a replica of the one described in the thesis of Sylvain Ravets [2014]. It has a finesse $\mathcal{F} \simeq 20000$ and a free spectral range of $1.5\,\text{GHz}$. The light at the output of the TiSaph is frequency doubled using an M-Squared ECD-X doubling cavity. The amount of power after the doubling cavity is $\sim 1.5\,\text{W}$. We use fused-silica optics where possible to avoid damage induced by such high power of near UV light. The laser beam goes through:

- A double-pass Acousto-Optic Modulator (AOM) used to dynamically shape the amplitude and the frequency of the light, discussed in Section 6.2.2.

- A free-space Electro-Optic Modulator (EOM) with extinction ratio $\sim 1/100$ and a fast switch time ($\sim 10\,\text{ns}$), used to produce sharp pulses.

- A polarization-maintaining fiber which brings the light to the experimental chamber. The maximum power we obtain on the atoms is 350 mW.

We then collimate the laser with a $1/e^2$ radius $w_{420} = 250\,\mu\text{m}$.
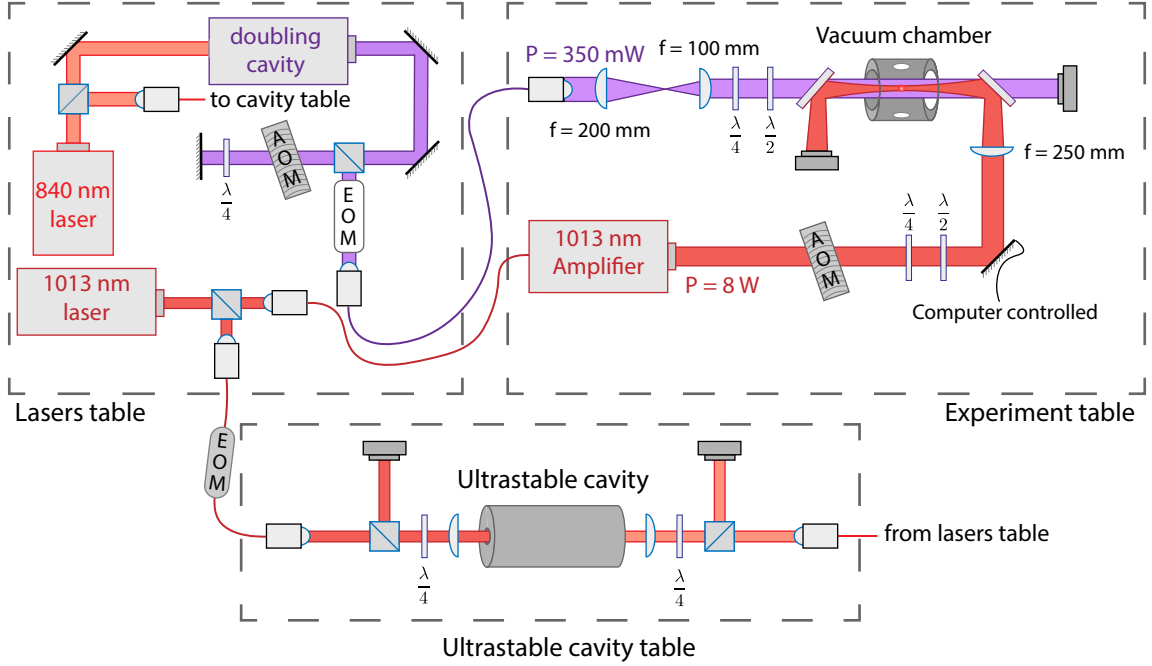
Figure 3.3: Overview of the new Rydberg setup. (only relevant optics are shown). After doubling the frequency of 840 nm light, the 420 nm goes through an AOM in double-pass configuration, an EOM, and is coupled into a polarization maintaining fiber. It brings the light to the experimental chamber as a collimated beam with a $1/e^2$ radius $w_{420} \simeq 250\,\mu$m. After being amplified, the 1013 nm light goes through an AOM, is reflected by a computer-controlled mirror and is focused on the atoms down to a waist $w_{1013} \simeq 130\,\mu$m. Both lasers are stabilized in frequency on an ultrastable cavity.

Probing the transition to the intermediate state. We probe the $5S_{1/2} \to 6P_{3/2}$ transition using the following experiment (see Figure 3.4 a)): we initialize the atoms in $\left|5S_{1/2}, F = 2, m_F = 2\right\rangle$, and shine the 420 nm laser as a weak probe ($\Omega_{420} \simeq \Gamma_{6P}$). When the laser is on resonance, the atoms are transferred into the $6P_{3/2}$ states, and then decay back to the ground states, both to $F = 1$ and $F = 2$. We measure the population in the $F = 1$ states using the push-out beam described in Section 2.2.2. Figure 3.4 b) shows a typical spectrum of the $6P_{3/2}$ hyperfine structure. The energy spacing is consistent with previous measurements [Glaser *et al.*, 2020].

We observe the $(6P_{3/2}, F' = 3) \to (5S_{1/2}, F = 1)$ transition, which is not intuitive as the selection rules prevent atoms in $(6P_{3/2}, F' = 3)$ from decaying directly to $(5S_{1/2}, F = 1)$. However, the atoms can decay back to the ground state by a multi-step process, presented in Figure 3.4 c) with the corresponding transition wavelengths. There are three possible routes: $(6P \to 5S)$, $(6P \to 6S \to 5P \to 5S)$ and $(6P \to$
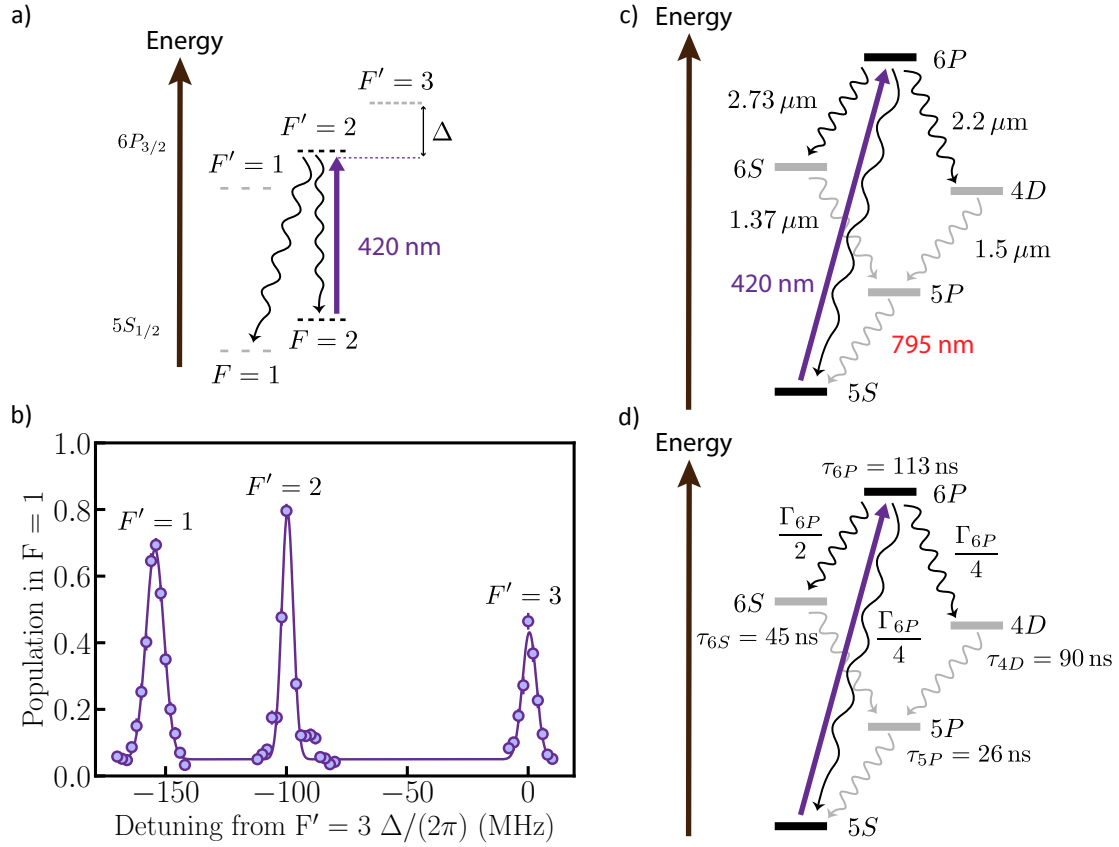
Figure 3.4: Observing the hyperfine structure of the $6P_{3/2}$ **state.** a) Sketch of the levels involved. b) Population in $F = 1$ as a function of the laser detuning from the $(5S_{1/2}, F = 2) \rightarrow (6P_{3/2}, F' = 3)$ transition. We observe three peaks corresponding to three hyperfine levels of the $6P_{3/2}$. c) and d) Decay channels from the $6P$ to the ground state, with the relevant levels and their lifetimes, transition wavelengths and (approximate) branching ratios.

$4D \rightarrow 5P \rightarrow 5S$). The associated branching ratios, presented in Figure 3.4 d), are $\sim \Gamma_{6P}/4$, $\sim \Gamma_{6P}/2$ and $\sim \Gamma_{6P}/4$ [Safronova, Williams, and Clark, 2004], and the level lifetimes are $\tau_{6S} = 45$ ns and $\tau_{4D} = 90$ ns [Marek and Munster, 1980]. This multi-step mechanism allows atoms from $F' = 3$ to decay to $F = 1$, and will be taken into account in the simulations of the Rabi oscillation.

3.2.2 1013 nm excitation laser

Optical setup. The 1013 nm laser is also a M-Squared SolTis laser pumped by an M-Squared Equinox. A small fraction of the light is sent into the ultrastable cavity
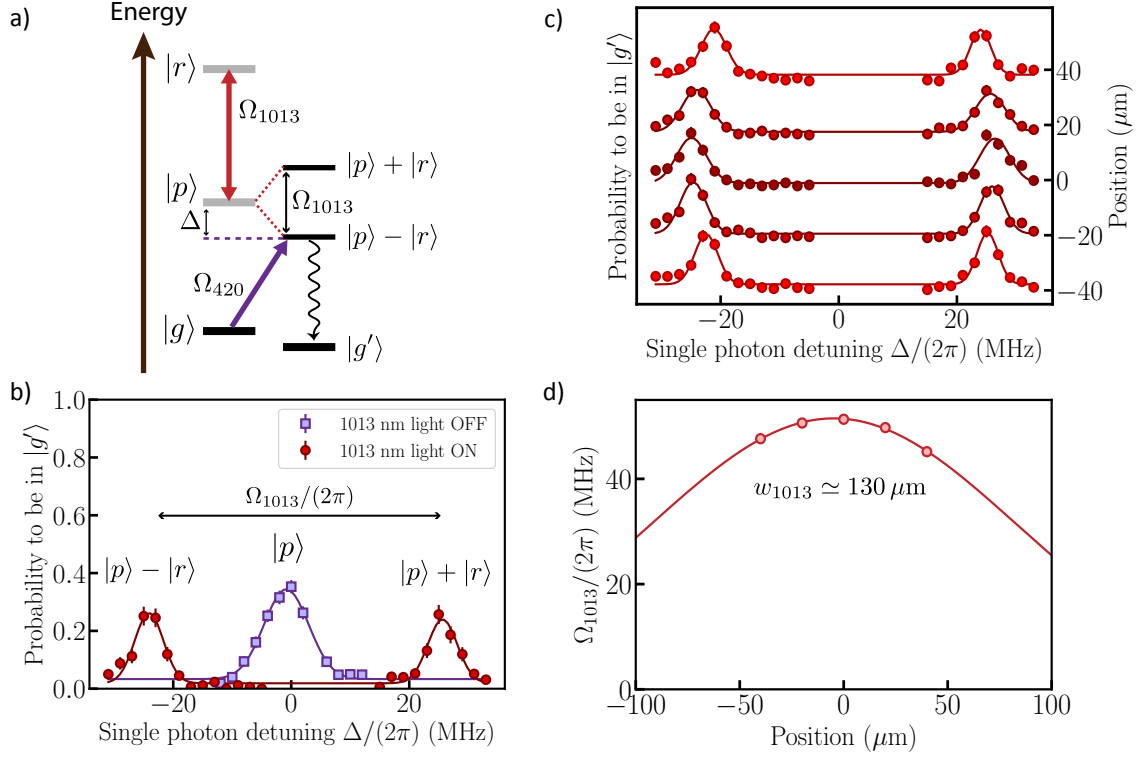
Figure 3.5: Autler-Townes effect. a) Principle of Autler-Townes splitting. b) Results of the experiment with (circle) and without (square) the 1013 nm laser. We measure the population in $|g'\rangle$ as a function of the detuning Δ. We observe the splitting of the $|p\rangle$ level by Ω_{1013}. c) Results of the experiment for atoms separated by $20\,\mu$m. d) By measuring Ω_{1013} for different positions of the atoms, we estimate the waist of the laser $w_{1013} \simeq 130\,\mu$m.

for frequency stabilization. The maximum laser output power is $\sim 850\,\mathrm{mW}$. As this transition has a small dipole matrix element, we want the highest power possible on the atoms. To do so, we use this light to seed an AzurLight fiber amplifier[2] delivering up to $\sim 10\,\mathrm{W}$. The amplified light is sent on the atoms in free space, and we use an AOM to switch on and off the beam. The beam is focused on the atoms with a $1/e^2$ beam radius waist $w_{1013} \simeq 130\,\mu$m. In these conditions, we reach the $75S_{1/2}$ level with $\Omega_{1013}/(2\pi) = 50\,\mathrm{MHz}$.

As the amplifier output is two meters away from the atoms and w_{1013} is relatively small, we have to realign the laser on a daily basis. We realign the laser using a computer-controlled mirror mount placed on piezo actuators, by maximizing the splitting of the $|p\rangle$ level due to the Autler-Townes effect, described below.

---

[2]The fiber amplifier is composed of three pump diodes combined with an Ytterbium doped fiber.
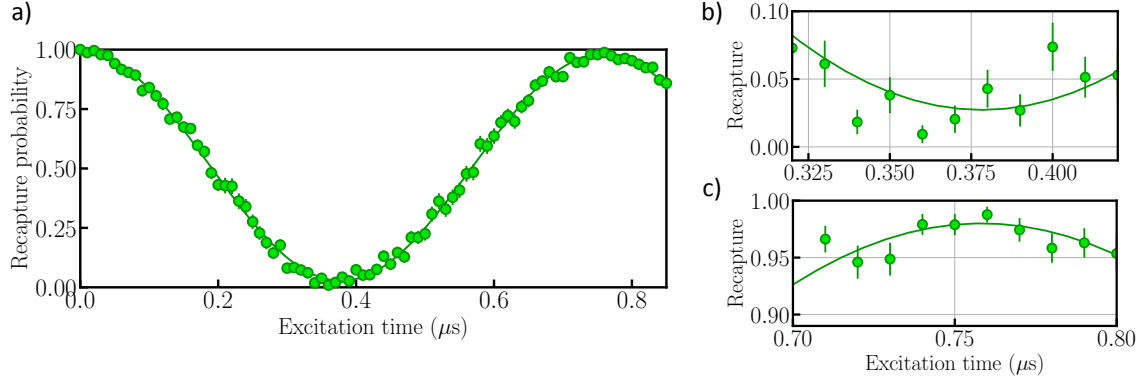
Figure 3.6: A closer look at the first period. a) First period of a Rabi oscillation involving the $75S$ level with contrast $\sim 97\%$. b), c) Focus on the π and 2π excitation time. Due to the initialization, the detection errors and the remaining damping, we recapture 2.5% of the atoms after a π-pulse and 98% after a 2π-pulse.

Autler-Townes splitting. In order to measure the Rabi frequency Ω_{1013} of the laser, we use the Autler-Townes effect, whose principle is summarized in Fig 3.5 a). When the 1013 nm light is resonant with the Rydberg state $|r\rangle$, the intermediate state $|p\rangle$ is split into the symmetric and antisymmetric $|p\rangle \pm |r\rangle$ superposition of these levels. The level energies are located at $\pm\hbar\Omega_{1013}/2$ from the laser-free transition. The experiment is the following: we initialize the atoms in $|g\rangle$ and set the 1013 nm light on resonance with the $|p\rangle \to |r\rangle$ transition. We perform spectroscopy by shining the 420 nm laser as a weak probe ($\Omega_{420} \simeq \Gamma_{6P}$) and scanning its detuning Δ. The atoms in $|g\rangle$ are excited when the 420 nm light is resonant, and eventually decay to $F = 1$ manifold, gathered under the notation $|g'\rangle$. We use the push-out beam to measure the population in $|g'\rangle$. We extract the $|p\rangle$ state splitting from this spectroscopy (see Figure 3.5 b)), which gives Ω_{1013}.

Doing this experiment with atoms located at different positions as shown in Figure 3.5 c), we map the spatial distribution of the 1013 nm laser Rabi frequency. As $\Omega \propto (1/w)$, the spatial distribution of Ω directly gives the waist of the laser which we extract from Figure 3.5 d). We use this experiment to center the 1013 nm laser on the array.

3.3 Limitations of the system

In this section, we assess the limitations of the Rydberg excitation by analyzing the various mechanisms leading to the damping and the finite contrast of the Rabi oscillations.

3.3.1 Finite contrast of the oscillations

The contrast of the Rabi oscillations is highlighted in Figure 3.6 a) for which we focus on the first period. We obtain a contrast of $\simeq 97\%$, which is improved compared to the $\sim 90\%$ contrast with the previous setup (see Figure 3.2) thanks to a reduction of the State Preparation And Measurement (SPAM) errors. This reduction of the SPAM errors have two origins: (i) recent technical improvements described in Chapter 2 which are not related to the new laser system, and (ii) improvements which are directly related to the new laser system (see below). I now describe the mechanisms leading to the finite contrast, and how we reduced their impact on the system.

Ground-state preparation. The contrast of the oscillation is directly limited by the initialization efficiency in the $|g\rangle$ state. The deficiency of the initialization η has two origins: the imperfect optical pumping procedure (see Section 2.2) and the Raman scattering induced by the tweezers (see Section 4.1.2). The typical values for the previous excitation scheme were in the range $\eta = 2-5\%$. During my PhD, we improved the efficiency of the optical pumping (see Section 2.2.2) to reach $\sim 99.5\%$. The Raman scattering increases the initialization deficiency by $\sim 0.2\%$, such that we typically obtain $\eta \sim 0.7\%$.

Ground-state detection. As we switch off the tweezers during the Rydberg excitation, the atom has a finite probability ε to escape the trapping region due to its temperature. An atom leaving the trapping region will be interpreted as a Rydberg atom, resulting in a detection error. During my PhD, we decreased the atom temperature, leading to a reduction in the typical value of ε from $\varepsilon = 0.02$ to $\varepsilon = 0.005$. The remaining value of $\varepsilon = 0.005$ mainly comes from background-gas collisions and losses due to the MOT cooling light. Figure 3.6 c) shows a magnification after one period: $\sim 2\%$ of the atoms are lost, which comes both from ε and the remaining damping of the oscillation.

Rydberg-state detection. The Rydberg state detection method relies on the ponderomotive potential the tweezers applies to the atom, (see Section 2.3.2). For the tweezers depth we use, the typical escape time is $\sim 20\,\mu$s. However, the Rydberg atom has a probability ε' to decay back to the ground state before leaving the trapping region. The atom is thus recaptured and interpreted as being in the ground state, resulting in a detection error. This error is dominated by the Rydberg state lifetime at $0\,$K (for fixed trap parameters), and thus scales as n^{-3}. We measure $\varepsilon' = 0.05$ for
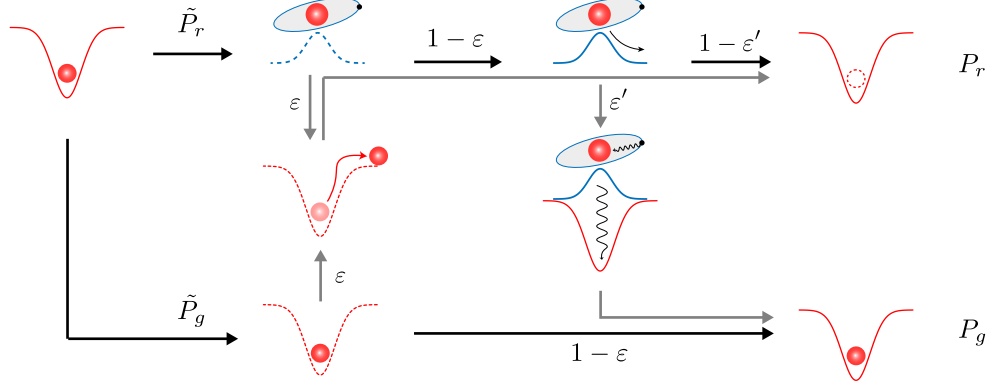
Figure 3.7: Errors induced by the detection process. Starting from a filled tweezers, we switch it off and shine the Rydberg excitation lasers. $\tilde{P}_g$ and $\tilde{P}_r$ are the real probabilities for the atom to be in $|g\rangle$ and $|r\rangle$. We infer the state of the atom by measuring the probability P_g (P_r) to recover (lose) the atom at the end of the experiment. Two types of error are possible: there is a probability ε for the atom to leave the trapping region, and a probability ε' that a Rydberg atom decays back to $|g\rangle$ before being expelled. By following the different paths leading to P_g and P_r, one can recover the coupled equations (3.4) with $\eta = 0$.

$n \sim 60$ [de Léséleuc *et al.*, 2018a]. Thanks to the increased Rabi frequency of the new setup we now use higher Rydberg states, here $n = 75$, implying $\varepsilon' = (75/60)^3 \simeq 0.025$. Using Figure 3.6 b) and taking into account the remaining damping of the oscillation, we measure $\varepsilon' \simeq 0.02$, consistent with the scaling of ε' and with numerical simulations of the detection error.

Extracting the real excitation probability. The physical processes at the origin of the ε and ε' errors are summarized in Figure 3.7. To extract the real probabilities $\tilde{P}_r$ and $\tilde{P}_g$ to find the atom in $|r\rangle$ and $|g\rangle$ from the measured ones P_r and P_g, we use the coupled equations

$$
\begin{aligned}
P_g &= \eta(1 - \varepsilon) + (1 - \eta)(1 - \varepsilon)[\tilde{P}_g + \varepsilon'\tilde{P}_r], \\
P_r &= \eta\varepsilon + (1 - \eta)[\varepsilon\tilde{P}_g + (1 - \varepsilon' + \varepsilon\varepsilon')\tilde{P}_r].
\end{aligned}
\tag{3.4}
$$

We calibrate independently the errors and use these coupled equations in our simulations to extract the real excitation probabilities.

Conclusions and prospects for further improvement. We divided by ~ 5 the imperfection in the initialization η, and by two the values of ε and ε'. By calibrating

these errors and using the coupled equations (3.4), we extract a detection-error free probability $\tilde{P_r} \simeq 99\%$ to reach the Rydberg state. The remaining percent lies in the imperfect initialization and the residual damping.

We here give a few ideas to further decrease their values:

- The remaining part of ε mainly comes from background-gas collision. A better vacuum would reduce its value. This can be achieved by placing the setup in a cryogenic environment which would have the additional benefit of suppressing the Rydberg states decay due to black-body radiation, hence increasing the Rydberg lifetime by a factor $\sim 2-3$. As demonstrated in Schymik *et al.* [2021], this solution leads to ~ 1000 times better vacuum, thus reducing the error by a factor 1000.

- We can reach even higher Rydberg states to decrease ε'. However, the Rydberg states sensitivity to static electric fields (scaling as n^7) combined with the small dipole matrix element (scaling as $n^{3/2}$) limit the achievable Rydberg states to $n \sim 90$.

- Another idea to decrease ε' is to ionize the Rydberg atoms, e.g., by applying a strong electric field [Löw *et al.*, 2012], or by using microwaves [Sirko *et al.*, 1994]. The successful implementation of the fast auto-ionization of Rydberg atom using the second electron of alkali-earth atoms has been demonstrated [Madjarov *et al.*, 2020].

3.3.2 Damping of the oscillations

Even though the coherence time of the Rabi oscillation has been largely increased, we still observe a finite damping. In this subsection, I present the main effects leading to the observed damping and compare the results to simulations taking into account those effects.

Doppler effect. As the atoms have a finite temperature T, for each realization of the experiment their velocity v, hence the frequency of the lasers seen by the atoms, changes. The velocity distribution is described by a Gaussian distribution with standard deviation $\Delta v = \sqrt{\frac{k_B T}{m}}$ where m is the mass of the atom. As the two beams are counter-propagating, the effective wavevector seen by the atoms is $k_{\text{eff}} = \frac{2\pi}{\lambda_{gp}} - \frac{2\pi}{\lambda_{pr}} \simeq 8.7 \times 10^6 \, \text{m}^{-1}$. The laser detuning seen by the atom is thus a random

variable with a centered Gaussian probability distribution of standard deviation $\delta = k_{\text{eff}}\Delta v \simeq 2\pi \times 40\,\text{kHz}$ for the typical atom temperature $T = 10\,\mu\text{K}$. This value is three times as small as for the previous setup [de Léséleuc *et al.*, 2018a]. We take into account the Doppler effect in the simulations by averaging the results over 1000 realizations with the corresponding random distribution of detuning.

Spontaneous emission from the intermediate state. The fundamental limitation on the coherence of two-photon processes is spontaneous emission from the intermediate state, which has an effective decay rate:

$$\Gamma_{\text{eff}} = \Gamma_p \times \frac{\Omega_{gp}^2 + \Omega_{pr}^2}{4\Delta^2}, \tag{3.5}$$

where Γ_p is the linewidth of the intermediate state. This formula indicates that: (i) one should aim for the highest intermediate state lifetime possible and (ii) for a fixed value of Δ, the maximum number of oscillations within a time $1/\Gamma_{\text{eff}}$ is achieved when $\Omega_{gp} = \Omega_{pr}$. The optimal effective Rabi frequency is thus $\Omega = \Omega_{pr}^2/(2\Delta)$.

The spontaneous emission populates other ground states than $|g\rangle$, gathered under the notation $|g'\rangle$. Atoms in $|g'\rangle$ do not participate to the coherent excitation but are still recaptured, leading to an asymmetric damping. To model the influence of spontaneous emission, we include this extra-level and solve the optical Bloch equations for the density matrix ρ:

$$\frac{\mathrm{d}\rho}{\mathrm{d}t} = \frac{1}{i\hbar}[H,\rho] + \mathcal{L}[\rho] \tag{3.6}$$

with H the Hamiltonian described in Eq (3.2) and $\mathcal{L}$ the dissipator operator which has the Lindblad form:

$$\mathcal{L}[\rho] = \sum_{i=g,g'} \frac{\Gamma_i}{2}(2\,|i\rangle\,\langle i|\,\rho\,|p\rangle\,\langle i| - |p\rangle\,\langle p|\,\rho - \rho\,|p\rangle\,\langle p|), \tag{3.7}$$

where the value of Γ_i depends on the intermediate state linewidth and the Clebsch-Gordon coefficients associated to the various decay channels. As pointed out in Section 3.2.1, an atom placed in the intermediate state can decay to the $5S$ states via three channels: $(6P \to 5S)$, $(6P \to 6S \to 5P \to 5S)$ and $(6P \to 4D \to 5P \to 5S)$. To simplify the simulation, we suppose that the three-step decaying routes are two-step processes (see Figure 3.8 a)), i.e., in the route $6P \to 6S \to 5P \to 5S$ $(6P \to 4D \to 5P \to 5S)$, the atom only goes through an effective level $|p_S\rangle$ $(|p_D\rangle)$. The lifetime of these effective levels is the sum of the level lifetimes: $\tau_{p_S} = \tau_{6S} + \tau_{5P} = 71\,\text{ns}$ and $\tau_{p_D} = \tau_{4D} + \tau_{5P} = 116\,\text{ns}$. The branching ratios are calculated by considering each
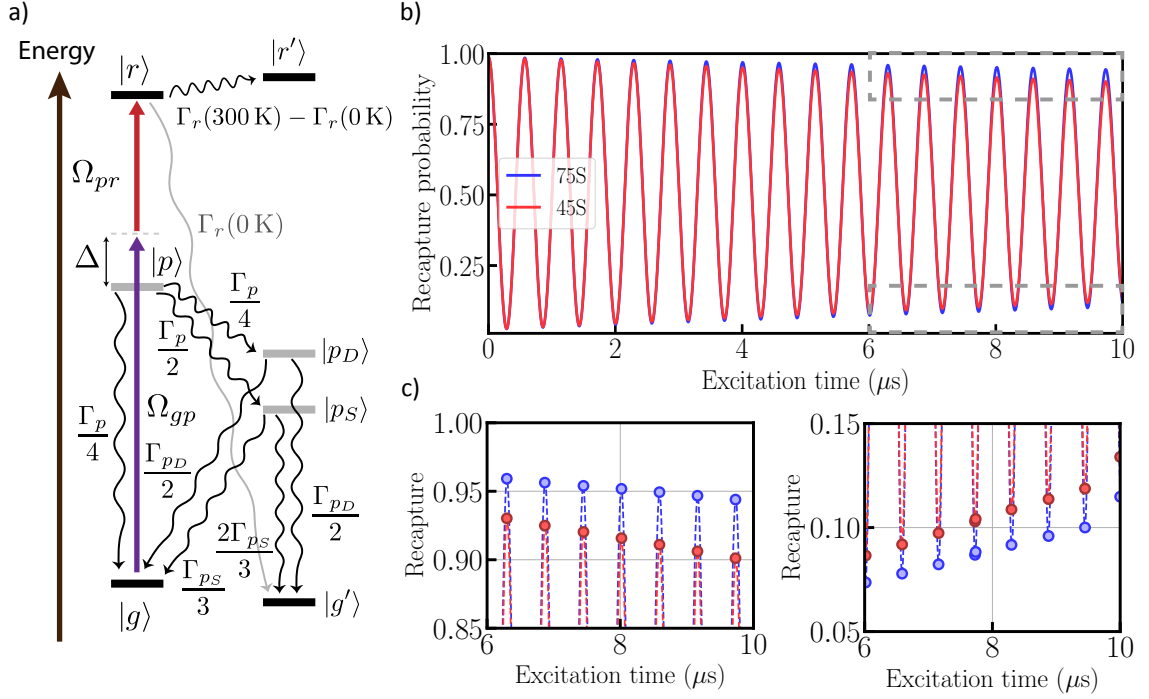
Figure 3.8: Levels used in the simulations and influence of the Rydberg lifetime.
a) Energy levels and their connections used in the simulation. b) Effect of the Rydberg
lifetime on the Rabi oscillations. The parameters are $\Omega_{420} = \Omega_{1013} = 2\pi \times 50\,\text{MHz}$ and
$\Delta/(2\pi) = 700\,\text{MHz}$. We show the results for the relevant level $75S$ and for a relatively
low Rydberg state $45S$. Its effect starts to play a role at longer times, highlighted in c)
which shows a magnification of b) at long times. Using the $75S$ level, we estimate a loss
in contrast of $\sim 2\%$ after $6\,\mu$s.

possible decay routes (including Zeeman sublevels).

Rydberg lifetime. Even though the Rydberg lifetime is large compared to the typical
Rabi oscillations duration, we include it in the simulations (see Figure 3.8 a)) as the
measured coherence time is now tens of microseconds. To simulate its effect accurately,
we distinguish between two decay channels:

- The Rydberg atom decays directly to a low-n, short-lifetime state which quickly
  decays back to the ground state. The corresponding decay rate is approximately
  given by the decay rate at $0\,\text{K}$, $\Gamma_r(T = 0\,\text{K})$. To simplify the simulation, we
  consider that the atom only decays to $|g'\rangle$. The atom is thus recaptured at the
  end of the experiment and does not participate in the Rabi oscillation.

- The atom decays to nearby long-lived Rydberg state due to the black-body
  radiations. The corresponding decay rate is $\Gamma_r(T = 300\,\text{K}) - \Gamma_r(T = 0\,\text{K})$. We

69

group these Rydberg states into a single state $|r'\rangle$. We neglect the decay of atoms from $|r'\rangle$ during the Rabi oscillation. $|r'\rangle$ is detected as a Rydberg state and does not participate in the Rabi oscillation.

In order to assess the effect of the Rydberg state lifetime on the damping of the Rabi oscillation, we perform the simulations (see Figure 3.8 b)) for the $75S$ (blue) level with lifetime $\tau_{75S}(300\,\text{K}) = 175\,\mu\text{s}$ and the $45S$ (red) with lifetime $\tau_{45S}(300\,\text{K}) = 47\,\mu\text{s}$. The simulation parameters are the typical experimental one: $\Omega_{420} = \Omega_{1013} = 2\pi \times 50\,\text{MHz}$ and $\Delta/(2\pi) = 700\,\text{MHz}$. The simulations include the initialization and detection imperfections, the Doppler effect, and the spontaneous emission from the intermediate state. Although being negligible at short times, the effect of the Rydberg lifetime starts to play a role after $6\,\mu\text{s}$ (see Figure 3.8 c)). We estimate a contrast loss of $\sim 2\%$ after $6\,\mu\text{s}$ using the $75S$ due to the finite Rydberg lifetime. Though this effect is not drastic, it starts to play a role and should then be included in the simulations.

Power fluctuations. Another major limitation of the excitation setup is the fluctuations of laser power. The power fluctuations during the experiment are measured to be negligible compared to shot-to-shot fluctuations, i.e., at each repetition of the experiment. We thus only take the latter into account. The 1013 nm amplifier has an active feedback stabilization of the output power and its shot-to-shot fluctuations are measured to be negligible. The main element causing shot-to-shot power fluctuations is the fiber which couples the 420 nm laser to the atoms, due to beam pointing instabilities before the fiber. The fluctuations follow a Gaussian distribution with standard deviation $\sim 1\%$ of the mean value. As a consequence, for each realization of the experiment, the Rabi frequency is slightly different. In order to obtain the Rabi oscillations shown in Figure 3.2, we typically repeat ~ 100 times the experiment. This leads to a damping even though the underlying mechanism is coherent. Figure 3.9 a) shows a simulation of the Rabi oscillation including the decoherence mechanisms described above. We compare situations for which the 420 nm laser power follows a Gaussian distribution with standard deviations of 0% (purple line, no fluctuations), 1% (blue line, measured one) and 3% (red line) of the mean value. The resulting damping dominates the other damping sources, and even strongly increases the damping by a factor ~ 10 when considering 3% of standard deviation as compared to 1%. Note that contrarily to the other sources of damping described above, power fluctuations lead to a Gaussian damping of the Rabi oscillations.
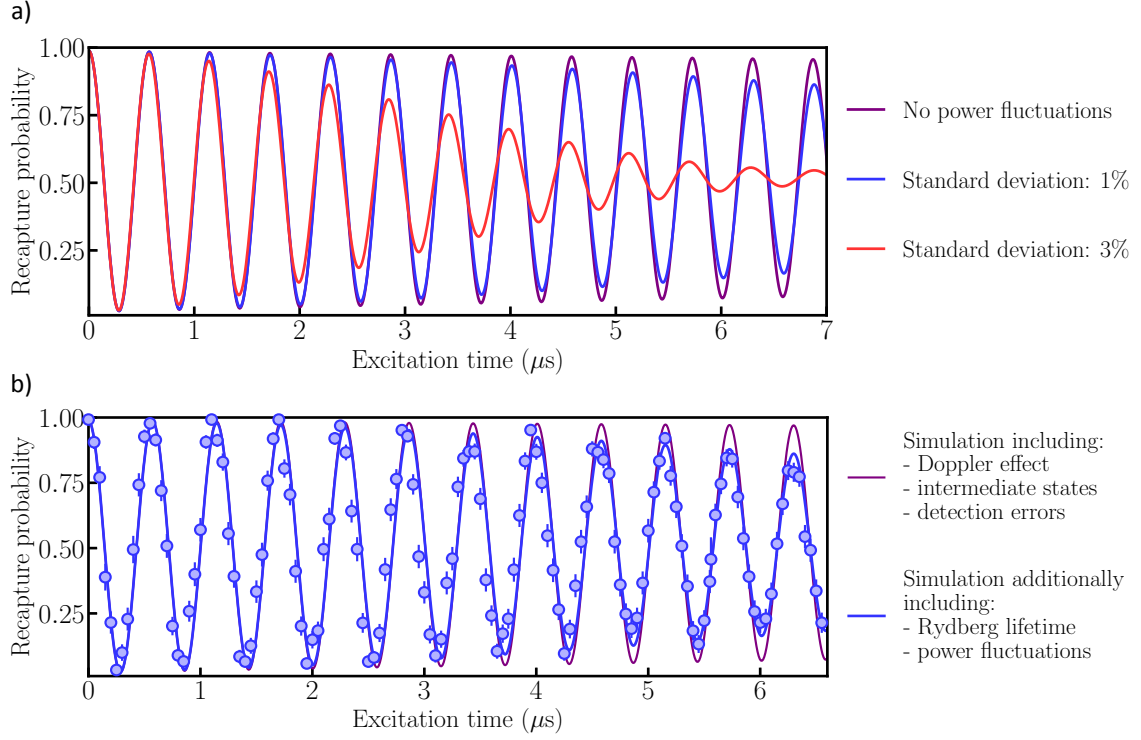
Figure 3.9: Effect of power fluctuations and comparison to the experiment. a) Effect of power fluctuations for various standard deviations. We observe a characteristic Gaussian damping of the oscillations. Its effect plays a major role in the damping of the oscillations when considering realistic standard deviations in the order of a few percent of the mean value. b) A typical experiment for which the power fluctuations were independently measured to be $\sim 1\%$ of the mean value. The complete simulation matches well the experiment. Taking into account only the Doppler effect and the spontaneous emission from the intermediate state show discrepancy after $\sim 3\,\mu$s.

Comparison between experiment and simulations. We finally compare the experimental results with the simulations. Figure 3.9 b) shows a typical Rabi oscillation with $\Omega_{420} = \Omega_{1013} = 2\pi \times 50\,\text{MHz}$ and $\Delta/(2\pi) = 700\,\text{MHz}$. We consider two simulations: (i) a simulation including the effects describing the previous setup [de Léséleuc *et al.*, 2018a] (purple) which ignores the power fluctuations and the Rydberg lifetime, and (ii) a simulation including them (blue). We conclude that:

- At short times ($< 2.5\,\mu$s), both simulations match the data, which validates the approach used to describe the Rabi oscillations of the previous scheme: as the oscillations could not last more than a few microseconds, it was not necessary to take into account the Rydberg lifetime and the power fluctuations.

- At longer times, we observe a discrepancy for the simulation used to describe the previous Rabi oscillations. Including power fluctuations and Rydberg lifetime in the simulations leads to a good agreement with the data, indicating that the evolution of the system is well understood.

The characteristic Gaussian damping of the Rabi oscillations confirms that power fluctuations dominate the damping. Although reducing the power fluctuations would increase the quality of the Rabi oscillations, its effect is negligible in the many-body experiment: we use quasi-adiabatic sweeps to drive the many-body systems for which the exact value of the Rabi frequency is not critical.

Prospects for further improvements. In order to reduce the power fluctuations, a solution would be to apply a feedback on the laser power, e.g. by monitoring the rf power sent to the AOM. To reduce the spontaneous emission, a solution is to increase the single-photon Rabi frequencies, such that for the same effective Rabi frequency we use a larger single-photon detuning. Increasing the single-photon Rabi frequencies can be done by increasing the laser power, e.g. by using an even more powerful amplifier, or to focus the lasers down to the atoms using spherical lenses.

To get rid of spontaneous emission from the intermediate state, the ideal solution would be to drive a single photon ground-Rydberg transition to reach nP states using a laser at 297 nm. Its successful implementation in the frame of quantum simulation has been achieved in the group of I. Bloch [Hollerith *et al.*, 2019]. Single-photon ground-Rydberg excitation using single atoms held in tweezers arrays have been achieved with other atomic species, such as ^{133}Cs [Jau *et al.*, 2016], and ^{88}Sr [Madjarov *et al.*, 2020].

3.4 Conclusion

In this chapter, I presented the new Rydberg excitation scheme. I explained how the new laser setup allowed us to increase both the contrast and the coherence of the Rabi oscillations. We obtain a very good agreement between our simulations and the data by including all of the described effects, showing that we understand the system's limits.

The improved coherence turned out to be crucial for the study of the transverse field Ising model: as compared to first investigations conducted by Lienhard *et al.* [2018], we are now in a regime in which decoherence effects are not predominant (see Chapter 6).

This gave us the ability to explore quantum magnetism in frustrated geometries (see Chapter 7). When performing many-body physics using the dipole-dipole interaction between Rydberg states (see Part III), the enhanced contrast of the Rabi oscillations results in a better initialization of the atoms in the Rydberg states, hence in more contrasted observations.

Large arrays of assembled atoms

Contents

In this chapter, I focus on the production of large 2D assembled arrays. The aim of quantum simulation is to mimic the behavior of real materials. To do so, we need to work with a number of atoms large enough such that the effect of the finite system size is negligible. Reaching a large number of atom is not a trivial task, as we need to rearrange them to work with a fixed configuration. Before I started my PhD, the limit was $N \sim 60$, but in practice the largest quantum simulation experiments were performed with with $N = 49$ atoms [de Léséleuc *et al.*, 2018b]. Technical improvements allowed us to extend this number to $N \sim 200$, with our largest many-body study involving $N = 196$ atoms (see Chapter 6). This extension in the number of atoms induces an increase of the system's Hilbert space size by a factor $2^{196}/2^{49} \sim 10^{44}$, putting the platform at a level for which numerical simulations of the system's evolution is not easily tractable. These improvements consisted of:

- Producing arrays containing up to ~ 700 traps, with area $\sim 130 \times 130 \, \mu\mathrm{m}^2$.

- Optimizing the rearrangement process by increasing its efficiency and scalability.

One of my major contributions was to implement these improvements on the apparatus.

4.1 Arrays with hundreds of traps

The maximum number of tweezers usable to trap atoms is limited by three factors:

- Our ability to produce tweezers arrays with homogeneous trap depth, which is limited by the procedure to generate the traps combined with the optical setup imperfections.

- As the amount of power required to trap the atoms scales linearly with the number of tweezers, we are eventually limited by the available laser power.

- The limited field of view in the focal plane of the Aspherical Lens (AL) imposes a boundary on the size of the arrays.

I detail how we addressed these issues in this section.

4.1.1 Generating homogeneous arrays

We use an optimization algorithm to generate the tweezers arrays based on the Gerchberg-Saxton (GS) algorithm [Gerchberg and Saxton, 1972], presented in the previous theses of the group [Labuhn, 2016; de Léséleuc, 2018]. I here give a brief overview of the algorithm. The Spatial Light Modulator (SLM) imprints a phase pattern $\phi_{\mathrm{SLM}}(y, z)$ on the trapping beam $A_{\mathrm{SLM}} = Ae^{i\phi_{\mathrm{SLM}}(y,z)}$. The optical setup is designed such that the field at the position of the AL is $A_{\mathrm{AL}} = A_{\mathrm{SLM}}$.

Gerchberg-Saxton algorithm. The aim is to produce an array of N tweezers. To calculate the field producing such array, we use the reverting principle of light and consider the tweezers as emitters. The corresponding field A_{em} at the position of the AL is:

$$A_{\mathrm{em}} = \sum_t A_t e^{i\phi_t(y,z)+\theta_t}, \tag{4.1}$$

with A_t the amplitude and $\phi_t(y, z)$ the phase of the field emitted by tweezers t, $t \in [1, N]$, and θ_t an offset phase. We thus need to produce a field $A_{\mathrm{SLM}} = A_{\mathrm{em}}$ in order to create the target array. The aim is to have the exact same amplitudes for each trap $A_t = A$, such that each tweezers share the same properties. However, this also requires control over the amplitude of the field. As the SLM only modifies the phase of the field, it is impossible to rigorously produce the target field. To circumvent this issue, we use the GS algorithm which acts on (A_t, θ_t) to create the target array by
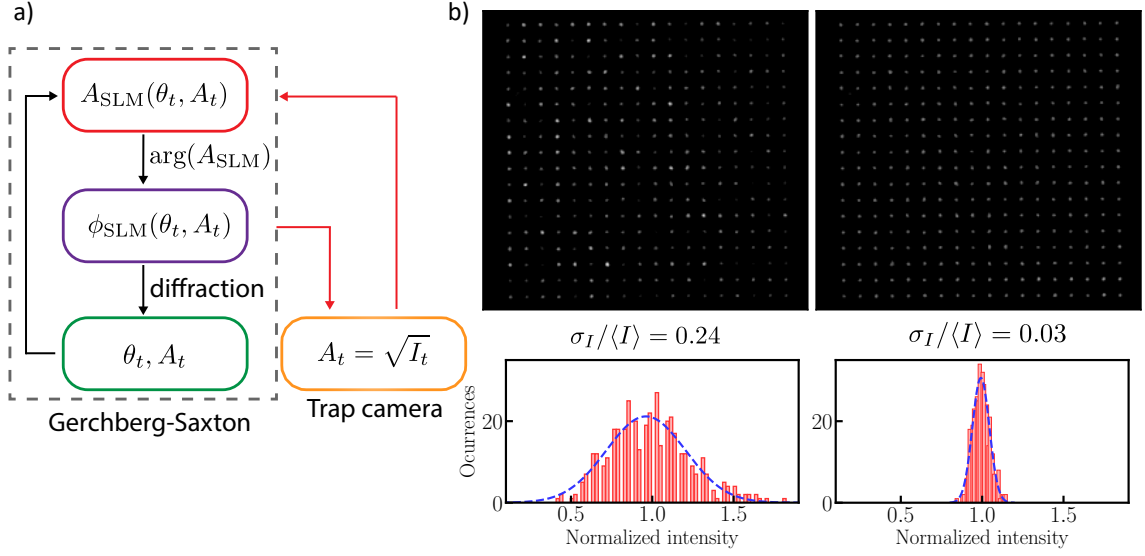
Figure 4.1: Trap power equalization using a camera. a) Sketch of the Gerchberg-Saxton optimization algorithm. The feedback loop uses a camera placed after the vacuum chamber. b) Images of a 18×18 array from the trap camera before (left) and after (right) the power equalization, with the corresponding traps intensity histograms.

only modifying the phase of the light. The algorithm, sketched in Figure 4.1 a), is a closed-loop optimization process [Spalding, Courtial, and Leonardo, 2008] taking as a starting point:

$$\phi_{\text{SLM}}^0 = \arg(A_{\text{em}}), \tag{4.2}$$

with equal amplitudes $A_t^0 = A$ and random phases θ_t^0. The algorithm then enters the optimization loop, in which it calculates the trap intensity V_t of each trap t using the diffraction formula:

$$V_t = \iint e^{i[\phi_{\text{SLM}}(y,z) - \phi_t(y,z)]} \mathrm{d}y \mathrm{d}z. \tag{4.3}$$

The algorithm tries to find the trap phase θ_t that maximizes the intensity of the traps, whilst equalizing the traps intensity by adjusting A_t. The number of steps is typically ~ 10. Using a Graphics card to run the calculation, we reach a computation time of $\sim 10\,\text{s}$ for ~ 1000 traps.

Feedback loop using a camera.   We measure the traps intensity using a camera placed at the exit of the vacuum chamber, which is called the *trap camera* in the following. After the traps generation using the GS algorithm, the power in the tweezers is not homogeneous (see Figure 4.1 b)) because of imperfections in the optical setup which are not taken into account in the diffraction formula. The distribution of the trap

intensity displays a Gaussian shape, with relative standard deviation $\sigma_I/\langle I \rangle \sim 20\%$. To solve this issue, we add an extra step to the GS algorithm consisting of measuring the real traps intensity I_t after the vacuum chamber, from which we extract the weight of the traps $A_t^{\text{real}} = \sqrt{I_t}$. We run the GS algorithm with the initial condition $A_t^0 = A_t^{\text{real}}$, and repeat ~ 10 times the process to reach inhomogeneities of $\sigma_I/\langle I \rangle \sim 3\%$. We have to repeat the equalization procedure every month due to long term misalignment of the optical setup.

The feedback using the camera introduces a bias: it corrects the intensity profile on the camera placed after the vacuum chamber, and not directly in the atomic plane. The bias is supposed to be negligible as the camera is optically conjugated with the atomic plane. However, imperfections of the optical components placed between the atoms and the camera distort the light field. Having a trap power equalized *on the camera*, we observe two phenomena *on the atoms*:

- A global gradient in trap depth of $\sim 50\,\text{kHz}/\mu\text{m}$ in the left-right direction, which has to be compared to the average trap depth $U/h \simeq 20\,\text{MHz}$.

- $\sim 1 - 5\%$ of the tweezers have $\sim 20\%$ lower trap depth, with random positions.

This shows that equalizing the trap power on the camera placed after the vacuum chamber is not the correct observable to have tweezers with equal trap depth inside the vacuum chamber.

In-situ feedback loop. To avoid the introduction of a bias, we devised an alternative version of the feedback loop to directly equalize the traps power at the position of the atoms. The conditions are the following: having the MOT light on, we let the atoms enter and leave the traps over a duration of 10 seconds, a long time compared to the average loading time (500 ms). The feedback is then performed on the filling fraction p_t of the atoms in the tweezers (see Figure 4.2 a)) as follows:

- If p_t is low, the trap depth is not high enough to keep the atoms in the tweezers.

- If p_t is high, the trap is deep enough. Due to the collisional blockade, the maximum value of p_t is 0.5.

We now use as the normalized trap weight $A_t = 2p_t$. The traps intensity after equalization, measured on the trap camera, is shown in Figure 4.2 b) for a 14×29 array with size $130 \times 140\,\mu\text{m}^2$. We observe a strong intensity inhomogeneity with a gradient along the $\hat{d}$ direction, whereas the traps are equalized in the atomic plane.
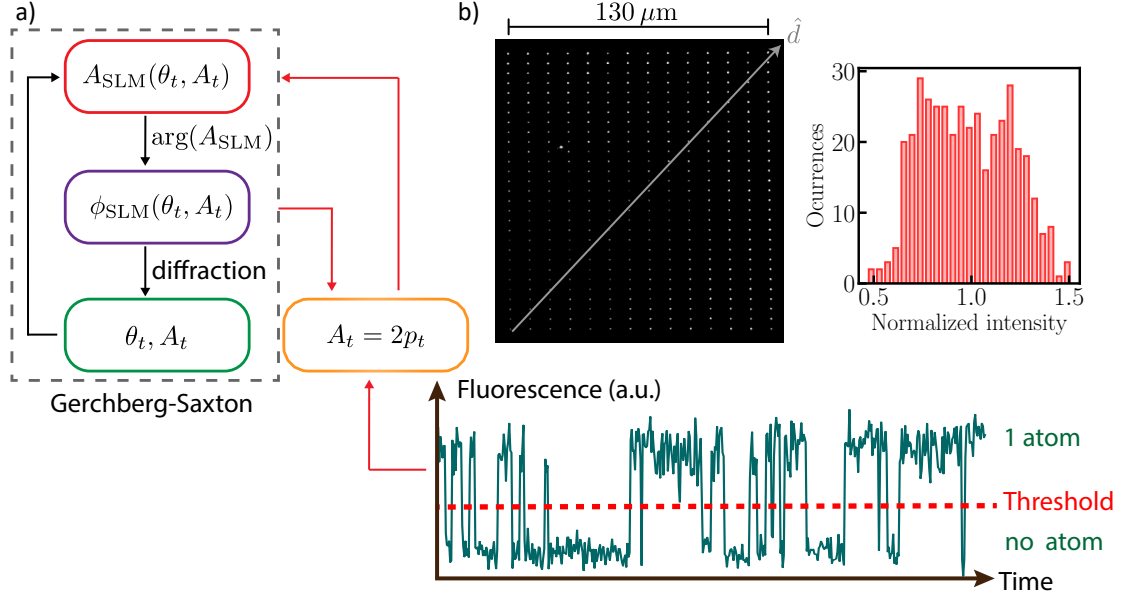
Figure 4.2: Trap power equalization using the atom fluorescence. a) The feedback loop uses as a signal the atom fluorescence by measuring the averaged probability of having an atom in the trap. b) Image of an equalized 14×29 array using the trap camera, with the corresponding histogram of the trap intensity. We observe a strong intensity inhomogeneity along the $\hat{d}$ direction, whereas the traps are equalized in the atomic plane.

Difficulties of the method and prospects for improvements. This method is challenging to perform for several reasons:

- The algorithm can diverge: if there is too much power in a trap, the fluorescence signal is small due to the strong light shift applied by the tweezers. The optimization loop thus considers that the trap has low power and will thus increase it.

- The equalization procedure can be unstable: as the method relies on observing the loading of atoms in the tweezers, variations of loading rate and background light can lead to wrong evaluations of p_t.

- The equalization procedure can be inaccurate: the algorithm attributes the same weight for all the traps displaying $p_t = 0.5$ and $p_t = 0$, whereas their trap depth may not be equal. We perform the method with a low average power to be in a regime where the traps are barely trapping atoms.

Despite these shortcomings, we were able to equalize arrays with up to ~ 700 atoms. To further improve the method, we could apply the following procedure: starting at

low trap power, we would increase it until observing the fluorescence of the atoms in the tweezers. The optimization loop observable would therefore be related to the moment at which the traps start to be filled. This improvement would avoid the divergence and the accuracy issues, and is currently being implemented in the lab.

4.1.2 Increasing the number of traps

As the required laser power scales linearly with the number of atoms, the total available laser power limits the number of tweezers. When I started my PhD, the maximum number of traps we could reliably produce was ~ 200. I will now explain how we pushed this number to ~ 700 during my PhD.

Increasing the trap power. The trapping laser is a M-Squared Titanium-Sapphire (TiSaph) laser. Due to the optical components on the beam path, the power in front of the vacuum chamber is only $\sim 30\%$ of its value at the laser output. When I started my PhD, the output TiSaph power was $\sim 3.5\,\mathrm{W}$ and the wavelength was 852 nm, corresponding to $\sim 1\,\mathrm{W}$ before the vacuum chamber. As the power required to trap an atom (measured before the chamber) at 852 nm is $\sim 5\,\mathrm{mW}$, the resulting maximum number of traps is ~ 200.

During my PhD, we changed the TiSaph pumping laser, from a Verdi V12 to a Verdi G18. The output power of the pump went from $12\,\mathrm{W}$ to $18\,\mathrm{W}$, allowing for powers up to $\sim 6\,\mathrm{W}$ at the output of the TiSaph, corresponding to an increase of $\sim 70\%$ of the number of traps. We also changed the trapping wavelength to 821 nm.

A change in the trapping wavelength. The tweezers trap depth is given by the light shift U/h applied to the atom, which is $U/h \simeq 20\,\mathrm{MHz}$ to trap an atom in our experiment. The tweezers are far-detuned by Δ_t from the $5S_{1/2} - 5P_{1/2}$ transition to avoid strong Raman scattering (see below). The tweezers light-shift reads:

$$U/\hbar = \Omega_t^2 \left(\frac{1}{\Delta_t} + \frac{1}{\Delta_t + \Delta_P} \right), \tag{4.4}$$

with Δ_P the frequency difference between the $5P_{1/2}$ and the $5P_{3/2}$ levels and Ω_t the tweezers' Rabi frequency (considered to be the same for both levels). Keeping U fixed, we decreased the power required to trap the atoms by changing Δ_t. We changed the trapping wavelength from 852 nm ($\Delta_t \simeq 2\pi \times 25.2\,\mathrm{THz}$) to 821 nm ($\Delta_t \simeq 2\pi \times 11.9\,\mathrm{THz}$) to divide by two the trapping power, i.e. $\sim 2.5\,\mathrm{mW}$, allowing us
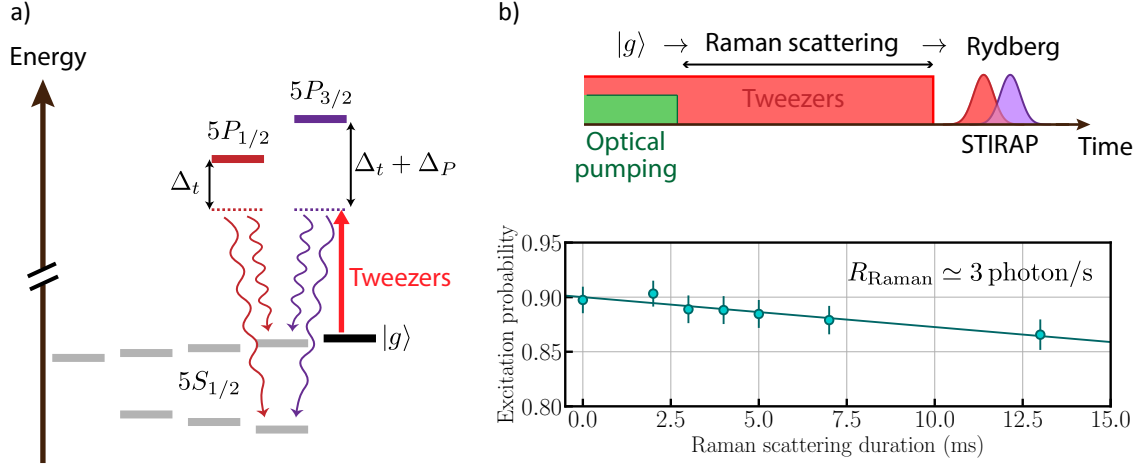
Figure 4.3: Raman scattering. a) Sketch of the Raman scattering by the tweezers beam, which depumps the atoms from $|g\rangle$ to other ground states. b) Sketch and results of the experiment measuring the Raman scattering rate R_{Raman}. After pumping the atoms in $|g\rangle$, we let the tweezers on for a variable Raman scattering duration. Atoms in $|g\rangle$ are then excited to a Rydberg state. The solid line is a fit to the data using a linear function from which we extract $R_{\mathrm{Raman}} \simeq 3\,\mathrm{photon/s}$ using the tweezers at 821 nm, consistent with the calculated value.

to double the number of traps using the same amount of total power. Following this argument, we could be tempted to further reduce Δ_t to increase the number of atoms. We are, however, eventually limited by inelastic scattering of the tweezers' light which heats the atom at a rate $\dot{U} = 2RE_r$, with $R \simeq 100\,\mathrm{photon/s}$ the scattering rate at 821 nm, and $E_r \simeq 300\mathrm{nK}$ the recoil energy. The typical holding time of the atom in the tweezers is at most $\sim 50\,\mathrm{ms}$. The corresponding heating is thus $\sim 3\,\mu\mathrm{K}$, far from being enough to expel the atom out of the tweezers. The actual issue is the Raman scattering, which I now describe.

Raman scattering. The Raman scattering process, detailed in the thesis of Jérôme Beugnon [2007] and firstly observed in Cline *et al.* [1994], is a phenomenon which transfers the atoms from one ground state to another one. In order to efficiently excite the atoms into their Rydberg states, we initialize them in $|g\rangle = \left|5S_{1/2}, F = 2, m_F = 2\right\rangle$ using optical pumping (see Section 2.2.2). Due to the Raman scattering, the atoms are depumped from $|g\rangle = \left|5S_{1/2}, F = 2, m_F = 2\right\rangle$, inducing a reduction of the Rydberg excitation efficiency. The Raman scattering corresponds to the scattering from the tweezers with a change of internal atomic state: the atom is (incoherently) transferred into $(F = 1, m_F = 1)$, or $(F = 2, m_F = 1)$ (see Figure 4.3 a)). Other states are not

reachable as the tweezers are linearly polarized. The scattering rate is given by:

$$R_{\mathrm{Raman}} \propto \left| \frac{1}{\Delta_t} - \frac{1}{\Delta_t + \Delta_P} \right|^2 . \tag{4.5}$$

By decreasing Δ_t, we calculate an increase of the Raman scattering from $R_{\mathrm{Raman}} \simeq 0.3$ photon/s (852 nm) to $R_{\mathrm{Raman}} \simeq 3$ photon/s (821 nm).

We measure R_{Raman} using the tweezers at 821 nm by performing the following experiment, presented in Figure 4.3 b): we initialize the atoms in $|g\rangle$ using the optical pumping, and leave the tweezers on for a variable Raman scattering duration t_{R} before Rydberg excitation. The probability p_{R} for the atom to be affected by Raman scattering over a duration t_{R}, and thus depumped out of $|g\rangle$, is $p_{\mathrm{R}} = 1 - e^{-t_{\mathrm{R}} R_{\mathrm{Raman}}}$. The experiment is performed with $t_{\mathrm{R}} R_{\mathrm{Raman}} \ll 1$, such that $p_{\mathrm{R}} \simeq 1 - t_{\mathrm{R}} R_{\mathrm{Raman}}$. We measure the Rydberg excitation efficiency which is directly linked to the $|g\rangle$ state population (up to detection errors, see Section 3.3.1). The solid line is a linear fit to the data from which we extract $R_{\mathrm{Raman}} \simeq 3\,\mathrm{photon/s}$, in good agreement with the calculated value.

The typical time between the initialization into $|g\rangle$ and the Rydberg excitation is $t_{\mathrm{R}} = 20\,\mathrm{ms}$ due to the adiabatic ramping down of the trap power, detailed in Section 2.2.1. Using tweezers at 852 nm, we obtain $p_{\mathrm{R}} \simeq 0.02\%$, which is negligible compared to other sources of errors (see Section 3.3.1). Now using tweezers at 821 nm, $p_{\mathrm{R}} \simeq 0.2\%$, comparable to the optical pumping imperfection. These values take into account the adiabatic ramping down of the traps power which decreases R_{Raman}.

Prospects for further improvements. If the Rydberg excitation would happen directly after the initialization in $|g\rangle$, the Raman scattering would not impact the system and we could further decrease the tweezers detuning. We could excite the atoms to their Rydberg states directly after the optical pumping stage which initializes the atoms into $|g\rangle$. Another solution would be to improve the optical setup by free-space coupling the laser to the atoms, which would allow us to double the number of tweezers. However using the current technologies, it seems hard to achieve more than thousands of tweezers, as the required power scales linearly with the number of traps.

4.1.3 Extending the size of the arrays

For the many-body experiments presented in this thesis, the typical distance between the atoms is $\sim 10 - 20\,\mu\mathrm{m}$. The size of hundreds-trap arrays is thus in the range
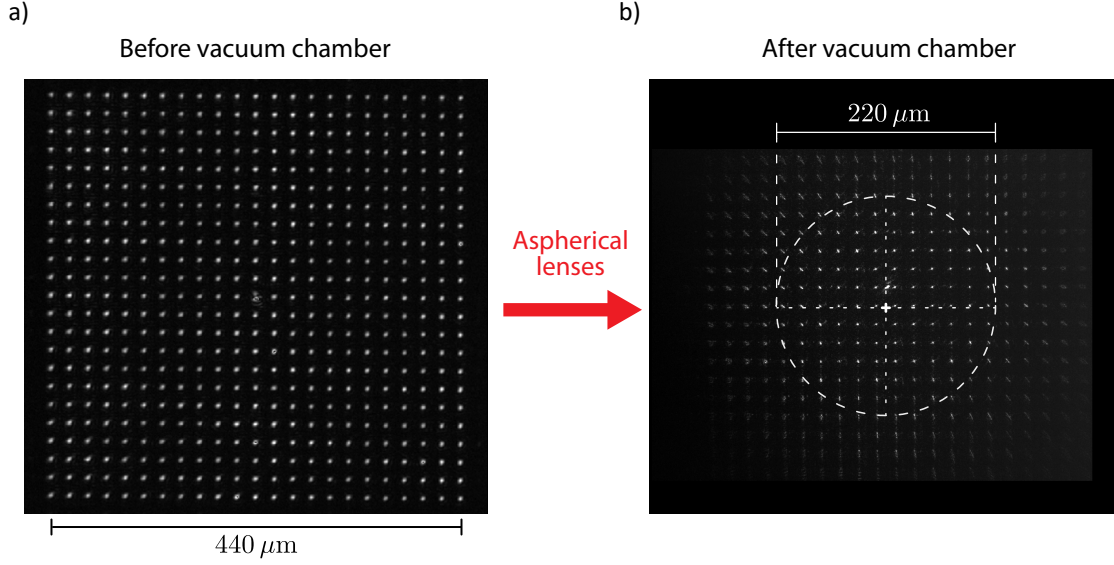
Figure 4.4: Field of view of the aspherical lenses. Images of a 23×23 array with a distance of $20\,\mu$m between the traps, before (left) and after (right) the vacuum chamber. The white cross represents the center of the AL field of view.

$\sim 100 - 150\,\mu$m, which is an issue as the field of view of the Aspherical Lenses (AL) is limited. In the thesis of Lucas Béguin [2013], the field of view is defined as the radius r_{FoV} for which the Strehl ratio is $S(r_{\mathrm{FoV}}) = 0.8$, which gives $r_{\mathrm{FoV}} \simeq 50\,\mu$m, smaller than the typical size of the arrays we use in this thesis. In this section, I describe the effects of the field of view on the tweezers, and how we compensated those effects (up to a certain radius) during my PhD.

Field of view of the aspherical lenses. A tweezers away from the optical axis exhibits aberrations with two qualitatively different behaviors:

- Close to the optical axis ($\leq 50\mu$m), the tweezers peak intensity $I_{\mathrm{peak}}(r)$ decreases linearly as $I_{\mathrm{peak}}(r) = I_0(1 - \alpha r)$ [Béguin, 2013] with r its distance from the optical axis, and I_0 the peak intensity on the optical axis. The tweezers waist is not affected.

- Far from the optical axis (defined below), aberrations strongly modify the light shape, which can no longer be considered as Gaussian, thus preventing atoms from being trapped.

The tweezers peak intensity reduction is not critical, as this reduction can be compensated for by performing the equalization procedure presented in Section 4.1.1. The

a)

b)
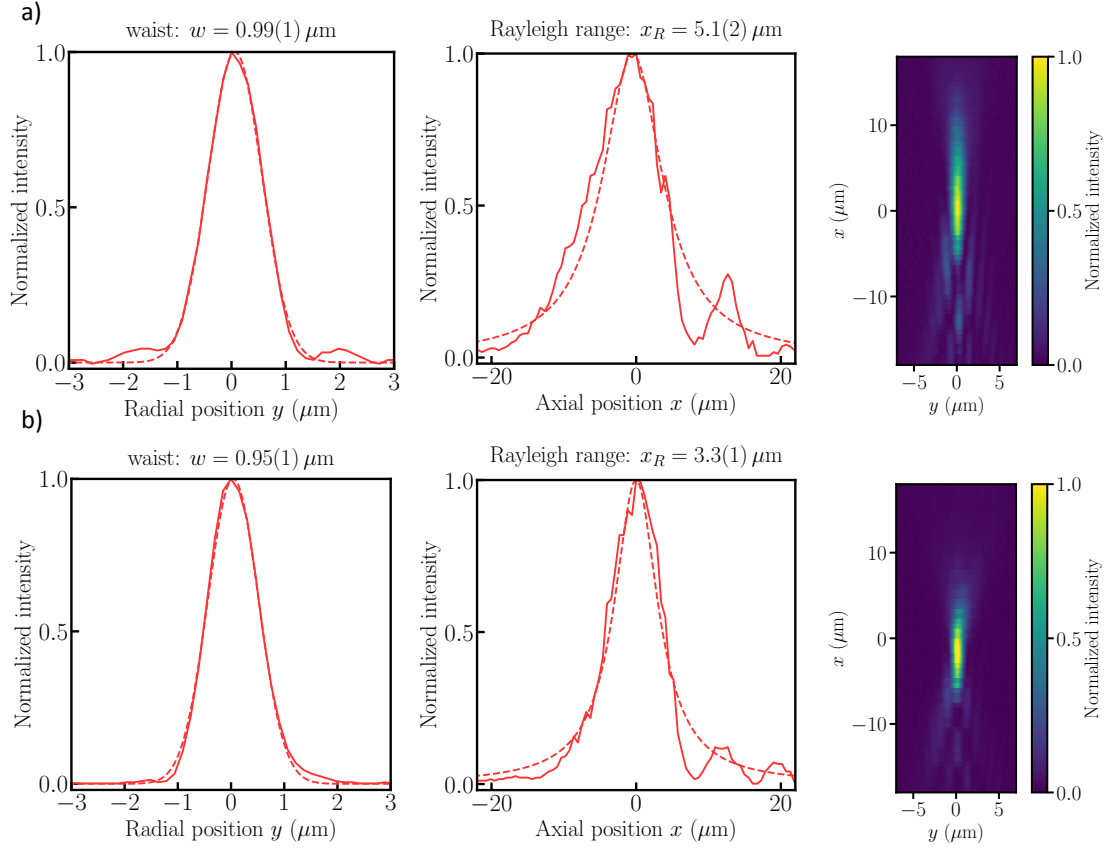
Figure 4.5: Effect of aberrations correction on the tweezers profile. Tweezers profiles in its radial (left panels) direction y at the AL focal point, in the axial (center panels) direction x along the optical axis, and in the (y, x) plane (right images). The profiles are recorded a) without and b) with corrections of the aberrations.

problematic part is far from the optical axis: every tweezers do not share the same properties, leading to, e.g., inhomogeneous atom temperatures, or a breaking of the collisional blockade in the extreme case.

We measure the effect of the AL field of view on the tweezers shape by creating a 23×23 array with a distance of $20\,\mu$m between the tweezers, giving an area of $440 \times 440\,\mu$m^2, see Figure 4.4 a). We measure, from the array after the vacuum chamber (see Figure 4.4 b)), a region with radius $\sim 110\,\mu$m for which the tweezers shape is not strongly modified. This experiment also allows us to center the array onto the AL optical axis, as the optical axis is positioned at the center of the field of view (white cross in Figure 4.4 b)). To center the array, we apply a global phase grating on the SLM.

Correction of the aberrations using a Shack-Hartmann   We correct for the aberrations using the SLM following a procedure decribed in detail in the thesis of Henning Labuhn [2016]. When I started my PhD, we were using a Shack-Hartmann (SH) device placed after the vacuum chamber, where the beam is collimated by the second AL, to measure the aberrations. Due to the aberrations, the wavefront is not flat and the SH measures its distortion and quantifies it using the Zernike polynomials [Love, 1997]. Figure 4.5 presents the impact of aberrations correction on a tweezers positioned $25\,\mu$m away from the AL optical axis. We record the tweezers' intensity profile (solid lines) after the vacuum chamber a) without and b) with aberrations correction along various directions:

- In the focal plane of the tweezers (left panels), along the radial direction y. The tweezers is a Gaussian (dashed line) in both cases, giving similar waists: $w = 0.99(1)\,\mu$m without correction and $w = 0.95(1)\,\mu$m with. The difference between the two profiles is the absence of residual intensity maxima around $\pm 2\,\mu$m from the tweezers center in the aberrations-corrected case, which induces a higher peak intensity.

- In the axial direction (center panels), recorded by using electro-tunable lenses [de Léséleuc, 2018; Barredo *et al.*, 2018] to change the distance x between the tweezers focal point and the camera plane. The solid line is the measured intensity at axial position x. Without aberrations correction, we observe a substantial deviation from the expected Lorentzian profile (dashed line). The aberrations correction strongly reduces the extracted Rayleigh range: $x_R = 5.1(2)\,\mu$m without to $x_R = 3.3(1)\,\mu$m with correction.

- In the (y, x) plane (right images) by stacking radial profiles along y for various axial positions x. The corrected tweezers displays a smaller area due to the Rayleigh range reduction.

In-situ correction of the aberrations.   Correcting for aberrations after the vacuum chamber is not ideal, as the second AL also introduces aberrations which we correct for whereas they are not present in the atomic plane. To circumvent this issue, we follow the approach of the in-situ trap power equalization and use as an observable the fluorescence signal from the atoms. As discussed above, the major effect of the aberrations (in the field of view) is to reduce the tweezers trap depth. We use this as an asset for aberration correction by performing the following experiment: having the MOT light on, we let the atoms enter and leave the traps. The tweezers trap

power is chosen such that the probability to have an atom in the tweezers p_t is low. The aberrations are corrected when p_t increases. The gain in power with aberration corrections depends on the size of the array. For typical arrays presented in this thesis, aberrations correction allows us to reduce by $\sim 20\%$ the total power required to trap the atoms.

Prospects for further improvements. To my knowledge, there is no simple solution to extend the size of the arrays above the AL field of view with the current setup. One solution, which requires changing the entire setup, would be to use a high numerical aperture microscope for which the typical field of view is $\sim 1\,\mathrm{mm}$. As its working distance is short (cm range) and as placing it under vacuum would be technically extremely challenging, it would be necessary to switch the vacuum system for a glass cell. This option will be developed in the group in the coming years.

4.2   Assembling hundreds-atom arrays

As the filling fraction of a tweezers is ~ 0.5, we rearrange the atoms to reach a desired configuration by superimposing onto the static traps generated by the SLM, a moveable tweezers (MT) generated by two orthogonal AODs. The MT rearranges the atoms between the static traps. The various devices used to perform the rearrangement are described in the thesis of Sylvain de Léséleuc [2018]. Before I started my PhD, the maximum number of atoms was $N \sim 60$ due to the limited efficiency of the assembling process, induced by (i) the fidelity of rearranging one atom and (ii) the process duration, due to the lifetime of the atoms in the tweezers. We improved these two limiting factors during my PhD. We pushed the number of traps to ~ 700, as described above. A comparison between the previous assembling efficiency [Barredo et al., 2016] and the current one is shown in Figure 4.6: we measure the probability P_{fill} to perfectly assemble arrays with various traps number N, in square (square markers) and triangular (triangle markers) geometries. Images of the largest arrays for both are shown. The solid lines are fits to the data using a function derived below (Equation (4.11)). We obtain a strong increase of P_{fill}: the production of arrays containing $N = 100$ atoms increased from $P_{\mathrm{fill}} \sim 0.5\%$ to $P_{\mathrm{fill}} = 25\%$. This section presents the various improvements leading to this increase of P_{fill}.
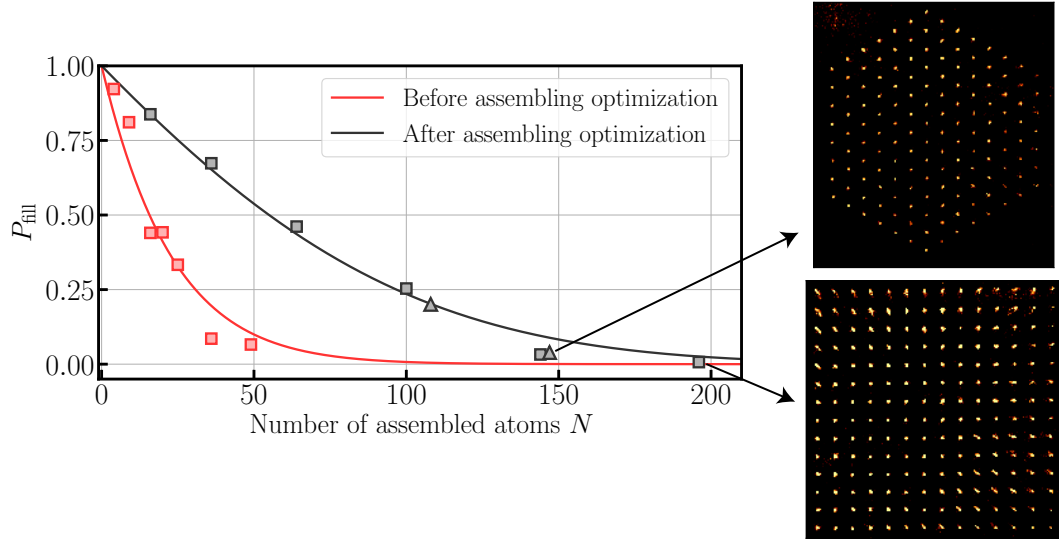
Figure 4.6: Comparison of the assembling success probability. Assembling success probability P_{fill} as a function of the atom number N, before (red) and after (grey) the various optimizations detailed in this section. The square and triangular markers represent arrays with square and triangular geometries. Image of the largest assembled array for both.

4.2.1 Analysis of the assembling efficiency

I detail here the various processes limiting the assembling efficiency, and derive the probability P_{fill} of assembling successfully a given array as a function of the number of atoms N.

Moving an atom. To move an atom from an initial trap to a target trap, we use the following procedure, already described in Section 2.1.2:

- We start by focusing the MT onto the initial trap with negligible power. We then ramp up the MT power to a trap depth of $\sim 10\,\text{mK}$ in $300 - 500\,\mu\text{s}$, which is 10 times higher than the trap depth of the static trap. The atom is thus transferred into the MT.

- We then move the MT from the initial static trap to the target trap at a speed of $100\,\text{nm}/\mu\text{s}$.

- We ramp down the MT power to zero in $300 - 500\,\mu\text{s}$. The atom is thus transferred into the target trap.

We will call this process a *move* in the following. The duration of each step is set to optimize the move fidelity η_{m}, and is much longer than the typical oscillation period of
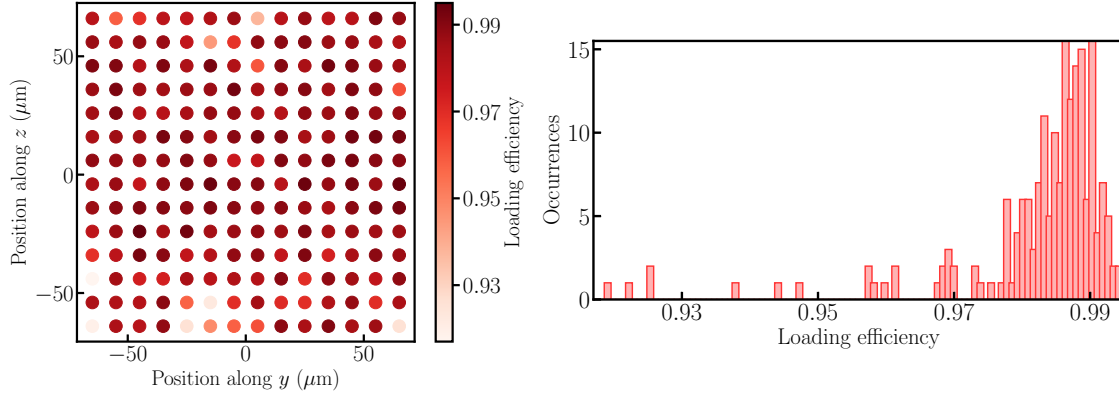
Figure 4.7: Inhomogeneous loading efficiency. Loading efficiency per trap after the rearrangement process of a 14×14 array with $10\,\mu$m between the traps.

the atom in the tweezers. The resulting typical move duration is $t_{\mathrm{m}} \simeq 1\,$ms. The finite efficiency of the process has two main origins: (i) the optical quality of both the static traps and the MT, and (ii) an imperfect matching between the MT and the static traps. I start by describing the latter.

Moving tweezers accuracy. We use a camera placed after the vacuum chamber to place the MT onto the static traps [de Léséleuc, 2018]. We record the MT position for various values of the rf frequency driving the MT AODs, and also record the position of the static traps. By matching both, we obtain the frequencies at which we have to drive the AODs to target a given trap. However, we observed that the array moves on the camera, on timescales of $\sim 1\,$s and on distances $\sim 25\%$ of the tweezers waist. Its possible origin is the air flow in the lab, which induces fluctuations of the air refractive index. The matching between the MT and the static trap is thus inaccurate. We partly solved this issue during my PhD by averaging over ~ 100 images the position of the array. Another uncertainty comes from the fact that the position matching is not performed directly on the atoms, which could be done by looking at their fluorescence inside the MT and the static traps.

Inhomogeneous assembling efficiency on large arrays. The assembling efficiency is inhomogeneous when rearranging large arrays, as shown in Figure 4.7 in which we look at the probability p_t of loading the traps after the assembling process, for a 14×14 array, with a distance of $10\,\mu$m between the traps. For most of the traps, $p_t \sim 98.5\%$. However, some specific traps have a smaller loading efficiency, which has two origins:
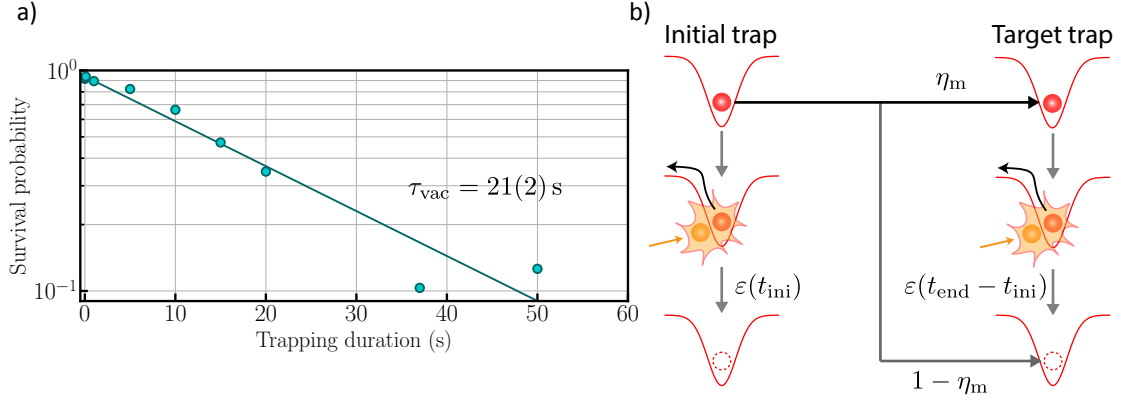
Figure 4.8: Lifetime of an atom in a tweezers. a) Survival probability of an atom held in a tweezers for various trapping durations. The solid line is a fit to the data using an exponential function, from which we extract $\tau_{\text{vac}} = 21(2)\,\text{s}$. b) Two mechanisms limit the assembling efficiency: the atom lifetime and the move fidelity.

- Close to the array center, we measure $p_t \sim 97\%$ for a few traps. This lower probability could come from an imperfect equalization of the static trap power (see Section 4.1.1), resulting in a trap depth lower than the rest of the array. This low trap depth could lead to losses when transferring atoms using the MT.

- Far from the array center: due to the limited field of view of the AL, the MT far from the optical axis exhibits strong aberrations which affect its shape and induce defocusing. The matching between MT and static traps is thus less good, which induces a loss in the move fidelity η_{m}. As the MT aberrations cannot be compensated, it is important to center the array on the aspherical lenses optical axis to minimize the aberrations (see Section 4.1.3).

The AL field of view strongly limits the assembled arrays area. In order to illustrate this on an example, let us consider a square lattice. As the required number of traps is $2N$ to assemble N atoms, the array area is twice as big compared to the assembled one. For the 14×14 assembled array shown here, we would need an initial array area of $190 \times 190\,\mu\text{m}^2$, which is out of the AL field of view (see Section 4.1.3) and thus impossible to realize. To solve this issue, we use arrays for which the $2N$ traps have the same area as the target array, by placing the traps which are not assembled in between the target ones (see Section 4.2.3). In the following, we will suppose that η_{m} is homogeneous over the array.

Lifetime of an atom in a tweezers. The main limitation in the assembling efficiency is the lifetime τ_{vac} of the atoms in the tweezers, which is dominated by background-gas collisions. We measure the atom lifetime by varying the trapping duration and looking at the survival probability of the atoms in the tweezers, see Figure 4.8 a). The solid line is a fit to the data using an exponential function, from which we extract $\tau_{\mathrm{vac}} = 21(2)\,\mathrm{s}$. We define the probability $\varepsilon(t)$ that the atom leaves the tweezers region after a duration t as $\varepsilon(t) = 1 - e^{-t/\tau_{\mathrm{vac}}}$. This error is negligible on a single move: $\varepsilon \simeq 5 \times 10^{-5}$. However, the atom lifetime becomes predominant when working with large arrays, as described below.

Probability to successfully assemble an array. Now that we have described the two processes leading to the limited assembling efficiency (move fidelity and lifetime of an atom in a tweezers), we derive the formula giving the success probability P_{fill} of assembling an array of N atoms. We consider an initial array of $2N$ traps and a target array of N traps. We suppose that the assembling process has a duration t_{tot}.

We first focus on moving a single atom, as depicted in Figure 4.8 b). The probability P_{fill}^{1} of successfully rearranging the atom at the end of the assembling process is limited by: (i) the single move fidelity η_{m}, and (ii) the atom lifetime, with the associated probability for the atom to be still in the tweezers at the end of the assembling process $1 - \varepsilon(t_{\mathrm{tot}})$. We thus obtain the success probability P_{fill}^{1} of moving the atom at the end of the assembling process:

$$P_{\mathrm{fill}}^{1} = \eta_{\mathrm{m}} e^{-t_{\mathrm{tot}}/\tau_{\mathrm{vac}}}. \tag{4.6}$$

We now move on to the entire array assembling probability $P_{\mathrm{fill}}^{\mathrm{arr}}$. To simplify the calculations, we consider that the move fidelity is homogeneous. Half of the atoms are initially held in the target array as the loading probability of a tweezers is ~ 0.5. We consider a perfect assembler algorithm, for which the number of moves N_{m} is equal to the number of atoms missing in the target array: $N_{\mathrm{m}} = N/2$. The influence of the assembler algorithm is discussed below. The atoms initially held in the target tweezers can also be lost due to their lifetime with a probability $\varepsilon(t_{\mathrm{tot}})$, such that:

$$P_{\mathrm{fill}}^{\mathrm{arr}} = \left[P_{\mathrm{fill}}^{1}\right]^{N/2} \times \left[e^{-t_{\mathrm{tot}}/\tau_{\mathrm{vac}}}\right]^{N} = \eta_{\mathrm{m}}^{N/2} e^{-N t_{\mathrm{tot}}/\tau_{\mathrm{vac}}}. \tag{4.7}$$

For a perfect assembler algorithm which instantaneously calculates the required moves to assemble an array, the total assembling time is $t_{\mathrm{tot}} = (N/2)t_{\mathrm{m}}$ with t_{m} the move

duration. The formula thus reads:

$$P_{\text{fill}}^{\text{arr}} = \eta_{\text{m}}^{N/2} e^{-\frac{N^2}{2\tau_{\text{vac}}} t_{\text{m}}}. \tag{4.8}$$

In the limit $\eta_{\text{m}} = 1$, P_{fill} decreases in a Gaussian fashion with N. The typical number of atoms N_c for which $P_{\text{fill}} = 1/e^2$, i.e., the number of atoms we can reasonably successfully assemble due to the atom lifetime is $N_c = \sqrt{2\tau_{\text{vac}}/t_{\text{m}}} \simeq 300$. We can find this result using the following reasoning: the lifetime of a configuration with N atoms is $t_{\text{arr}} = \tau_{\text{vac}}/N$, and we need a time t_{tot} to assemble the array. The number of atoms we can reasonably assemble is when $t_{\text{arr}} = t_{\text{tot}}$, giving $\tau_{\text{vac}}/N = (N/2)t_{\text{m}}$.

Influence of the assembler algorithm. In the above calculation, we neglected two things: (i) we also have to calculate the moves to reach the target configuration which takes a time t_{calc}, and (ii) the number of moves $N_{\text{m}} = N_{\text{extra}} + N/2$ can be higher than $N/2$ due to geometrical constraints described below. The values of t_{calc} and N_{extra} depend on the moves computation algorithm, which is the topic of the next section. Considering these two points, the Equation (4.7) reads:

$$P_{\text{fill}} = \eta_{\text{m}}^{N_{\text{m}}} e^{\frac{N}{\tau_{\text{vac}}}(N_{\text{m}} t_{\text{m}} + t_{\text{calc}})}, \tag{4.9}$$

which can be written as

$$P_{\text{fill}} = P_{\text{fill}}^{\text{arr}} \times \eta_{\text{m}}^{N_{\text{extra}}} e^{\frac{N}{\tau_{\text{vac}}}(N_{\text{extra}} t_{\text{m}} + t_{\text{calc}})}, \tag{4.10}$$

with $P_{\text{fill}}^{\text{arr}}$ given by Equation (4.8). This shows the importance of having an optimized algorithm for the moves computation. The scaling of N_{extra} and t_{calc} with N is derived below.

4.2.2 A new rearrangement algorithm

Now that I have introduced the importance of having an optimized algorithm for the assembler, I briefly describe the change of algorithm done during my PhD, which was one of the PhD project of Kai Nicklas-Schymik [Schymik *et al.*, 2020].

Two types of moves. The way we assemble the atoms drastically affects the performance of the moves computation algorithm. I thus briefly discuss it here. We distinguish two possibilities: moving the atoms in between the static traps, and

moving them along the traps. These two approaches are detailed in the thesis of Sylvain de Léséleuc [2018]. Whilst moving the atoms in between the static traps avoid encountering atoms on the path, we prefer to move the MT along the traps. When performing many-body experiment, we are in a situation for which the minimal distance between the atoms is $\sim 5\,\mu$m. The aberrations on the MT leads to a spread of intensity at $\sim 2.5\,\mu$m from the tweezers focal point (see Section 4.1.3): when the MT travels in between the traps, the MT light affects the surrounding static traps. In the following, we will consider that the MT moves along the static traps. This means that when moving one atom from a source trap S to a target trap T, it might happen that the MT has to cross a filled trap F. The process would result into a collision, thus a loss of both atoms. To perform the $(S \to T)$ move, we split it into two moves and first do $(F \to T)$, then $(S \to F)$. An optimized algorithm aims at reducing as much as possible these events.

"Shortest-move first" algorithm. When I started my PhD, we were using a moves computation algorithm which we named the "shortest-move first" algorithm [de Léséleuc, 2018], which works as follows: at each repetition of the experiment, the algorithm (i) looks at the position of the N atoms in the array, (ii) calculates the N^2 distances D between each atom and each target trap (including $D = 0$), and (iii) creates the list $\mathcal{L}$ of moves to perform, ordering them by increasing D. The moves involving traps or atoms already involved in a previous move are not added to $\mathcal{L}$.

The algorithm does not take into account the fact that some assembled atoms may block the path for others, as sketched in Figure 4.9 a) on the simplest case of two atoms in a 1D chain of four traps: the number of moves calculated by the algorithm is three, whereas the assembling could be intuitively done with two moves. To measure the algorithm computation efficiency, we compute the number of moves N_m for the typical array shape we use (see Section 4.2.3) as a function of the number of atoms N, see Figure 4.9 c) (red markers). The displayed data are extracted from simulations (performed by Kai-Niklas Schymik *et al.* [2020]) of 1000 random initial configurations. The dashed line is a linear fit to the data, from which we extract a typical evolution of the number of moves $N_\mathrm{m} \simeq 0.85N$. The computation time scales as $t_\mathrm{calc} \propto N^2$, with typical value $t_\mathrm{calc} \sim 100\,$ms for $N \sim 200$.

Linear sum assignment problem and post-processing. In order to improve both the number of moves and the calculation time, we now use an optimization algorithm based on Linear Sum Assignment Problem (LSAP) [Crouse, 2016]. The LSAP algorithm
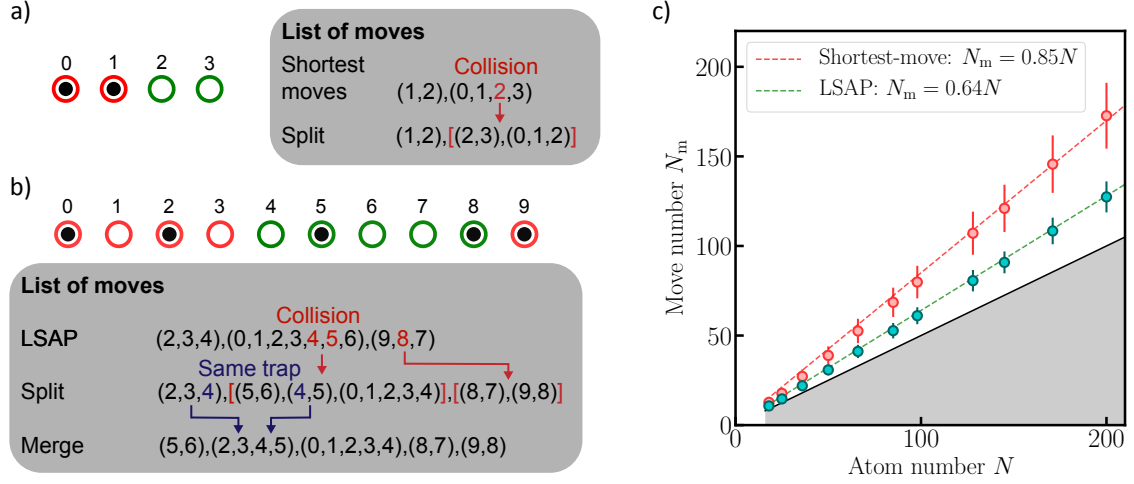
Figure 4.9: Moves computation algorithms. Moves computation using a) the 'shortest-moves first' algorithm, and b) the LSAP algorithm on two simple examples. c) Number of moves N_m as a function of the number of atoms N for the two algorithms with the typical array geometries we use (see Section 4.2.3). The markers are data extracted from a simulation of the computed moves over 1000 initial, random configurations of the atoms position. The dashed lines are linear fits to the data, from which we extract $N_\mathrm{m} \simeq 0.85N$ for the shortest-moves first algorithm (red), and $N_\mathrm{m} \simeq 0.64N$ for the LSAP algorithm (blue). The dark line represents the minimum number of moves $N_\mathrm{m} = N/2$.

cost function that needs to be minimized is the total rearrangement distance $L = \sum l_i$, with l_i the length of move i. To reduce the events in which we have to move an atom along filled traps, inducing an increase of N_m, we post-process the moves calculated by the algorithm in the following way: (i) we split the calculated moves to avoid collisions, (ii) reorder the moves by increasing length, and (iii) merge the moves for which their target trap is the same as the initial trap of another move. The post-processing is illustrated on an example in Figure 4.9 b). Using this algorithm, we find $N_\mathrm{m} \simeq 0.64N$ (see Figure 4.9 c), blue markers), and the computation time scales as N^2, with typical value $t_\mathrm{calc} \sim 10\,\mathrm{ms}$ for $N \sim 200$.

Effect of the algorithm on the assembling efficiency. As we have now calculated the scaling of N_m and t_calc for both algorithms, the Equation (4.10) can be written including them:

$$\text{Shortest-move algorithm:} \quad P_\mathrm{fill} = \eta_\mathrm{m}^{0.85N} e^{\frac{0.85N^2}{\tau_\mathrm{vac}} t_\mathrm{m} + 100 \frac{(N/200)^2}{\tau_\mathrm{vac}}}.$$

$$\text{LSAP algorithm:} \quad P_\mathrm{fill} = \eta_\mathrm{m}^{0.64N} e^{\frac{0.64N^2}{\tau_\mathrm{vac}} t_\mathrm{m} + 10 \frac{(N/200)^2}{\tau_\mathrm{vac}}}.$$

$$(4.11)$$
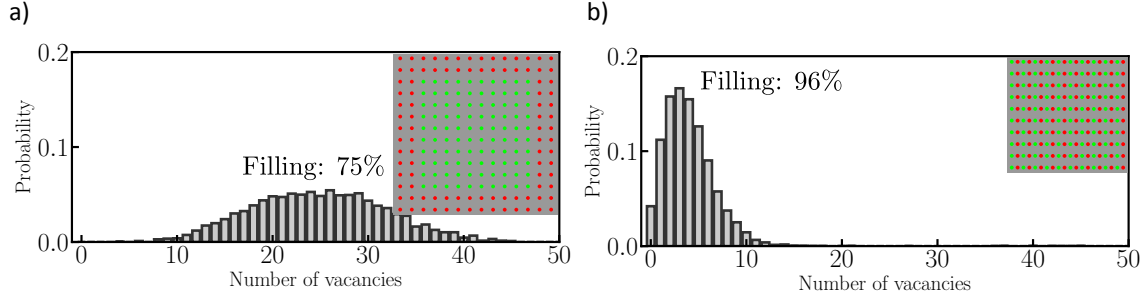
Figure 4.10: Use of 'compact' arrays. Histograms of the assembling probability of a 10×10 array with a) a regular square lattice and b) a 'compact' array. The insets show the target traps (green) and the non-assembled traps (red).

As a reminder: η_{m} is the fidelity of a move, t_{m} its duration and τ_{vac} the atom lifetime in the tweezers. Changing the algorithm reduced the required number of moves by $\sim 30\%$, and divided by ~ 10 the computation time[1]: for $N = 200$ and $\eta_{\mathrm{m}} = 0.98$, P_{fill} is increased by a factor ~ 8 using the LSAP algorithm. The fits to the data of P_{fill} presented in this chapter are performed using the above equation, with only fitting parameter η_{m}.

4.2.3 Increasing the assembling efficiency

Whilst the optimization of the moves computation algorithm improved the assembler efficiency, we also added two other important improvements during my PhD, which I describe now.

Minimizing the distance between the traps. This point was already partly motivated in Section 4.2.1: in order to reduce the MT traveling distance and the size of the arrays, we place the traps which are not assembled in between the target traps. It also reduces the number of moves: the events for which the atoms have to be moved twice are rare since the MT can travel *in between* the target traps. The gain in assembling efficiency is demonstrated on a 10×10 array, with a distance of $10\,\mu m$ between the target traps, see Figure 4.10. We assemble the array using a) a regular square lattice and b) a 'compact' array, for which we double the number of traps along one direction (see inset). We show the histogram of the number of vacancies, i.e. the number of target traps which are not filled after the assembling process. The mean filling probability is $\sim 75\%$ with the square lattice and $\sim 96\%$ using a compact array.

---

[1]The values given here are the ones obtained on the specific computer used to calculate the moves.
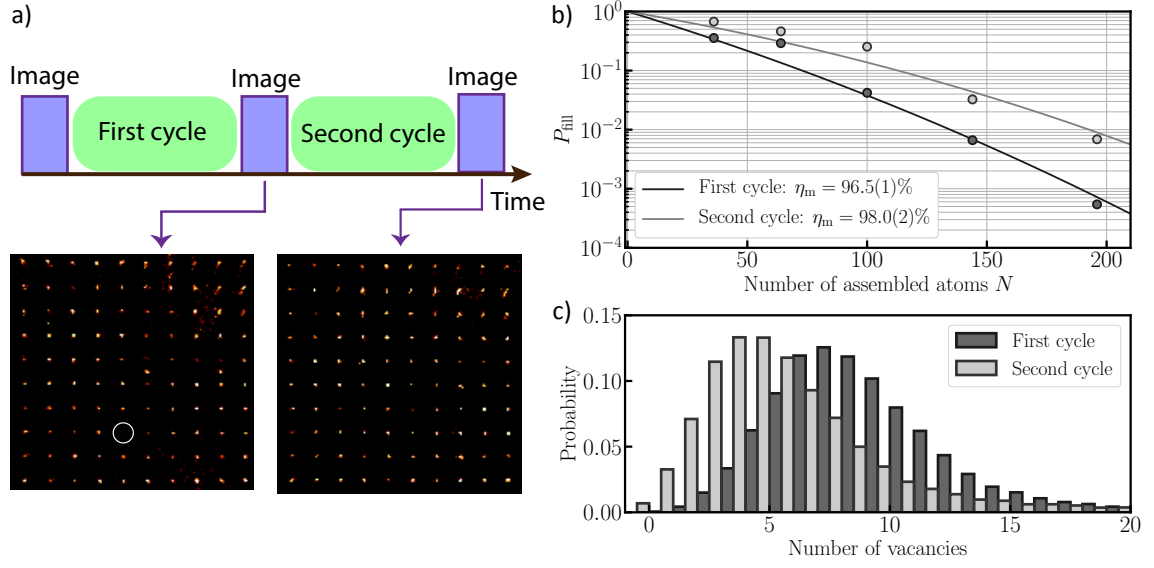
Figure 4.11: Use of two rearrangement cycles. a) Sketch of the experimental protocol. We perform two rearrangement cycles, taking an image of the atoms position after each of them. After the first cycle, the target array is almost filled, shown on the example of a 10×10 array in which only one atom is missing (white circle). b) Success probability P_{fill} as a function of the atom number N after the first, and after the second cycle. The solid lines are fits to the data using Equation (4.10) with the move fidelity η_{m} as a free parameter. c) Histogram of the number of vacancies in the target array after the first cycle (dark grey), and after the second cycle (light grey).

Second rearrangement cycle. The implementation of a second rearrangement cycle, sketched in Figure 4.11 a), consists of the following: we rearrange the atoms twice and take an image of the atoms after each cycle. Considering the high assembling efficiency, the second cycle mainly aims at filling the few remaining holes in the target array, shown on the example of a 10×10 array in which only one atom is missing (white circle) after the first cycle. We show in Figure 4.11 b) the gain in assembling efficiency by comparing the probability P_{fill} to successfully assemble the target array as a function of the atom number N after the first cycle (dark), and after the second cycle (grey). The solid lines are fits to the data using Equation (4.11), from which we extract $\eta_{\text{m}} = 96.5(1)\%$ after the first cycle, and $\eta_{\text{m}} = 98.0(2)\%$ after the second. The fit matches better for the first cycle than the second, as Equation (4.11) is derived assuming only one set of moves.

For the largest array considered here with $N = 196$, P_{fill} is ~ 10 times higher after two cycles than after one. To understand in more detail the second rearrangement cycle effect, we show in Figure 4.11 c) the histogram of the number of vacancies
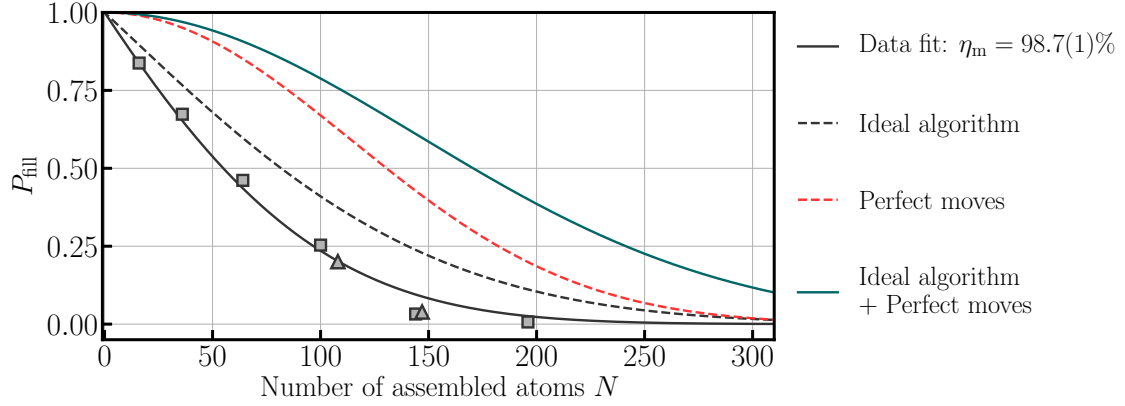
Figure 4.12: Prospects for further improvements. Assembling success probability P_{fill} as a function of the atom number N. We perform the fit to the data using Equation (4.10) with the move fidelity η_{m} as a free parameter, from which we extract $\eta_{\text{m}} = 98.7(1)\%$. We also show the results of Equation (4.10) with: an ideal algorithm (dark dashed line), perfect moves (red dashed line) and the combination of both (green line).

in the $N = 196$ array, after one (dark) and two (grey) cycles. We observe a shift of the distribution towards lower number of vacancies (from seven to four), whilst the distribution width remains the same, thus increasing the probability of having zero vacancies P_{fill}. Analyzing these results, one could be tempted to add other rearrangement cycles to further shift the vacancies distribution towards zero. However, we observed that increasing further the number of cycles does not improve the results for two reasons: (i) each cycle is time consuming, and the system is eventually limited by the atom lifetime, and (ii) taking many images of the atoms induce losses, with a finite probability to misinterpret the position of the atoms.

As we now use two assembly cycles, we need more than $2N$ traps to have enough atoms for the second rearrangement cycle. We typically use arrays with $\sim 2.2N$ traps, such that $\sim 1.1N$ atoms are initially loaded. The assembling probability is increased at the expense of decreasing the maximum value of N. It is not a limit here, as the maximum number of traps is ~ 700 (see Section 4.1.2).

Conclusions and prospects for further improvements. I briefly summarize the improvements made on the assembler efficiency described in this section:

- By changing the moves computation algorithm, we reduced by $\sim 30\%$ the number of moves required to assemble the target array, and divided by ~ 10 the computation time.

- By carefully matching the MT position onto the static traps, using 'compact' arrays and two rearrangement cycles, we increased the single move fidelity from $\eta_{\mathrm{m}} = 95.6(3)\%$ to $\eta_{\mathrm{m}} = 98.7(1)\%$.

There are two ways to further improve the assembling efficiency: increasing the moves fidelity, and using a better moves computation algorithm. To check their effect on the assembling efficiency, we use Equation (4.10) in various conditions, see Figure 4.12. We show the results of the assembling success probability P_{fill} as a function of N with: (i) an ideal algorithm ($N_{\mathrm{m}} = N/2$ and $t_{\mathrm{calc}} = 0$) but the current moves fidelity (dark dashed line), (ii) perfect moves ($\eta_{\mathrm{m}} = 1$) but using the current algorithm (red dashed line), and (iii) an ideal algorithm and perfect moves (green line). We conclude that to increase the assembling efficiency of arrays in the range $N \sim 200 - 250$, the improvements should be focused on the moves fidelity. To reach $N \geq 300$, we need to improve both, which is challenging as the move fidelity and the algorithm optimality decrease with N.

4.3 Conclusion

In this chapter, I presented the way we increased the number of available atoms to perform many-body physics, by improving two points: the ability to trap atoms in large arrays, and the efficiency of the rearrangement process. These improvements allowed us to probe the transverse field Ising model in a regime where the boundaries are not dominating the properties of the system, especially with triangular arrays (see Chapter 7). Increasing the number of atoms to $N \sim 200$ also allows us to enter in a regime for which numerical simulations of the system's evolution is extremely challenging. This make our platform a possible route to study many-body phenomena which cannot be easily grasped by numerical simulations, which is eventually one goal of quantum simulation.

Part II.

Quantum simulation of Ising antiferromagnets

Van der Waals interaction and transverse field Ising model

Contents

In this chapter, I explain how we use the van der Waals interaction between Rydberg atoms to: (i) entangle two atoms and (ii) implement the transverse field Ising model. The quantum simulation of the transverse field Ising model is one of the main projects conducted during my PhD. Here, I give an overview of the model's main features for the simplest case of a 1D chain of N atoms. I briefly explain how we experimentally probe these features, and demonstrate that the platform can be readily used to investigate the model in 2D geometries, which will be the topic of Chapter 6 and Chapter 7.

5.1 Van der Waals interaction between two Rydberg atoms and entanglement

In this section, I detail the effect of the van dar Waals interactions on two Rydberg atoms, and demonstrate their entanglement. The entanglement of two atoms via this interaction in views of realizing quantum gates [Jaksch *et al.*, 2000; Lukin *et al.*, 2001] has been extensively studied during the last decades [Saffman, Walker, and
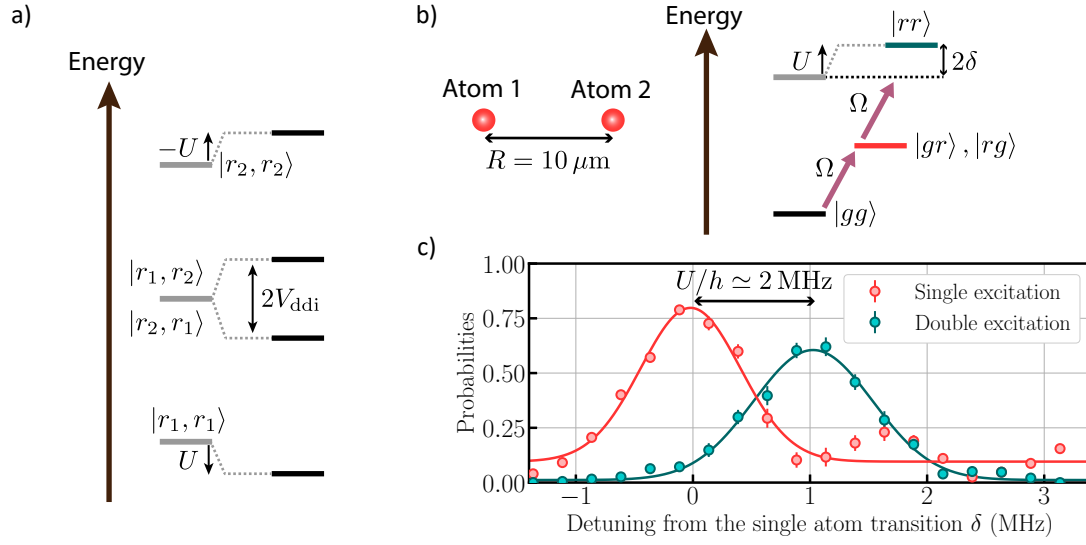
Figure 5.1: Van der Waals interaction between two atoms. a) Sketch of the two-atom levels. The resonant dipole-dipole interaction between $|r_1, r_2\rangle$ and $|r_2, r_1\rangle$ induces an energy shift U on the $|r_1, r_1\rangle$ state, and $-U$ on the $|r_2, r_2\rangle$ state. b) Sketch of the ground-Rydberg spectroscopy involving two interacting atoms with inter-atomic distance $R = 10\,\mu$m. The involved levels are $|g\rangle = |5S_{1/2}, F = 2, m_F = 2\rangle$ and $|r\rangle = |75S_{1/2}, m_J = 1/2\rangle$. c) Probability to excite one (red) or both (green) atoms into $|r\rangle$ as a function of the laser's detuning δ from the single atom transition frequency. The solid lines are fits to the data using Gaussian functions, from which we extract $U/h \simeq 2\,$MHz.

Mølmer, 2010; Browaeys, Barredo, and Lahaye, 2016; Browaeys and Lahaye, 2020]. These quantum gates are key ingredients for building digital quantum computers. The creation of such quantum computers is an active field of research in superconducting circuits [Arute *et al.*, 2019] and ion-based [Blatt and Wineland, 2008] platforms. Digital quantum computation proved to be an efficient method for simulating the dynamics of many-body quantum systems [Lanyon *et al.*, 2011; Smith *et al.*, 2019]. One challenge these quantum computers face is the fidelity of the quantum gates, which is directly limited by the *entanglement fidelity*. The realization of quantum gates using the van dar Waals interaction is out of the scope of this thesis. However, we present here a method to measure a lower bound of the entanglement fidelity [Madjarov *et al.*, 2020], and show that we obtain entanglement fidelities close to those obtained using similar platforms, indicating that our experiment could be used to realize quantum gates.

5.1.1 Van der Waals interaction

The van der Waals interaction arises from the dipole-dipole interaction V_{ddi} between Rydberg atoms (discussed in Chapter 8). We consider two atoms placed at a distance R in a state $|r_1, r_1\rangle$ with energy E_{r_1,r_1}, and nearby Rydberg states $|r_i, r_j\rangle$ with energy E_{r_i,r_j}. The two atoms in the $|r_1, r_1\rangle$ state are not coupled via the dipole-dipole interaction at first order. This can be understood in a semi-classical picture: as the two atoms are in the same state, there is no rigid dipole associated to these atoms, hence no coupling between them.

The dipole-dipole interaction instead acts on the $|r_1, r_1\rangle$ state at the second order: consider the superposition of the states $|r_1, r_i\rangle$ and $|r_i, r_1\rangle$, with r_i having a different parity to r_1. The atoms now exhibit a rigid dipole and are thus coupled via the dipole-dipole interaction. This coupling acts on the $|r_1, r_1\rangle$ state at the second order and shifts its energy by:

$$U = \sum_{i,j} \frac{|\langle r_i r_j | V_{\mathrm{ddi}} |r_1 r_1\rangle|^2}{E_{r_i,r_j} - E_{r_1,r_1}} = C_6/R^6, \tag{5.1}$$

where the sum runs over all the nearby $|r_i, r_j\rangle$ states, and C_6 is the van der Waals coefficient. We neglect here the possibility for $|r_1, r_1\rangle$ to be degenerated in energy with another Rydberg pair state, which would give rise to Förster resonances [Gallagher, 1988; Walker and Saffman, 2005; Ravets *et al.*, 2014].

The arising of the van der Waals interaction from the resonant dipole-dipole interaction is summarized in Figure 5.1 a), in which we consider only two Rydberg states $|r_1, r_1\rangle$ and $|r_2, r_2\rangle$.

Measurement of the Van der Waals interaction. We show the effect of the van der Waals interaction on the simplest case of two atoms by performing a ground-Rydberg spectroscopy (see Figure 5.1 b)), setting an inter-atomic distance $R = 10\,\mu\mathrm{m}$, and using $|g\rangle = \left|5S_{1/2}, F = 2, m_F = 2\right\rangle$ as the ground state and $|r\rangle = \left|75S_{1/2}, m_J = 1/2\right\rangle$ as the Rydberg state. We measure the single (red) and double (green) excitation probabilities into $|r\rangle$ as a function of the laser's detuning δ, see Figure 5.1 c). The van der Waals interaction has two effects:

- When setting the excitation laser on resonance with the single atom transition ($\delta = 0$), the single excitation probability is maximum. Both atoms cannot be excited at the same time as $|rr\rangle$ is shifted in energy due to the van der Waals interaction. This phenomenon is called the *Rydberg blockade* and allows
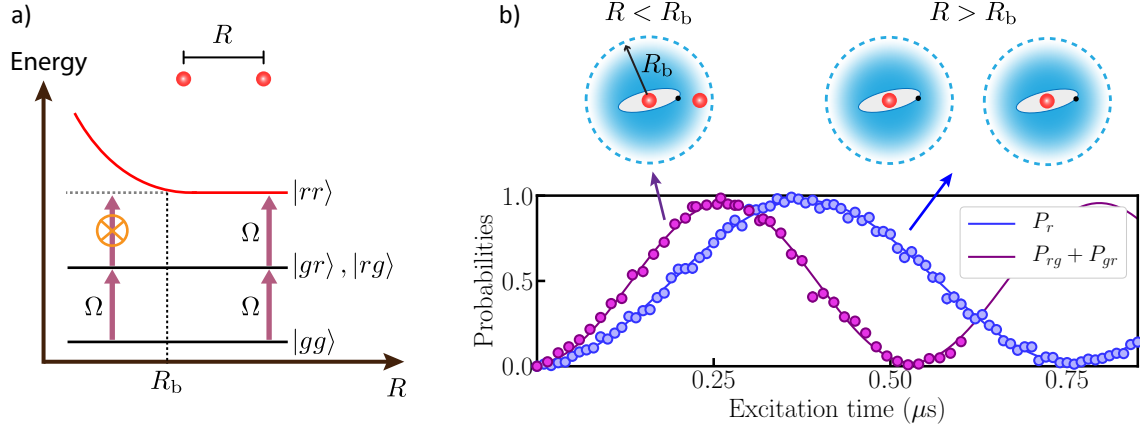
Figure 5.2: Entanglement using the blockade mechanism. a) Two-atom level energies as a function of the inter-atomic distance R. Exciting both atoms to their Rydberg state is impossible for $R < R_b$. b) 2-atom ground-Rydberg Rabi oscillation involving the Rydberg state $|r\rangle = \left|75S_{1/2}, m_J = 1/2\right\rangle$. We show the average Rydberg excitation probability P_r for $R > R_b$ (blue), and the single excitation probability $P_{gr} + P_{rg}$ for $R < R_b$ (purple). The solid lines are fits to the data using a sine function, from which we extract an enhancement of the Rabi frequency by a factor $1.42(2) \simeq \sqrt{2}$.

excitation of the atoms to the entangled state $(|rg\rangle + |gr\rangle)/\sqrt{2}$, as discussed below.

- When the laser's detuning matches half the interaction energy $\delta = U/(2h)$, the double excitation probability is maximum as we couple to the $|rr\rangle$ state. We measure $U/h \simeq 2\,\text{MHz}$, compatible with the expected $C_6 \simeq 1947\,\text{MHz}.\mu\text{m}^6$ for $75S$ [Šibalić *et al.*, 2017].

Tunability of the interaction.   The van der Waals interaction strongly varies with the principal quantum number n and the inter-atomic distance R, as $U \propto n^{11}/R^6$. Considering the typical parameters we use $n \sim 60 - 90$ and $R \sim 5 - 40\,\mu\text{m}$, we can vary U on seven orders of magnitude. We use this asset to easily tune the system from a predominant interaction strength to a negligible one, as performed in the next subsection.

5.1.2 Entangling two atoms using the van der Waals interaction

We use the van der Waals interaction to entangle two atoms. The aim is to transfer the system into the state $(|rg\rangle + |gr\rangle)/\sqrt{2}$. We thus set the excitation lasers on resonance

with the single atom ground-Rydberg transition frequency, and use a Rabi frequency Ω. Depending on the distance R between the atoms, thus on the value of U, the system exhibits two regimes: (i) if $U \ll \Omega$, the interactions can be neglected and the system's behavior is identical to the single atom case, and (ii) if $U \gg \Omega$, the $|rr\rangle$ state is not reachable, and the excitation lasers couple the atoms to the state $(|rg\rangle + |gr\rangle)/\sqrt{2}$. The boundary between the two regimes is the distance R_b for which $U(R_\mathrm{b}) = \Omega$, also called the "Rydberg blockade radius". This wording is slightly misleading, as for $R \sim R_\mathrm{b}$ there is a finite probability to populate the $|rr\rangle$ state. In order to entangle the two atoms, we will use $R < R_\mathrm{b}$. The excitation laser thus couples the $|gg\rangle$ state to the $(|rg\rangle + |gr\rangle)/\sqrt{2}$ state. This results in an enhancement of the Rabi frequency by a factor $\sqrt{2}$, which we measure on the experiment.

Measurement of the $\sqrt{2}$ enhancement. In order to observe these two regimes experimentally, we drive Rabi oscillations between $|g\rangle$ and $|r\rangle = \left|75S_{1/2}, m_J = 1/2\right\rangle$ with a Rabi frequency $\Omega/(2\pi) = 1.3\,\mathrm{MHz}$, see Figure 5.2 b). The corresponding Rydberg blockade radius is $R_\mathrm{b} \simeq 10\,\mu\mathrm{m}$. We perform the experiment: (i) with $R = 30\,\mu\mathrm{m}$ ($U/h = 3\,\mathrm{kHz}$) and show the average Rydberg excitation probability P_r (blue), and (ii) with $R = 6\,\mu\mathrm{m}$ ($U/h = 42\,\mathrm{MHz}$) and show the single excitation probability $P_{gr} + P_{rg}$ (purple). We measure an enhancement of the oscillation frequency by a factor $1.42(2) \simeq \sqrt{2}$ in the blockade regime, proving that the $|gg\rangle$ state is coupled to $(|rg\rangle + |gr\rangle)/\sqrt{2}$ as expected. We apply a π-pulse to produce the entangled state. However, due to the various limitations of the platform, the produced state is not exactly $|W\rangle = (|gr\rangle + |rg\rangle)/\sqrt{2}$, which we now quantify.

Entanglement fidelity. As can be observed in Figure 5.2 b), the contrast of the oscillation is finite due to the various state preparation and detection errors described in Section 3.3.1. These limit the entanglement fidelity F, defined as the overlap between the prepared state with density matrix ρ and $|W\rangle = (|gr\rangle + |rg\rangle)/\sqrt{2}$. The entanglement fidelity is an important quantity to measure, as it directly limits the fidelity of Rydberg-blockade-based quantum gates. The entanglement of two atoms through the van der Waals interaction has already been implemented 10 years ago in the group [Wilk *et al.*, 2010], and a fidelity $F = 0.75$ was obtained. As many technological advances have been realized since then, it is interesting to compare the fidelity with the current one. F can be written as:

$$F = \frac{1}{2}\left(\rho_{gr,gr} + \rho_{rg,rg} + 2|\rho_{gr,rg}|\right), \tag{5.2}$$

$\rho_{i,j}$ being the density matrix elements with $(i,j) \in \{gg, gr, rg, rr\}$. Measuring F requires having access to the coherence term $\rho_{gr,rg}$, which is non trivial to measure as high fidelity single-qubit rotations have to be performed [Roos *et al.*, 2004]. Even though the machine is in principle capable of doing so, we use a method detailed in Madjarov *et al.* [2020], which gives a lower bound for F by simply measuring the population terms $\rho_{i,i}$. We use

$$\text{Tr}(\rho^2) = \sum_{i,j} |\rho_{i,j}|^2 = \sum_i \rho_{i,i}^2 + \sum_{i \neq j} |\rho_{i,j}|^2. \tag{5.3}$$

As $\text{Tr}(\rho) = \sum_i \rho_{i,i} = 1$, the above equation can be rewritten as:

$$\text{Tr}(\rho^2) = \sum_i \rho_{i,i} \left(1 - \sum_{j \neq i} \rho_{j,j} \right) + \sum_{i \neq j} |\rho_{i,j}|^2. \tag{5.4}$$

By isolating the terms involving $|\rho_{gr,rg}|^2 = |\rho_{rg,gr}|^2$ and $\rho_{gr,gr}\rho_{rg,rg}$ in the above sums, we obtain

$$\text{Tr}(\rho^2) - 1 = 2|\rho_{gr,rg}|^2 - 2\rho_{gr,gr}\rho_{rg,rg} + \sum_{i \neq j, (i,j) \neq (gr,rg)} \left(|\rho_{i,j}|^2 - \rho_{i,i}\rho_{j,j} \right). \tag{5.5}$$

Using the Cauchy inequality: $|\rho_{i,j}|^2 \leq \rho_{i,i}\rho_{j,j}$ for each term of the above sum, we obtain:

$$|\rho_{gr,rg}|^2 \geq \frac{1}{2} \left(\text{Tr}(\rho^2) - 1 \right) + \rho_{gr,gr}\rho_{rg,rg}. \tag{5.6}$$

We thus obtain a lower bound for $|\rho_{gr,rg}|$ as a function of $\text{Tr}(\rho^2)$. We use another lower bound to determine the value of $\text{Tr}(\rho^2)$:

$$\text{Tr}(\rho^2) \geq \sum_i \rho_{i,i}^2. \tag{5.7}$$

This lower bound seems extremely strong, as we totally lose the coherence parts. In order to reduce the imprecision of this lower bound, we measure $\sum_i \rho_{i,i}^2$ when the coherence terms are the lowest, i.e. when the atoms are in the $|gg\rangle$ state. We measure $\sum_i \rho_{i,i}^2$ after one period of the Rabi oscillation and not directly after the initialization to make sure that we do not overestimate the value of this sum. The resulting formula is:

$$F \geq \frac{1}{2} \left(\rho_{gr,gr} + \rho_{rg,rg} + 2\sqrt{(\sum_i \rho_{i,i}^2 - 1)/2 + \rho_{gr,gr}\rho_{rg,rg}} \right). \tag{5.8}$$

	Quantity	Measured value
At π pulse	$\rho_{gr,gr}$	0.48(1)
	$\rho_{rg,rg}$	0.48(1)
At 2π pulse	$\rho_{gg,gg}$	0.964(5)
	$\rho_{gr,gr}$	0.006(2)
	$\rho_{rg,rg}$	0.013(3)
	$\rho_{rr,rr}$	0.008(2)

Table 5.1.: Population probabilites. The values are extracted from Figure 5.2 b).

The values of the various terms involved in the calculation of F are derived from Figure 5.2 b), and given in Table 5.1. We derive from this measurement an entanglement fidelity $F \geq 0.92(2)$. Considering the uncertainties, we conclude that the entanglement fidelity is at least $F \geq 0.9$, which is close to the ones obtained with the same type of platform in recent works [Graham *et al.*, 2019; Levine *et al.*, 2019]. The fidelity measured here does not take into account the fact that we imprint the phase of the laser on the prepared state, which we now discuss.

Phase factor. When we drive the Rabi oscillation to prepare the $|W\rangle$ state, we imprint the laser's phase onto the prepared state, which can be written as $(|rg\rangle + e^{i\phi}|gr\rangle)/\sqrt{2}$, where the phase factor $\phi = kr$ arises from the difference in position r between the two atoms. This phase has no impact on the measured populations: $P_{gr} = |\langle gr| e^{i\phi}|gr\rangle|^2 = 1$. However, as $F = |(1 + e^{i\phi})/2|^2$, it has an impact on the entanglement fidelity. Due to shot-to-shot fluctuations of the atoms position (see Section 6.2.2), at each repetition of the experiment r changes. The typical variation Δr of the inter-atomic distance is larger than the laser's wavelength λ, such that $k\Delta r > 1$ which implies $\langle e^{i\phi}\rangle \sim 0$. We thus obtain $F = 1/2$: the produced states behave in the same way as a statistical mixture of $|gr\rangle$ and $|rg\rangle$. This phase issue can be solved by applying a π-pulse towards another ground state $|g'\rangle$ after preparing the $|W\rangle$ state [Wilk *et al.*, 2010]. As the difference in λ between the two pulses is negligible, the imprinted phase during the second π-pulse cancels the phase factor.

5.2 Implementation and exploration of the transverse field Ising model

We use the van der Waals interaction between Rydberg atoms to implement the Transverse Field Ising (TFI) model. This model has been experimentally investigated on many synthetic platforms: using ultracold atoms in optical lattices [Simon *et al.*,

2011; Meinert *et al.*, 2013] excited to Rydberg states [Schauß *et al.*, 2012; Guardado-Sanchez *et al.*, 2018]; trapped ions [Blatt and Roos, 2012; Monroe *et al.*, 2021]; and superconducting circuits [Song *et al.*, 2017; King *et al.*, , 2018]. Over recent years, its implementation has been demonstrated using Rydberg tweezers arrays in 1D [Bernien *et al.*, 2017; Omran *et al.*, 2019], 2D [Lienhard *et al.*, 2018] and 3D [Song *et al.*, 2021] geometries. However, these works used relatively small system sizes, and with a limited coherence. We revisited the model in 2D on large arrays with an improved coherence [Scholl *et al.*, 2021a]. The team of M. Lukin explored the model in a similar configuration in a companion publication [Ebadi *et al.*, 2021].

I explain here how we implement this model by considering the simplest case of the nearest-neighbor 1D TFI model. I derive the main features of the model and describe the experiments we conducted during my PhD. The study of the model in 2D geometries is the subject of Chapter 6 and Chapter 7.

5.2.1 Nearest-neighbor transverse field Ising model on a 1D chain

We consider a 1D chain of N spin-1/2 with states denoted as $|\downarrow\rangle$ and $|\uparrow\rangle$, interacting with a strength U. The chain is placed in a magnetic field. Considering a magnetic field component along the spin direction $B_\parallel$ (longitudinal field) and the component transverse to the spin direction $B_\perp$ (transverse field), the Hamiltonian H_{TFI} of the TFI model is:

$$H_{\text{TFI}} = B_\perp \sum_{i=1}^{N} \sigma_i^x + B_\parallel \sum_{i=1}^{N} \sigma_i^z + U \sum_{i=1}^{N-1} \sigma_i^z \sigma_{i+1}^z, \tag{5.9}$$

where σ^x and σ^z are the usual Pauli matrices. The different terms of H_{TFI} can be understood as follows:

- The transverse field $B_\perp$ changes the spin states and favors their alignment on the transverse direction $|\rightarrow\rangle = (|\uparrow\rangle + |\downarrow\rangle)/\sqrt{2}$.

- The longitudinal field $B_\parallel$ changes the states energy. Depending on its sign, an alignment of the spins along $|\uparrow\rangle$ or $|\downarrow\rangle$ is favored.

- The effect of the interactions depend on the sign of U: if $U < 0$, the interactions favor the alignment of the spins (ferromagnetic ordering), whereas if $U > 0$ the interactions favor the anti-alignment of the spins (antiferromagnetic ordering).

In the following, and for the rest of this thesis, we will always study systems with $U > 0$, which corresponds to antiferromagnetic ordering. As opposed to the

ferromagnetic case, the TFI model with $U > 0$ features geometric frustration e.g. in triangular lattices, which we will be studied and discussed in Chapter 7.

Mapping of the Rydberg platform onto the TFI model. The repulsive van der Waals interaction naturally implements the interaction term of the TFI model: there is an energy cost $U = C_6/R^6 > 0$ associated to having two atoms separated by R in the $|r\rangle$ state. We map the ground and Rydberg states onto the spin states: $|g\rangle \equiv |\downarrow\rangle$ and $|r\rangle \equiv |\uparrow\rangle$. The excitation laser implements the transverse and longitudinal magnetic fields: the laser Rabi frequency Ω flips the spins, depending on its detuning δ. Defining the operator $n_i = (1 + \sigma_i^z)/2$ acting on atom i, we obtain the Hamiltonian in the rotating wave approximation:

$$H_{\mathrm{Ryd}} = \frac{\hbar\Omega}{2} \sum_{i=1}^{N} \sigma_i^x - \hbar\delta \sum_{i=1}^{N} n_i + \sum_{i<j} \frac{C_6}{R_{i,j}^6} n_i n_j, \tag{5.10}$$

where $R_{i,j}$ is the distance between atoms i and j. There are two differences between H_{Ryd} and H_{TFI}:

- The interaction energy decreases as $1/R^6$, and is thus acting beyond nearest neighbors. We set a distance a between the atoms such that the nearest neighbor interaction energy $U = C_6/a^6 > 0$ is $U \sim \Omega$. In these conditions, the next-nearest neighbor interaction energy is $U/64 \ll \Omega, \delta$ and the long-range interaction is negligible. In the following, we will consider the interactions as only acting on the nearest neighbors.

- As the van der Waals interaction and the detuning act on the system via the n operator rather than via σ^z, $H_{\mathrm{Ryd}} = H_{\mathrm{TFI}} + N\hbar(U - 2\delta)/4 + U \sum_i \sigma_i^z$. The second term is diagonal and can be thus ignored. The third term act as a longitudinal field: in our implementation, $B_\parallel \equiv U - \hbar\delta$. This effect changes the position of the phases in the system's phase diagram (without changing their nature) which is described below (see Figure 5.4).

Due to these differences, the van der Waals interaction implements an "Ising-like" Hamiltonian. We will see in the following that the features of both Hamiltonians are the same (see Figure 5.4) in our range of parameters. The effect of long-range interactions in 2D is actually not negligible and is discussed in Section 6.1.1.
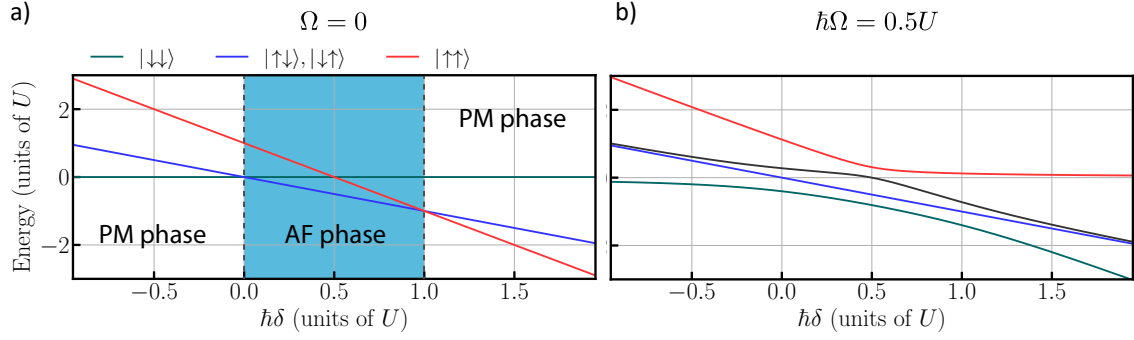
Figure 5.3: Energy diagram for two atoms. a) Energy diagram for $\Omega = 0$. The antiferromagnetic states $|\uparrow\downarrow\rangle$ and $|\downarrow\uparrow\rangle$ are the ground states of the system for $0 < \hbar\delta < U$. b) Energy diagram for $\hbar\Omega = 0.5U$. The degeneracy for $\delta = 0$ and $\hbar\delta = U$ is lifted.

5.2.2 Exploration of the phase diagram

An important question regarding the study of a model is to determine the ground states of the system depending on the Hamiltonian parameter, i.e. to determine the system's phase diagram. In the case of the nearest-neighbor 1D TFI model considered here, the phase diagram was calculated analytically 70 years ago in the thermodynamic limit [Lieb, Schultz, and Mattis, 1961]. Studying this model is thus of limited interest. However, showing that we can implement the model, and that we have the ability to observe its features allows us to benchmark the platform, which is the first step towards the implementation of more interesting Hamiltonians. In this section, I present the basic features of the TFI model, and how we measure them. I will present the exploration of the TFI model in 2D geometries (for which our implementation is not analytically solved) in Chapter 6 and Chapter 7.

Ground states for two atoms. To characterize the TFI model phase diagram, let us start with the simplest case of two spins (denoted as 1 and 2) and in the absence of transverse field. The corresponding Hamiltonian is:

$$H = -\hbar\delta(n_1 + n_2) + Un_1n_2. \tag{5.11}$$

The spectrum as a function of δ is shown in Figure 5.3 a). The system's ground state displays two behaviors depending on δ:

- For $\hbar\delta < 0$ ($\hbar\delta > U$), the ground state is $|\downarrow\downarrow\rangle$ ($|\uparrow\uparrow\rangle$), and the spins align along the effective longitudinal field. This behavior is the signature of a paramagnet

(PM).

- For $0 < \hbar\delta < U$, the ground states are ($|\uparrow\downarrow\rangle$ and $|\downarrow\uparrow\rangle$) (blue line). Even in the presence of a moderate effective longitudinal field, the spins are anti-aligned. The system behaves as an antiferromagnet (AF).

We now add the transverse field, see Figure 5.3 b) for $\hbar\Omega = 0.5U$. The ground state degeneracy at $\delta = 0$ and $\hbar\delta = U$ is lifted: an energy gap E_{gap} appears between the ground state and the first excited state, minimal for $\hbar\delta = 0.5U$ with value $E_{\mathrm{gap}} \sim \hbar\Omega/2$. In the limit $\hbar\Omega \gg U$, the system's ground state is $|\leftarrow\leftarrow\rangle = (|\uparrow\uparrow\rangle + |\downarrow\downarrow\rangle - (|\uparrow\downarrow\rangle + |\downarrow\uparrow\rangle)))/2$. The spins align along the effective transverse field, which is again a PM behavior.

From the above analysis with two atoms, we conclude that there are two possible ground state behaviors in the implemented TFI model in 1D: (i) paramagnetic (PM) ground states, for which the spins align along the effective magnetic field, and (ii) antiferromagnetic (AF) ground states, for which the spins are anti-aligned. The delimitation between the two phases, i.e. the critical line, is derived below.

Phase diagram. We now move on to the study of a 1D chain of N spins. The system's ground states determined for two spins remain the same when considering N spins. For $\Omega = 0$, the PM phase ground states are $|\downarrow\downarrow ... \downarrow\downarrow\rangle$ (for $\delta < 0$) and $|\uparrow\uparrow ... \uparrow\uparrow\rangle$ (for $\hbar\delta > 2U$), and the AF phase ground states are $|\uparrow\downarrow ... \uparrow\downarrow\rangle$ and $|\downarrow\uparrow ... \downarrow\uparrow\rangle$ (considering N even). The critical points are $\delta_{\mathrm{c}} = 0$ and $\hbar\delta_{\mathrm{c}} = 2U$ in a 1D chain: as each spin has two neighbors, the interaction energy felt by one spin is $2U$. Determining the position of the critical line for $\Omega \neq 0$ is not a trivial task. We determine it using simulations involving up to $N = 14$ in periodic boundary conditions. We locate the values $(\Omega_{\mathrm{c}}, \delta_{\mathrm{c}})$ for which the energy gap E_{gap} between the ground state and the first excited state is minimal. The critical line position depends on the number of atoms, as shown in Figure 5.4 a) for $\hbar\Omega_{\mathrm{c}} = 0.16U$. We use an exponential function to fit the data (solid line), and extract the value of δ_{c} for $N \to \infty$ in order to draw the phase diagram of an infinite system.

The obtained phase diagram is shown in Figure 5.4 c). The markers are the values of $(\Omega_{\mathrm{c}}, \delta_{\mathrm{c}})$ determined using the simulation presented above. The solid line is a phenomenological fit to the data using a biquadratic function. The critical line follows a 'dome' shape, with its apex located at $(\hbar\Omega_{\mathrm{c}} = 0.5U, \hbar\delta_{\mathrm{c}} = U)$. We compare the implemented phase diagram to the one of the original TFI Hamiltonian H_{TFI} described in Equation (5.9) (see Figure 5.4 d)). Both phase diagrams are similar: they display the same phases with the same corresponding ground states. The only difference is
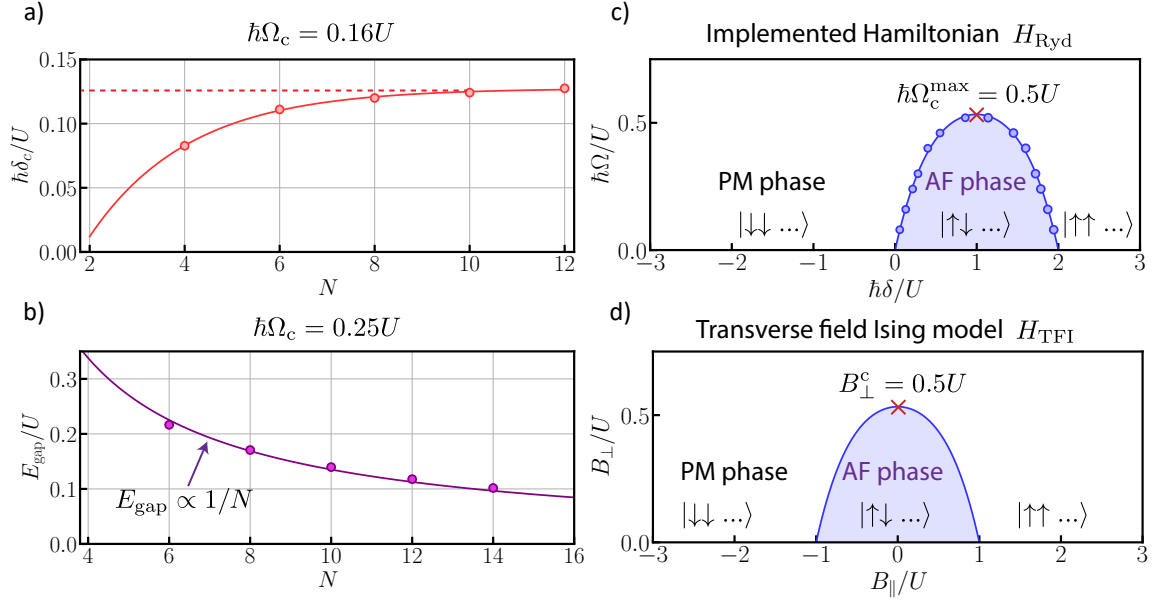
Figure 5.4: Phase diagram of the nearest-neighbor transverse field Ising model in 1D. a) Value of δ_c as a function of N, for $\hbar\Omega_c = 0.16U$. The solid line is a fit to the data using an exponential function, from which we extract $\hbar\delta_c/U(N \to \infty) = 0.13(1)$. b) Scaling of E_{gap} as a function of N, for $\hbar\Omega = 0.25U$. The solid line is a fit to the data using the function $E_{gap} = A/N$, with A a fitting parameter. c,d) Phase diagrams of c) the implemented Hamiltonian H_{Ryd} and of d) the transverse field Ising model H_{TFI}. The blue line represent the critical line between the PM and the AF phases. The only difference is the position of the AF phase.

the position of the AF phase. This difference in position comes from the van der Waals interaction which acts on the system via the n operator rather than via σ^z, as discussed in Section 5.2.1. Other phases exist in H_{Ryd} when considering the long-range interactions beyond nearest-neighbors and setting $\Omega, \delta \ll U$ [Bernien *et al.*, 2017], which is out of the scope of the works conducted in this thesis.

Experimental implementation. In order to show that we can implement and explore the TFI model, we prepare the ground states of its various phases. The PM phase ground state for $\delta < 0$ is already initially prepared: the starting point of the experiment is the state $|\downarrow\downarrow \dots \downarrow\downarrow\rangle$, which is produced using the optical pumping procedure described in Section 2.2. The challenge is thus to prepare the AF phase ground state. To do so, we dynamically tune the Hamiltonian parameters δ and Ω to transfer the system from its initial PM ground state into the AF phase.

Typical sweep parameters. We use the following procedure to reach the AF phase. We start in the PM phase with $\delta < 0$ such that the initial state is the ground state of the system. We then vary the parameters of the Hamiltonian δ and Ω (see Figure 5.5 b)) whilst trying to remain in the system's ground state in the following way:

- We start by increasing Ω, keeping $\delta < 0$ fixed. It lifts the degeneracy of the levels at $\delta = 0$ by a quantity $E_{\mathrm{gap}} \propto \Omega$. We aim for $\Omega > \Omega_{\mathrm{c}}$.

- We then vary the detuning to reach $0 < \hbar\delta < 2U$, keeping Ω fixed. At this point, we are in the PM phase above the AF phase.

- We finish by linearly reducing Ω down to 0 at a rate $\dot{\Omega}$. We cross the critical line during this step, which can be seen as a Landau-Zener transition with a probability $P_{\mathrm{cross}} = \exp[-\pi E_{\mathrm{gap}}^2/\hbar^2\dot{\Omega}]$ for the system to be transferred to excited states.

We will refer to this process as a *sweep* in the following.

The corresponding path in the phase diagram is summarized in Figure 5.5 a) (red arrow). In order to remain in the system's ground state, we aim for $P_{\mathrm{cross}} \ll 1$, which means $\dot{\Omega} \ll E_{\mathrm{gap}}^2/\hbar^2$. This condition (which is an adiabaticity criteria) is hard to fully achieve in practice as: (i) the size of the gap at the critical line decreases as $E_{\mathrm{gap}} \propto 1/N$ (see Figure 5.4 b)) and (ii) we are limited in the sweep duration. A detailed analysis of the optimal sweep durations is presented in Section 6.2.1.

Effect of the two-photon transition. As discussed in Chapter 3, the Rydberg excitation is performed using a two photon transition of wavelengths 420 nm and 1013 nm, with effective ground-Rydberg Rabi frequency $\Omega = \Omega_{420}\Omega_{1013}/(2\Delta)$, Δ being the single-photon detuning from the intermediate state, and Ω_{420}, Ω_{1013} the Rabi frequencies of the 420 nm and 1013 nm lasers. In order to dynamically tune Ω and δ, we keep Ω_{1013} constant and vary both Ω_{420} and δ using an acousto-optic modulator (see Section 3.2.1). As Ω_{420} is varied, the value of δ changes due to the varying light-shift induced by the two photon transition as $\Omega_{420}^2/(4\Delta)$ (see Section 3.1.2). We compensate this effect by measuring the real temporal evolution of Ω_{420} with a photodiode, calculating the corresponding value of the light-shift and changing δ accordingly.

Experimental results. We perform the sweep presented above on a chain of $N = 47$ atoms (see Figure 5.5 d)). The chain is twisted due to the limited field of view of the
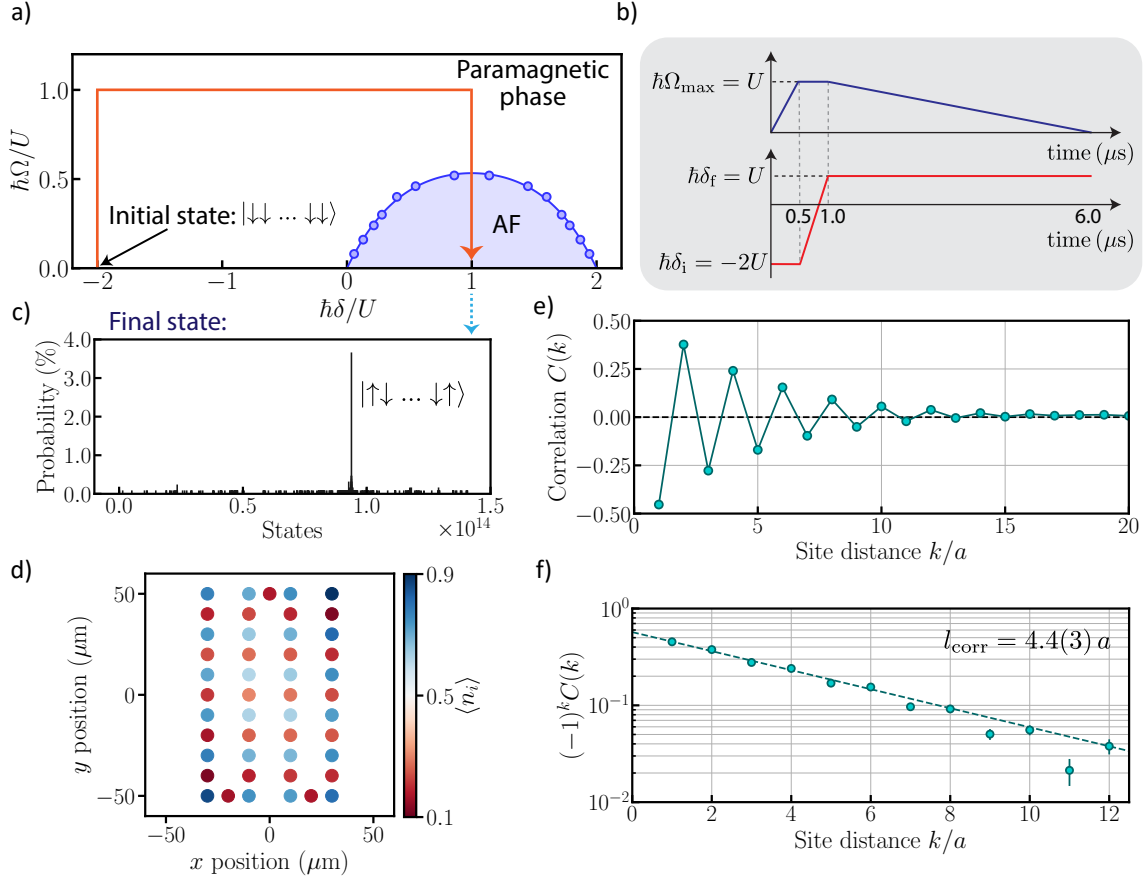
Figure 5.5: Antiferromagnetic ordering on a 47-atom line. a) Path in the phase diagram followed in the experiment, with b) the corresponding temporal evolution of Ω and δ. c) State histogram after the sweep. The prominent peak corresponds to the ground state of the AF phase $|\uparrow\downarrow \ldots \downarrow\uparrow\rangle$. d) Rydberg density $\langle n_i \rangle$ along the chain. e) Correlations $C(k)$ between two spins separated by a distance of k sites. We observe the alternation of the correlation sign, characteristic of antiferromagnetic ordering. f) Decay of the correlations shown in semi-log scale. The dashed is a fit to the data using an exponential function, from which we extract a correlation length $l_{\text{corr}} = 4.4(3)\,a$.

optical setup (see Section 4.1.3). We use $|r\rangle = \left|75S_{1/2}, m_J = 1/2\right\rangle$ with an inter-atomic distance $a = 10\,\mu\text{m}$, leading to $U/h \simeq 2\,\text{MHz}$. The sweep parameters (see Figure 5.5 b)) are the following: we start with an initial detuning $\delta_i/(2\pi) = -4\,\text{MHz}$ and ramp up the Rabi frequency up to $\Omega_{\text{max}}/(2\pi) = 2\,\text{MHz}$ in $0.5\,\mu\text{s}$. We then sweep the detuning to $\delta_f/(2\pi) = 2\,\text{MHz}$ in $0.5\,\mu\text{s}$. As we cross the critical line during the last step, we slowly decrease the Rabi frequency down to 0 in $5\,\mu\text{s}$.

We perform this sweep on the experiment, and measure the state of the system at the end of the process. We typically repeat ~ 1000 times the experiment, and

reconstruct the corresponding state histogram after the sweep, see Figure 5.5 c). Out of the $2^{47} \sim 10^{14}$ possible states, we obtain one prominent peak with probability $\sim 3.5\%$, which corresponds to the AF phase ground state $|\uparrow\downarrow \ldots \downarrow\uparrow\rangle$. This shows that we efficiently probe the AF phase of the TFI model in 1D. Due to (i) the imperfect adiabaticity of the driving and (ii) the state preparation and detection errors, we prepare various states at the end of the sweep which are not the AF phase ground state. Even though these states are not the AF ground state, they still exhibit strong antiferromagnetic ordering. To confirm this, we measure the Rydberg density of each atom $\langle n_i \rangle = (1 + \langle \sigma_i^z \rangle)/2$, see Figure 5.5 d): $\langle n_i \rangle = 1$ ($\langle n_i \rangle = 0$) if the atom is in the $|\uparrow\rangle$ ($|\downarrow\rangle$) state. We observe the alternance between up spins (blue) and down spins (red) along the chain, characteristic of antiferromagnetic ordering. We also compute the normalized connected correlations $C(k)$ defined as:

$$C(k) = \frac{4}{N_k} \sum_i \langle n_i n_{i+k} \rangle - \langle n_i \rangle \langle n_{i+k} \rangle, \tag{5.12}$$

with N_k the number of pairs separated by a number of sites k. The value is ± 1 for fully correlated pairs, and 0 if uncorrelated. The results are shown in Figure 5.5 e). We observe the sign alternance of $C(k)$, which is characteristic of antiferromagnetic ordering: two spins separated by an even (odd) number of sites k are positively (anti-) correlated. As we do not systematically prepare the perfect antiferromagnetic state, the correlations do not extend over the whole chain. The correlations decay exponentially (see Figure 5.5 f)) with a typical correlation length $l_{\mathrm{corr}} = 4.4(3)\, a$. This value indicates the mean number of sites for which the antiferromagnetic ordering is maintained before a defect occurs, i.e., two consecutive spins in the same state.

5.3 Conclusion

In this chapter, I presented the use of the van der Waals interaction to (i) entangle two atoms with a fidelity $F > 0.9$, and (ii) implement the Transverse Field Ising (TFI) model. I presented the model's main features on the example of a 1D chain by deriving the corresponding phase diagram. I explained how we experimentally explore the phase diagram, and demonstrated this in the case of a 47-atom chain by preparing the ground state of the antiferromagnetic phase.

The results presented here show that we are able to explore the TFI model phase diagram. In the two next chapters, I will focus on the exploration of the model in square

and triangular geometries, for which the phase diagram is not known analytically. In particular, we will characterize the dynamical growth of the antiferromagnetic ordering during the sweep, close to and after the critical line. The triangular geometry displays high geometric frustration, a phenomenon which is hard to study numerically. This implies that the nature of the various phases composing the phase diagram are not exactly known. We will show that we are able to observe the emergent features of geometric frustration using our Rydberg quantum simulator.

Chapter 6

Transverse field Ising model on square lattices

Contents

In this chapter, I will focus on the quantum simulation of the 2D transverse field Ising model in square arrays. The model is not analytically solved: its properties, such as the position of its various phases or the value of its critical exponents, are only known through approximate numerical calculations. I will show here that our platform is capable of probing and studying these features in large systems, demonstrating that quantum simulation using Rydberg arrays is now at a level which is comparable to numerical simulations.

This model has already been successfully implemented in our group by Lienhard *et al.* [2018]. The main features of the model, such as the short time expansion of

antiferromagnetic ordering, have been observed. However, decoherence effects limited the possible studies. The improvements presented in Chapter 3 drastically increased the system's coherence and allowed us to revisit the model. As synthetic platforms are subject to numerous limitations, an important aspect of quantum simulation is the ability to assess the quality of the simulator's output. In this spirit, we compare the experimental results in systems with up to 100 atoms with approximated numerical methods, and show that we understand the output of the platform on such large systems. This benchmark allows us to trust the various studies I present in this chapter: (i) probing the system's phase diagram, (ii) a comparison of the results with classical thermal equilibrium and (iii) a study of the dynamical evolution of the system at a phase transition. The simulations and theoretical concepts discussed here were developed by the team of A. Laüchli. Part of the results presented here are published in Scholl *et al.* [2021a].

6.1 Exploration of the phase diagram

We consider N atoms placed on a square lattice with spacing a, and coupled by the (repulsive) van der Waals interaction. The atoms are initially prepared in the $|\downarrow\rangle = \left|5S_{1/2}, F = 2, m_F = 2\right\rangle$ state, and are coupled to the Rydberg state $|\uparrow\rangle = \left|75S_{1/2}, m_J = 1/2\right\rangle$ via a laser field with Rabi frequency Ω and detuning δ. In these conditions, the implemented Hamiltonian H_{Ryd} reads:

$$H_{\mathrm{Ryd}} = \frac{\hbar\Omega}{2} \sum_{i=1}^{N} \sigma_i^x - \hbar\delta \sum_{i=1}^{N} n_i + \sum_{i<j} \frac{C_6}{R_{i,j}^6} n_i n_j, \tag{6.1}$$

where $n = (1 + \sigma^z)/2$ is the Rydberg operator, σ^x and σ^z are the usual Pauli matrices, $R_{i,j}$ is the distance between atom i and j and $C_6 \simeq 1942\,\mathrm{GHz}.\mu\mathrm{m}^6$ is the van der Waals coefficient. Ω and δ act as effective transverse and longitudinal fields (see Section 5.2.1). We set $a = 10\,\mu\mathrm{m}$, leading to a nearest-neighbor interaction energy $U \simeq 1.87\,\mathrm{MHz}$ (see Section 6.2.2).

The first step to characterize the model is to determine its various ground states depending on the Hamiltonian parameters, i.e. to explore its phase diagram. We start by drawing the phase diagram for an infinite system, then show how we experimentally probe its various phases, and finally explore the phase diagram in finite-size systems.

6.1.1 Phase diagram for an infinite system

We first consider the case of an infinite system, and suppose that the interactions only act between the nearest neighbors. The effects of both the finite size and the interactions beyond nearest neighbors are discussed below. Under these assumptions, the phase diagram is similar to the one in 1D presented in Section 5.2. The phase diagram exhibits two phases [Lienhard *et al.*, 2018]: a paramagnetic (PM) phase for which the spins align onto the effective magnetic field, and an antiferromagnetic (AF) phase for which the spins are anti-aligned. In the absence of transverse field ($\Omega = 0$), the extension of the AF phase is set by the total interaction strength felt by one atom, here $4U$ as each atom has four neighbors. The AF phase extends over $0 < \hbar\delta < 4U$. For $\Omega > 0$, the critical line follows a 'dome' shape, with its apex located at $(\hbar\Omega_\mathrm{c} \simeq 1.52U, \hbar\delta_\mathrm{c} = 2U)$. The value of Ω_c is estimated from Monte-Carlo simulations [Blöte and Deng, 2002].

Effect of long-range interactions. Due to the $1/R^6$ decay of the van der Waals interaction, the interactions extend beyond the nearest neighbors, such that the phase diagram exhibits crystalline phases when considering $\Omega, \delta \ll U/\hbar$, recently observed in Ebadi *et al.* [2021]. In the present thesis, we will always remain in the regime $\Omega, \delta \sim U/\hbar$, in which those phases can be neglected. Even in this regime, the long-range interactions modify the boundaries of the AF phase: the distance to the next-nearest neighbor is $\sqrt{2}a$ leading to an interaction strength $U/8$, which is not negligible. As the width of the AF phase at $\Omega = 0$ is given by the total interaction energy felt by one spin i, $U_\mathrm{m} = U \sum_{j \neq i} 1/|i - j|^6$, the long-range interaction modifies the width of the AF phase. Considering the $1/R^6$ decay, we obtain $U_\mathrm{m} \simeq 4.66U$, the extension of the AF phase is thus $0 < \hbar\delta \lesssim 4.66U$. The size of the AF phase in Ω is also altered by the long range interactions, with its apex located at $(\hbar\Omega_\mathrm{c} \simeq 1.25U, \hbar\delta_c \simeq 2.33U)$. The value of Ω_c is estimated from Monte-Carlo simulations including the long-range interactions [Fey, Kapfer, and Schmidt, 2019]. The corresponding phase diagram of H_Ryd is drawn in Figure 6.1 a). We now explore the phase diagram experimentally.

6.1.2 Reaching and characterizing the antiferromagnetic phase

We experimentally explore the model's phase diagram in the same spirit as performed in Section 5.2.2. The starting point of the experiment is the state $|\downarrow\downarrow \ldots \downarrow\downarrow\rangle$, which is the ground state of the PM phase for $\delta < 0$. In order to probe the phase diagram of
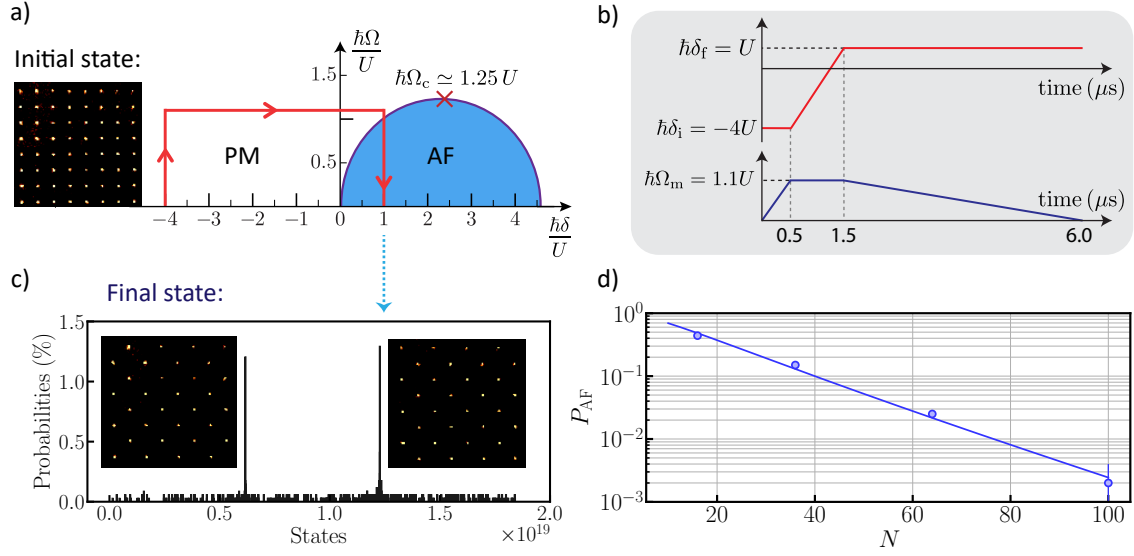
Figure 6.1: Reaching the antiferromagnetic phase of the TFI model on a square. Infinite size phase diagram of H_{Ryd}. The red line represents the path followed to reach the AF phase. b) Time evolution of Ω and δ. c) State histogram after the sweep for a 8×8 array. The two prominents peaks are the AF phase ground states, with their corresponding fluorescence images. The missing atoms are in the $|\uparrow\rangle$ state while the detected atoms are in the $|\downarrow\rangle$ state. d) Probability to obtain one of the AF ground state P_{AF} as a function of the number of atoms N. The probability evolution is well fitted by a function of the type $A^N(1 - e^{-BN})$ (see text), consistent with the scaling of the energy gap $E_{\text{gap}} \propto 1/\sqrt{N}$.

H_{Ryd}, we sweep Ω and δ over time, starting in the PM phase ($\delta < 0$) and reaching the AF phase (see Figure 6.1 a)). We aim at adiabatically driving the system such that it remains in the instantaneous ground state at all time. However, the energy gap E_{gap} between the ground state and the first excited state vanishes when crossing the critical line, scaling here as $1/\sqrt{N}$ [Schuler *et al.*, 2016]. In order to limit the transfer to high excited states, the sweeps are designed such that we cross the critical line as slowly as possible, but keeping them short enough to avoid strong decoherence effects (see Section 6.2.1). The typical sweep parameters, presented in Figure 6.1 b), are the following:

- We start with a detuning $\hbar\delta_{\text{i}} = -4U$, deep in the PM phase. We ramp up the Rabi frequency to reach $\hbar\Omega_{\text{m}} = 1.1U$ in $0.5\,\mu s$.

- We then sweep the detuning to reach $\hbar\delta_{\text{f}} = U$ in $1\,\mu s$.

- We finally decrease the Rabi frequency down to zero in $4.5\,\mu s$. This step is longer than the others to cross the critical line as slowly as possible.

We perform this sweep and measure the state of the atoms at the end of the procedure. We repeat the process typically ~ 1000 times, and obtain the state histogram presented in Figure 6.1 c) for an 8×8 array. Out of the $2^{64} \sim 2 \times 10^{19}$ possible states, we observe two prominent peaks corresponding to the two AF ground states. The insets are real images of the atom fluorescence. The missing atoms are in the $|\uparrow\rangle$ state, and the detected atoms are in the $|\downarrow\rangle$ state. We obtain a probability $P_{\mathrm{AF}} \simeq 2.5\%$ to prepare one of the AF ground states. These results show that, starting in the PM phase, we are capable of preparing the AF phase ground states, hence of exploring the TFI model. Owing to the experimental imperfections (see Section 6.2.2) and the scaling of the energy gap, the state preparation becomes more challenging with increasing system size. We observe this experimentally by measuring P_{AF} for different system sizes comprising N atoms, see Figure 6.1 d). The solid line is a fit to the data using a function of the form: $P_{\mathrm{AF}} = A^N(1 - e^{-BN})$, which phenomenologically takes into account (i) the detection errors which scale as A^N, and (ii) the scaling of the energy gap at the critical line $E_{\mathrm{gap}} \propto 1/\sqrt{N}$ combined with the finite probability to cross the energy gap following the Landau-Zener formula, which gives $(1 - e^{-BN})$.

At the end of the sweep, most of the prepared state are not the AF ground states. However, these states are expected to be weakly excited states, and thus to exhibit strong AF ordering. To characterize their AF ordering, we compute the various quantities presented in Figure 6.2 for two system sizes: a 6×6 and a 14×14 array. I now present these various quantities.

Staggered magnetization. We first compute the order parameter of the PM to AF phase transition, which is the normalized *staggered magnetization* $m_{\mathrm{stag}} = \langle |n_A - n_B| \rangle / (N/2)$, giving the difference in the number of Rydberg excitations on the two sublattices A and B, defined in Figure 6.2 a). The two perfect AF states correspond to one of the two sublattices being fully excited, such that $m_{\mathrm{stag}} = 1$. We visualize the shot-wise contributions to m_{stag} using a 2D histogram of the probability $P(n_A, n_B)$ of number of excitations n_A and n_B of the two sublattices A and B. The two ground states appear as points at $(N/2, 0)$ and $(0, N/2)$. The results are shown in Figure 6.2 b) for the 6×6 array and the 14×14 array. For both systems, we observe the presence of points along the diagonal, highlighting that the average Rydberg density is $\sim 50\%$. For the 6×6 array, we observe a conglomeration of points around the two corners belonging to ground states, which is expected as $P_{\mathrm{AF}} \simeq 15\%$. The elongated histogram for the 14×14 array pointing towards perfect AF ordering indicates that we prepare strongly AF ordered states, even for such large systems.
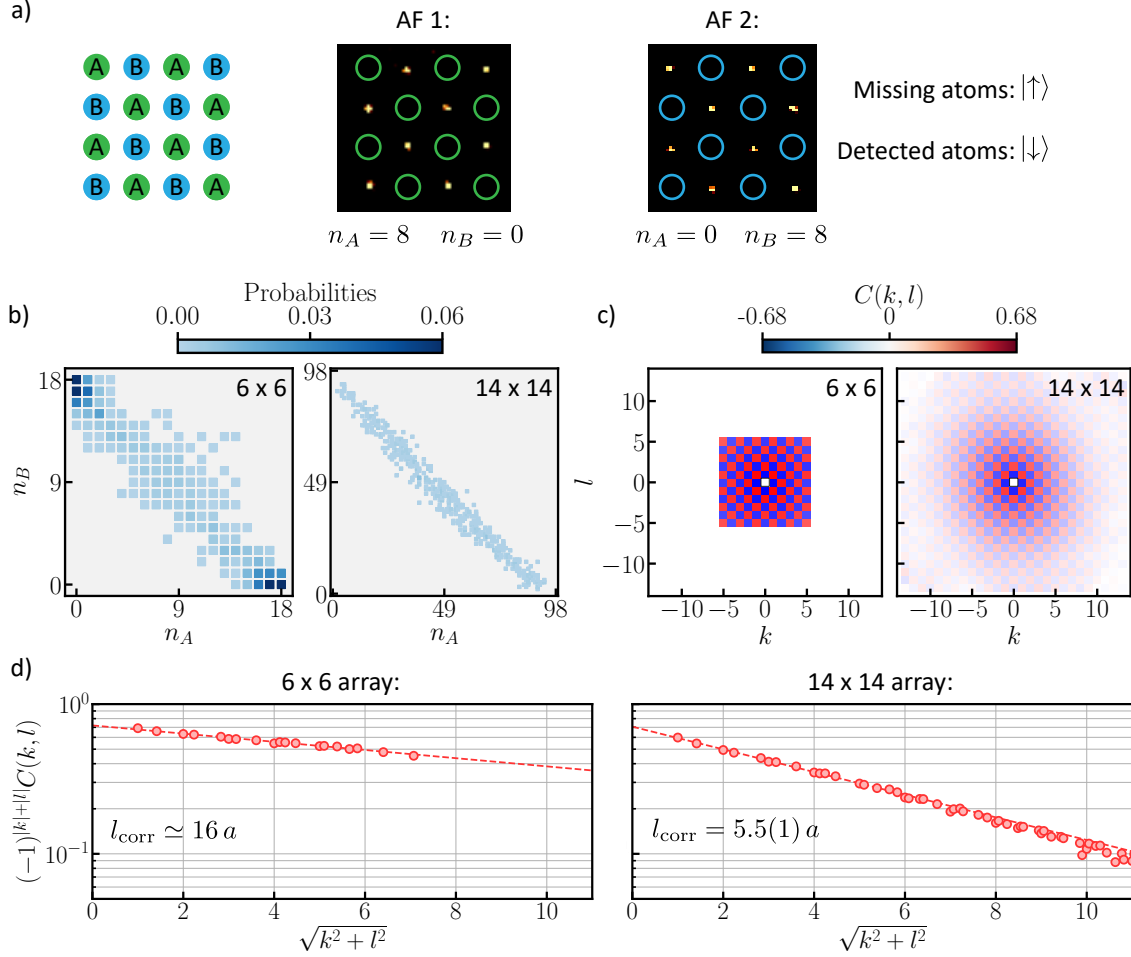
Figure 6.2: Characterization of the antiferromagnetic ordering for 6×6 **and** 14×14 **arrays.** a) Sketch of the bipartite square lattice. When a perfect antiferromagnetic ordering is obtained, each atom in $|\uparrow\rangle$ (missing atoms in the pictures) lies on sublattice A or sublattice B. b-d) Experimental results using the sweep described in Figure 6.1 for a 6×6 and a 14×14 array. We characterize the AF ordering of the obtained states by looking at: b) the 2D histogram of the number of Rydberg excitations on the two sublattices, c) the correlation map and d) the 1D correlations. We extract from the latter results a correlation length $l_{\mathrm{corr}} \simeq 16\,a$ for the 6×6 array, and $l_{\mathrm{corr}} = 5.5(1)\,a$ for the 14×14 array.

Connected spin-spin correlations. The second observable we compute is the normalized connected spin–spin correlation function, defined as:

$$C(k,l) = \frac{4}{N_{k,l}} \sum_{i,j} \langle n_i n_j \rangle - \langle n_i \rangle \langle n_j \rangle, \tag{6.2}$$

where the sum runs over all pairs of atoms i and j separated by $k\boldsymbol{e_1} + l\boldsymbol{e_2}$, with $\boldsymbol{e_1}$, $\boldsymbol{e_2}$ denoting the two vectors of the underlying lattice, k and l are two integer numbers, and $N_{k,l}$ being the number of such pairs. The values of $C(k,l)$ are ± 1 for the AF ground states. The $C(k,l)$ correlation maps of the 6×6 and the 14×14 arrays are shown in Figure 6.2 c). In both cases, we observe the alternation of positive correlations (red) and negative correlations (blue), characteristic of antiferromagnetic ordering. We also compute the corresponding 1D correlations $(-1)^{|k|+|l|}C(k,l)$, see Figure 6.2 e). We observe an exponential decay of the correlations, from which we extract a typical correlation length $l_{\mathrm{corr}} \simeq 16\,a$ for the 6×6 array and $l_{\mathrm{corr}} = 5.5(1)\,a$ for the 14×14 array, a being the lattice spacing. For the 6×6 array, the correlation length is larger than the system side length, meaning that on average the produced AF state is close to being a perfect AF state.

Conclusion. The results presented here show that we are able to produce highly AF ordered states on system sizes as large as $N = 196$. As expected from the scaling of the energy gap, the quality of the prepared AF ordering decreases with N. Nevertheless, even on the largest array, we obtain strong AF ordering. This shows our ability to probe the TFI model phase diagram, which we now explore in more details.

6.1.3 Exploration of the phase diagram in finite-size systems

I now present our experimental exploration of the phase diagram. As the phase diagram only exhibits two phases and the initial state is the ground state of the PM phase, we will probe the AF phase. The AF phase presented in the phase diagram of Section 6.1.1 is calculated for an infinite system size. We show here that the finite size affects the shape of the AF region. The phase diagram is altered due to: (i) the limited number of atoms and (ii) the open boundaries. The limited number of atoms reduces the extension of the AF phase in Ω, whilst the open boundaries reduce the extension of the AF phase in δ. We now show these two effects.
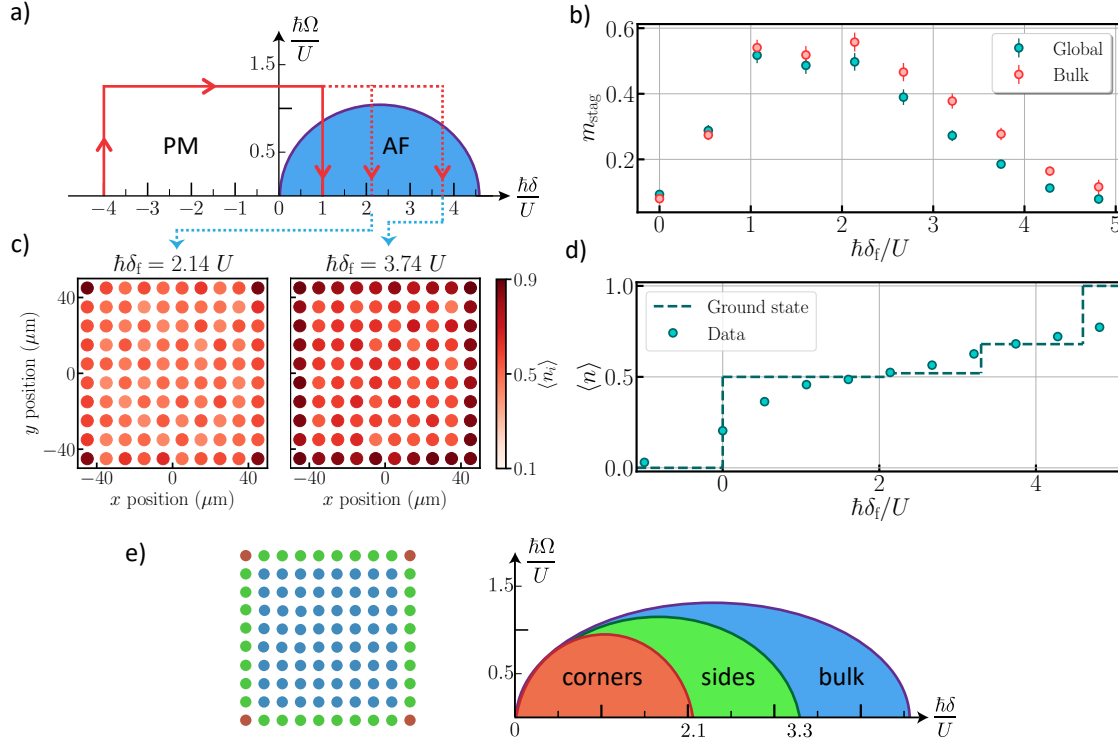
Figure 6.3: Effect of open boundaries on a 10×10 array. a) Parameters of the performed experiment in the phase diagram. We vary the final detuning δ_f. b) m_stag as a function of δ_f. The quality of the prepared antiferromagnet drastically varies depending on the final detuning, and is maximum for $U < \hbar\delta_\mathsf{f} < 2U$. c) Rydberg density per atom for $\hbar\delta_\mathsf{f} = 2.14U$ and $\hbar\delta_\mathsf{f} = 3.74U$. Due to edge effects, the Rydberg density in the corners and on the sides is higher than in the bulk. d) Mean Rydberg density $\langle n \rangle$ as a function of δ_f. $\langle n \rangle$ is not constant in the AF ground state (dashed line). e) Influence of the edge effects on the phase diagram. As the atoms in the corner and on the side have fewer neighbors than in the bulk, the width of the AF phase depends on the atom position.

Width of the AF phase. We start by characterizing the width of the AF phase, i.e. its extension in δ. The experimental procedure is the following. We consider a 10×10 array, and use the sweep timings described in Figure 6.1 b). We set $\hbar\delta_\mathsf{i} = -4U$, $\hbar\Omega_\mathsf{m} \simeq 1.25U$, and vary the final detuning δ_f (see Figure 6.3 a)). For an infinite system, the quality of the prepared AF ordering would not depend on the final detuning. However, for the array considered here, we observe that the value of m_stag varies inside the AF phase (see Figure 6.3 b)) and is maximum in the range $U < \hbar\delta_\mathsf{f} < 2U$. By comparing the value of m_stag between the whole system (green) and its bulk (red), we observe a substantial difference for $\hbar\delta_\mathsf{f} > 2U$, indicating that boundary effects play a role in the reduction of m_stag.

In order to understand why the AF ordering is low for $2U < \hbar\delta_{\mathrm{f}}$, we look at the Rydberg density map $\langle n_i \rangle$ for two values of final detuning: $\hbar\delta_{\mathrm{f}} = 2.14U$ and $\hbar\delta_{\mathrm{f}} = 3.74U$, see Figure 6.3 c). In the bulk of the system, the Rydberg density is $\sim 50\%$, which is expected from AF ordered states. However, in the corners and the sides of the system, the Rydberg density is large ($\langle n_i \rangle \sim 0.9$), which thus reduces the value of m_{stag} as both sublattices are filled. Due to this high value of $\langle n_i \rangle$ on the edges, the average Rydberg density $\langle n \rangle$ is not constant in the whole AF phase, see Figure 6.3 d). We also compute the value of $\langle n \rangle$ in the system's ground state (dashed line) [Lienhard *et al.*, 2018]. The atoms at the boundaries are more easily excited to the Rydberg state when δ_{f} increases, leading to three density plateaus. In the region $0 < \hbar\delta_{\mathrm{f}} < 2.1U$, $\langle n \rangle = 0.5$ and the ground state behaves the same as the infinite system ground state. For $\hbar\delta_{\mathrm{f}} > 2.1U$, $\langle n \rangle > 0.5$: the ground state of the system is not AF ordered on the whole array. This means that the actual width of the AF phase, considering the entire array, is $0 < \hbar\delta_{\mathrm{f}} < 2.1U$ at $\Omega = 0$.

This variation of Rydberg density in the AF phase is due to the open boundaries. The following heuristic argument explains the effect of boundaries on the phase diagram. We divide the system into three parts: the corners, the edges and the bulk. We draw the corresponding phase diagram for each "sub-system". The atoms on the edges have fewer neighbors, meaning that the total interaction energy felt by these atoms is lower than $4.66U$: $\sim 3.3U$ for the atoms on the side, and $\sim 2.1U$ for the atoms in the corners. The "width of the AF phase" thus depends on the considered atom in the cluster, as sketched in Figure 6.3 d): for $3.3U < \hbar\delta_{\mathrm{f}} < 4.6U$, only the bulk atoms are in the AF phase, while the boundaries are in the PM phase. In practice, we choose $0 < \hbar\delta_{\mathrm{f}} < 2.1U$ such that all the atoms are in the AF phase and the boundary effects thus have a limited impact.

Height of the AF phase. Now that we have characterized the width of the AF phase, we move on to the study of the height of the phase, i.e., the highest value Ω_{c} of the critical line. We start in the PM phase with initial detuning $\hbar\delta_{\mathrm{i}} = -2U$, and use as final detuning $\hbar\delta_{\mathrm{f}} \simeq 2U$ to end up close to the center of the AF phase. The path followed in the phase diagram is summarized in Figure 6.4 a). We vary the maximum Rabi frequency Ω_{m} and measure the corresponding value of m_{stag} obtained at the end of the sweep. Depending on the value of Ω_{m}, the critical line is crossed while sweeping δ ($\Omega_{\mathrm{m}} < \Omega_{\mathrm{c}}$), or while decreasing Ω ($\Omega_{\mathrm{m}} > \Omega_{\mathrm{c}}$). The sweep timings are shown in Figure 6.4 b): we ramp up the Rabi frequency in $0.5\,\mu$s, then slowly sweep the detuning in $4\,\mu$s, and finally rapidly ramp down the Rabi frequency in $0.5\,\mu$s. The
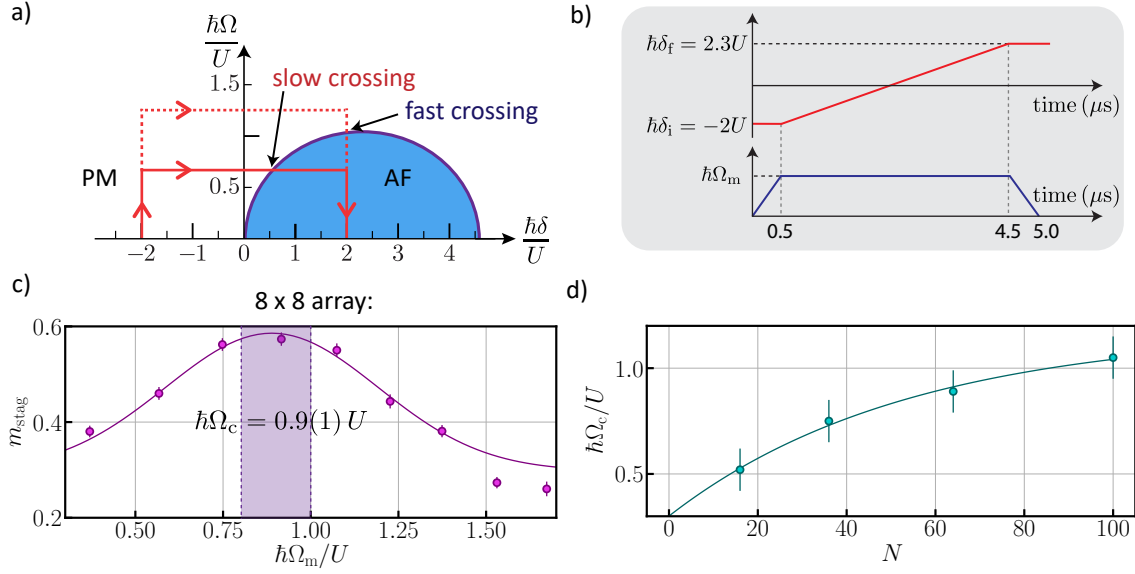
Figure 6.4: Measuring the height of the AF phase. a) Parameters of the experiment in the phase diagram. We vary the maximum Rabi frequency Ω_m. b) Sweep parameters. c) m_{stag} as a function of Ω_m for an 8×8 array. The AF ordering is the highest for $\Omega_m \sim \Omega_c$. The solid line is a fit to the data using a Gaussian function, from which we extract $\hbar\Omega_c = 0.89(5)\,U$, far from the value for an infinite system $\hbar\Omega_c \simeq 1.25\,U$. d) Value of Ω_c as a function of N determined using the present method. The solid line is a fit to the data using an exponential function of the form: $A(1 - e^{-B(N+N_0)})$ from which we extract $\hbar\Omega_c(N \to \infty) = 1.2(1)\,U$, consistent with the value obtained in Fey, Kapfer, and Schmidt [2019].

results of the experiment for an 8×8 array are presented in Figure 6.4 c). We observe two different regimes:

- For small values of Ω_m, m_{stag} increases when increasing Ω_m. In this regime, the critical line is crossed while sweeping δ. The increase of m_{stag} is due to the increase of the energy gap with Ω_m (see Section 5.2.2), inducing a higher probability to cross the gap without populating highly excited states.

- For high values of Ω_m, m_{stag} decreases when increasing Ω_m. In this regime, the critical line is crossed while sweeping Ω. The speed at which the critical line is crossed increases when increasing Ω_m, inducing a higher probability to populate highly excited states, hence reducing m_{stag}.

The bound between the two regimes is indicative of the value of Ω_c. We use a fit to the data with a Gaussian function to extract its value. For the 8×8 array, we

obtain $\hbar\Omega_c = 0.9(1)U$, which is far from the expected value for an infinite system $\hbar\Omega_c \simeq 1.25U$. We repeat this experiment for various number of atoms N and measure the corresponding value of Ω_c, see Figure 6.4 d). We observe an increase of Ω_c with N, showing that the value of Ω_c depends on the system size. We extrapolate the value of Ω_c for an infinite system by fitting the data with an exponential function of the form: $A(1 - e^{-B(N+N_0)})$, from which we extract $\hbar\Omega_c(N \to \infty) = 1.2(1)\,U$. The obtained value is consistent with the numerical results obtained via Monte-Carlo simulations in Fey, Kapfer, and Schmidt [2019]. The dependency of Ω_c with N is also observed on the numerical simulations of the 1D chain presented in Section 5.2.1. We have numerically checked (using exact diagonalization) on a 4×4 array that the results of the above experiment are the same in open boundary conditions and periodic boundary conditions, indicating that edge effects are not impacting the value of Ω_c. We could not come up with an intuitive explanation for the dependency of Ω_c with N as it is already not trivial to understand why $\hbar\Omega_c \simeq 1.25U$ for an infinite system.

Conclusions.   In this section, we experimentally explored the phase diagram of the AF phase. As our systems have finite sizes, we observed two phenomena: (i) due to the open boundaries, the width of the AF phase is reduced to $0 < \hbar\delta < 2.1U$ and (ii) due to the limited number of atoms, the extension of the AF phase in Ω is reduced. The above experiment indicates that the extension of the AF phase in Ω is close to the infinite system one for $N \sim 200$, which is experimentally accessible as demonstrated earlier. Regarding the boundaries effect, a solution to get closer to the infinite system would be to apply local light-shifts on the edge atoms using the addressing technique presented in Section 2.3.3. The value of the light-shift would be the missing interaction energy: $2.5\,U$ for the corner atoms and $1.3\,U$ for the side atoms. This technique was used in Omran *et al.* [2019] to prepare GHZ states on a 1D chain. Its extension to large 2D arrays would be however more demanding as one would need to light-shift all of the atoms on the edges.

6.2   Benchmarking of the results and current limitations

In the previous section, I showed that we are able to probe the phase diagram of H_{Ryd}, and prepare highly ordered AF states on systems with up to $N = 196$ atoms. In order to (i) build trust in our exploration of the H_{Ryd} phase diagram (including the results presented above) and (ii) understand what are the current limitations of the driving, we need to compare the outcome of the apparatus with simulations. However, for such

large number of atoms, it is not easy to check the validity of the experimental results with simulations. To overcome this problem, we first benchmark our results with exact simulations on a 4×4 array. We compare the results to simulations including decoherence effects, from which we extract the range of optimal timings to perform the sweeps. For larger arrays, the exact diagonalization of the system is not possible anymore. We compare the experimental results to Matrix Product States (MPS) simulations on arrays up to $N = 100$ atoms and identify the various limitations in the preparation of the AF ground states. The simulations were performed by the team of A. Läuchli.

6.2.1 Optimal sweep duration

We first investigate the duration of the sweeps. As discussed above, the optimal timing is a trade off between (i) crossing the critical line slowly enough to avoid populating excited states and (ii) being fast enough to avoid strong decoherence effects. To determine a range of optimal durations, we first focus on the preparation of AF order in a 4×4 array, and compare the experimental results with simulations. We then give more details on the origin of the decoherence in the system, and show its effect on the example of a 10×10 array.

Varying the sweep duration on a 4×4 array. The 4×4 array can be simulated by solving the Schrödinger Equation (SE). The simulations were performed by the group of A. Läuchli. The simulations take into account the detection errors (see Section 6.2.2). We assess the adiabaticity of the drive by performing three sweeps of durations $2.5\,\mu$s, $4\,\mu$s and $8\,\mu$s. The parameters of the sweeps, shown in Figure 6.5 a), are as follows: at a detuning $\hbar\delta_i = -4U$, Ω is linearly increased from 0 to $\sim 0.75U$. We then linearly sweep the detuning to $\sim U$ while keeping Ω constant, and finally decrease Ω to 0. We use as observables the average Rydberg density $\langle n \rangle$ and the staggered magnetization m_{stag}, see Figure 6.5 b) and c). We measure these quantities for various times t_{off} throughout the sweep by rapidly switching off the excitation lasers in $\sim 50\,$ns. For the shortest sweep, we observe experimentally oscillations in the evolution of $\langle n \rangle$, a feature showing that we fail to adiabatically drive the system. This is confirmed by the value of m_{stag} at the end of the sweep (about 0.5) which would be 1 if the sweep were adiabatic. As the sweep time increases, the oscillatory behaviour is reduced and the value of m_{stag} increases.

We observe a good agreement between experiment and simulation using the SE
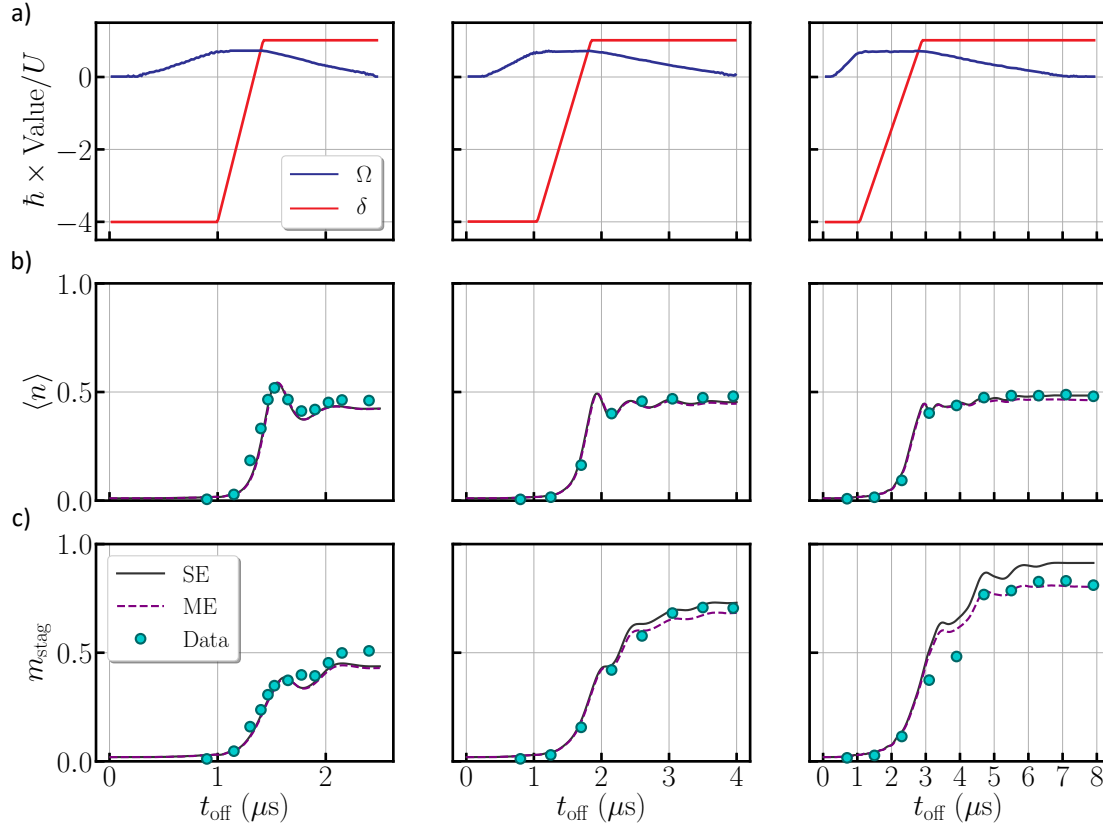
Figure 6.5: Benchmarking of the sweeps duration on a 4×4 array. Time evolution of a) Ω and δ, b) the Rydberg density and c) the staggered magnetization for three distinct sweeps of durations $2.5\,\mu$s (left), $4\,\mu$s (middle) and $8\,\mu$s (right) on the 4×4 array. The solid (dashed) line is the simulation of the Schrödinger (Lindblad master) equation. We need to take into account the decoherence to simulate accurately the longest sweep.

(solid line), especially in the evolution of $\langle n \rangle$, for the shortest sweeps. The discrepancy is larger for the longest sweep, indicating that decoherence has an important role. To study this effect, we solve the Lindblad Master Equation (ME) (see Section 3.3.2) using a single atom decoherence rate $\gamma = 0.05\,\mu\text{s}^{-1}$, measured on single-atom ground-Rydberg Rabi oscillations. These numerical results (dashed line) agree closely with the experimental data, indicating that decoherence at the single-particle level is sufficient to describe the system.

We conclude from this study that the optimized sweep duration is $\sim 6 - 7.5\,\mu$s.

Effect of the intermediate state lifetime. As discussed in Section 3.3.2, the main contribution to the measured value of γ is the spontaneous emission rate Γ from the
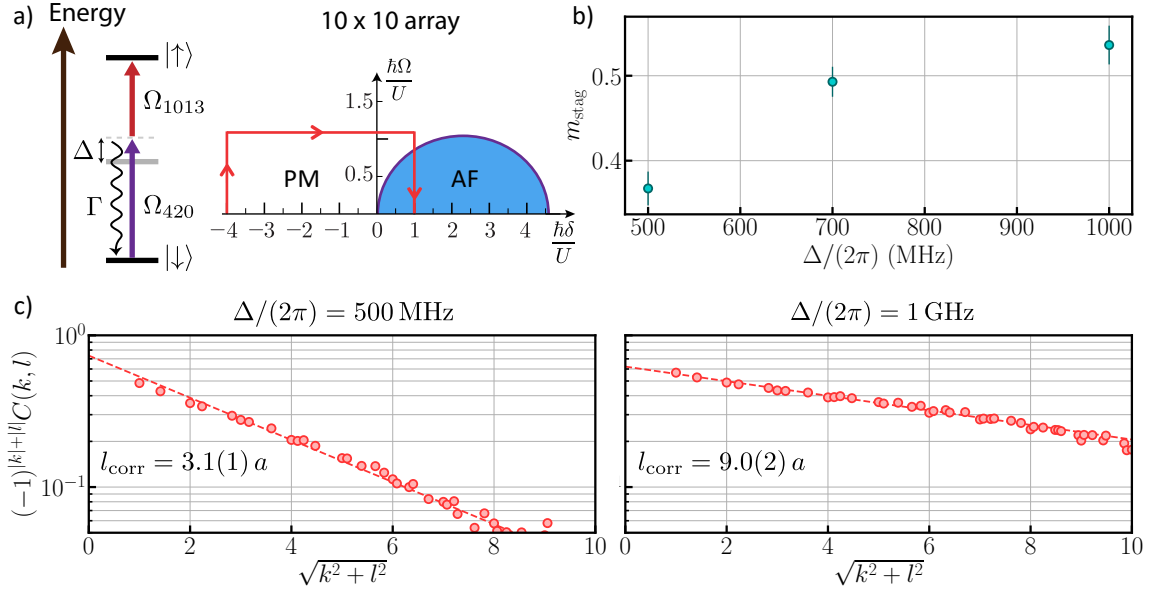
Figure 6.6: Effect of the intermediate state lifetime on a 10×10 array. a) Influence of the spontaneous emission from the intermediate state. b) We measure m_{stag} as a function of the intermediate detuning Δ, and show c) the corresponding correlations for $\Delta = 2\pi \times 500\,\text{MHz}$ and $\Delta = 2\pi \times 1\,\text{GHz}$. The quality of the prepared antiferromagnet strongly depends on Δ, showing the importance of the spontaneous emission on the driving's coherence.

intermediate state, given by:

$$\Gamma = \Gamma_{6P} \frac{\Omega_{1013}^2 + \Omega_{420}^2}{4\Delta^2}, \tag{6.3}$$

with Ω_{1013} and Ω_{420} the Rabi frequencies of the 1013 nm and the 420 nm excitation lasers, Γ_{6P} the decay rate of the intermediate level, and Δ the single photon detuning (see Figure 6.6 a)). To limit the effect of spontaneous emission, we work in the regime $\Delta \gg \Omega_{420}, \Omega_{1013}, \Gamma_{6P}$, for which the effective Rabi frequency connecting the ground state to the Rydberg state is $\Omega = \Omega_{1013}\Omega_{420}/2\Delta$ (see Chapter 3).

We probe the effect of spontaneous emission on the preparation of AF ordered states on a 10×10 array. We use the sweep parameters described in Figure 6.1 b), and sketched in Figure 6.6 a). We measure the value of m_{stag} at the end of the sweep for various values of Δ, see Figure 6.6 b). To keep the same sweep parameters for all of the experiments, we change the value of Ω_{420} while keeping $\Omega_{1013}/(2\pi) = 37\,\text{MHz}$ fixed. We observe that the value of m_{stag} increases when increasing Δ. This result is

expected from the above equation, which can be rewritten as:

$$\frac{\Gamma}{\Gamma_{6P}} = \frac{\Omega_{1013}^2}{4\Delta^2} + \frac{\Omega^2}{\Omega_{1013}^2}. \tag{6.4}$$

The spontaneous emission rate decreases when Δ increases. This equation shows that for a fixed sweep, the smallest spontaneous emission rate is obtained for the highest values in Rabi frequencies and Δ.

To get a better idea of the difference in the results quality, we show the obtained correlations for $\Delta/(2\pi) = 500\,\mathrm{MHz}$ and $\Delta/(2\pi) = 1\,\mathrm{GHz}$. The corresponding decay rates are $\Gamma \simeq 0.04\,\mu\mathrm{s}^{-1}$ and $\Gamma \simeq 0.03\,\mu\mathrm{s}^{-1}$. We observe that between the two experiments, the correlation length is increased by a factor 3, whereas Γ is only increased by 30%, showing the strong effect of decoherence on the system. For the results presented in this chapter, the typical parameters we use are $\Omega_{1013} = 50\,\mathrm{MHz}$, $\Omega_{420} = 60\,\mathrm{MHz}$ and $\Delta = 700\,\mathrm{MHz}$.

6.2.2 Experimental imperfections

Besides decoherence effects, the experiment is subjected to various imperfections. The good agreement between the simulations which only included the detection errors and the results on the 4×4 array presented above shows that those imperfections did not need to be considered for such small array. However, we will see in the next section that their contribution is major to understand and accurately simulate the experimental results on large arrays. I describe here those imperfections and how we implement them in simulations.

Detection errors. As discussed in Section 3.3.1, the probability to misinterpret a $|\downarrow\rangle$ as a $|\uparrow\rangle$ atom is $\varepsilon \simeq 1\%$. The value is measured by performing the experimental sequence without the excitation lasers. The probability to misinterpret a $|\uparrow\rangle$ as a $|\downarrow\rangle$ atom is inferred from simulations using the experimental parameters [de Léséleuc *et al.*, 2018a] to be $\varepsilon' \simeq 3\%$. This effect is taken into account in simulations by including a probability to misinterpret the atom state at the end of the system's dynamics.

Residual disorder in atomic position. The finite temperature $(10\,\mu\mathrm{K})$ of the atoms in the tweezers leads to shot-to-shot fluctuations in the atoms position, with a standard deviation of $\sigma_r = 170\,\mathrm{nm}$ in the plane of the array and $\sigma_z = 1\,\mu\mathrm{m}$ in the transverse direction. This results in a variation of the interatomic distance, as shown in Figure 6.7
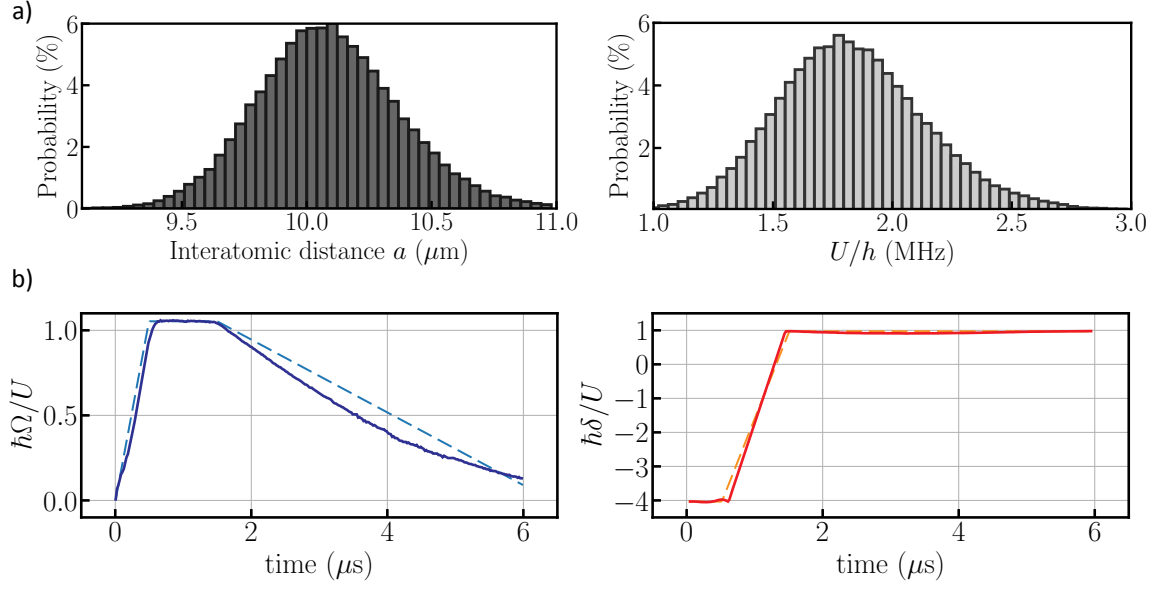
Figure 6.7: Interatomic distance fluctuations and deviation from linear sweeps. a) Histograms of the interatomic distance and the corresponding interaction energy. b) Due to non-linearities in the AOM used to perform the sweeps, the variations of Ω and δ (solid lines) are not linear (dashed lines).

a) in the case of two atoms. The mean interatomic distance is slightly higher than the set value $a = 10\,\mu\text{m}$ as the atom position also fluctuates out of the atomic plane. The interaction energy U is thus varying across the array, following a non-Gaussian distribution with mean value $U/h \simeq 1.87\,\text{MHz}$. This effect is included in simulations by repeating the simulation with randomly assigned atom positions chosen from the distribution shown in Figure 6.7 a).

Exact sweep shape. The sweeps are performed by dynamically driving an Acousto-Optic Modulator (AOM) in double-pass configuration (see Section 3.2.1), used to shape the 420 nm Rabi frequency Ω_{420} and the detuning δ. The 1013 nm laser is kept at a constant Rabi frequency during the whole sweep duration. As we drive a two-photon transition, the atoms experience a changing light shift as Ω_{420} is swept. We counteract this effect by changing δ accordingly. The measured value of Ω is shown in Figure 6.7 b) as a solid line. We observe a deviation from a linear evolution (dashed line), which we attribute to non-linear effects in the AOM, as we dynamically drive the rf power on timescales close to the band pass of the AOM. The light-shift correction takes into account this deviation from a linear evolution. This effect is included in the simulations by using the actual measured time evolution of Ω and δ
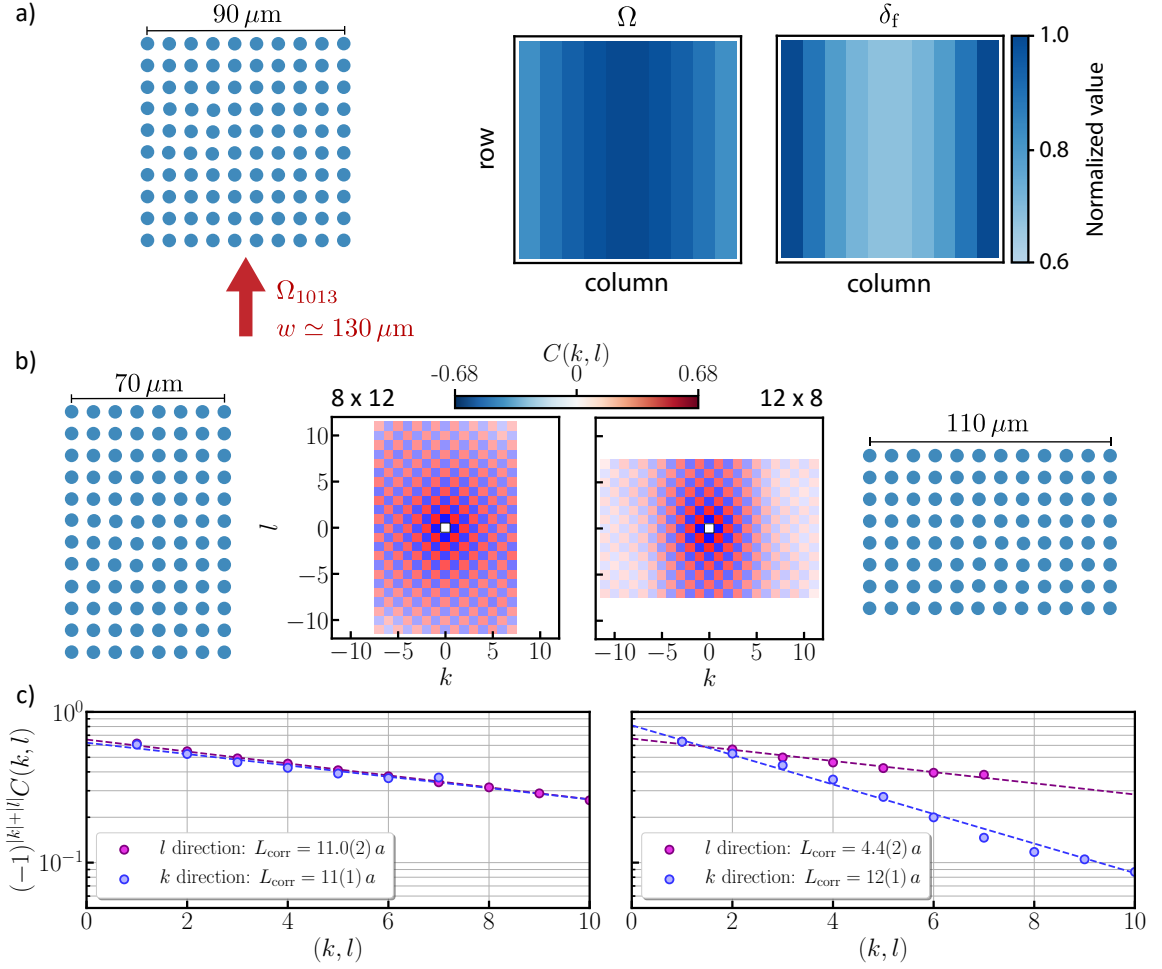
Figure 6.8: Influence of the finite-size excitation lasers. a) The width of the arrays is comparable to the waist of the excitation laser beam, resulting in a spatial variation of Ω and δ column by column. b) Effect of the fields inhomogeneity on the AF preparation demonstrated by considering two rectangular clusters: an 8×12 array and a 12×8 array. We show the correlations maps and c) the corresponding correlation lengths. For the 8×12 array, the decay of the correlations is isotropic. For the 12×8 array, we observe a strong anisotropy due to the finite size of the excitation laser.

and using the expected formula giving the two photon transition induced light-shift $(\Omega_{420}^2 - \Omega_{1013}^2)/4\Delta$ (see Section 3.1.2).

Finite size of the excitation laser beams. As the extension of the arrays is comparable to the size of the excitations beams, the atoms experience inhomogeneous fields Ω and δ across the array. The effect is dominated by the 1013 nm laser, which has a waist $w \simeq 130\,\mu\mathrm{m}$ (see Section 3.2.2). The inhomogeneity in δ is due to the

inhomogeneous light-shift of the two-photon transition. As the laser propagates vertically (see Figure 6.8 a)), the values of Ω and δ are different for each column. We measure the inhomogeneities in Ω by performing single-atom Rabi oscillations, and the inhomogeneities in δ by measuring the frequency of the transition at low Ω_{420}. The spatial distributions of Ω and δ_{f} are shown in Figure 6.8 a) in the case of a 10×10 array. We include this effect in simulations by setting the experimentally measured values of the field inhomogeneities.

To demonstrate the effect of the finite size of the excitation beams on the system, we measure the quality of the AF ordering at the end of the sweep described in Figure 6.1 b) considering two rectangular geometries with the same number of atoms: an 8×12 array with a width of $70\,\mu\mathrm{m}$ and a 12×8 array with a width of $110\,\mu\mathrm{m}$, see Figure 6.8 b). We show the correlations maps for both geometries and the corresponding 1D correlations, in the vertical (l) direction and the horizontal (k) direction (see Figure 6.8 c)). For the 8×12 array, the decay of the correlations is isotropic, with a measured correlation length $l_{\mathrm{corr}} \simeq 11\,a$. However, for the 12×8 array, we observe a strong anisotropy in the decay of the correlations: in the vertical direction, the correlation length is the same as for the 8×12, and in the horizontal direction the correlation length is $l_{\mathrm{corr}} = 4.4(2)\,a$. This experiment shows the strong impact of fields inhomogeneity on the preparation of AF ordered states.

The variations of Ω and δ throughout the array could be overcome by shaping the excitation beams in a square shape (rather than a Gaussian shape) at the position of the atoms, e.g. by using a spatial light modulator.

6.2.3 Benchmark of the results on large arrays

In this subsection, we compare the evolution of the AF ordering against simulations for large arrays. The sweep parameters, described in Figure 6.7 b), are the following: at a detuning $\hbar\delta = -4U$, Ω is increased from 0 to $\simeq 1.1U$ in $0.5\,\mu\mathrm{s}$. We then sweep the detuning to $\sim U$ in $1\,\mu\mathrm{s}$ while keeping Ω constant, and finally decrease Ω to 0 in $4.5\,\mu\mathrm{s}$. We perform this experiment for various sizes, from 6×6 to 10×10 arrays. Considering the number of involved atoms, it is not possible to perform an exact simulation of the system's dynamics. We thus use an approximate numerical method called Matrix Product States (MPS) [Schollwöck, 2011; Paeckel *et al.*, 2019] and simulate the dynamics of systems with up to $N = 100$ atoms. The MPS technique relies on (i) the decomposition of the system's state onto the product of matrices with sizes much smaller than the Hilbert space, and (ii) the use of the time-dependent
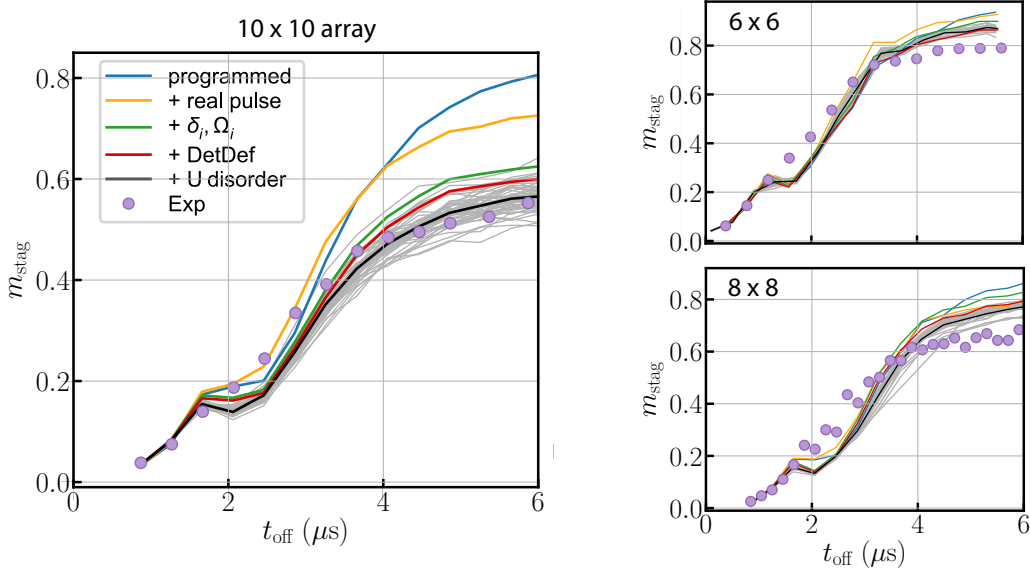
Figure 6.9: Benchmark of the AF ordering growth using MPS simulations. a) Evolution of m_{stag} throughout the sweep for the 10×10 array. The different lines show successive additions of imperfections on the MPS simulations. Starting from the programmed pulse shape without imperfections (blue), we include the real pulse shape measured in the experiment (yellow), add the inhomogeneous fields (green), apply the detection deficiency (red) and, finally, include the interaction disorder from fluctuations in the atom positions. The grey lines show individual samples of atom positions and the black line shows the sample average. b) Same as a) for 6×6 and 8×8 arrays.

variational principle applied to calculate the time-evolution of the decomposed state. Originally designed to simulate dynamics in 1D systems, the MPS method have proven to be reliable to simulate quasi-2D cylinders with finite extent in one direction or finite 2D systems. Prominent examples, particularly related to the system discussed here, include the computation of the phase diagram for Rydberg atoms arranged in square and Kagome geometries [Samajdar *et al.*, 2020, 2021]. The simulations were performed by the group of A. Läuchli. The implementation of the MPS simulation for our actual work is detailed in the supplementary informations in Scholl *et al.* [2021a].

Comparison to simulations using the staggered magnetization for various system sizes. We first compare the results using the staggered magnetization m_{stag} as an observable, see Figure 6.9. We perform the MPS simulation without experimental imperfections (blue line). We find good agreement with the experimental data over the first $1.5\,\mu\mathrm{s}$, after which the simulation shows a kink, not observed in the experimental

results. We also observe that m_{stag} eventually saturates on the experiment at values lower than the MPS, and that this effect worsens for larger systems. In order to check whether the discrepancy between the MPS simulation and the data comes from the experimental imperfections detailed above, we include in the simulations these imperfections. We add the imperfections one by one to appreciate their contribution: we perform the simulations using the experimentally measured sweep shape (yellow), add the inhomogeneous fields δ and Ω (green), the detection errors (red) and, finally, the shot-to-shot fluctuations of the interaction energies caused by the fluctuating atom positions (black). The grey lines show the full dynamics simulations for various atom positions. The imperfections are not able to explain the overshoot of m_{stag} at intermediate times. However, at later times, we observe better agreement for all system sizes. For the 6×6 array and the 8×8 array, each imperfection has a small contribution, which tends to decrease the final value of m_{stag}. For the 10×10 array, the largest contribution to the disagreement with the MPS results (considering the real sweep shape) is the inhomogeneity of the fields. This is not surprising as the waist of the 1013 nm laser is comparable to the size of the array.

Comparison with the correlation maps and staggered magnetization histograms on the 10×10 **array.** To further compare the MPS calculations to the experimental results, we show the correlation maps and the staggered magnetization histograms for various time steps t_{off} in the sweep on the 10×10 array, see Figure 6.10. In order to compare the results and considering the fact that the correlation maps display a symmetry along the horizontal axis, the upper part of each map show the experimental results, whereas the lower part show the MPS results. The same technique is used for the staggered magnetization histograms. The correlation maps show that the correlations start to develop at $1.3\,\mu$s, and are growing from nearest neighbor across the array. By $3.7\,\mu$s, the expected correlation pattern fills the entire array, and from then on, the strength of the correlations continues to increase. The corresponding m_{stag} histograms show the growth in the number of Rydberg excitations as the distribution of points moves from about $(0,0)$ to higher values of $n_A + n_B$. As the correlations begin to grow across the array, we see that the distribution of points stretches along the diagonal. After $3.7\,\mu$s, the points start to conglomerate around the corners $(N/2, 0)$ and $(0, N/2)$. The MPS results show qualitative agreement throughout the sweep for both observables, with slight differences appearing at times that correspond to disagreements in Figure 6.9.
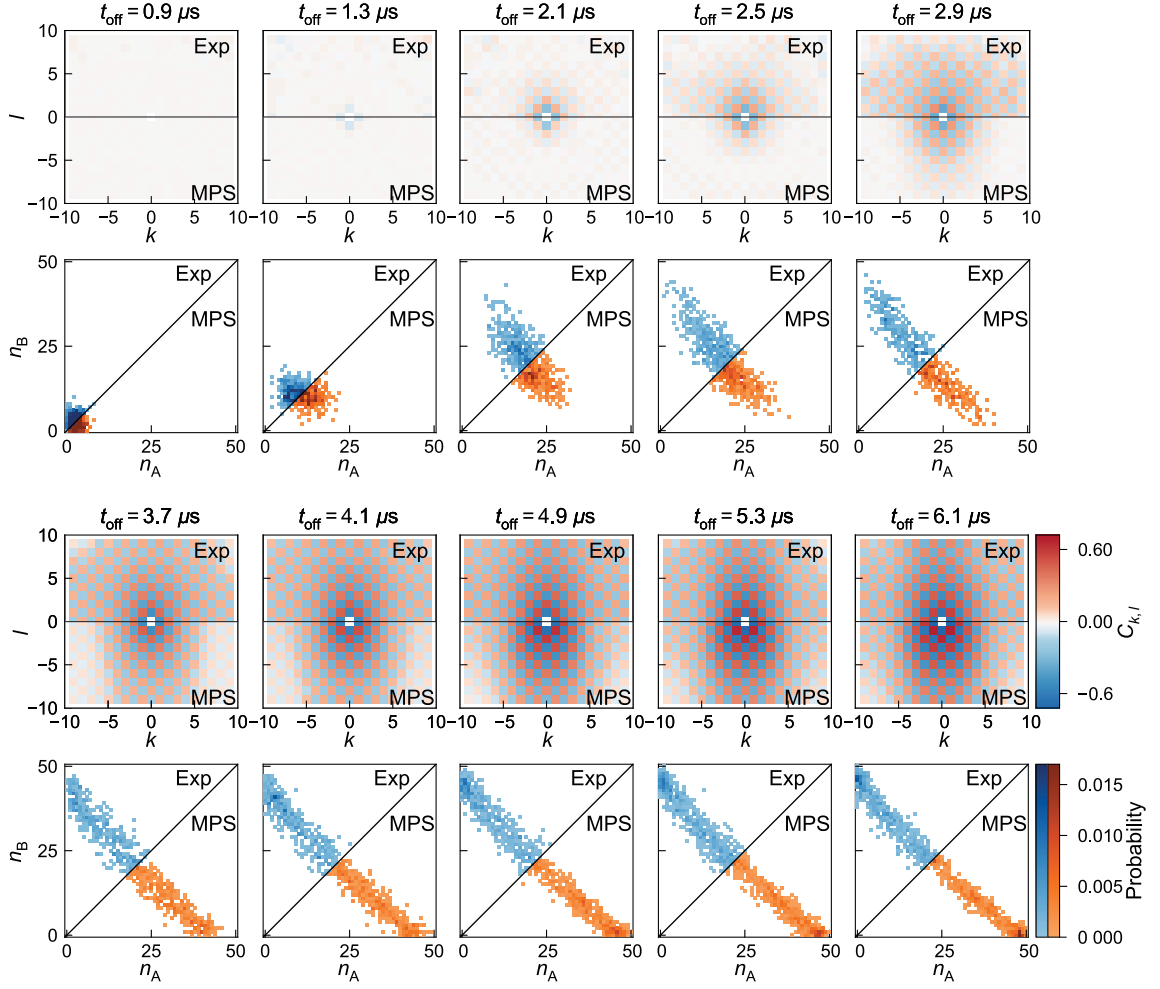
Figure 6.10: Comparison of the correlations maps and the staggered magnetization histogram between the MPS simulation and the data. The MPS simulation takes into account all the experimental imperfections described above.

Conclusion. The comparisons conducted above confirm that the dynamical evolution of the atomic system is well approximated by the MPS calculations for all observables. This indicates that we understand and have good control over our platform. The remaining discrepancy at long times could come from residual effects of decoherence due to spontaneous emission from the intermediate state or atomic motion, not taken into account in the MPS simulations, that start to play a role for timings around $6\,\mu$s. The discrepancy at short time could come from a slight mismatch in the sweep timings, in particular the evolution of δ, which is hard to measure.

As discussed above, we can perform this experiment on sizes as large as $N = 196$, however for such size the MPS calculations becomes intractable. We enter a regime in which exploring the TFI model with our platform is faster than with simulations,

which is eventually one aim of quantum simulation. To assess this, we compare the computation time of the MPS simulation for the 10×10 array and the experimental data acquisition. The MPS computation is ~ 14 days, whereas the data acquisition took ~ 10 hours (taking into account the various calibrations).

6.3 Comparison with classical thermal equilibrium

In the previous section, I showed that the dynamics of the system is well described by H_{Ryd} for sweeps that are short enough and taking into account the various imperfections of the experimental setup. As the transverse field term in Ω does not commute with the interactions, the system evolution is quantum, with no classical analog. However, at the beginning and at the end of the sweep, $\Omega = 0$ and the quantum and classical descriptions coincide. The Hamiltonian describing the system is:

$$H_{\mathrm{class}} = -\hbar \sum_{i=1}^{N} \delta_i n_i + \sum_{i<j} \frac{C_6}{R_{i,j}^6} n_i n_j, \tag{6.5}$$

where we take into account the field inhomogeneity δ_i (see Section 6.2.2). It is thus interesting to check whether the states at the end of the sweep can be described by a classical thermal equilibrium, i.e. if performing a quantum process eventually leads to a classical thermal distribution of states. The results are compared to Metropolis Monte Carlo simulations, performed by the team of A. Läuchli. We use Monte Carlo simulations because they accurately describe the system's ground states, and their computational cost is low compared to other methods. The results are averaged over 500 individually equilibrated samples of random atom positions, and take into account detection errors. We first extract the hypothetical temperature T_{hyp} of the system, then compare the experimental results to the classical thermal equilibrium. We will restrict to the study of the 10×10 array, although the conclusions we will come to are true for all sizes we used.

6.3.1 Extracting a classical temperature

To assign a hypothetical temperature T_{hyp}, we match the classical Ising energy E_{class} of the final state $|\Psi\rangle$ of the experimental data and the Monte Carlo simulations. Its expression is:

$$E_{\mathrm{class}} = \langle \Psi | H_{\mathrm{class}} | \Psi \rangle \tag{6.6}$$

We focus on the classical energy for two reasons: (i) the energy is the variable conjugate of temperature in thermodynamics and (ii) we can measure the Ising energy on the experiment.

Measuring the classical Ising energy on the experiment. We measure the value of $E_{\text{class}}^{\text{exp}}$ on the experiment by analyzing the snapshots for each run of the experiment. In our implementation, the missing atoms are in the Rydberg states. We measure E_{class} by identifying (i) the number of missing atoms, which gives the energy associated to the longitudinal field $-\hbar \sum_{i=1}^{N} \delta_i n_i$ and (ii) the relative positions of the missing atoms, which gives the energy associated to the interactions $\sum_{i<j} \frac{C_6}{R_{i,j}^6} n_i n_j$. An example is provided in Figure 6.11 a) for the 10×10 array. The first image show the lowest energy state (for the detuning considered here): half of the atoms (50) are in the Rydberg state, and each of them are separated by a ground state atom. In the second image: (i) we count only 49 atoms in the Rydberg states, and (ii) there are 4 pairs of adjacent Rydberg atoms. We perform this analysis for each run of the experiment, and measure the resulting mean value of E_{class}.

Classical Ising energy in Monte Carlo simulations. To extract E_{class} as a function of the temperature T via Monte Carlo simulations, we estimate the classical thermodynamic partition function and compute the energy expectation value:

$$E_{\text{class}}^{\text{MC}}(T) = \sum_c H_{\text{class}}(c) e^{-\beta H_{\text{class}}(T)} / Z \tag{6.7}$$

where the sum runs over all classical spin configurations c, $\beta = 1/(k_B T)$ and $Z = \sum_c e^{-\beta H_{\text{class}}(c)}$. The hypothetical temperature T_{hyp} at the end of the sweep is then computed by matching the Monte Carlo and experimentally extracted Ising energies: $E_{\text{class}}^{\text{MC}}(T) \equiv E_{\text{class}}^{\text{exp}}$. We obtain a hypothetical temperature $T_{\text{hyp}} = 0.3U$, close to the critical temperature $T_{\text{c}} = 0.298(1)U$, extracted from finite-size extrapolations using the method described in Binder [1981]. The fact that the extracted temperature is above the AF phase does not preclude the emergence of long-range order as: (i) the system considered here is finite, and (ii) we will see below that the state of the system after the sweep is not reproduced by thermal equilibrium.
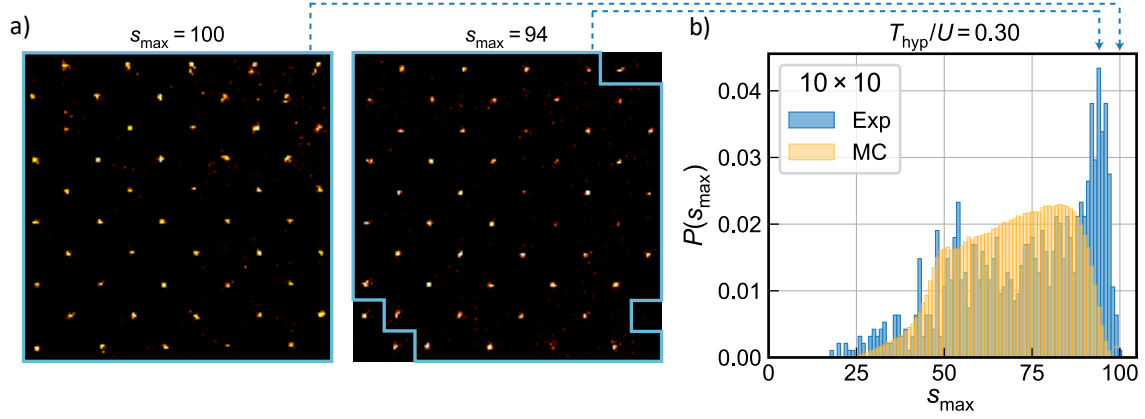
Figure 6.11: Comparison of the cluster sizes histogram between the experimental results and classical equilibrium on the 10×10 **array.** a) Fluorescence images measured at the end of the sweep on a 10×10 array illustrating how we extract the largest AF domains, here comprising 100 and 94 sites, indicated by the blue boundaries. b) Distributions of $s_{\max}$ at the end of the sweep (blue) compared with the classical equilibrium result (yellow) with the corresponding hypothetical temperature T_{hyp}.

6.3.2 Cluster size histogram

Now that we extracted the hypothetical temperature at the end of the sweep, we compare the quantum evolution and the thermal equilibrium on the distribution of the AF clusters [Stoli and Domb, 1979]. For each run of the experiment, we decompose the snapshot into individual clusters obeying local AF ordering (see examples in Figure 6.11 a)). We count the number of atoms inside each individual cluster, and record the largest size, $s_{\max}$. From the full set of snapshots, we reconstruct the probability distribution $P(s_{\max})$, see Figure 6.11 b). For a perfectly AF-ordered state, this distribution presents a single peak of unit probability at $s_{\max} = N$, while imperfect ordering shows up as a distribution broadened towards smaller $s_{\max}$. We show the results at the end of the sweep (blue) and the corresponding classical equilibrium distribution (yellow). We observe that the distributions do not match. In particular, the probability of creating larger ordered states is higher in the quantum real-time evolution than in the classical equilibrium case. We observe the same feature in the case of the triangular lattice, see Section 7.2.2. More than 27% of the shots in the experiment contain AF clusters of at least 90 sites, that is, $s_{\max} \geq 90$.

Conclusion. Our analysis reveals that despite residual imperfections, the experiment (i) does not thermalize during the state preparation protocol, and (ii) we showed

in the previous section that the system's dynamics is well reproduced by a unitary quantum mechanical real-time description. The classical equilibrium approach also results in shorter correlation lengths than the one measured.

6.4 Dynamical growth of the correlation length

In this section, we look in more details at the dynamical growth of the correlation length in the transition from the PM to the AF phase. As we deal with a second order transition, at equilibrium and for an infinite system, one would expect a divergence of the correlation length close to the critical line. In our case, because of the finite duration of the sweep, crossing a critical point leads to finite correlations in the system, which can be described by the quantum Kibble-Zurek (KZ) mechanism [Polkovnikov, 2005], theoretically investigated in the TFI model in 1D [Zurek, Dorner, and Zoller, 2005; Dziarmaga, 2005] and in 2D [Schmitt *et al.*, 2021]. This mechanism yields a universal scaling relation between the correlation length and the rate of the parameter change across the phase transition, which has been experimentally measured in 1D [Keesling *et al.*, 2019], and in 2D [Ebadi *et al.*, 2021] using a Rydberg quantum simulator. The KZ mechanism takes place in a wide variety of physical systems and describes the non-equilibrium dynamics in second-order phase transitions [del Campo and Zurek, 2013]. The quantum KZ mechanism has also been observed in Bose-Einstein condensates [Anquez *et al.*, 2016]. This scaling allows us to extract the critical exponent of the PM to AF transition, which had never been measured for the TFI model on a square, and is only known through approximate calculations.

Here, we explore the dynamical growth of the correlation length in two ways:

- We fix the sweep parameters and measure the evolution of the correlation length throughout the sweep. This is the approach we followed in Section 6.2.3 to benchmark the experimental results against simulations.

- We vary the sweep duration and measure the correlation length after crossing the phase transition.

I present here these two ways of probing the system. I will show that, on our platform, the growth of the correlation length is compatible with the KZ mechanism for a restricted range of parameters.
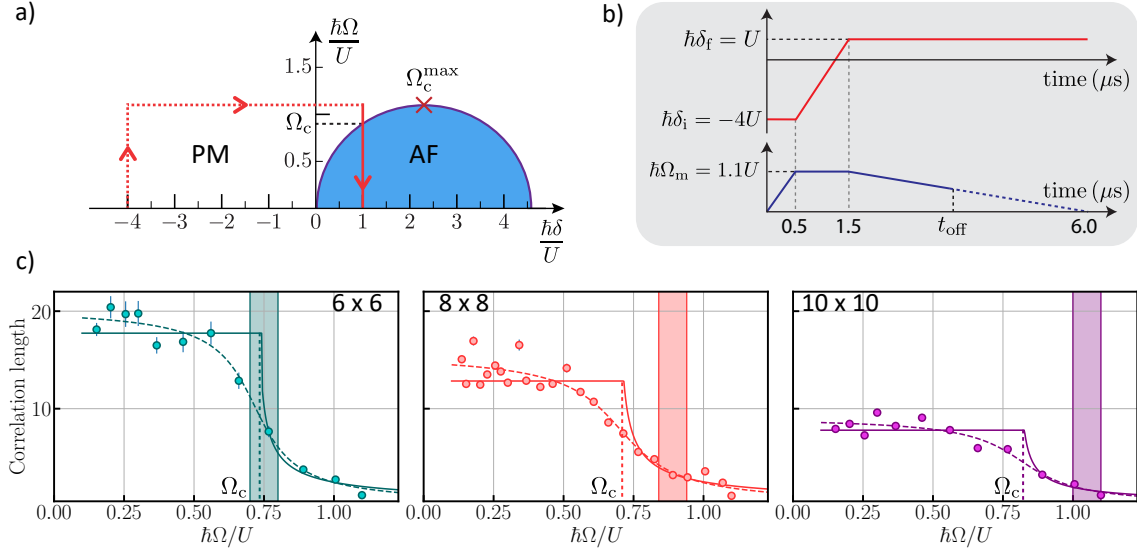
Figure 6.12: Growth of the correlation length throughout the sweep. Sweep parameters a) in the phase diagram and b) as a function of time. c) Correlation length as a function of Ω throughout the sweep, for various array sizes. The dashed lines are phenomenological fits to the data using an arctangent function. The solid lines are fits to the data using a function of the type $A(\Omega - \Omega_c)^{-0.63}$, with A and Ω_c as free parameters. The shaded regions indicate the estimated position of the AF phase apex Ω_c^{max} (which is not where we cross the critical line here), extracted from Figure 6.4.

6.4.1 Growth of the correlation length throughout the sweep

The sweep parameters, described in Section 6.2.3, are the following (see Figure 6.12 a) and b)): at a detuning $\hbar\delta = -4U$, Ω is increased from 0 to $\simeq 1.1U$ in $0.5\,\mu s$. We then sweep the detuning to $\sim U$ in $1\,\mu s$ while keeping Ω constant, and finally decrease Ω to 0 in $4.5\,\mu s$. We perform this experiment for various sizes, and record the growth of the correlation length l_{corr} throughout the sweep, by rapidly switching off the excitation lasers at various Ω during the system's evolution, see Figure 6.12 c). We show the results for the 6×6, 8×8 and 10×10 arrays, and only for sweep timings $t_{off} > 1.5\,\mu s$, in which we decrease Ω. We observe a growth of l_{corr} for Ω close to the critical point, and eventually l_{corr} saturates for low values of Ω. The solid line is a fit to the data using the expected evolution of l_{corr} with respect to the KZ mechanism, which I now briefly describe.

Evolution of the correlation length near the critical point. When the Rabi frequency Ω is tuned close to its critical value Ω_c with $\Omega > \Omega_c$, the correlation length

l_{corr} is expected to diverge algebraically with the critical exponent ν as

$$l_{\mathrm{corr}} \sim (\Omega - \Omega_c)^{-\nu}. \tag{6.8}$$

The critical exponent for the transition considered here is the one of the (2+1)D Ising model, which is not analytically known. Its value is estimated through simulations to be $\nu \simeq 0.63$ [Samajdar *et al.*, 2020].

For $\Omega > \Omega_{\mathrm{c}}$, the solid line is a fit to the data using a function of the type $A(\Omega - \Omega_c)^{-\nu}$, with A and Ω_c as free parameters. For all sizes, we observe that for low values of l_{corr}, the growth agrees well with a potential divergence near the critical point. However, we observe that the correlation length does not diverge and eventually saturates, which is expected due to the finite duration of the sweep, according to the KZ mechanism.

Kibble-Zurek mechanism. As l_{corr} increases, the relaxation time τ of the system is also expected to increase as:

$$\tau \sim (\Omega - \Omega_c)^{-z\nu}, \tag{6.9}$$

where z is the dynamical exponent which relates spatial with temporal critical fluctuations, which in the case of the (2+1)D Ising universality class is $z = 1$ [Sachdev, 2011]. Close to the critical point, an infinite amount of time is required to drive adiabatically the phase transition. As the system approaches the critical point, it freezes due to the critical slowing down, resulting in a saturation of l_{corr} [Keesling *et al.*, 2019]. The growth of l_{corr} in a KZ mechanism can be summarized as follows: far enough from the critical point, l_{corr} increases following a power law with the critical exponent of the (2+1)D Ising model, until it freezes due to the finite duration of the driving.

We indeed observe a freeze of l_{corr} on the data for Rabi frequencies $\hbar\Omega \lesssim 0.5U$. However between the two regimes expected in KZ mechanism, which are (i) a growth of $l_{\mathrm{corr}} \sim (\Omega - \Omega_c)^{-\nu}$ and (ii) a sudden saturation of l_{corr}, we observe an intermediate regime, in which l_{corr} continues to grow, which would indicate that the system does not completely follow a KZ mechanism.

6.4.2 Varying the speed at the phase transition

In order to further probe the KZ mechanism and extract the value of ν, we perform another experiment in which we vary the sweep duration, and measure the corresponding l_{corr} at the end of the sweep, similarly to the work conducted in Keesling *et al.* [2019].
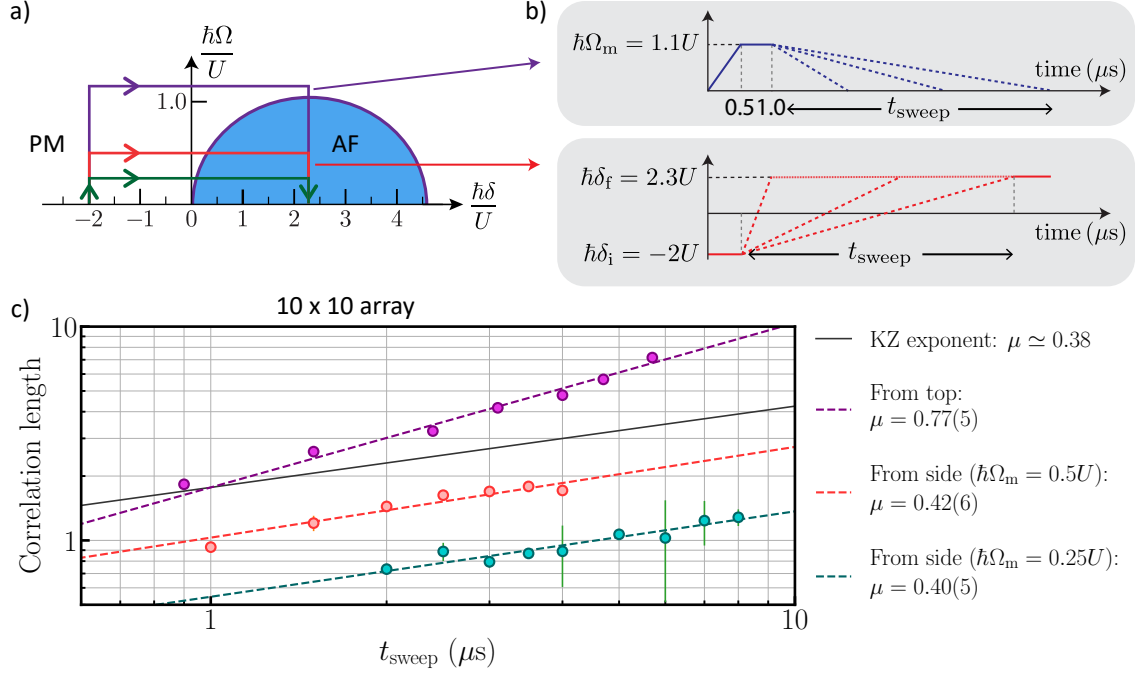
Figure 6.13: Evolution of the correlation length with the sweeping time for various sweep shapes. a) We use three different sweep shapes to probe the correlation length evolution. b) We vary the duration of the step corresponding to the crossing of the critical line. Depending on the sweep, we either (i) vary the step duration of sweeping δ (green and red), or (ii) we vary the step duration of decreasing Ω for the sweep with high Ω (purple). c) Correlation length as a function of t_{sweep}. The dashed lines are fits to the data using a power law function. The solid line represents the expected evolution for a Kibble-Zurek mechanism.

We consider a 10×10 array. We perform this experiment by entering the AF phase in three different ways, see Figure 6.13 a): (i) from the top while decreasing Ω (purple), (ii) from the side while sweeping δ with $\hbar\Omega_{\text{m}} = 0.5U$ (orange), and (iii) from the side with $\hbar\Omega_{\text{m}} = 0.25U$ (orange). In the first experiment, we vary the sweep duration t_{sweep} of the decrease of Ω, while in the two other experiments we vary the sweep duration t_{sweep} of δ, see Figure 6.13 b). The results are presented in Figure 6.13 c). We observe that in the three cases, the evolution of l_{corr} reasonably follows a power law, with various power law exponents μ. The black solid line is indicative of the expected evolution for a KZ mechanism, which I now derive.

Dynamic Kibble-Zurek exponent. We derive here the evolution of l_{corr} as a function of t_{sweep} in the case of a system governed by the KZ mechanism. As the critical line is crossed either by sweeping Ω or δ in the experiment, we define a general control

parameter λ in the below derivation. We suppose that the phase transition is located at $\lambda = 0$. In the performed experiment, the control parameter is linearly swept at a varying speed v, such that we can write $\lambda = v t_{\text{sweep}}$.

As described earlier, in a system governed by the KZ mechanism, the growth of l_{corr} diverges algebraically with the critical exponent ν, until the system's relaxation time reaches: $\tau \sim t_{\text{sweep}}$. The system's evolution is then not adiabatic any longer and l_{corr} freezes. We now derive the value of l_{corr} when the system freezes. Using Equation (6.9) and considering that $\lambda = v t_{\text{sweep}}$ and $\tau \sim t_{\text{sweep}}$, we can write $\lambda \sim v \lambda^{-z\nu}$. We thus obtain the relation between λ and v:

$$v \sim \lambda^{1+z\nu}. \tag{6.10}$$

By replacing λ in Equation (6.8), we obtain:

$$l_{\text{corr}} \sim v^{-\frac{\nu}{1+z\nu}}, \tag{6.11}$$

which can be expressed as:

$$l_{\text{corr}} \sim t_{\text{sweep}}^{\frac{\nu}{1+z\nu}} = t_{\text{sweep}}^{\mu_{\text{KZ}}}, \tag{6.12}$$

where we introduced the dynamic critical exponent $\mu_{\text{KZ}} = \frac{\nu}{1+z\nu}$. In the case of the (2+1)D Ising universality class considered here, $\mu_{\text{KZ}} \simeq 0.38$.

Comparison of the critical exponents. Now that we derived the value of μ_{KZ}, we come back to the experimental results of Figure 6.13 c). As t_{sweep} is not varied over more than a decade, we cannot really claim from these data that (i) l_{corr} follows as a power law, and that (ii) we measure a value of the power exponent. It is experimentally challenging to increase the range of t_{sweep}, as (i) smaller values of t_{sweep} would lead to vanishing correlation lengths, and (ii) higher values of t_{sweep} are prohibited due to the limited coherence of the driving.

Nevertheless, we can still compare the experimental results with the expected evolution for a KZ mechanism (black line). We observe that depending on the chosen path to enter the AF region, we obtain results which are either (i) compatible with the expected growth of l_{corr} following the KZ mechanism, when entering the AF region while sweeping δ, and (ii) incompatible when entering from the apex of the AF region. In the latter case, the growth of l_{corr} still follows a power law even though the power exponent is not the expected one.

This discrepancy could be explained by the fact that the KZ mechanism is expected
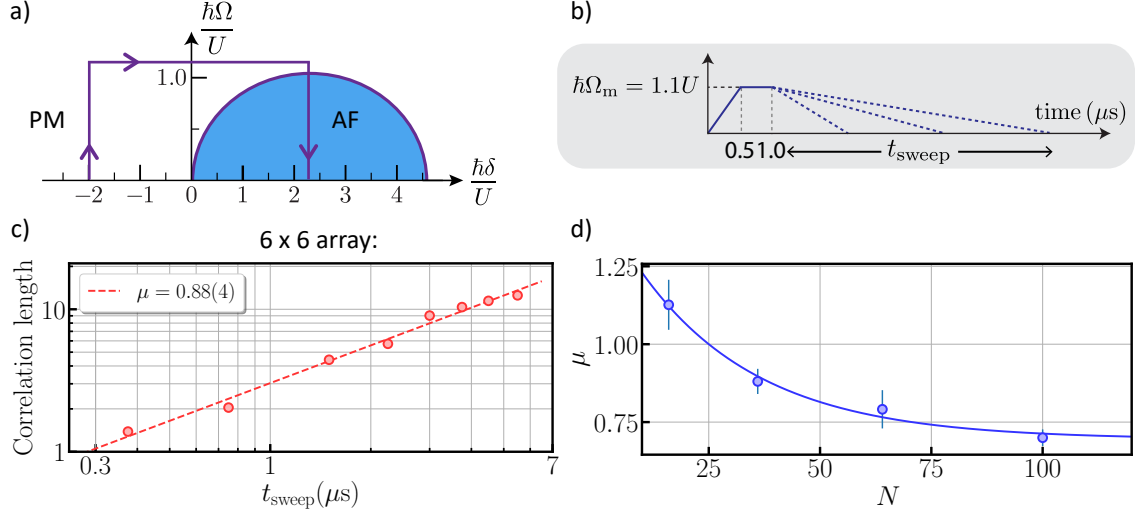
Figure 6.14: Power law exponent when entering the AF region from its apex for various array sizes. a) Sweep path in the phase diagram and b) the corresponding time evolution of Ω. We vary the sweeping time t_{sweep} of Ω when crossing the critical line. c) Results for the 6×6 array. The dashed line is a fit to the data using a power law, from which we extract the power exponent $\mu = 0.88(4)$. d) μ as a function of the number of atoms N. The solid line is a phenomenological fit to the data using an exponential decaying function, which would indicate that even for $N \to \infty$, the power law exponent is far from $\mu_{\text{KZ}} \simeq 0.38$.

to be valid only for a high number of particles, such that we have not considered here big enough arrays. We show however in the following that the array size is not the problem.

Size-dependent critical exponent. We measure the critical exponent as a function of the array size N, when crossing the critical line from the AF region apex. The sweeps parameters, shown in Figure 6.14 a) and b), were previously described. We vary the sweep duration t_{sweep} of the decrease of Ω. We perform the experiment on 4×4, 6×6, 8×8 and 10×10 arrays. For each size, the growth of l_{corr} follows reasonably well a power law, as shown for the 6×6 array in Figure 6.14 c). We observe a decrease of the power law exponent with N. The solid line is a fit to the data using an exponential function, from which we extract $\mu(N \to \infty) = 0.68(4)$, which is far from the expected KZ exponent $\mu_{\text{KZ}} \simeq 0.38$. These experiments would indicate that, even for $N \to \infty$, the growth of l_{corr} is not following the KZ mechanism. This experiment should be conducted on larger arrays to verify the observed scaling of μ with N.
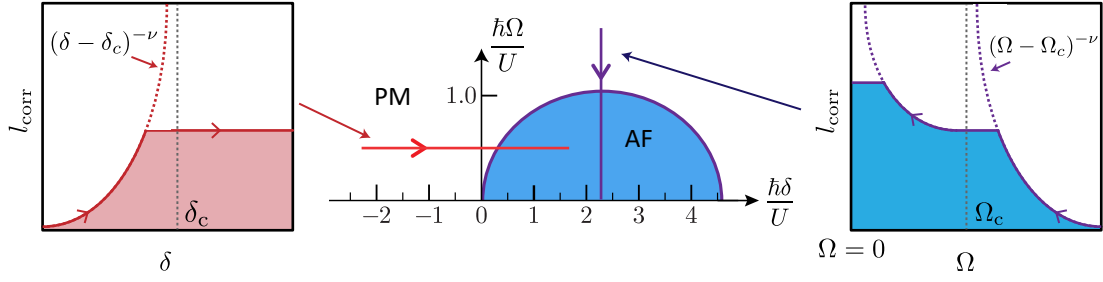
Figure 6.15: Qualitative difference between the two experiments: crossing the critical line while sweeping δ or Ω. When crossing the critical line while sweeping δ (red), the growth of the correlation length follows the Kibble-Zurek law. When crossing the critical line while sweeping Ω (blue), the system experiences two divergences of l_{corr}: at the critical point, and when $\Omega \to 0$.

Entering the AF phase from the side or from the top. I discuss here another explanation for the different measured exponents between sweeping δ or Ω to enter the AF phase, sketched in Figure 6.15. For various δ, l_{corr} diverges at the critical point and then saturates, according to the KZ mechanism. However, when sweeping Ω, l_{corr} is expected to diverge twice:

- At $\Omega = \Omega_{\mathrm{c}}$, where the system experiences the KZ mechanism.

- At $\Omega = 0$: the system's ground states for $\Omega = 0$ exhibits an infinite correlation length.

In the experiments presented in this subsection, we always measured the value of l_{corr} at $\Omega = 0$. The evolution of l_{corr} might thus be related to both the growth of l_{corr} at $\Omega = \Omega_{\mathrm{c}}$ and at $\Omega = 0$. In order to check this hypothesis, one should perform again the above experiments and set the final value of Ω just below the critical value rather than $\Omega = 0$.

Conclusions. In this section, I presented an analysis of the correlation length growth across the phase transition. We observe a growth which is compatible with a Kibble-Zurek mechanism, also observed in Ebadi *et al.* [2021] for the same range of parameters. We also observed that this compatibility strongly depends on the chosen parameters. Recent numerical investigations show that the KZ mechanism in the 2D TFI model on a square lattice is still debated [Schmitt *et al.*, 2021]. Further experimental investigations are required to understand under which assumptions the KZ mechanism describes the system's dynamics.

6.5 Conclusion

In this chapter, I presented various experimental investigations of the 2D transverse field Ising model in square geometry. I showed that we are able to produce highly antiferromagnetically ordered states on arrays containing up to 196 atoms, which is beyond what can be exactly simulated classically. We have validated the experimental results with comprehensive numerical simulations up to computationally feasible sizes, and showed that the results cannot be reproduced by thermal equilibrium. Finally, I presented a study of the dynamical growth of the correlations in the system, showing a compatibility with a Kibble-Zurek mechanism depending on the parameters. These results demonstrate that our platform is now able to study quantum spin models in regimes beyond those accessible via numerical investigations.

Transverse field Ising model on triangular lattices

Contents

In this chapter, I will focus on the quantum simulation of the 2D Transverse Field Ising (TFI) model in triangular arrays. The model's phase diagram is richer than in the square lattice, and features strong geometric frustration. The effect of geometric frustration on spin systems is an active research field both on the theoretical side [Balents, 2010] and on the experimental side with its exploration on various synthetic platforms, such as trapped ions [Kim *et al.*, 2010], or ultracold atoms in optical lattices [Becker *et al.*, 2010; Jo *et al.*, 2012]. The TFI model is not analytically solved, and the system's properties are only known through approximate calculations. Furthermore, the strong geometric frustration exhibited by the model limits the numerical methods which can be used to explore the system [Henelius and Sandvik, 2000]. In the spirit of what was presented in Section 5.2.2, I will start by giving an intuition for the model's phase diagram on the simplest case of 3 atoms. I will

then explore experimentally the phase diagram, compare the results with simulations involving up to $N = 108$ atoms, and study the dynamical growth of the correlations in the system at the phase transitions. I will finish by showing first signatures of the model's highly frustrated phase. The experiments presented here are similar to the one conducted for the 2D TFI model on the square lattice (see Chapter 6). Part of the results presented in here are published in Scholl *et al.* [2021a].

7.1   Introduction to the triangular lattice phase diagram

We consider N atoms placed on a triangular lattice with spacing a, and coupled by the (repulsive) van der Waals interaction. The atoms are initially placed in the $|\downarrow\rangle = |5S_{1/2}, F = 2, m_F = 2\rangle$ state, and are coupled to the Rydberg state $|\uparrow\rangle = |75S_{1/2}, m_J = 1/2\rangle$ via a laser field with Rabi frequency Ω and detuning δ. In these conditions, the implemented Hamiltonian H_{Ryd} reads:

$$H_{\mathrm{Ryd}} = \frac{\hbar\Omega}{2} \sum_{i=1}^{N} \sigma_i^x - \hbar\delta \sum_{i=1}^{N} n_i + \sum_{i<j} \frac{C_6}{R_{i,j}^6} n_i n_j, \tag{7.1}$$

where $n = (1 + \sigma^z)/2$ is the Rydberg density operator, σ^x and σ^z are the usual Pauli matrices, $R_{i,j}$ is the distance between atom i and j and $C_6 \simeq 1942\,\mathrm{GHz}.\mu\mathrm{m}^6$ is the van der Waals coefficient. Ω and δ act as effective transverse and longitudinal fields (see Section 5.2.1). We set $a = 10\,\mu\mathrm{m}$, leading to a nearest-neighbor interaction energy $U \simeq 1.87\,\mathrm{MHz}$ (see Section 6.2.2).

7.1.1 A three atom toy model

To characterize the system's phase diagram, we start with the simplest case of three spins placed on the vertices of an equilateral triangle with side length a.

Ground states without transverse field.   The energy spectrum as a function of δ is shown in Figure 7.1 a) in the absence of transverse field ($\Omega = 0$). There exist three different types of ground states depending on δ:

- For $\hbar\delta < 0$ ($\hbar\delta > 2U$), the ground state is $|\downarrow\downarrow\downarrow\rangle$ ($|\uparrow\uparrow\uparrow\rangle$). The spins align along the effective longitudinal field. This behavior is the signature of a paramagnet (PM).
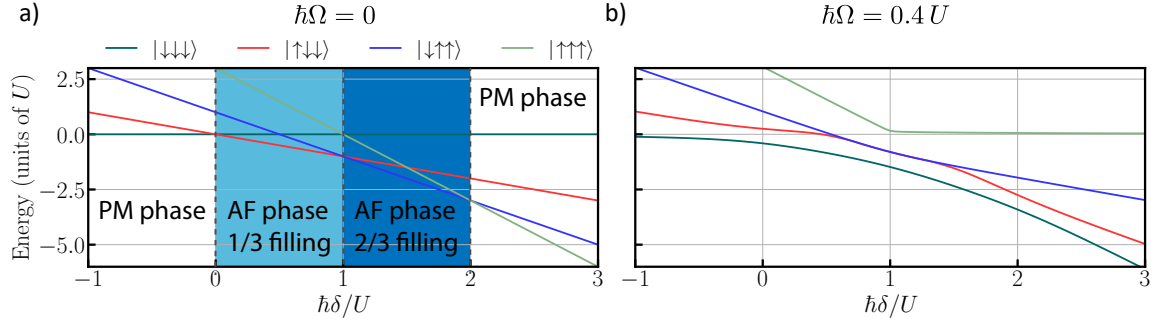
Figure 7.1: Energy diagram for three atoms. a) Energy diagram for $\Omega = 0$. There exist two antiferromagnetic phases: (i) for $0 < \hbar\delta < U$, the ground states are two spins down and one spin up, giving a Rydberg density of 1/3, and (ii) for $0 < \hbar\delta < U$, the ground states are two spins up and one spin down, giving a Rydberg density of 2/3. b) Energy diagram for $\hbar\Omega = 0.4U$. The degeneracies at $\hbar\delta = 0, 1, 2\,U$ are lifted.

- For $0 < \hbar\delta < U$, the ground states are $|\uparrow\downarrow\downarrow\rangle$, $|\downarrow\uparrow\downarrow\rangle$ and $|\downarrow\downarrow\uparrow\rangle$ (red line). We gather these states under the notation $AF_{1/3}$. One spin is anti-aligned with respect to the other ones. The system behaves as an antiferromagnet (AF), with a Rydberg fraction equals to 1/3.

- For $U < \hbar\delta < 2U$, the ground states are $|\downarrow\uparrow\uparrow\rangle$, $|\uparrow\downarrow\uparrow\rangle$ and $|\uparrow\uparrow\downarrow\rangle$ (blue line). We gather these states under the notation $AF_{2/3}$. As in the region $0 < \hbar\delta < U$, one spin is anti-aligned with respect to the other ones. The system behaves as an antiferromagnet (AF), with a Rydberg fraction equals to 2/3.

The system exhibits a peculiar behavior for $\hbar\delta = U$, where the mean Rydberg fraction is 1/2. The system cannot simultaneously minimize the interaction energy for each pair, resulting in a "macroscopic" ground-state degeneracy: out of the $2^3 = 8$ states, 6 are degenerate. This property is related to geometric frustration, which is discussed below.

Effect of the transverse field. We now add the transverse field. The energy diagram for $\hbar\Omega = 0.4U$ is presented in Figure 5.3 b). The ground state degeneracy at $\hbar\delta = 0$, $\hbar\delta = U$ and $\hbar\delta = 2U$ is lifted, an energy gap E_{gap} appears between the ground state and the first excited state. In particular, at $\hbar\delta = U$, the "macroscopic" ground-state degeneracy is lifted. The ground state exhibits an interesting symmetry: $\forall\,\Omega \neq 0$, the weights of the wavefunction on $AF_{1/3}$ and $AF_{2/3}$ are equal (in absolute value). The ground state thus contains a superposition of $AF_{1/3}$ and $AF_{2/3}$. This property is

related to a process called "Order By Disorder" (OBD) [Villain, J. *et al.*, 1980], which is discussed in Section 7.3.2.

In the limit $\hbar\Omega \gg U$, the system's ground state is $|\leftarrow\leftarrow\leftarrow\rangle$. The spins align along the effective transverse field, which is again a PM behavior.

Conclusions. From the above analysis with three atoms, we conclude that there are two possible ground state behaviors in the model: (i) paramagnetic (PM) ground states, for which the spins align along the effective magnetic field, and (ii) antiferromagnetic (AF) ground states, for which the spins are anti-aligned. The various ground states of the model are thus very close to the one of the chain (see Section 5.2) and the square lattice (see Section 6.1). However, the AF ground states are separated into two phases, with Rydberg fractions 1/3 and 2/3. Frustration shows up for $h\delta = U$ where the Rydberg fraction is 1/2.

7.1.2 Phase diagram of the infinite lattice

We now consider the case of an infinite triangular lattice, and first assume that the interactions only act between the nearest neighbors. The effects of the interactions beyond nearest neighbors are discussed below, and the effects of finite size are studied in Section 7.2.1. The infinite triangular lattice exhibits three underlying sublattices, sketched in Figure 7.2 a), referred in the following as sublattices A, B and C. The system's ground states are qualitatively the same as in the case of three spins. For $\Omega = 0$, the PM phase ground states are $|\downarrow\downarrow \dots \downarrow\downarrow\rangle$ and $|\uparrow\uparrow \dots \uparrow\uparrow\rangle$. The AF phase at 1/3 Rydberg density exhibits three degenerate ground states, corresponding to Rydberg excitations on one of the three sublattices. The second AF phase with Rydberg density 2/3 is the "particle–hole" inverse, with two sublattices being fully excited and one sublattice containing ground-state atoms. We refer to these two phases as the 1/3 and the 2/3 phases in the following. In between these phases, at 1/2 filling, another phase exists at finite Ω, stabilized by the OBD process [Moessner, Sondhi, and Chandra, 2000; Moessner and Sondhi, 2001; Isakov and Moessner, 2003]. We refer to this as the OBD phase in the following, which is also called "clock phase" in the literature. The characterization of the OBD will be discussed in Section 7.3.2.

Extension of the phases. In the absence of transverse field ($\Omega = 0$), the extension of the AF region is set by the total interaction strength U_{m} felt by one atom. As each atom has six neighbors, $U_{\mathrm{m}} = 6U$ and the AF region extends over $0 < \hbar\delta < 6U$.
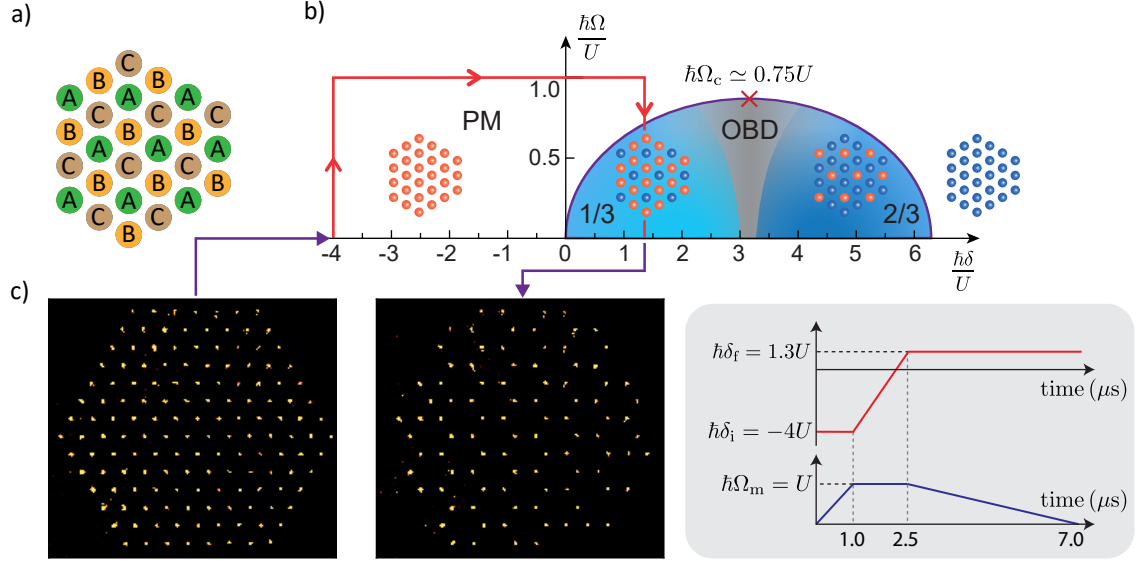
Figure 7.2: Reaching the 1/3 antiferromagnetic phase of the TFI model on a triangular lattice. a) Sketch of the tripartite triangular lattice. b) Phase diagram of the infinite system, displaying four phases: a paramagnetic phase (PM), two antiferromagnetic phases with 1/3 and 2/3 Rydberg density, and the order-by-disorder (OBD) phase. c) Fluorescence images of a 147-atom array before (left) and after (right) performing the sweep whose timings are displayed in the panel. The missing atoms are in the $|\uparrow\rangle$ state while the detected atoms are in the $|\downarrow\rangle$ state. Almost all of the missing atoms belong to one specific sublattice.

Inside the AF region, the 1/3 phase extends over $0 < \hbar\delta < 3U$ and the 2/3 phase over $3U < \delta < 6U$. For $\Omega > 0$, the critical line follows a "dome" shape, with its apex located at $(\hbar\Omega_c \simeq 0.82U, \hbar\delta_c = 3U)$. The value of Ω_c is estimated from Monte-Carlo simulations [Isakov and Moessner, 2003].

Effect of long-range interactions. Due to the $1/R^6$ decay of the van der Waals interaction, the interactions extend beyond the nearest neighbors. We obtain $\hbar U_m \simeq 6.3U$, such that the extension at $\Omega = 0$ of the 1/3 phase is $0 < \hbar\delta \lesssim 3.15U$ and the 2/3 phase is $3.15U \lesssim \hbar\delta \lesssim 6.3U$. The size of the AF region in Ω is also altered by the long range interactions, with its apex located at $(\hbar\Omega_c \simeq 0.75U, \hbar\delta_c \simeq 3.15U)$. The value of Ω_c including the long-range interactions has been calculated very recently using Monte-Carlo simulations [Koziol *et al.*, 2019]. The corresponding phase diagram of H_{Ryd} is drawn in Figure 7.2 b).

7.1.3 Experimental implementation

We explore the triangular phase diagram by considering hexagonal clusters of various sizes, built shell by shell around a central three atom triangle (see Figure 7.2). We use this shape because of its compactness: for the same number of atoms N, the width of hexagonal clusters is smaller than the width of a triangle. The reduced width improves the efficiency of the assembling process (see Section 4.2.1) and limits the imperfections due to the finite size of the excitation beams (see Section 6.2.2). The number of ground states in the 1/3 phase is lower using hexagonal clusters as compared to triangular clusters (see Section 7.2.1).

Typical experimental sequence.   As performed for the TFI in square lattices, we probe the phase diagram of H_{Ryd} by sweeping Ω and δ over time, starting in the PM phase ($\delta < 0$) and reaching the AF phase (see red arrow in Figure 7.2 b)). We initialize the system by optical pumping (see Section 2.2.2) in the state $|\downarrow\downarrow \ldots \downarrow\downarrow\rangle$, which is the ground state for $\delta < 0$. We aim at adiabatically driving the system such that it remains in the instantaneous ground state at all time. However, the energy gap E_{gap} between the ground state and the first excited state vanishes when crossing the critical line. The PM to 1/3 phase is expected to be a first order transition [Janke and Villanova, 1997], which implies $E_{\mathrm{gap}} \propto e^{-\alpha N}$ [Laumann *et al.*, 2015]. In order to limit the transfer to highly excited states, the sweeps are designed to cross as slowly as possible the critical line, but keeping them short enough to avoid strong decoherence effects (see Section 6.2.1). The typical sweep parameters, presented in Figure 7.2 c), are the following:

- We start with a detuning $\hbar\delta_{\mathrm{i}} = -4\,U$, deep in the PM phase. We ramp up the Rabi frequency to reach $\hbar\Omega_{\mathrm{m}} = U$ in $1.0\,\mu$s.

- We then sweep the detuning to reach $\hbar\delta_{\mathrm{f}} = 1.3\,U$ in $1.5\,\mu$s.

- We finally decrease the Rabi frequency down to zero in $4.5\,\mu$s. This step is longer than the other to cross the critical line as slowly as possible.

We perform this sweep and measure the state of the atoms at the end of the procedure. An example of fluorescence images for a 147-atom array before (left) and after (right) the sweep is provided in Figure 7.2. The missing atoms in the image corresponds to atoms in the $|\uparrow\rangle$ state while the detected atoms are in the $|\downarrow\rangle$ state (see Section 2.3.2). Starting with a fully-loaded array of atoms in $|\downarrow\rangle$, we observe that $\sim 1/3$ of the atoms

are in the $|\uparrow\rangle$ state at the end of the sweep. The missing atoms are mainly positioned on one of the three sublattices. This shows that we can produce highly AF ordered states in the 1/3 phase.

We repeat the process typically ~ 1000 times. To characterize the AF ordering of the prepared states at the end of the sweep, we compute the various quantities presented in Figure 7.3 for two system sizes: a 48-atom array and a 147-atom array. I now present those various observables.

Staggered magnetization. The first observable is the order parameter of the PM to AF phase transition, which is the normalized *staggered magnetization* $m_{\text{stag}} = \langle|n_A + n_B e^{2i\pi/3} + n_C e^{4i\pi/3}|\rangle/(N/3)$ [Isakov and Moessner, 2003], giving the difference in the number of Rydberg excitations on the three sublattices A, B and C, defined above. The three perfect AF states correspond to one of the three sublattices being fully excited, such that $m_{\text{stag}} = 1$. We visualize the shot-wise contributions to m_{stag} in the complex plane using a 2D histogram, see Figure 6.2 a). The three ground states would appear as points on the hexagon vertices along the three directions $n_{A,B,C}$. For both systems, we observe a triangular distribution of m_{stag} pointing towards the three above-mentioned vertices. For the 48-atom array, we observe a conglomeration of points around these three corners, which would indicate that the quality of the AF ordering is higher for the 48-atom array than for the 147-atom array.

Connected spin-spin correlations. The second observable is the normalized connected spin–spin correlation function, defined as:

$$C_{k,l} = \frac{9}{2N_{k,l}} \sum_{i,j} \langle n_i n_j \rangle - \langle n_i \rangle \langle n_j \rangle, \qquad (7.2)$$

where the sum runs over all pairs of atoms i and j separated by $k\boldsymbol{e_1} + l\boldsymbol{e_2}$, with $\boldsymbol{e_1}$, $\boldsymbol{e_2}$ denoting the two vectors of the underlying lattice, k and l are two integer numbers, and $N_{k,l}$ being the number of such pairs. As compared to the square lattice case, the maximum value of $C_{k,l}$ is not the same for positive and negative correlations. We choose the normalization factor 9/2 such that the perfect AF state would have $C_{k,l} = 1$ for correlated sites and $C_{k,l} = -1/2$ for anticorrelated sites. The $C_{k,l}$ correlation maps of the 48-atom array and the 147-atom array are shown in Figure 6.2 b). In both cases, we observe a pattern characteristic of three-sublattice ordered states, where atoms belonging to the same sublattice are positively correlated (red), and anticorrelated (blue) otherwise. We also reconstruct the corresponding normalized 1D correlations
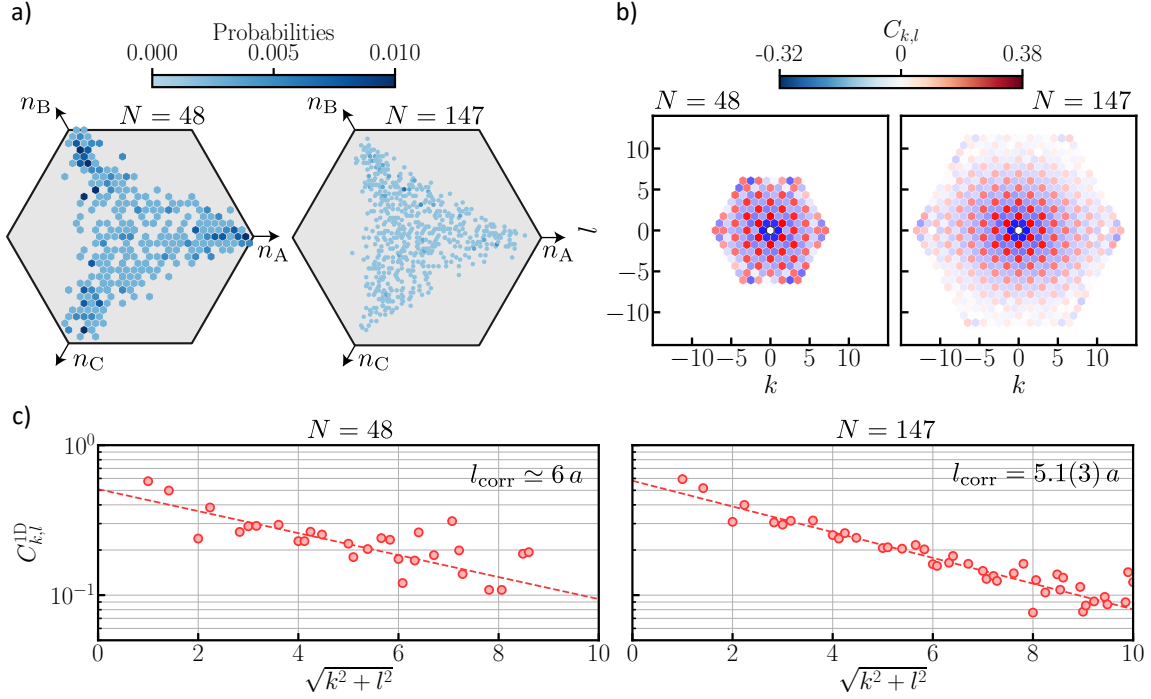
Figure 7.3: Characterization of the 1/3 AF phase for the 48-atom and 147-atom triangular arrays. We perform the sweep described in Figure 7.2 and characterize the AF ordering of the obtained states by looking at: a) the staggered magnetization histograms plotted in the complex plane, b) the correlations maps and c) the 1D correlations. We extract from the latter results a correlation length $l_{\mathrm{corr}} \simeq 6\,a$ for the 48-atom array, and $l_{\mathrm{corr}} = 5.5(1)\,a$ for the 147-atom array.

$C_{k,l}^{1D}$ (see Figure 6.2 c)) in the following way: (i) if the two atoms belong to the same sublattice, $C_{k,l}^{1D} = C_{k,l}$ and (ii) if the two atoms do not belong to the same sublattice, $C_{k,l}^{1D} = -2C_{k,l}$. This allows us to normalize the correlations for both correlated and anti-correlated sites. In both cases, we observe an exponential decay of the correlations, from which we extract a typical correlation length $l_{\mathrm{corr}} \simeq 6\,a$ for the 48-atom array and $l_{\mathrm{corr}} = 5.1(3)\,a$ for the 147-atom array, a being the lattice spacing. The correlation lengths for both systems are very close, which is surprising considering the closing of the energy gap with the number of atoms $E_{\mathrm{gap}} \propto e^{-\alpha N}$. This could be due to (i) the system's boundaries (discussed below) and (ii) the fact that the exponential closure of the gap is expected near the thermodynamic limit and might not be valid considering the number of atoms we use, as discussed in Section 7.2.3.

Conclusion. The results presented above show that we are able to produce highly AF ordered states on triangular lattices with system sizes as large as $N = 147$. Contrarily

to what has been measured in the case of the square lattice (see Section 6.1.2), we observe that the quality of the prepared AF ordering hardly depends on N.

Hence, we are able to probe the TFI model phase diagram on triangular lattices with arrays containing up to $N = 147$ atoms, which we now explore in more detail.

7.2 Characterization of the 1/3 phase

In this section, we focus on the exploration and the characterization of the 1/3 phase. The 1/3 phase is the analogue of the AF phase on the square lattice, where neighboring sites cannot be excited simultaneously, leading to one of the three sublattices being filled with Rydberg excitations. The investigations presented here are close to the one performed in Chapter 6. We first detail the effect of the finite size, compare the experimental results to simulations, and finally study the dynamical growth of the correlations.

7.2.1 Finite-size effects

As discussed in Section 6.1.3, the finite size effects can be divided into two contributions: (i) the limited number of atoms and (ii) the open boundaries. Their impact on the 1/3 phase is discussed now. We consider a 75-atom array.

Effect of open boundaries on the 1/3 phase. We explore the effect of open boundaries on the 1/3 phase using the sweep described in Figure 7.4 a) and vary the final detuning δ_f. For an infinite system, the AF ordering would not depend on the final detuning (in the range $0 < \hbar\delta < 3.15U$). However, for the array considered here, we observe that the value of m_{stag} strongly varies inside the AF phase (see Figure 7.4 b)) and is maximum in the range $1.3U < \hbar\delta_f < 2.2U$. By comparing the value of m_{stag} between the whole system (green) and in the bulk (red), we observe a substantial difference in m_{stag}, indicating that boundary effects have an impact on the quality of the AF ordering.

In order to understand why the AF ordering is low for $\hbar\delta_f > 2.2U$, we compute the mean Rydberg density $\langle n \rangle$ as a function of δ_f, see Figure 7.4 c). For an infinite system, we would expect $\langle n \rangle = 1/3$ in the whole phase (dashed line). We indeed observe a plateau at 1/3, but its extension is limited to $0.8U \lesssim \hbar\delta_f \lesssim 2.2U$. For $\hbar\delta_f > 2.2U$, $\langle n \rangle > 1/3$ which thus induces a reduction of m_{stag} as at least two sublattices are filled.
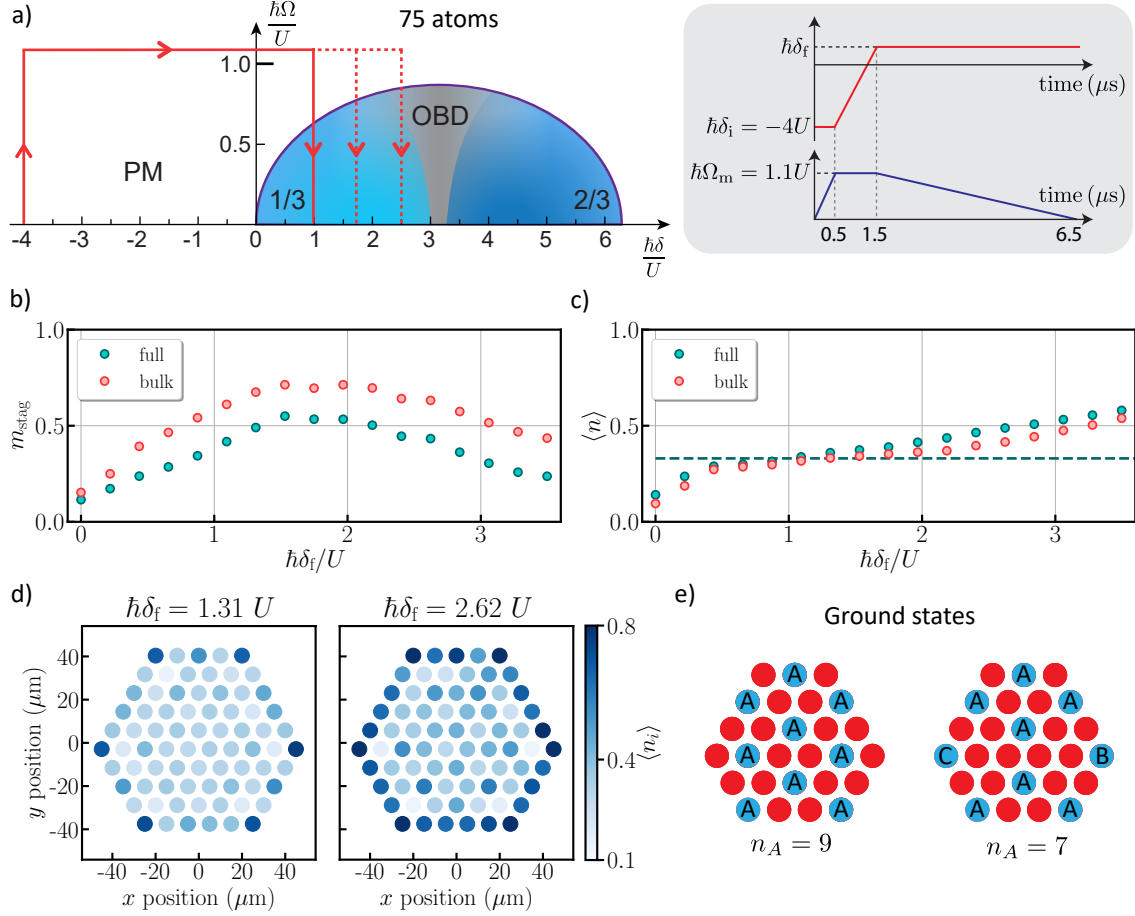
Figure 7.4: Effect of open boundaries on a 75-atom array. a) Parameters of the experiment in the phase diagram and the corresponding temporal evolution of δ and Ω. We vary the final detuning δ_f. b) m_stag as a function of δ_f, considering the full system (green) and only the bulk (red). The quality of the prepared antiferromagnet is maximum for $1.3U < \hbar\delta_\mathrm{f} < 2U$. The value of m_stag is higher in the bulk, indicating that edge effects reduce the value of m_stag. c) Mean Rydberg density $\langle n \rangle$ as a function of δ_f. We observe a plateau at $\langle n \rangle = 1/3$ for $0.8U \lesssim \hbar\delta_\mathrm{f} \lesssim 2.2U$. d) Rydberg density per atom for $\hbar\delta_\mathrm{f} = 1.31U$ and $\hbar\delta_\mathrm{f} = 2.62U$. The Rydberg density on the edges is higher than in the bulk. e) Sketch of the edge effects on the AF ground states. The number of ground states is higher than 3, which reduces the value of m_stag.

As discussed in Section 6.1.3, the increase of Rydberg density in the AF phase is due to the open boundaries. The atoms on the edges have less neighbors, meaning that the total interaction energy U_{m} felt by these atoms is lower than $6.3U$: $U_{\mathrm{m}} \simeq 4.2U$ for the atoms on the side, and $U_{\mathrm{m}} \simeq 3.1U$ for the atoms in the corners. As the extension of the 1/3 phase is $U_{\mathrm{m}}/2$, the edges are in the 1/3 phase for $\hbar\delta_{\mathrm{f}} \lesssim 2.1U$. We check this experimentally by looking at the Rydberg density map $\langle n_i \rangle$ for two values of final detuning: $\hbar\delta_{\mathrm{f}} = 1.31U$ and $\hbar\delta_{\mathrm{f}} = 2.62U$, see Figure 6.3 d). In the bulk of the system, $\langle n \rangle \sim 1/3$ as expected. However, for $\hbar\delta_{\mathrm{f}} = 2.62U$ the Rydberg density is large on the edges ($\langle n_i \rangle \sim 0.7$). In the next subsections, we will remain in the region $\hbar\delta_{\mathrm{f}} \lesssim 2.1U$ in order to avoid this effect due to open boundaries.

The effect of open boundaries described above is the same as in the case of the square lattice. However, another effect arises which only occurs for triangular lattices: the number of ground states is increased by the open boundaries. An example is provided in Figure 7.4 e), in which we show two ground states: (i) one in which the sublattice A is fully filled, compatible with the infinite-system ground state, and (ii) one in which the Rydberg excitations are in the left and right corners rather than filling sublattice A. There is thus 4 possible ground states for each sub-lattice, giving a total of 12 ground states instead of three. This induces a higher Rydberg fraction in the corners, which we experimentally observe on the Rydberg density map for $\hbar\delta_{\mathrm{f}} = 1.31U$. The ground state multiplicity reduces the value of m_{stag}: even if the sweep were fully adiabatic, we would not obtain $m_{\mathrm{stag}} = 1$ due to edge effects.

Hexagonal clusters are more robust against open boundaries than other geometries. As a comparison, the use of triangle clusters implies that (i) the corners get excited for lower values of δ_{f} as they have only two nearest neighbors, and (ii) the number of ground state at 1/3 filling is higher (at least 26 for all sizes, and 28 when considering $N = 36$ [Lienhard *et al.*, 2018]).

Location of the 1/3 phase in the phase diagram. Now that we discussed the effect of open boundaries on the AF ordering at the end of the sweep, we move to the study of the critical line position. In the case of the square lattice, we observed that the apex of the critical line $\Omega_{\mathrm{c}}^{\mathrm{max}}$ strongly depends on the number of atoms N (see Section 6.1.3), and estimated that $\Omega_{\mathrm{c}}^{\mathrm{max}}$ is close to the infinite-system one for $N \sim 200$. We show here that the triangular lattice does not seem to behave in the same way. The critical line apex for $N = 75$ is already close to the infinite-system one, located at $\hbar\Omega_{\mathrm{c}}^{\mathrm{max}} \simeq 0.75U$ [Koziol *et al.*, 2019].

In order to estimate the position of the critical line, we perform the same sweeps as
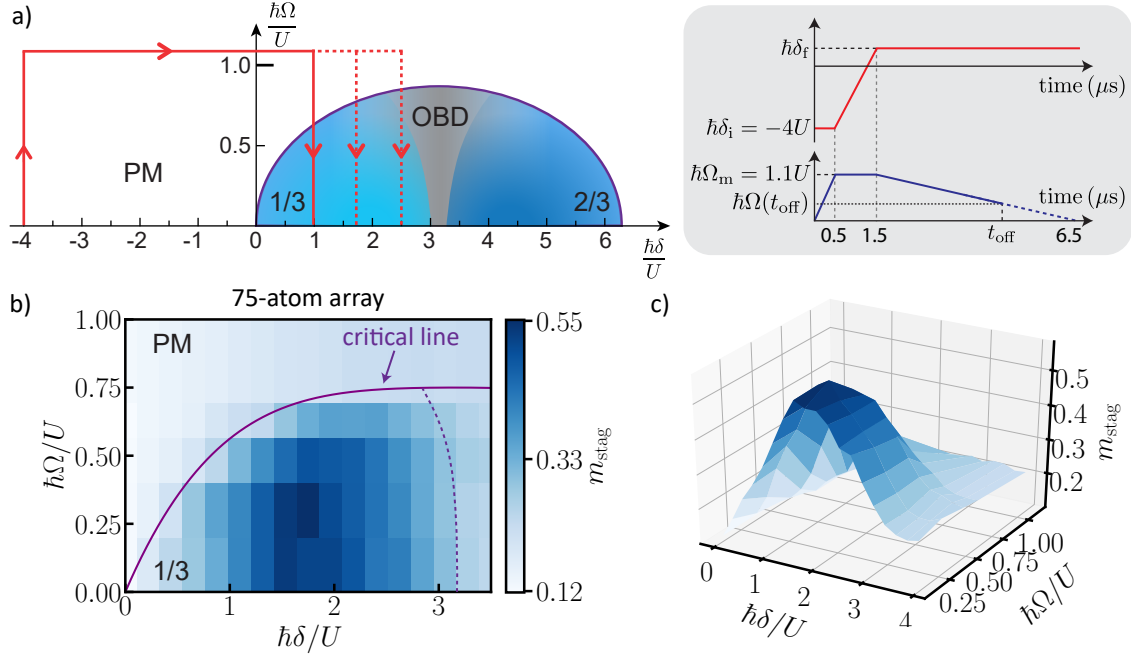
Figure 7.5: Location of the 1/3 phase for the 75-atom array. a) Parameters of the performed experiment in the phase diagram and the corresponding temporal evolution of δ and Ω. We vary the final detuning δ_{f} and measure m_{stag} for various times t_{off} throughout the sweep. b-c) m_{stag} as a function of Ω and δ in 2D and in 3D. The solid line is a fit of the critical line using a biquadratic function. We observe a good agreement with the expected apex of the AF phase $\hbar\Omega_{\mathrm{c}} \simeq 0.75U$ [Koziol *et al.*, 2019]. The dashed line is indicative of the position of the critical line which separates the 1/3 phase from the order-by-disorder phase (probed in Section 7.3.2).

described above (see Figure 7.5 a)). We measure m_{stag} for various values of $\Omega(t_{\mathrm{off}})$ throughout the sweeps by rapidly switching off the excitation lasers at various times t_{off}. We repeat this process for various δ_{f}. We thus obtain the value of m_{stag} in the phase space (Ω, δ). The results are presented in Figure 7.5 b) as a 2D plot and c) as a 3D plot. This experiment maps the 1/3 phase in the phase diagram: the value of m_{stag} in the PM is low (white), and high in the 1/3 phase (blue). The solid line is a fit of the critical line position using a biquadratic function, which is performed by (i) fixing $\hbar\Omega_{\mathrm{c}}^{\mathrm{max}} = 0.75U$ at $\hbar\delta_{\mathrm{c}}^{\mathrm{max}} = 3.15U$, (ii) fixing $\hbar\Omega_{\mathrm{c}} = 0$ for $\hbar\delta_{\mathrm{c}} = 0$, and (iii) fitting the data where $m_{\mathrm{stag}} \simeq 0.2$. We use a biquadratic function because it describes well the numerically calculated position of the critical line in the 1D TFI model, see Section 5.2.2. This fit describes well the boundaries of the 1/3 phase, which would indicate that the value of $\Omega_{\mathrm{c}}^{\mathrm{max}}$ is already close to the one of the infinite system for $N = 75$. This is also confirmed by performing the experimental protocol we used for

the square lattice, described in Section 6.1.3, from which we obtain $\hbar\Omega_\mathrm{c}^\mathrm{max} \simeq 0.70(5)\,U$. The dashed line is indicative of the position of the critical line which separates the 1/3 phase from the order-by-disorder phase (probed in Section 7.3.2).

Comparison with the square lattice. The results presented in this subsection are close to the one derived for the square lattice in Section 6.1.3. The boundaries reduce the range in δ_f over which we obtain strong AF ordering. However, there are two differences with the square lattice case: (i) the boundaries effect on the 1/3 phase impacts more the quality of the prepared AF because it induces an increase in the number of AF ground states and (ii) the critical line position is close to the infinite system already for $N = 75$. We now compare the experimental results to simulations.

7.2.2 Comparison with simulations

I showed above that we are able to probe the 1/3 phase, and prepare highly AF ordered states on systems with up to $N = 147$ atoms. In order to benchmark the validity of the results, we compare the experimental results with simulations, as we did in square lattices (see Section 6.2). We compare the experimental results to Matrix Product States (MPS) simulations on arrays with up to $N = 108$ atoms. We also compare the results to classical Monte Carlo (MC) simulations, and show that the results are not reproduced by thermal equilibrium. The simulations were performed by the team of A. Läuchli.

Comparison with MPS simulations. We first compare the experimental data to MPS simulations on the growth of AF ordering throughout the sweep for a 75-atom array. The sweep parameters (see Figure 7.6 a)) are the following. At a detuning $\hbar\delta = -4U$, Ω is increased from 0 to $\hbar\Omega_\mathrm{m} \simeq U$ in $1\,\mu\mathrm{s}$. We then sweep the detuning to $\sim 1.3\,U$ in $1.5\,\mu\mathrm{s}$ while keeping Ω constant, and finally decrease Ω to 0 in $5\,\mu\mathrm{s}$. We measure m_stag throughout the sweep by rapidly switching off the excitation lasers at various times t_off. The results are presented in Figure 7.6 b). We compare the experimental results to two types of MPS simulation: with (real) and without (programmed) taking into account the various experimental imperfections described in Section 6.2.2. The experimental imperfections are: the finite detection efficiencies, the shot-to-shot fluctuation of the interatomic distances, the finite size of the excitation beams and the exact sweep shape. We observe the growth of the AF ordering both in the experiment and the simulations, which agree well during the first $5\,\mu\mathrm{s}$ of the
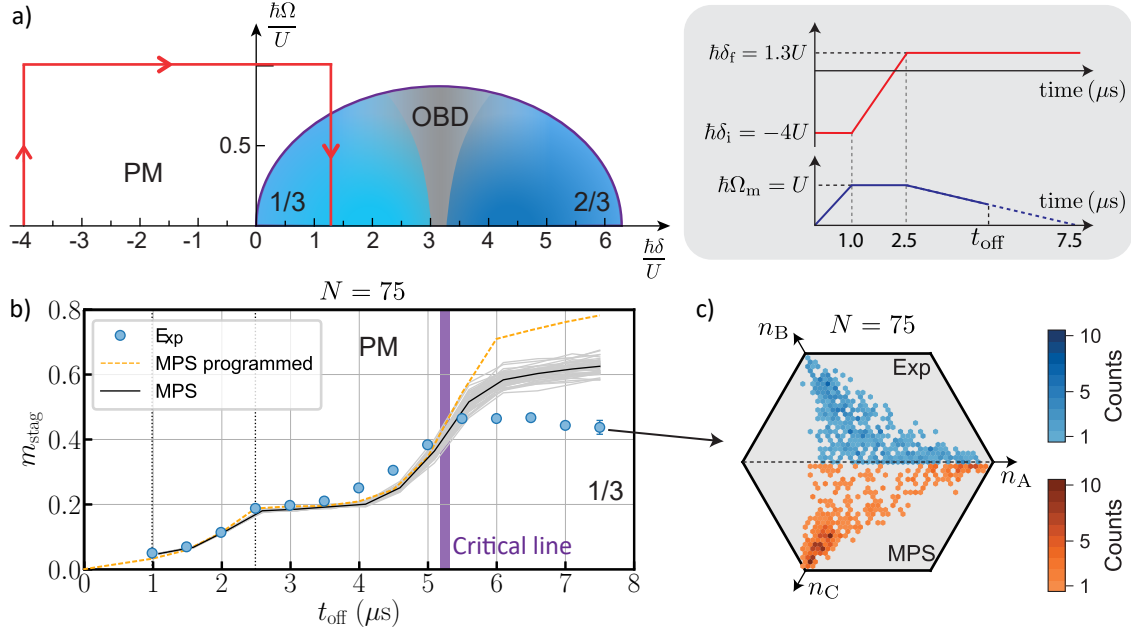
Figure 7.6: Comparison of the AF ordering growth between experiment and MPS simulations on the 75-atom array. a) Parameters of the experiment in the phase diagram and the corresponding temporal evolution of δ and Ω. b) Growth of AF ordering throughout the sweep. We show the results of MPS simulations without (dashed line) and with (grey lines) experimental imperfections for which 50 disorder instances are shown, with their average shown in black. The purple thick line represents the numerically calculated position of the critical line. c) Staggered magnetization histogram at the end of the sweep. The upper half of the histogram shows the experimental results, and the lower half shows the analogous MPS results.

sweep. After this, the experimental results plateau at a lower value of m_{stag} than expected from the MPS. The inclusion of experimental imperfections decreases the final value of m_{stag}; however, there is still a discrepancy with the experimental results. A possible explanation could be that the MPS simulation does not take into account the residual decoherence of the excitation lasers, which starts to play a role for timings $\sim 6\,\mu\text{s}$, as shown in Section 6.2.1.

We compare the prepared states at the end of the sweep between the MPS simulation and the experiment by computing the staggered magnetization histogram, see Figure 7.6 c). As the histogram displays a symmetry along the horizontal axis, we compare the results on the same histogram, where the upper part shows the experimental results and the lower part shows the MPS results. We observe a good agreement, although there is a higher accumulation of points at the corners in the MPS results, which
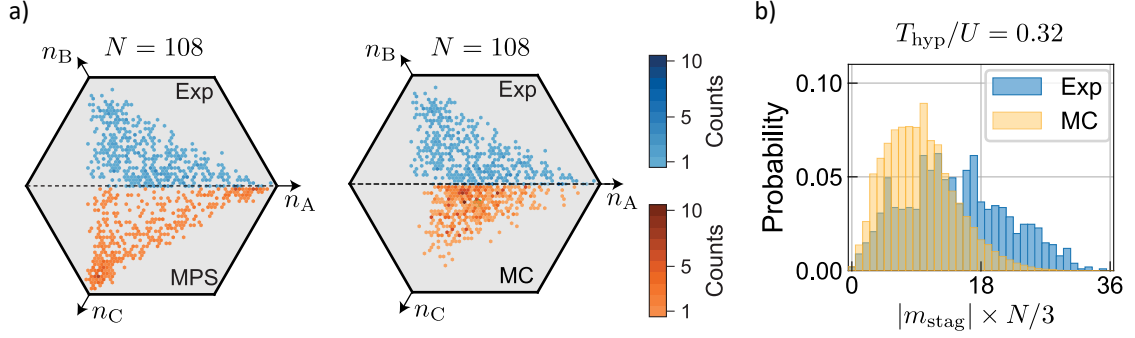
Figure 7.7: Comparison between experiment and simulations at the end of the sweep for the 108-atom array. a) Staggered magnetization histogram at the end of the sweep presented in Figure 7.6. The upper half of the histogram shows the experimental results, and the lower half shows the analogous MPS (left) and MC (right) results. b) Histogram of $|m_{\text{stag}}| \times N/3$ for the experiment (blue) and the MC simulation (yellow).

corresponds to a higher value of m_{stag}.

We run the same type of comparison for a 108-site array, see Figure 7.7 a). We observe the same features as in the 75-atom array: there is a higher accumulation of points at the corners in the MPS results.

Comparison with classical Monte-Carlo simulations. At the end of the sweep, $\Omega = 0$, such that the quantum and classical descriptions coincide (see Section 6.3). In order to check whether the states at the end of the sweep can be described by a classical thermal equilibrium, i.e. if performing a quantum process eventually leads to a classical thermal distribution of states, we compare the experimental results to classical Monte Carlo (MC) simulations. The simulations were performed by the team of A. Läuchli. As performed with square arrays, we assign a temperature T_{hyp} to the prepared states by matching the classical Ising energy between the MC simulation and the experiment (see Section 6.3.1). We obtain $T_{\text{hyp}} = 0.32\,U$, and compare the experiment and the corresponding MC simulation on the staggered magnetization histogram, see Figure 7.7 a). Contrarily to the comparison with MPS simulations, here we observe that the prepared states are more elongated towards the corners than the MC simulation.

In order to confirm the higher AF ordering on the experiment as compared to the results of MC simulations, we compute the 1D distribution of $|m_{\text{stag}}| \times N/3$, see Figure 7.7. For a perfectly AF ordered state, this distribution presents a single peak of unit probability at $|m_{\text{stag}}| \times N/3 = N/3$, while imperfect ordering shows up as a

distribution broadened towards smaller $|m_{\text{stag}}| \times N/3$. We show the results at the end of the sweep (blue) and the corresponding classical equilibrium distribution (yellow). We observe that the distributions do not match. In particular, the probability of creating larger ordered states is higher in the quantum real-time evolution than in the classical equilibrium case. We observed the same feature in the case of the square lattice, see Section 6.3.2.

7.2.3 Dynamical growth of the correlation length

In this subsection, we look in more detail at the dynamical growth of the correlation length in the transition from the PM to the 1/3 phase. The PM to 1/3 phase transition is believed to belong to the (2+1)D 3-state Potts model universality class, which is a weakly first order transition [Blöte and Swendsen, 1979; Janke and Villanova, 1997], recently confirmed by numerical studies of the 2D quantum Ising model in triangular geometries [Da Liao *et al.*, 2021]. We thus expect a discontinuity in the order parameter at the phase transition. However, as can be observed in Figure 7.6 b), we do not observe such discontinuity. This is expected for weakly first order transition: the discontinuity only forms very slowly with system size, and for the typical system sizes considered here, we expect the transition to behave similarly to a second order phase transition. In particular, the correlation length is expected to diverge algebraically close to the critical line.

Here, we experimentally verify this by measuring the growth of the correlation length close to the phase transition. We start by fixing the sweep parameters and measure the evolution of the correlation length throughout the sweep. We then check whether the Kibble-Zurek mechanism applies to this phase transition by varying the sweep duration and measuring the correlation length after crossing the transition. The conducted experiments are similar to the one described in Section 6.4. We perform the experiments on a 75-atom array.

Growth of the correlation length throughout the sweep. We first look at the growth of the correlation length throughout the sweep described in Figure 7.8 a). We compute the correlation length l_{corr} as a function of Ω for timings $t_{\text{off}} > 2.5\,\mu\text{s}$, in which we decrease Ω. The results are presented in Figure 7.8 b). For $\Omega > \Omega_{\text{c}}$, we observe the growth of l_{corr}, which eventually saturates for $\Omega < \Omega_{\text{c}}$. If the phase transition were
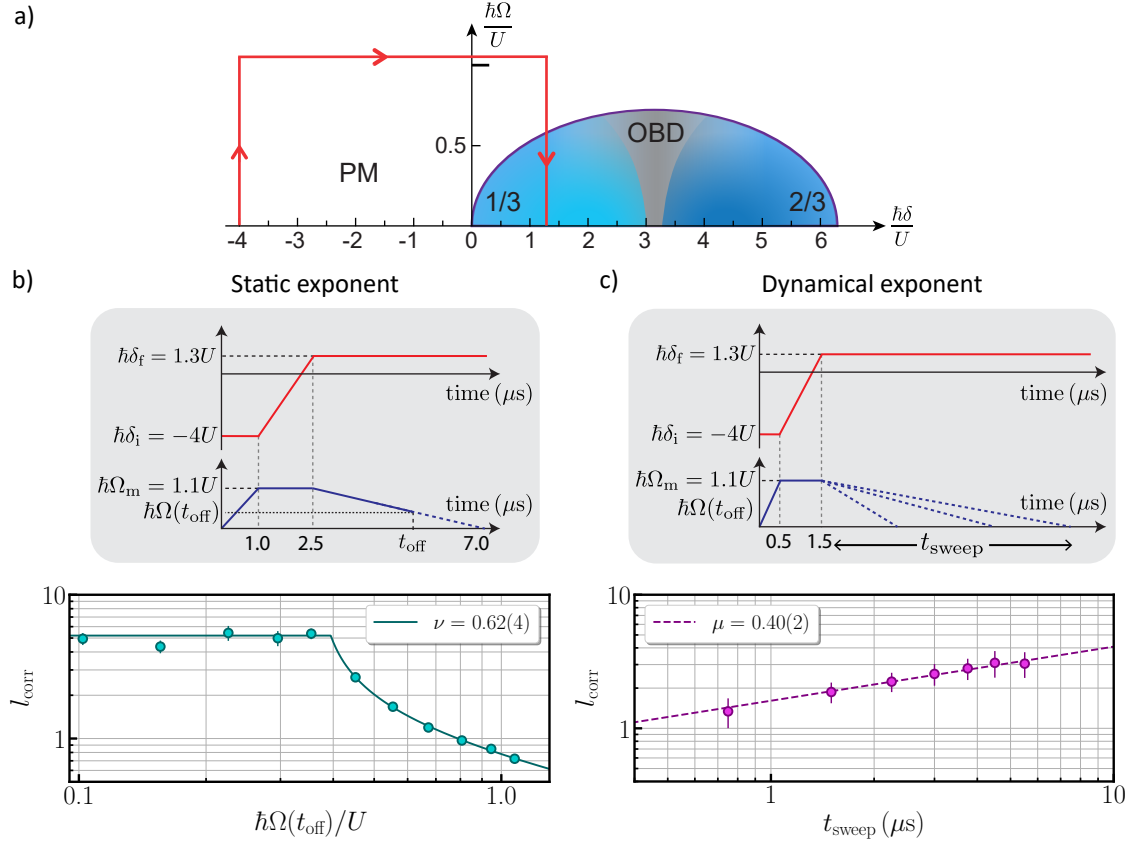
Figure 7.8: Growth of the correlation length on the 75-atom array. a) Experimental parameters sketched in the phase diagram. b) Measurement of the static exponent. We measure l_{corr} throughout the sweep. The solid line is fit to the data using a function of the form: $A(\Omega - \Omega_c)^{-\nu}$, from which we extract $\nu = 0.62(4)$. c) Measurement of the dynamical exponent. We measure l_{corr} for various durations t_{sweep} of the ramping down of Ω. The dashed line is a fit to the data using a power law, from which we extract $\mu = 0.40(2)$.

second order, we would expect a growth of l_{corr} near the critical point of the form:

$$l_{\text{corr}} \sim (\Omega - \Omega_c)^{-\nu}, \tag{7.3}$$

where ν is the critical static exponent of the phase transition. Before saturation, the data are compatible with an algebraic evolution of the correlation length: the solid line is a fit to the data of the form $A(\Omega - \Omega_c)^{-\nu}$, with A, Ω_c and ν as free parameters. We observe a good agreement between the data and the fit, from which we extract a critical exponent $\nu = 0.62(4)$. The saturation point is compatible with the numerically calculated value of the critical point $\hbar\Omega_c \simeq 0.4U$. These results indicate that the transition behaves as if it was second order, which might be related to the finite size of

the system.

For $\Omega < \Omega_{\mathrm{c}}$, we observe that l_{corr} saturates. This behavior, also observed in the case of the square lattice (see Section 6.4.1), can be related to the Kibble-Zurek (KZ) mechanism described in Section 6.4.2. We now experimentally investigate its validity.

Varying the speed at the phase transition. We use the sweep described in Figure 7.8 c) to probe the validity of the KZ mechanism. We vary the switching off time of Ω, t_{sweep}, and measure the corresponding value of l_{corr} at the end of the sweep, as described in Section 6.4. If the system follows the KZ mechanism, l_{corr} and t_{sweep} are related by:

$$l_{\mathrm{corr}} \sim t_{\mathrm{sweep}}^{\frac{\nu}{1+z\nu}} = t_{\mathrm{sweep}}^{\mu_{\mathrm{KZ}}}, \tag{7.4}$$

with z the dynamical exponent which relates spatial with temporal critical fluctuations. This formula is derived in Section 6.4.2. The results are presented in Figure 7.8 c). We observe an increase of l_{corr} with t_{sweep} compatible with a power law, from which we extract the dynamic exponent $\mu = 0.40(2)$. If the system follows the KZ mechanism and considering the extracted value of the static exponent $\nu = 0.62(4)$ and $z = 1$, we should obtain $\mu_{\mathrm{KZ}} = 0.38(3)$. This value is in agreement with the measured dynamic exponent μ, which would indicate that the system follows a KZ mechanism.

Conclusion. Even though the PM to 1/3 phase transition is expected to be first order, the experiments presented here indicate that: (i) the behavior of the system near the critical point is the same as for a second order phase transition, and (ii) the growth of the correlations seems to follows a KZ mechanism. Note that these conclusions should be considered with caution. First, these conclusions are valid for the specific 75-atom triangular array presented here. We have not checked how the system behaves for other system sizes. Second, the range over which we can tune the parameters is restricted (the reasons are discussed in Section 6.4.2). The measured power exponents might thus be valid only for this specific range. However, we can claim that our experimental results are compatible with a second order transition governed by the KZ mechanism for our specific system.

7.3 Exploration of the phase diagram

Now that we showed our ability to accurately study the 1/3 phase, we focus on the exploration of the other phases. In particular, we are interested in probing the
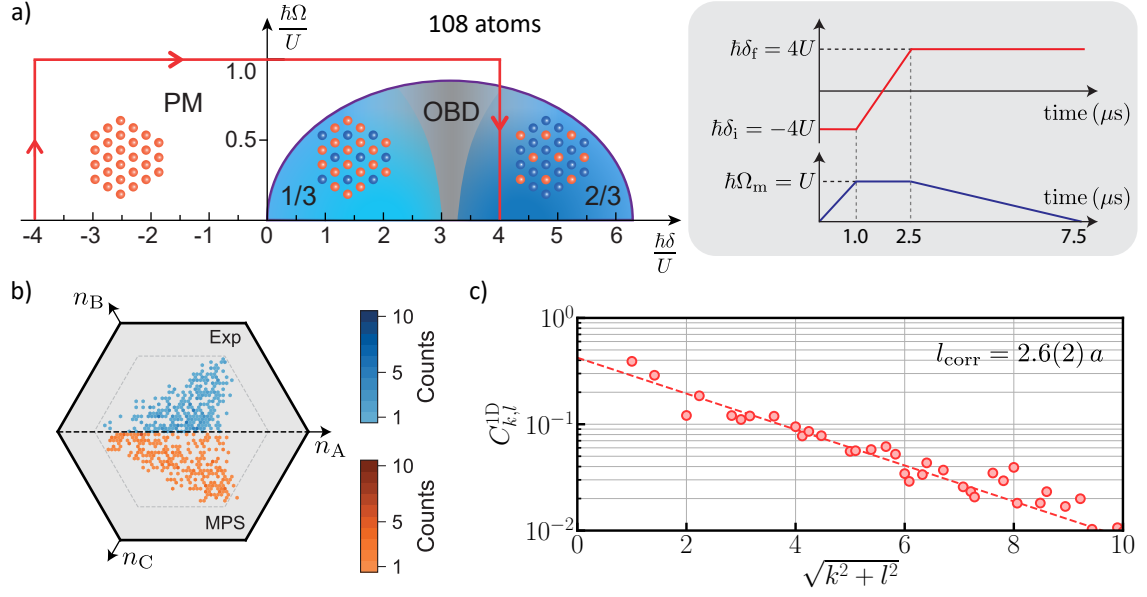
Figure 7.9: Preparation of the 2/3 phase on the 108-atom array. a) Parameters of the sweep used to prepare the 2/3 phase, in the phase diagram and the corresponding temporal evolution. b-c) Characterization of the prepared state at the end of the sweep. We show b) the 1D correlations from which we extract $l_{\text{corr}} = 2.6(2)\, a$ (with a the lattice spacing), and c) the staggered magnetization histogram, which is compared to the results of MPS simulations.

properties of the OBD phase, which exhibits strong geometric frustration. We first probe the 2/3 phase, then present a first attempt to observe the features of the OBD phase.

7.3.1 Preparation of the 2/3 phase

In this subsection, I show that we are able to prepare AF ordered states belonging to the 2/3 phase. We use the following sweep. At a detuning $\hbar\delta_{\text{i}} = -4U$, Ω is increased from 0 to $\hbar\Omega_{\text{m}} = U$ in $1.0\,\mu$s. We then sweep the detuning to $\hbar\delta_{\text{f}} = 4U$ in $1.5\,\mu$s while keeping Ω constant, and finally decrease Ω to 0 in $5\,\mu$s (see Figure 7.9 a)). In order to characterize the prepared 2/3 phase, we compute the staggered magnetization histogram at the end of the sweep, see Figure 7.9 b). Perfectly ordered AF states exhibit two sublattices filled with Rydberg excitations, which would correspond to points on the three hexagon vertices in the opposite directions as $n_{A,B,C}$. We observe a triangular distribution pointing towards these three vertices, showing that we indeed prepare states which belong to the 2/3 phase. We obtain a good agreement between

167
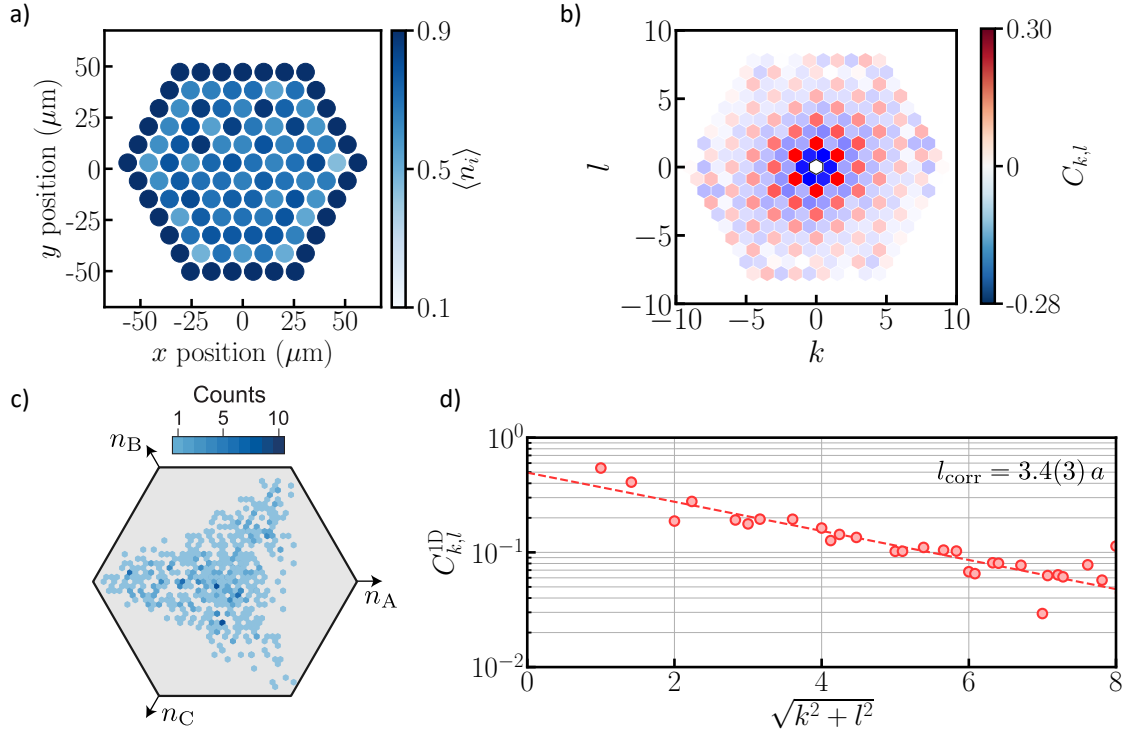
Figure 7.10: Influence of edge effects on the 2/3 phase. a) Rydberg density per atom at the end of the sweep described in Figure 7.9. b-d) We only consider the atoms in the bulk and compute b) the correlations map, c) the staggered magnetization histogram and d) the 1D correlations, from which we extract $l_{\mathrm{corr}} = 3.4(3)\,a$ (with a the lattice spacing). We observe a stronger AF ordering when considering the system's bulk, showing the impact of edge effects on the system.

the data and the MPS results, taking into account the experimental imperfections described in Section 6.2.2 (detection errors, finite size of the excitation beams and shot-to-shot fluctuations in the atomic positions).

As compared to the 1/3 phase, here the triangle (both in the simulation and in the experiment) does not reach the vertices of the hexagon, which indicates that the quality of the prepared AF ordering is lower than in the 1/3 phase. This is confirmed by computing the 1D correlations, see Figure 7.9 c). We obtain $l_{\mathrm{corr}} = 2.6(2)\,a$ (a is the lattice spacing), which has to be compared to $l_{\mathrm{corr}} \simeq 6\,a$ for the 1/3 phase. This difference in the quality of AF ordering is partly due to edge effects, which we now discuss.

Influence of edge effects. As discussed in Section 7.2.1, one effect of system's boundaries is to induce a high Rydberg filling on the system's boundaries. The mean

interaction energy U_m felt by the atoms on the sides is $U_m \simeq 4.2U$. In order to remain in the 2/3 phase for all the atoms, the final detuning should remain low $\hbar\delta_f < 4.2U$ (see Section 6.1.3 for an heuristic argument on the square lattice). In our experiments dealing with the square lattice and the 1/3 phase, we always targeted low final detuning to avoid filling the edges with Rydberg atoms. However, as the 2/3 phase only exists at high final detuning, we are always in the regime $\hbar\delta_f \simeq U_m$, meaning that the atoms on the edges are highly filled with Rydberg excitations. This reduces the maximal possible extent of the staggered magnetization distribution, as the three sublattices are equivalently filled with Rydberg atoms on the boundaries. We experimentally check this fact by computing the Rydberg density map $\langle n_i \rangle$ at the end of the sweep, see Figure 7.10 a). The boundaries are highly excited ($\langle n_i \rangle > 0.9$), whereas the Rydberg density of the system's bulk is $\langle n_i \rangle \sim 2/3$, as expected for the 2/3 phase.

In order to show that the system's bulk is strongly AF ordered, we compute the various observables characterizing AF ordering by only considering the 75 atoms inside the bulk, see Figure 7.10 b-d). We now observe on the staggered magnetization histogram that the triangular distribution extends close to the hexagon vertices, in a similar fashion as for the 1/3 phase. We extract a correlation length $l_{corr} = 3.4(3) \, a$. This shows that the edge effects strongly reduce the quality of the prepared AF ordering.

Conclusion. We showed that we are able to prepare ordered states belonging to the 2/3 phase. However, the ordering is weaker than in the case of the 1/3 phase, which is partly explained by the edge effects. The lower ordering can also be explained by the sweep timings. We use the same timings as for the preparation of the 1/3 phase. However, the range over which δ is swept is $\sim 50\%$ higher to prepare the 2/3 phase. This results in sweeping the detuning $\sim 50\%$ faster, inducing a higher probability to cross the gaps, hence reducing the adiabaticity of the driving.

7.3.2 Probing the order-by-disorder phase

Now that we observed the main features of the 1/3 and the 2/3 phases, we focus on the 1/2 region, located at $\hbar\delta_{OBD} \simeq 3.15U$. In this region, the system is highly frustrated: at $\Omega = 0$, the ground state is massively degenerated, leading to a finite entropy even at zero temperature [Wannier, 1950]. The massive degeneracy can be heuristically understood as follows. As $\langle n \rangle = 0.5$, every triangular plaquette of the lattice has one atom in the $|\downarrow\rangle$ state, and one in the $|\uparrow\rangle$ state. The orientation of the third atom is
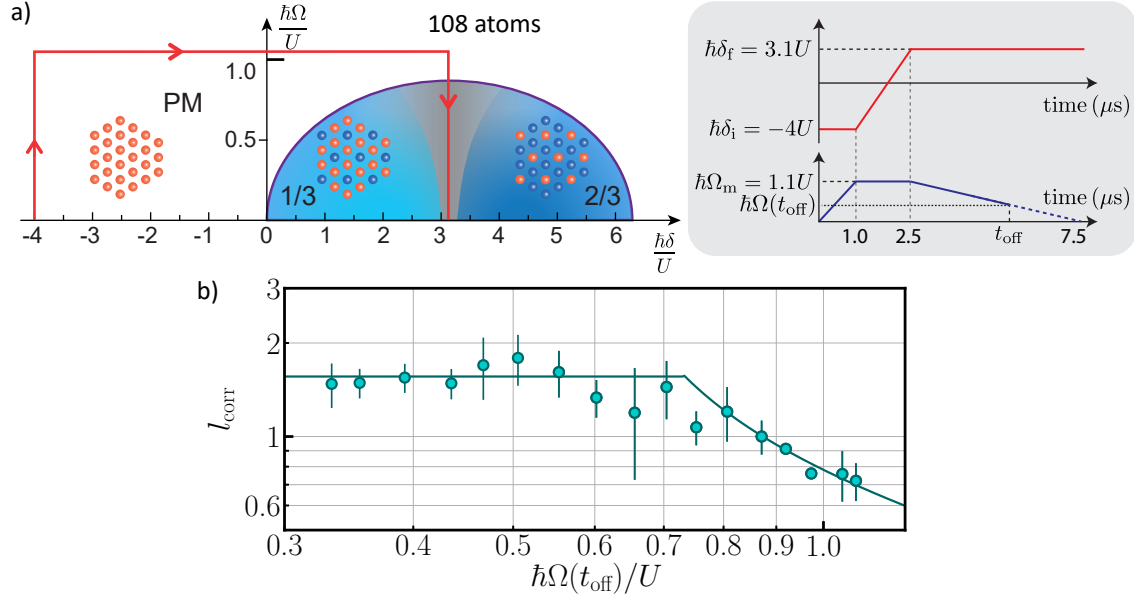
Figure 7.11: Paramagnet to OBD phase transition on the 108-atom array. a) Parameters of the experiment. b) Evolution of l_{corr} throughout the sweep. The solid line is a fit to the data using of function of the form $A(\Omega - \Omega_c)^{-0.67}$, showing that the growth of the correlation length is compatible with the expected critical exponent $\nu \simeq 0.67$.

left undetermined, leading to $\sim 2^{N/3}$ degenerate ground states [Menu, 2020].

The application of a longitudinal field $\delta \neq \delta_{OBD}$ lifts the degeneracy, and chooses either the 1/3 ($\delta < \delta_{OBD}$) or the 2/3 phase ($\delta > \delta_{OBD}$) as the system's ground state. The transverse field is expected to act in a similar way by lifting the degeneracy through the "Order-By-Disorder" (OBD) mechanism [Villain, J. *et al.*, 1980], which was first introduced to explain how the disorder caused by thermal fluctuations lead to an ordered phase. This OBD mechanism is expected to also apply for the quantum fluctuations induced by Ω. The ground state is expected to be a combination of the 1/3 and the 2/3 phase ground states [Menu, 2020].

The precise characteristics of the OBD phase are not well known, especially considering the long-range interactions and the limited system size used in the experiment. Here, we show that despite all the experimental imperfections, we obtain some experimental guesses that we probe the OBD phase. We first investigate the system's behavior at the phase transition, then characterize the obtained states. The experiments presented below are performed on the 108-atom array.

Paramagnet to OBD phase transition. In order to characterize the OBD phase, we first study the system's behavior near the critical line. Here, the transition is

expected to be second order [Moessner, Sondhi, and Chandra, 2000; Moessner and Sondhi, 2001] and to belong to the universality class of the (2+1)D classical XY model. Interestingly enough, the transition does not belong to the Ising universality class. We can give an intuitive argument to this. The classical XY model can be seen as the classical version of the Ising model, in which the spins orientation can be continuously varied. In the OBD phase, the spins orientation is partly undetermined, which can thus be interpreted as a potential continuous variation of the spin orientation. The critical exponent of the (2+1)D classical XY model universality class is $\nu \simeq 0.67$, and is estimated from Monte-Carlo simulations [Plumer and Mailhot, 1995].

In order to probe this phase transition, we measure the growth of the correlation length throughout the sweep described in Figure 7.11 a), similar to the ones described above. We set a final detuning $\hbar\delta_{\mathrm{f}} = 3.1U$, in between the 1/3 and the 2/3 phases. The results are presented in Figure 7.11 b). For $\Omega > \Omega_{\mathrm{c}}$, we observe a growth of l_{corr} which is consistent with the expected critical exponent (solid line). The correlation length saturates for $\hbar\Omega_{\mathrm{c}} \simeq 0.75\,U$, consistent with the expected position of the critical line [Koziol $et\ al.$, 2019]. This experiment shows that: (i) we enter in an AF ordered phase and (ii) the growth of l_{corr} is consistent with the expected PM to OBD phase transition.

Characterization of the OBD phase. We now characterize the prepared state at the end of the sweep. As shown in Figure 7.11 b), the correlation length inside the phase is weak ($l_{\mathrm{corr}} \simeq 1.5\,a$). As discussed in Section 7.3.1, the system's boundaries strongly reduce the AF ordering when considering high final detunings. In order to mitigate their impact, we only consider the 45 atoms inside the system's bulk by removing the two outer shells. We compute the 1D correlations and the corresponding 2D correlations map, see Figure 7.12 a). We now observe strong AF ordering in the bulk, with a correlation length $l_{\mathrm{corr}} = 3.0(3)\,a$, close to the one obtained in the 2/3 phase (for the same array). This long range AF ordering is expected in the OBD phase [Moessner, Sondhi, and Chandra, 2000; Moessner and Sondhi, 2001].

In order to further characterize the prepared states, we compute the corresponding staggered magnetization histogram, see Figure 7.12 b). As a comparison, we also show the ones obtained for the 1/3 and 2/3 phases, considering only the bulk of the 108-atom array. As compared to the other phases, the OBD histogram is isotropic and spreads towards high values of $|m_{\mathrm{stag}}|$ in all directions. Even though the distribution is isotropic, we observe strong AF ordering, a feature which is expected for the OBD phase. Numerical studies [Da Liao $et\ al.$, 2021] show that the OBD ground states

should exhibit a circle in the magnetization histogram. Although we do not observe the expected behavior, the histogram points towards a circular shape. The fact that the histogram points towards the expected ground state behavior also happens for the 1/3 and 2/3 phases: if we were preparing their ground states, we would observe three peaks located on the hexagon vertices. However, we observe triangles pointing towards these vertices, which is enough to claim observing the 1/3 and 2/3 phases. In the OBD phase, we observe an isotropic distribution, with maxima of probability located at high value of $|m_{\text{stag}}|$. These maxima are close to form a circle, and is thus very indicative of preparing the OBD phase.

Numerical simulations performed by the team of A. Laüchli suggest that observing a circle would be reachable by reducing the experimental imperfections (presented in Section 6.2.2), keeping the same sweep parameters.

Conclusions. In this subsection, I presented the experiment we conducted towards the observation of the OBD phase. Although its signatures are not clear both on the experimental side and on the numerical side (considering our implementation of the TFI model), we were able to show that: (i) we observe a transition from the disordered PM phase to an AF ordered phase in a consistent way with the PM to OBD phase transition and (ii) the characteristics of this phase are different from the 1/3 and 2/3 phases, which is proved by the isotropic staggered magnetization histogram, a feature expected for the OBD phase. Exploring in more detail this phase will be the subject of future work.

7.4   Conclusion

In this chapter, I presented the various experimental investigations we performed on the 2D transverse field Ising model in triangular arrays. I showed that we are able to produce highly antiferromagnetically ordered states on arrays containing up to 147 atoms, which is beyond what can be exactly simulated classically. We explored all the (nearest-neighbor) phases of the model, and studied the dynamical growth of the correlations in the system, showing a compatibility with a Kibble-Zurek mechanism. The above results demonstrate the preparation of the 1/3 and 2/3 phases using a synthetic quantum many-body system, which had never been achieved to that extent. In particular, we probed the highly frustrated OBD phase which has not been experimentally observed so far. We obtained first signatures of this phase, showing that its observation and study is reachable using a Rydberg quantum simulator.
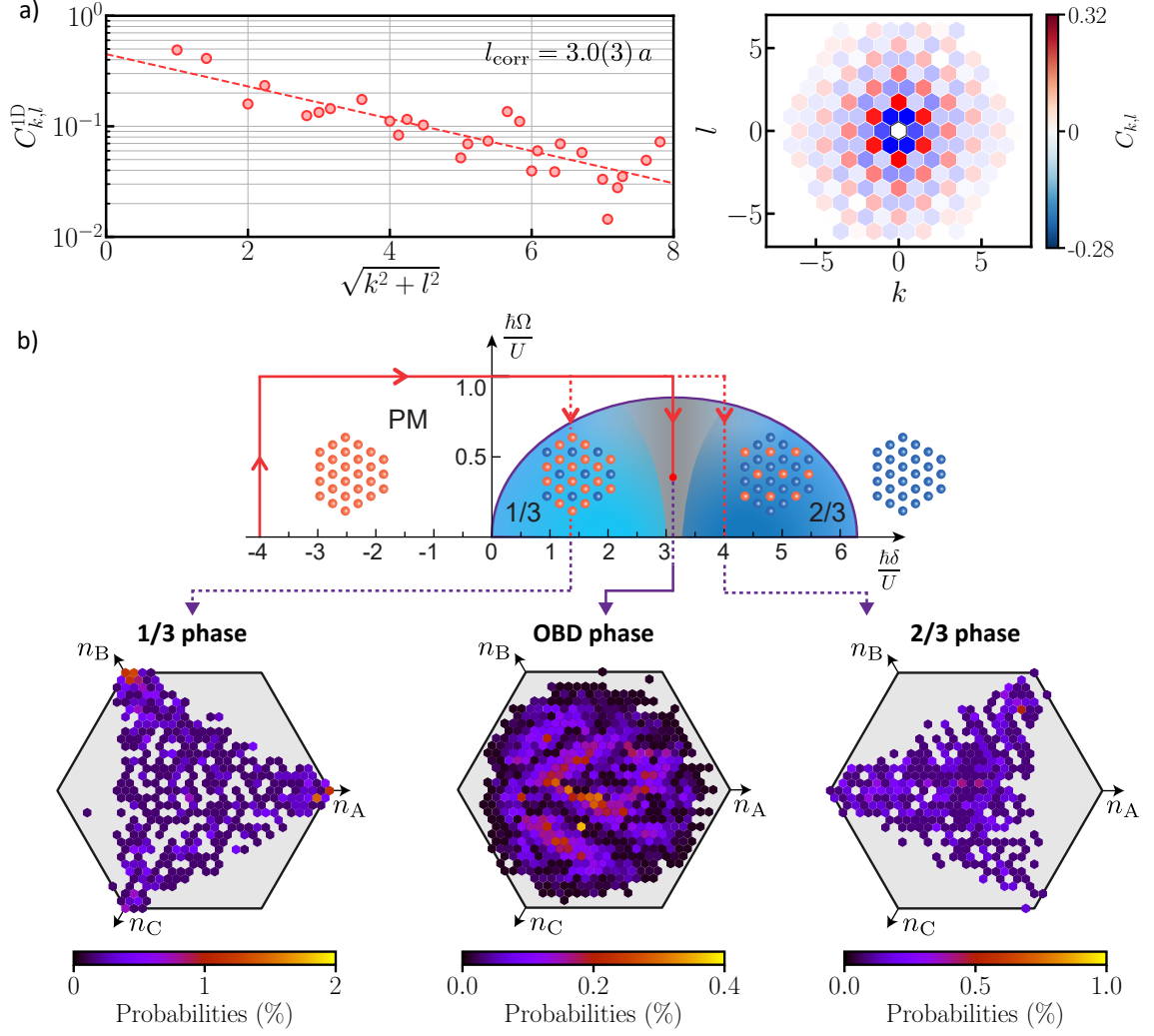
Figure 7.12: Probing the OBD phase on the 108-atom array. We only consider the bulk of the array. a) Correlation length and correlation map in the OBD phase. We extract a correlation length $l_{\text{corr}} = 3.0(3)\,a$, showing that the prepared states are AF ordered. b) Bulk staggered magnetization histogram for the 1/3 phase (left), the OBD phase (middle) and the 2/3 phase (right). The histogram of the OBD phase is isotropic with an important extension towards high values of $|m_{\text{stag}}|$. These features are expected in the OBD phase.

Part III.

Engineering of spin-1/2 Hamiltonians using the dipole-dipole interaction between Rydberg atoms

Dipole-dipole interaction between a few Rydberg atoms

Contents

In this chapter, I explain how we use the dipole-dipole interaction between Rydberg atoms to implement two models. I first show the implementation of the XX model on two atoms, characterized by

$$H_{\mathrm{XX}} = \sum_{i,j} J_{ij}(\sigma_i^x \sigma_j^x + \sigma_i^y \sigma_j^y), \tag{8.1}$$

where $\sigma^{x,y}$ are the usual Pauli matrices acting on the spin-1/2 states denoted as $|\downarrow\rangle$ and $|\uparrow\rangle$. This model is also known as the "XY model" in the literature. As compared to the Ising case, the model is in a sense more quantum, as there are no classical configurations for the system's ground states. The model's properties, such as its phase diagram and the corresponding nature of the quantum phase transitions for various geometries are an active research field [Balents, 2010; Radgohar and Montakhab, 2018;

Knolle and Moessner, 2019]. Studying those properties, as performed in Chapter 6 and Chapter 7 for the 2D transverse field Ising model, is however out of the scope of this thesis.

Instead, we focus on the exploration of transport phenomena: in the XX model, the interaction term leads to the hopping of spin excitations between sites. Transport properties of spin excitations are actively studied, both experimentally and theoretically in various models [Cheneau *et al.*, 2012; Bertini *et al.*, 2021]. This transfer of excitations driven by the interactions may also occur in biological systems, which makes the XY model relevant to study photochemistry or photosynthesis [Collini, 2013]. The exploration of transport dynamics in many-body systems will be studied in Chapter 9.

In the present chapter, I also show the implementation of density-dependent and complex hopping of spin excitations between sites on the minimal setup of three atoms, which mimics the dynamics of charged particles in a magnetic field [Dalibard *et al.*, 2011; Aidelsburger, Nascimbene, and Goldman, 2018] with the prospective view of studying topological properties of matter, such as the quantum Hall effect [Klitzing, Dorda, and Pepper, 1980]. The results presented here are the first step towards an implementation on large systems, which will be the subject of future works.

8.1   Dipole-dipole interaction and mapping to the XX model

The dipole-dipole interaction between two Rydberg atoms placed at positions $\boldsymbol{r_1}$ and $\boldsymbol{r_2}$, with electric dipoles operators $\hat{\boldsymbol{d_1}}$ and $\hat{\boldsymbol{d_2}}$, is expressed as:

$$\hat{V}_{\mathrm{ddi}} = \frac{\hat{\boldsymbol{d_1}} \cdot \hat{\boldsymbol{d_2}} - 3 \left(\hat{\boldsymbol{d_1}} \cdot \boldsymbol{n} \right) \left(\hat{\boldsymbol{d_2}} \cdot \boldsymbol{n} \right)}{4\pi\epsilon_0 R^3}, \tag{8.2}$$

with $R = |\boldsymbol{r_2} - \boldsymbol{r_1}|$ the distance between the atoms, and $\boldsymbol{n} = (\boldsymbol{r_2} - \boldsymbol{r_1})/R$ the unit vector defining the internuclear axis.

We consider in this manuscript the interaction between Rydberg states belonging to the $nS_{1/2}$ and $nP_{3/2}$ manifolds. The interaction strength between these states depends on the relative orientation of the magnetic field with respect to the internuclear axis. We used this property to engineer anisotropic interaction energies in previous works [de Léséleuc *et al.*, 2019]. In this thesis, we will study 2D systems with isotropic interactions, which is achieved when the magnetic field is perpendicular to the atomic array. I thus write the above expression in this case, explain its various terms and show that we can map the system onto the XX Hamiltonian.
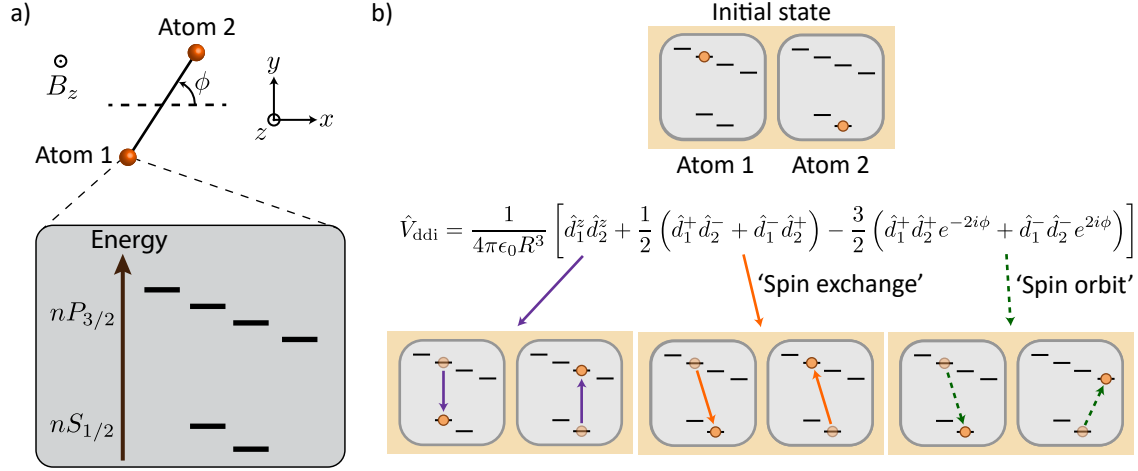
Figure 8.1: Illustration of the dipole-dipole interaction in the presence of a magnetic field perpendicular to the atomic plane. a) We consider two atoms and their $nS_{1/2}$ and $nP_{3/2}$ manifolds. The magnetic field is perpendicular to the atomic plane, and the internuclear axis has an angle ϕ with the x direction. b) Effect of the various terms of $\hat{V}_{\text{ddi}}$ illustrated on the $\left|nP_{3/2}, m_J = -1/2\right\rangle \otimes \left|nS_{1/2}, m_J = 1/2\right\rangle$ state.

Dipole-dipole interaction in a perpendicular magnetic field. We consider two atoms placed in the (x, y) plane, and submitted to a static magnetic field B_z along the z direction (see Figure 8.1 a)). The unit vector defining the internuclear axis is $\boldsymbol{n} = (\cos\phi, \sin\phi, 0)$, with ϕ the angle between the internuclear axis and the x direction. In this basis, the dipole-dipole interaction can be written using the components of the dipole operator $\hat{d}^x$, $\hat{d}^y$ and $\hat{d}^z$:

$$\hat{V}_{\text{ddi}} = \frac{1}{4\pi\epsilon_0 R^3} \left[\hat{d}_1^z \hat{d}_2^z + \frac{1}{2} \left(\hat{d}_1^+ \hat{d}_2^- + \hat{d}_1^- \hat{d}_2^+ \right) - \frac{3}{2} \left(\hat{d}_1^+ \hat{d}_2^+ e^{-2i\phi} + \hat{d}_1^- \hat{d}_2^- e^{2i\phi} \right) \right], \quad (8.3)$$

with $\hat{d}_j^\pm = \mp(\hat{d}_j^y \pm i\hat{d}_j^z)/\sqrt{2}$ for atom j. The action of these five terms is sketched in Figure 8.1 b) on the example of the $\left|nP_{3/2}, m_J = -1/2\right\rangle \otimes \left|nS_{1/2}, m_J = 1/2\right\rangle$ state. These terms can be classified as follows:

- The first three terms couple states which conserve the total internal angular momentum of the two atoms. In particular, the terms $\hat{d}_1^+ \hat{d}_2^- + \hat{d}_1^- \hat{d}_2^+$ couple states which are degenerate in energy. These latter terms exchange the state of the atoms, and will be referred as the "spin exchange" terms in the following.

- The last two terms describe the spin-orbit coupling: those couple two-atom states with different internal angular momentum. The conservation of the total angular momentum requires that these terms exhibit a phase $e^{\pm 2i\phi}$. These terms

will be used in Section 8.3 to implement an effective spin-1/2 Hamiltonian with density-dependent, complex interactions.

In the presence of the typical magnetic field $B_z \sim 30 - 50\,\mathrm{G}$ we apply, only the spin exchange terms are resonant. The other terms are out of resonance by $\mu/h \sim 100\,\mathrm{MHz}$, two orders of magnitude higher than the typical interaction energy $\langle \hat{V}_{\mathrm{ddi}}/h \rangle \sim 1\,\mathrm{MHz}$ for typical experimental parameters $R = 10\,\mu\mathrm{m}$ and $n \sim 60$. We will thus consider in this section and in Section 8.2 that these terms are negligible. The application of a controlled, strong electric field (see Section 2.4.2) allows us to bring the spin-orbit terms close to resonance, as discussed in Section 8.3.1.

Mapping to the XX model.   As we now only consider the "spin exchange" term of the dipole-dipole interaction, we can restrict ourselves to a qubit basis and set as an example the spin-1/2 states $|\downarrow\rangle = \left| nS_{1/2}, m_J = 1/2 \right\rangle$ and $|\uparrow\rangle = \left| nP_{3/2}, m_J = 1/2 \right\rangle$. By defining the interaction energy $J = |\langle\uparrow| d^+ |\downarrow\rangle|^2/(8\pi\epsilon_0 R^3) = C_3/(2R^3)$, we obtain the XX Hamiltonian:

$$H_{\mathrm{XX}} = J(\sigma_1^+ \sigma_2^- + \sigma_1^- \sigma_2^+) = \frac{J}{2}(\sigma_1^x \sigma_2^x + \sigma_1^y \sigma_2^y), \qquad (8.4)$$

where $\sigma^{x,y}$ are the usual Pauli matrices acting on the spin-1/2 states $|\downarrow\rangle$ and $|\uparrow\rangle$. We now present our experimental implementation of H_{XX}, and characterize its main features.

8.2   Implementation of the XX model with two atoms

In this section, we consider the simplest case of two atoms. I first give an overview of the experimental sequence when working with the XX model, then present the effect of the dipole-dipole interaction on the system's spectroscopy, and finally study two features of the model: the oscillation of the magnetization along the y axis, and the coherent exchange of an $\uparrow$ excitation between the two Rydberg atoms. These latter experiments will be revisited beyond two atoms in Chapter 9.

Experimental sequence.   In order to implement the XX model in the conditions described above, we need to (i) initialize the atoms in a specific Rydberg state $|\downarrow\rangle$, (ii) apply a magnetic field perpendicular to the atomic plane and (iii) isolate one Rydberg state in both the nS and nP manifolds. These operations were described in Chapter 2. I briefly summarize them here:

- **Rydberg state initialization.** We first place the atoms in the state $|g\rangle = \left|5S_{1/2}, F = 2, m_F = 2\right\rangle$ through optical pumping (see Section 2.2). We then use the stimulated Raman adiabatic passage technique presented in Section 2.3.1 to transfer them into $|\downarrow\rangle$.

- **Magnetic field rotation.** During the optical pumping stage, the magnetic field is in the atomic plane. We rotate the magnetic field after optical pumping as described in Section 2.4.1.

- **Isolating two Rydberg states.** We set a strong magnetic field $B_z \simeq 30 - 50\,\mathrm{G}$ (see Section 2.4.1) in order to isolate two Rydberg states.

In order to read the system's state, we selectively transfer the atoms from the $|\downarrow\rangle$ state back to the ground state using the de-excitation technique presented in Section 2.3.1.

8.2.1 Microwave spectroscopy

In this subsection, we show the effect of the resonant term of the dipole-dipole interaction on the spectroscopy of two atoms. We consider the states $|\downarrow\rangle = \left|60S_{1/2}, m_J = 1/2\right\rangle$ and $|\uparrow\rangle = \left|60P_{3/2}, m_J = -1/2\right\rangle$, see Figure 8.2 a).

Single atom spectroscopy. As discussed in Section 2.3.3, the transition frequency f_{MW} with $n \sim 60 - 90$ is $f_{\mathrm{MW}} \sim 1 - 20\,\mathrm{GHz}$, which is accessible to microwave synthesizers. We use here a magnetic field $B_z \simeq 53\,\mathrm{G}$. In order to check the splitting of the levels induced by the Zeeman effect, we perform a broad spectroscopy of all the accessible levels of the $60P_{3/2}$ manifold, see Figure 8.2 b). The splitting of the m_J levels is $\Delta/(2\pi) \simeq 100\,\mathrm{MHz}$, as expected from the applied magnetic field. The splitting is two orders of magnitude higher than any interaction energies. We can thus safely assume that only the "spin-exchange" terms of the dipole-dipole interaction will contribute to the interactions.

Two atom spectroscopy. We now perform the spectroscopy with two atoms separated by $R = 10\,\mu\mathrm{m}$. The results are presented in Figure 8.2 d). We show (i) the single-excitation probability $P_{\uparrow\downarrow} + P_{\downarrow\uparrow}$ for the atoms to be in the $|\uparrow\downarrow\rangle$ or $|\downarrow\uparrow\rangle$ state (blue), and (ii) the double excitation probability $P_{\uparrow\uparrow}$ for the atoms to be in the $|\uparrow\uparrow\rangle$ state (red). The single-excitation transition is shifted from the double-excitation transition by the dipole-dipole interaction: the degeneracy of the $|\downarrow\uparrow\rangle$ and $|\uparrow\downarrow\rangle$ states is
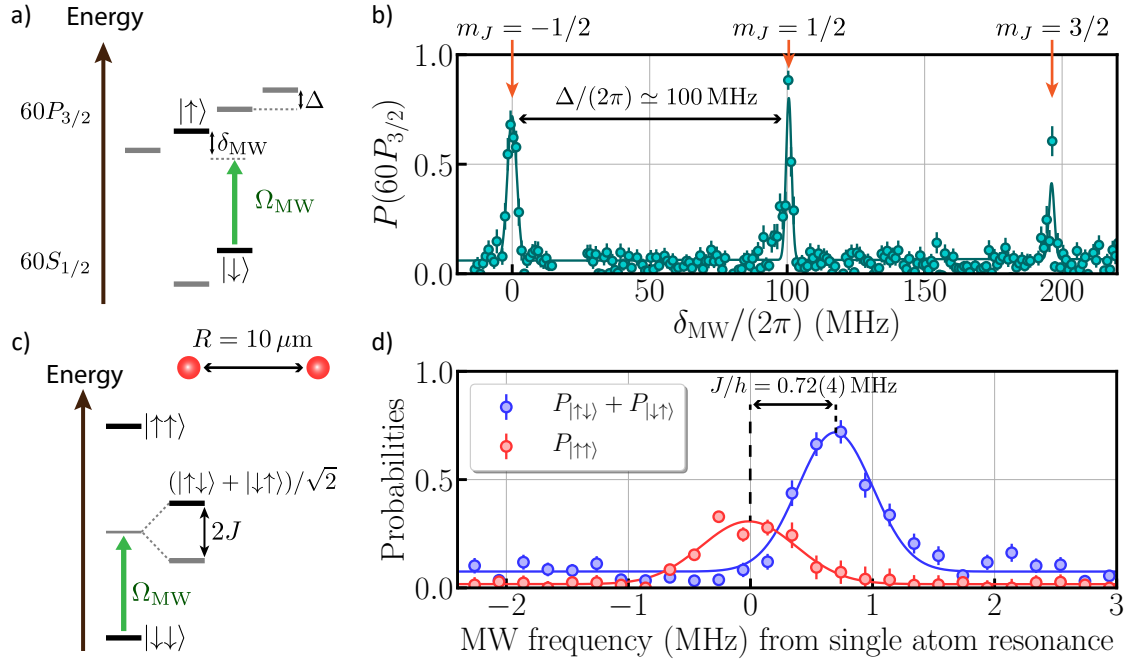
Figure 8.2: Measurement of the interaction energy via spectroscopy. a) Structure of the single-atom levels. b) Probability $P(60P_{3/2})$ to measure the atom in one of the $60P_{3/2}$ states as a function of the detuning δ_{MW} from the $|\downarrow\rangle \rightarrow |\uparrow\rangle$ transition. The application of a magnetic field $B_z \simeq 53\,$G allows us to detune the nearby states by $\Delta/(2\pi) \simeq 100\,$MHz. c) Sketch of the two-atom states. The dipole-dipole interaction lifts the degeneracy of the $|\uparrow\downarrow\rangle$ and $|\downarrow\uparrow\rangle$ states by $2J$. d) Single-excitation (blue) and double-excitation (red) probabilities as a function of the detuning from the single atom resonance. The microwaves couple to the $|\uparrow\uparrow\rangle$ state and the $(|\uparrow\downarrow\rangle + |\downarrow\uparrow\rangle)/\sqrt{2}$ state. Their difference in energy gives $J/h = 0.72(4)\,$MHz, consistent with $C_3 \simeq 1.5\,$GHz.μm^3 [Weber et al., 2017] and $R = 10\,\mu$m.

lifted by an energy $2J$ (see Figure 8.2 c)). We measure the shift in transition frequency and obtain the interaction energy: $J/h = 0.72(4)\,$MHz. This value is consistent with numerical calculations: for the levels considered here, $C_3 \simeq 1.5\,$GHz.μm^3 [Weber et al., 2017] which leads to $J/h = C_3/(2R^3) \simeq 0.75\,$MHz.

Microwave coupling. The dipole-dipole interaction gives rise to the two entangled eigenstates $|+\rangle = (|\uparrow\downarrow\rangle + |\downarrow\uparrow\rangle)/\sqrt{2}$ and $|-\rangle = (|\uparrow\downarrow\rangle - |\downarrow\uparrow\rangle)/\sqrt{2}$. Here, we briefly discuss the microwave coupling to these two states. The $|\downarrow\downarrow\rangle \rightarrow |+\rangle$ coupling is enhanced by a factor $\sqrt{2}$, as the contribution from both the $|\uparrow\downarrow\rangle$ and $|\downarrow\uparrow\rangle$ states are adding up. We qualitatively observe this feature by observing the relative height of the two peaks in the spectrum. On the contrary, the $|\downarrow\downarrow\rangle \rightarrow |-\rangle$ coupling vanishes: due to the minus

sign, the contribution from both the $|\uparrow\downarrow\rangle$ and $|\downarrow\uparrow\rangle$ states cancels. We indeed observe the absence of signal at $-J$. This vanishing coupling to the $|-\rangle$ state implies that the adiabatic preparation of XY antiferromagnets on square lattices using microwaves is challenging, which is discussed in detail in the thesis of Vincent Lienhard [2019].

8.2.2 Oscillation of the magnetization

In this subsection, we study the effect of H_{XX} on the atoms magnetization. We consider the states $|\downarrow\rangle = \left|90S_{1/2}, m_J = 1/2\right\rangle$ and $|\uparrow\rangle = \left|90P_{3/2}, m_J = 3/2\right\rangle$, and set a distance $R = 30\,\mu\mathrm{m}$ between the two atoms, leading to an interaction energy $J/h \simeq 0.9\,\mathrm{MHz}$ (see Figure 8.3 a)). As the XX Hamiltonian conserves the number of excitations, the z magnetization $\langle\sigma^z\rangle$ is constant. We show here that after magnetizing the system along the y axis, the y-magnetization evolves under H_{XX}.

Experimental sequence. The experimental sequence is sketched in Figure 8.3 b). After initializing the atoms in the $|\downarrow\downarrow\rangle$ state using the STimulated Raman Adiabatic Passage (STIRAP) technique, we apply a strong microwave $\pi/2$-pulse (with a Rabi frequency $\Omega_{\mathrm{MW}}/(2\pi) \simeq 7.2\,\mathrm{MHz}$) in order to prepare the fully magnetized state along the y axis:

$$|\rightarrow\rightarrow\rangle_y = \frac{1}{2}(|\downarrow\rangle + i\,|\uparrow\rangle) \otimes (|\downarrow\rangle + i\,|\uparrow\rangle) = \frac{1}{2}\left[|\downarrow\downarrow\rangle - |\uparrow\uparrow\rangle + i(|\uparrow\downarrow\rangle + |\downarrow\uparrow\rangle)\right]. \qquad (8.5)$$

We then let the system freely evolve under H_{XX} for a duration t_{int}, and finally measure the magnetization along the y axis $\langle\sigma^y\rangle$ by applying a second microwave $\pi/2$-pulse and a de-excitation pulse (see Section 2.3.1) to read the system's state in the z basis.

Oscillation of the y magnetization. We measure $\langle\sigma^y\rangle$ for various t_{int} and observe an oscillation of $\langle\sigma^y\rangle$, see Figure 8.3 c). The solid line is a fit to the data using a damped sine function, from which we extract an oscillation frequency $J/h = 0.91(1)\,\mathrm{MHz}$, consistent with the expected interaction energy $J/h \simeq 0.9\,\mathrm{MHz}$. This magnetization oscillation is expected in the XX model. The prepared state, $(|\downarrow\downarrow\rangle - |\uparrow\uparrow\rangle + i\sqrt{2}\,|+\rangle)/2$, is composed of three eigenstates with different eigenenergies: $|\downarrow\downarrow\rangle$ and $|\uparrow\uparrow\rangle$ are located at zero energy, whilst $|+\rangle$ has an eigenenergy J. The state thus evolves as $(|\downarrow\downarrow\rangle - |\uparrow\uparrow\rangle + e^{iJt_{\mathrm{int}}/\hbar}i\sqrt{2}\,|+\rangle)/2$ and $\langle\sigma^y\rangle$ oscillates. The natural evolution of the system's magnetization is an important feature of the XX model, and will be studied in a 2D many-body system in Section 9.2.
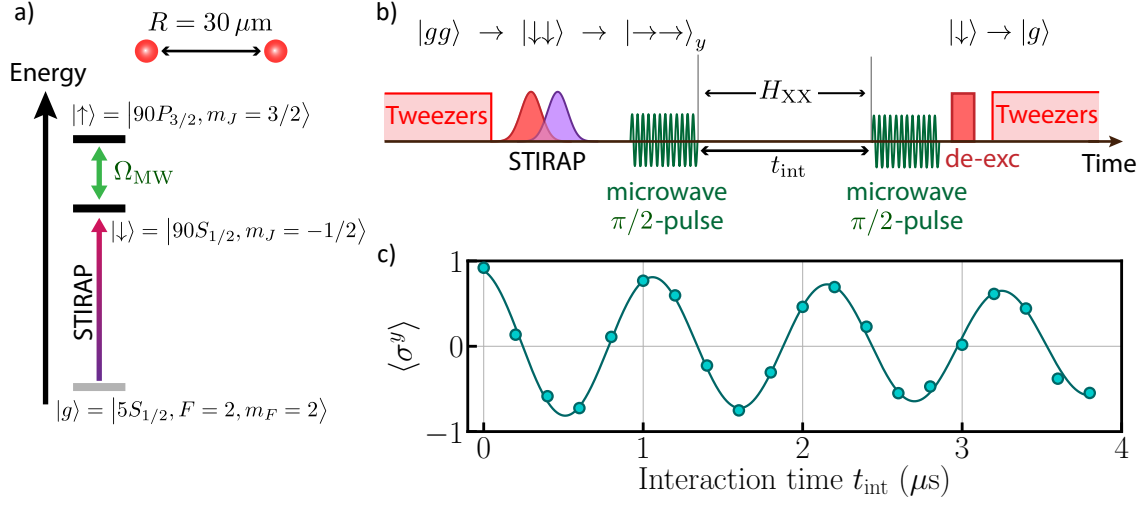
Figure 8.3: Oscillation of the magnetization along y. a) Sketch of the single-atom levels. b) Sketch of the experimental sequence. We prepare the $|\rightarrow\rightarrow\rangle_y$ state using a $\pi/2$ microwave pulse, let the system evolve under H_{XX} for a duration t_{int}, then read the system's state using a second a $\pi/2$ microwave pulse and a de-excitation beam (see Section 2.3.1). c) Magnetization along the y axis $\langle \sigma^y \rangle$ as a function of t_{int}. The solid line is a fit to the data using a damped sine function from which we extract $J/h = 0.91(1)\,\mathrm{MHz}$.

8.2.3 Coherent exchange of a spin excitation

The last feature of the model we experimentally demonstrate here is the coherent exchange of a $\uparrow$ spin excitation between the two atoms. We perform the experiment in the same conditions as above, see Figure 8.4 a). We start by preparing the system in the $|\uparrow\downarrow\rangle$ state, observe the coherent exchange and discuss the various limits in the system's coherence and the contrast in the exchange. We finally discuss the link between this experiment and the Bose-Hubbard model for hard-core bosons.

Experimental sequence. We prepare the state $|\uparrow\downarrow\rangle$ following the procedure sketched in Figure 8.4 b). We excite the atoms to the $|\downarrow\downarrow\rangle$ state using the STIRAP technique, then apply a microwave π-pulse to transfer the atoms to the $|\uparrow\uparrow\rangle$ state. We use $\Omega_{MW} \simeq 2\pi \times 18\,\mathrm{MHz} \gg J$ to avoid populating the $|+\rangle$ state. In order to selectively transfer a single atom back to the $|\downarrow\rangle$ state, we use a single-site addressing beam at 1013 nm (see Section 2.3.3) which shifts the $|\uparrow\rangle \rightarrow |\downarrow\rangle$ transition by an energy $\delta_{addr} \sim 2\pi \times 20\,\mathrm{MHz}$ for only one atom. We then apply a second π-pulse with the condition $\Omega_{MW} \simeq 2\pi \times 2\,\mathrm{MHz} \ll \delta_{addr}$ to avoid the transfer of the addressed atom. Once the system is in $|\uparrow\downarrow\rangle$, we switch off the addressing and let the system evolve under
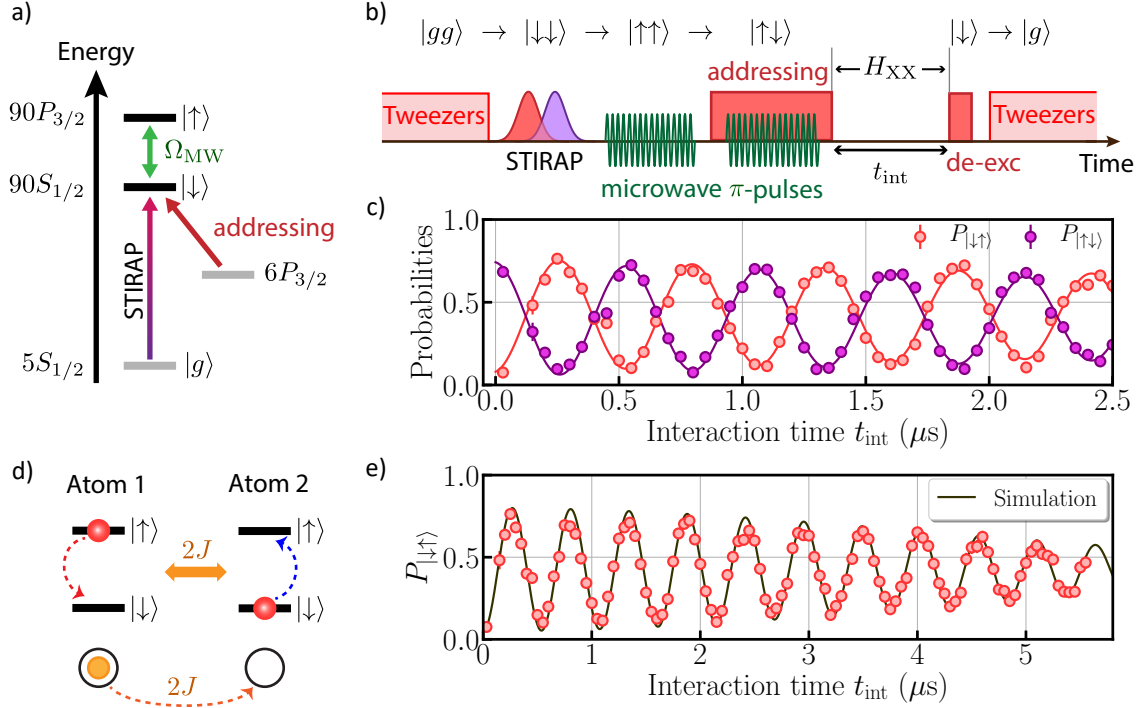
Figure 8.4: Coherent transfer of an ↑ excitation between two Rydberg atoms. a) Sketch of the single-atom levels. b) Sketch of the experimental sequence. We prepare the $|\uparrow\downarrow\rangle$ state using a single-site addressing beam (see Section 2.3.3), let the system freely evolve for a duration t_{int}, then read the system's state using a de-excitation beam (see Section 2.3.1). c) Probability for the atoms to be in the $|\uparrow\downarrow\rangle$ state (purple) and in the $|\downarrow\uparrow\rangle$ state (red) as a function of t_{int}. The system oscillates between these two states. The solid lines are fits to the data using damped sine functions. d) The oscillation can be seen as a coherent transfer of the ↑ excitation between the two atoms. e) Comparison of the experimental results of c) with simulations, including longer times. The black line is a simulation taking into account the finite efficiency of the $|\uparrow\downarrow\rangle$ preparation and the shot-to-shot fluctuations of the atom positions.

H_{XX} for a duration t_{int}. We then rapidly de-excite the atoms in $|\downarrow\rangle$ back to the ground state in $\sim 50\,\text{ns}$ (see Section 2.3.1) to freeze the dynamics and read the system's state. We perform the experiment for various t_{int}, and measure the populations in $|\uparrow\downarrow\rangle$ and $|\downarrow\uparrow\rangle$, see Figure 8.4 c).

Spin-exchange. We observe an oscillation between the $|\uparrow\downarrow\rangle$ and the $|\downarrow\uparrow\rangle$ state, which is expected in the XX model. As the initial state is $|\uparrow\downarrow\rangle = (|+\rangle + |-\rangle)/\sqrt{2}$, and the $(|+\rangle, |-\rangle)$ states have eigenergies $(J, -J)$, the system evolves as $(|+\rangle + e^{i2Jt_{\text{int}}/\hbar}\sqrt{2}|-\rangle)/\sqrt{2}$. In particular, for $t_{\text{int}} = h/(4J)$, the system's state is $(|+\rangle -$

185

$|-\rangle)/\sqrt{2} = |\downarrow\uparrow\rangle$. The system thus oscillates between $|\uparrow\downarrow\rangle$ and $|\downarrow\uparrow\rangle$ at a frequency $2J/h$. We experimentally check that we obtain the correct oscillation frequency by fitting the data using damped sine functions (solid lines). We extract an oscillation frequency $2J/h = 1.85(1)$ MHz, in good agreement with $J/h = 0.91(1)$ MHz determined above with the magnetization oscillation experiment.

Analysis of the contrast and the damping. We briefly discuss here the finite contrast of the oscillation and its damping. The contrast is limited by the efficiency of the $|\uparrow\downarrow\rangle$ state preparation, with typical values $P_{\uparrow\downarrow} \sim 0.7$. The major limitation is the Rydberg excitation efficiency. For the experiment conducted here, the efficiency of the STIRAP technique is ~ 0.92 per atom, which gives $P_{\downarrow\downarrow} \sim 0.85$. The first microwave pulse is close to be perfect, however we observed that the second one (in presence of the addressing) has a finite efficiency, and the fidelity of the preparation is ~ 0.95 per atom. Adding the detection errors to misinterpret the states of the atoms $\varepsilon \sim 0.02$ and $\varepsilon' \sim 0.02$ (see Section 3.3.1), we obtain $P_{\uparrow\downarrow} \sim 0.7$.

We now analyze the damping of the spin-exchange experiment. In order to appreciate the damping, we show in Figure 8.4 e) the results presented above of $P_{\downarrow\uparrow}$ over an extended duration (the conclusions obtained here are the same for $P_{\uparrow\downarrow}$). The black line is a simulation taking into account (i) the finite efficiency of the preparation and (ii) the shot-to-shot fluctuations of the interatomic distance (see Section 6.2.2). We observe that the damping is well reproduced by the simulation, showing that other sources of decoherence are negligible.

These results show that, for the simplest case of two atoms, we are able to observe the interaction-induced transport dynamics of an $\uparrow$ excitation. The extension of this experiment to the many-body case is the subject of Section 9.2.

Link to the Bose-Hubbard model. This experiment can be seen as a particle (a $\uparrow$ excitation) hopping between two sites (the two Rydberg atoms), with a hopping strength $2J$ (see Figure 8.4 d)). We define the states $|0\rangle = |\downarrow\rangle$, $|1\rangle = |\uparrow\rangle$, the bosonic annihilation and creation operators $b_i^\dagger |0\rangle = |1\rangle$ and $b_i |1\rangle = |0\rangle$ for site $i \in [1, 2]$. However, as a Rydberg atom can only carry a single $\uparrow$ excitation, the operators verify the relation $(b^\dagger)^2 = b^2 = 0$. This property is referred as the hard-core boson constraint. We used this feature to prepare a symmetry protected topological phase in 1D, described in detail in the thesis of Sylvain de Léséleuc [2018]. The Hamiltonian then reads:

$$H_{\mathrm{BH}} = 2J(b_1^\dagger b_2 + b_2^\dagger b_1), \tag{8.6}$$

where $2J$ is the tunneling strength. This Hamiltonian describes the Bose-Hubbard model in the limit where the on-site interaction energy is infinite. We will use this description in terms of bosonic operators in the next section.

Conclusion. In this section, I presented the two main features of the XX model we will study on many-body systems in Chapter 9. I showed that we can accurately observe these features, and link the spin-exchange experiment to the Bose-Hubbard model for hard-core bosons.

8.3 Implementation of a density-dependent Peierls phase with three atoms

In this section, I explain how we go beyond this hopping of excitations and engineer *complex* hopping amplitudes between Rydberg atoms using the spin-orbit coupling of the dipole-dipole interaction (see Equation (8.3)). The discussions and experimental protocols presented here are, most of them, also presented in the thesis of Vincent Lienhard [2019]. However, after his pioneering work, we modified the parameters of the experiments to obtain more convincing data, published in [Lienhard *et al.*, 2020], which I show here.

Motivations. One of the current challenges of quantum simulators is to investigate the interplay between the non-trivial topology of a band-structure and the interactions between the particles [Bergholtz and Liu, 2013; Cooper, Dalibard, and Spielman, 2019]. The topology of a band-structure can be studied from the single-particle transport properties of the system. The signature of topological properties for finite-size systems is the existence of chiral edge modes, characterized by the circular motion of the particle along the edges of the system, in a preferential direction (this feature is also known as the "bulk-edge" correspondence). The systems hosting chiral edge modes are called topological insulators, as they are conducting on the edges but insulating in the bulk. They trigger a lot of interest due to their unique transport properties [Moore, 2010; Wang, Dou, and Zhang, 2010].

Experimental realization on synthetic platforms. One way to engineer such topological band structures is to implement an effective magnetic field for the hopping particles, which can be simulated by implementing complex hopping amplitudes

$te^{i\varphi}$ between the sites of an array, characterized by a Peierls phase φ [Hofstadter, 1976; Jaksch and Zoller, 2003; Dalibard *et al.*, 2011; Goldman and Dalibard, 2014]. A particle circulating around a closed loop then acquires a phase analog to the Aharonov-Bohm phase, which is proportional to the enclosed magnetic flux [Aharonov and Bohm, 1959]. Effective magnetic fields and complex-valued hopping amplitudes have been implemented on ultra-cold atom-based platforms [Aidelsburger *et al.*, 2011; Galitski and Spielman, 2013; Zhai, 2015], by using laser-assisted tunneling in an optical superlattice [Aidelsburger *et al.*, 2011], high-frequency driving of a lattice [Kolovsky, 2011; Jotzu *et al.*, 2014; Wang *et al.*, 2020], and implementing synthetic dimensions [Mancini *et al.*, 2015; Stuhl *et al.*, 2015]. Alternative platforms have also emerged such as superconducting qubits where complex-valued hopping amplitudes were demonstrated [Roushan *et al.*, 2017], and photonic [Ozawa *et al.*, 2019] or phononic [Liu, Chen, and Xu, 2020] systems operating so-far in the non-interacting regime.

Outline. Here, I present the experimental realization of Peierls phases using the intrinsic spin-orbit coupling present in dipolar exchange interactions between Rydberg atoms, initially proposed theoretically [Peter *et al.*, 2015; Kiffner, O'Brien, and Jaksch, 2017; Weber *et al.*, 2018]. I first explain how we experimentally implement these complex hopping amplitudes using three Rydberg levels in a V-structure. Operating at the single-particle level, I explain how we can use this complex hopping to observe a chiral motion on a minimal setup of three atoms. I finally show how this complex hopping is modified by the presence of other particles, thus creating a density-dependent hopping. The majority of the results were presented here are published in Lienhard *et al.* [2020], and the text here is adapted from this publication.

8.3.1 Spin-orbit coupling in a V-structure and effective model

We use the intrinsic spin-orbit coupling of the dipole-dipole interaction: $\hat{d}_1^+ \hat{d}_2^+ e^{-2i\phi} + \hat{d}_1^- \hat{d}_2^- e^{2i\phi}$ (see Equation (8.3)) to implement a complex hopping. This term couples two-atom states with different total internal angular momentum. We thus need to work with three Rydberg states in a V-structure. Here, we choose the states $|0\rangle = \left|60S_{1/2}, m_J = 1/2\right\rangle$, $|-\rangle = \left|60P_{3/2}, m_J = -1/2\right\rangle$ and $|+\rangle = \left|60P_{3/2}, m_J = 3/2\right\rangle$, see Figure 8.5 a).

In order to isolate this V-structure from the other states, we apply (i) a magnetic field $B_z \simeq -8.5\,\text{G}$ and (ii) an electric field $E_z \simeq 0.4\,\text{V/cm}$ (see Section 2.4.2). Both fields are
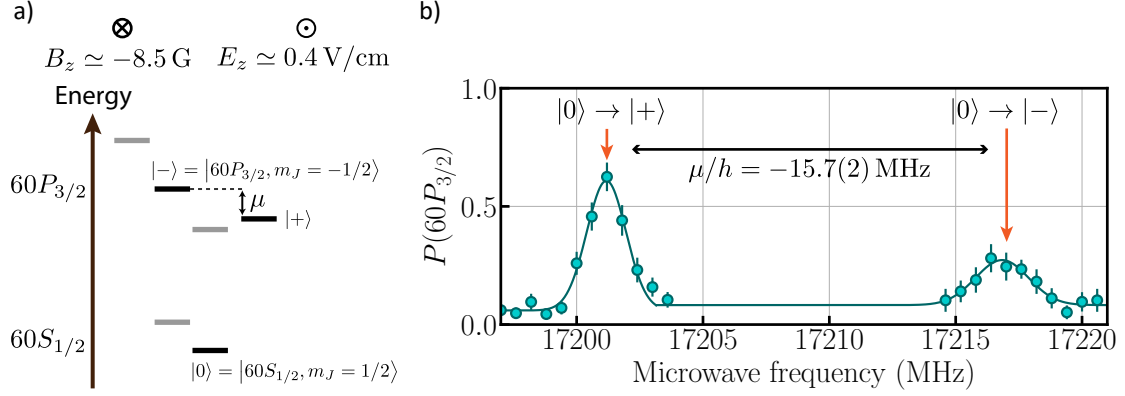
Figure 8.5: Spectroscopy of the V-structure. a) Sketch of the three levels used in this work. The three levels in a V-structure (highlighted in black) involved in the implementation of the complex interaction are: $|0\rangle = |60S_{1/2}, m_J = 1/2\rangle$, $|+\rangle = |60P_{3/2}, m_J = 3/2\rangle$ and $|-\rangle = |60P_{3/2}, m_J = -1/2\rangle$. The energy difference μ between $|+\rangle$ and $|-\rangle$ is controlled by DC magnetic B_z and electric fields E_z perpendicular to the atomic array. b) Microwave spectroscopy with $B_z \simeq -8.5$ G and $E_z \simeq 0.4$ V/cm G, from which we extract $\mu/h = -15.7(2)$ MHz.

perpendicular to the atomic array. The magnetic field lifts the degeneracy between all the Zeeman sublevels, whilst the electric field allows us to shift the $|60P_{3/2}, m_J = 1/2\rangle$ state away from the V-structure. We define the energy difference between the $|+\rangle$ and $|-\rangle$ states: $\mu = E(|+\rangle) - E(|-\rangle)$. In the following, we intentionally set a relatively high value for μ compared to the interaction energies, such that the spin-orbit coupling is an off-resonant process and can be treated perturbatively (see below). The target value for μ is not as high as in Section 8.2 to still see the effect of the spin-orbit coupling term. A good control over the value of μ is thus required. We measure $\mu/h = -15.7(2)$ MHz by performing microwave spectroscopy of the $60S_{1/2} \rightarrow 60P_{3/2}$ transition, see Figure 8.5 b). In the following, we only consider the three states of the V-structure.

Dipole-dipole interaction in the V-structure.   We consider three Rydberg atoms (denoted as 1, 2 and 3) arranged in an equilateral triangle with side length $r_{12} = 11\,\mu$m, each of them displaying the V-structure described above, see Figure 8.6 a). For each atom pair (i, j), the internuclear axis forms an angle ϕ_{ij} with the x axis. The

Hamiltonian describing the system is:

$$H = \sum_{i \neq j} \begin{pmatrix} a_i^\dagger & b_i^\dagger \end{pmatrix} \begin{pmatrix} -t_b & w e^{-i2\phi_{ij}} \\ w e^{i2\phi_{ij}} & -t_a \end{pmatrix} \begin{pmatrix} a_2 \\ b_2 \end{pmatrix} + \sum_i \frac{\mu}{2} \left(n_i^a - n_i^b \right), \qquad (8.7)$$

where the two bosonic operators $a_i^\dagger$ and $b_i^\dagger$ on site i are defined by $a_i^\dagger |0\rangle = |+\rangle_i$, $b_i^\dagger |0\rangle = |-\rangle_i$, and $n^a = a^\dagger a$, $n^b = b^\dagger b$. The hopping amplitudes are related to the dipole matrix elements (see Equation (8.3)) by:

$$t_{a,b} = \frac{|\langle \pm | \hat{d}_+ |0\rangle|^2}{8\pi\epsilon_0 r_{12}^3}, \quad w = \frac{3 \langle + | \hat{d}_+ |0\rangle \langle 0 | \hat{d}_- |-\rangle}{8\pi\epsilon_0 r_{12}^3} \qquad (8.8)$$

and $n_i^{a,b} = |\pm\rangle \langle \pm|$ are the excitation density operators. For the distance $r_{12} = 11\,\mu\mathrm{m}$ between the atoms considered here, we measure $t_a/h \simeq 1.5\,\mathrm{MHz}$ and $t_b/h \simeq 0.55\,\mathrm{MHz}$ by performing the spin-exchange experiment described in Section 8.2.3. These values are in good agreement with theoretical calculations of the interaction energies [Weber *et al.*, 2017]. We then deduce $w/h \simeq 2.7\,\mathrm{MHz}$ using the above equations (see also Figure 8.1).

The various terms of the Hamiltonian are sketched in Figure 8.6 b) and can be understood as follows. Considering a $|-\rangle$ excitation on site i and a vacancy $|0\rangle$ on site j, there are two ways for the excitation to hop to site j: (i) via a direct hopping with amplitude $-t_b$ (diagonal term in the Hamiltonian), or (ii) the $|-\rangle$ excitation is annihilated from site i and a $|+\rangle$ excitation is created on site j, with amplitude $w e^{-2i\phi_{ij}}$ (off-diagonal term in the Hamiltonian). As the internal momentum is *increased* by two quanta, the orbital phase factor is $e^{-2i\phi_{ij}}$. Because the $|+\rangle$ and $|-\rangle$ states are not degenerated in energy, the latter process has a cost $\mu/h = -15.7(2)\,\mathrm{MHz}$. As $\mu \gg w$, the probability for the internal state-flipping process to happen is weak. This means that a $|-\rangle$ excitation only has a small probability of becoming a $|+\rangle$ excitation. We use this feature to derive an effective spin-1/2 Hamiltonian by adiabatically eliminating the $|+\rangle$ state, which gives rise to a complex hopping amplitude for the $|-\rangle$ excitation.

Adiabatic elimination of the $|+\rangle$ state and effective Hamiltonian. We now derive the expression of the complex hopping amplitude of a $|-\rangle$ excitation. For this demonstration, we suppose that we prepare the system in the state $|-00\rangle$. As the internal state-flipping hopping is off-resonant, the $|-\rangle$ excitation only has a small probability of becoming a $|+\rangle$ excitation. In addition, as the interaction conserves the number of excitations, once the atoms are initialized in the $|-00\rangle$ state, they mostly
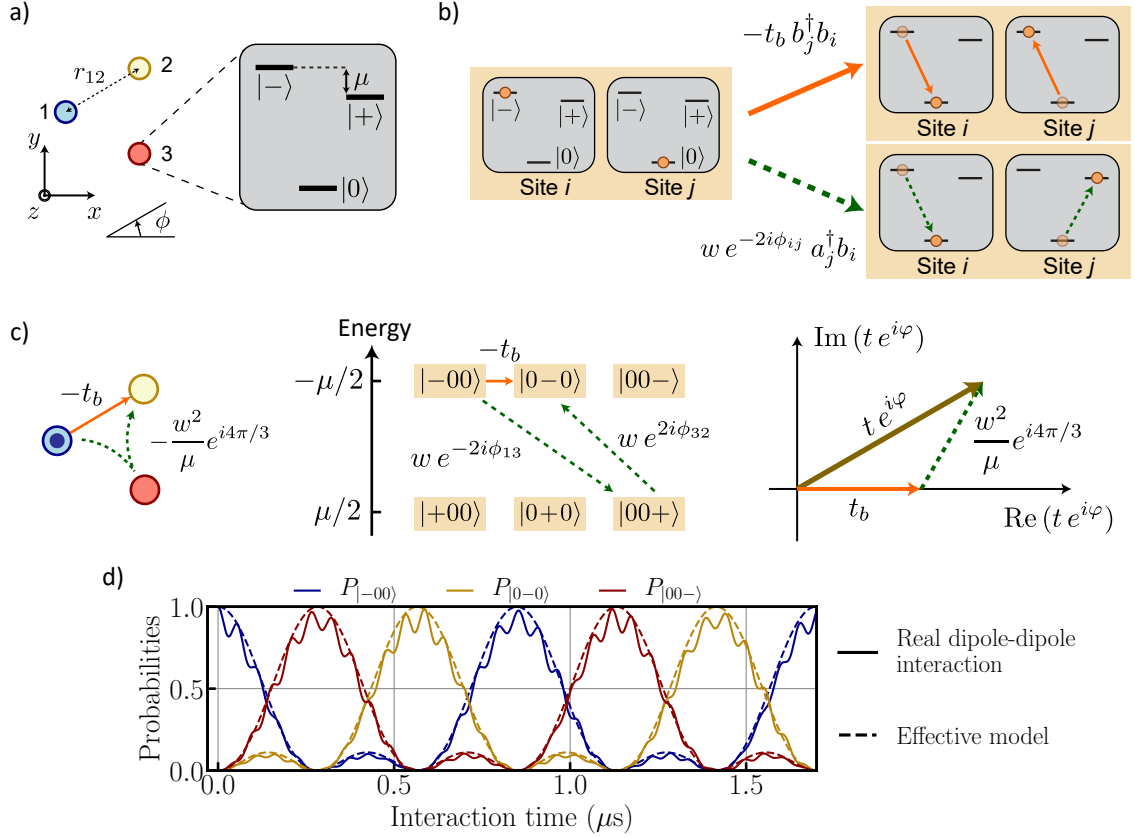
Figure 8.6: Spin-orbit coupling in a triangle and effective model. a) Experimental configuration of three atoms arranged in an equilateral triangle. We consider for each of them the $|0\rangle$, $|+\rangle$ and $|-\rangle$ states. b) The two processes for a $|-\rangle$ excitation to hop from site i to site j: the $|-\rangle$ excitation is annihilated on site i, and a $|-\rangle$ (solid arrow) or a $|+\rangle$ (dashed arrow) excitation is created on site j. c) The hopping of a $|-\rangle$ excitation from $|-00\rangle$ to $|0-0\rangle$ can be seen, in an effective picture, as the sum of (i) the direct hopping with amplitude $-t_b$, and (ii) two virtual hoppings through $|00+\rangle$ with amplitude $w^2 e^{i4\pi/3}/\mu$. This leads to an effective complex hopping amplitude $te^{i\varphi}$. d) Calculated evolution of the site probabilities after preparing $|-00\rangle$, for the effective model with hopping amplitude $te^{i\varphi}$ with $\varphi = \pi/6$ (dashed lines), and for our experimental implementation considering the V-structure (solid lines). The excitation does not spread as time flows, and moves from site to site in a chiral way.

remain in the one excitation subspace consisting of the states $|-00\rangle$, $|0-0\rangle$ and $|00-\rangle$. The hopping of a $|-\rangle$ excitation from site 1 to 2, i.e., the change of the three-atom state from $|-00\rangle$ to $|0-0\rangle$ (see Figure 8.6 c)), proceeds either by a direct hopping with amplitude $-t_b$, or by a second-order coupling via the intermediate state $|00+\rangle$ consisting in two successive flips of the internal state. The latter has an amplitude $-w^2 \, e^{2i(\phi_{32}-\phi_{13})}/\mu$, with $\phi_{32} - \phi_{13} = 2\pi/3$. Consequently, the hopping amplitude $-te^{i\varphi}$ from site 1 to 2 is the sum of the amplitudes of these two processes

$$te^{i\varphi} = t_b + e^{i4\pi/3}\frac{w^2}{\mu}. \tag{8.9}$$

The representation of the amplitudes in the complex plane is shown in Figure 8.6 c). In this perturbative picture, the $|+\rangle$ excitation is adiabatically eliminated, and the problem reduces to the hopping of the $|-\rangle = b_i^\dagger|0\rangle$ excitation described by the effective Hamiltonian

$$H_{\text{eff}} = -t \sum_{i=1}^{3} \left[e^{i\varphi}b_{i+1}^\dagger b_i + e^{-i\varphi}b_i^\dagger b_{i+1} \right] \;, \tag{8.10}$$

with $b_4 \equiv b_1$. The Peierls phase φ can be interpreted as the result of an emergent gauge field and the magnetic flux through the triangle is thus 3φ. Experimentally, both the effective hopping amplitude t and the flux 3φ are controlled by the distance between the atoms and the energy separation μ. For non-zero flux (modulo π), the excitation exhibits a chiral motion when evolving in the triangle. In particular, for $3\varphi = \pm\pi/2$ [Roushan et al., 2017], the excitation hops sequentially from site to site in a preferred direction. Figure 8.6 d) shows the expected motion: we plot the site probabilities as a function of time (i) in the case of the complex hopping of a $|-\rangle$ excitation described by the effective Hamiltonian (8.10) (dashed lines), and (ii) for the three-level structure involving the $|+\rangle$ state, governed by the Hamiltonian (8.7) (solid lines). The fast oscillations exhibit a frequency close to μ/h, and result from the non-perfect elimination of the $|+\rangle$ state. We now present the experimental results.

8.3.2 Observation of chiral motion

Experimental sequence. To experimentally demonstrate the chiral motion of a $|-\rangle$ excitation resulting from the complex hopping of Equation (8.9), we perform the sequence described in Figure 8.7 a). After initializing the atoms into $|g\rangle = \left|5S_{1/2}, F = 2, m_F = -2\right\rangle$ using optical pumping, we rotate the magnetic field along B_z (see Section 2.4.1). For $B_z < 0$ the resulting atomic state is thus $\left|5S_{1/2}, F = 2, m_z = 2\right\rangle$.

After switching off the dipole traps, we prepare the $|000\rangle$ state in $2\,\mu\mathrm{s}$ using a STImulated Raman Adiabatic Passage (STIRAP) (see Section 2.3.1) via the intermediate state $\left|5P_{1/2}, F = 2, m_z = 2\right\rangle$ (this experiment was performed with the previous excitation scheme, see Chapter 3). Finally, we address atom 1 with a focused laser beam tuned near the $6P_{3/2} - 60S_{1/2}$ transition (see Section 2.3.3), which light shifts the transition frequency by $\sim 6\,\mathrm{MHz}$, and apply a 400 ns microwave π-pulse resonant with the *light-shifted* $|0\rangle \rightarrow |-\rangle$ transition. This prepares a $|-\rangle$ excitation on site 1.

After the preparation of the system in the state $|-00\rangle$, we let it evolve under the action of the dipole-dipole interaction for a time t_{int}. We then apply a 400 ns read-out pulse to de-excite the atoms in $|0\rangle$ back to the $5S_{1/2}$ manifold, and switch on the dipole traps again. Atoms in the $5S_{1/2}$ state are recaptured, whereas atoms still in Rydberg states are lost (see Section 2.3.2). A final fluorescence image reveals, for each site, if the atom is in the $|0\rangle$ state (the atom is recaptured), or in another Rydberg state (the atom is lost). Our detection method does not distinguish between these other Rydberg states, including $|+\rangle$ and $|-\rangle$. We will denote the Rydberg states other than $|0\rangle$ as a single state $|1\rangle$. As the $|+\rangle$ subspace is hardly populated in our experiment, the loss of an atom corresponds mainly to its detection in the $|-\rangle$ state.

Chiral motion. The result of this first experiment is presented in Figure 8.7 b), where we show the three-site probabilities to be in the states $|100\rangle$, $|010\rangle$ and $|001\rangle$ as a function of the interaction time t_{int}. As expected, we observe a chiral motion of a localized $|-\rangle$ excitation in the counterclockwise direction $1 \rightarrow 3 \rightarrow 2 \rightarrow 1$. This is the signature of an effective magnetic field acting on the hopping excitation, described by the Peierls phases. The fact that the three probabilities do not sum to 1 comes from the imperfect preparation of the state $|100\rangle$ and detection errors.

To reverse the direction of motion, we reverse the sign of B_z after the optical pumping stage. The initial atomic state is now $\left|5S_{1/2}, F = 2, m_z = -2\right\rangle$. In this configuration, following the Rydberg excitation, the V-structure in the Rydberg manifold involves $|0\rangle = \left|60S_{1/2}, m_J = -1/2\right\rangle$, $|+\rangle = \left|60P_{3/2}, m_J = -3/2\right\rangle$, and $|-\rangle = \left|60P_{3/2}, m_J = +1/2\right\rangle$. The value of μ remains unchanged, as the Stark shift only depends on $|m_j|$. The hopping of a $|-\rangle$ to a $|+\rangle$ excitation now corresponds to a *decrease* of the internal momentum by two quanta: the orbital phase factor is thus $\mathrm{e}^{2i\phi_{ij}}$, and the sign of the Peierls phase is changed. Figure 8.7 c) shows the same three-site probabilities as in Figure 8.7 c) for this opposite direction of B_z. As expected, we now observe a chiral motion of the $|-\rangle$ excitation in the clockwise direction $1 \rightarrow 2 \rightarrow 3 \rightarrow 1$.
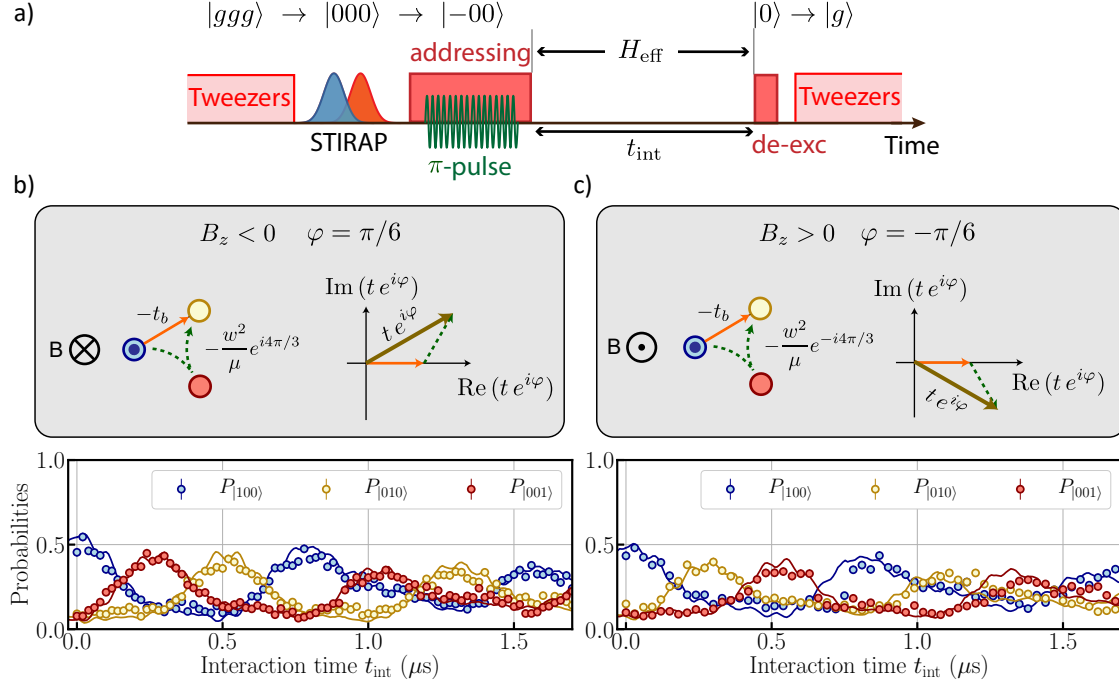
Figure 8.7: Observation of the chiral motion of a single $|-\rangle$ excitation. a) Sketch of the experimental sequence. We prepare the state $|-00\rangle$ using a single-site addressing which light-shifts atom 1, then apply the microwave field at the light-shifted transition. We then let the system freely evolve for a duration t_{int}, and finally lift the dynamics and read the system's state by de-exciting the atoms in $|0\rangle$ to the ground state. b) and c) Evolution of the three-site probabilities to be in the states $|100\rangle$, $|010\rangle$ and $|001\rangle$ as a function of t_{int} for two opposite directions of B_z. The solid lines are simulations including experimental errors in the preparation and the detection, as well as shot-to-shot fluctuations in the atomic position (which lead to the observed damping of the oscillations).

Comparison to simulations. Finally, we compare the experimental data for the chiral motion in both directions with a theoretical model solving the Schrödinger equation for this three-atom system including all the Zeeman sublevels of the $60S_{1/2}$ and $60P_{3/2}$ manifold, and the full dipole-dipole interaction. The simulations were performed by the team of H.P. Büchler. The simulations take into account the full experimental protocol to prepare the $|-00\rangle$ excitation: (i) the finite efficiency of the STIRAP process of 83% and (ii) a leakage to the other states outside the V-structure of 5% when performing the microwave π-pulse. We also consider shot-to-shot fluctuations of the positions of the atoms (see Section 6.2.2). Importantly, due to these fluctuations, the atoms can also be positioned in such a way that the interatomic axis is not exactly perpendicular to the quantization axis. In this case, the dipolar interaction can change

the magnetic quantum number by one, provoking additional leakage to states outside the V-structure. These experimental imperfections are responsible for the observed damping of the dynamics.

These imperfections are included in the simulations by sampling over 500 different realizations of the initial configuration of the triangles. Finally, detection errors are included through a Monte Carlo sampling of the numerical results. In the simulations we account for the fact that the detection scheme does not distinguish between states other than $|0\rangle$ by computing the probabilities $P_{|100\rangle}$, $P_{|010\rangle}$ and $P_{|001\rangle}$ as measured in the experiment. In both situations, we obtain a good agreement with the model, which reproduces the frequency, the amplitude and the damping of the chiral motion.

8.3.3 Tunability of the Peierls phase

Now that we observed the chiral motion of a $|-\rangle$ excitation, we demonstrate the control of the Peierls phase by tuning the geometry of the triangle, while keeping the same value for μ. To do so, we study an isosceles triangle parametrized by the angle γ, see Figure 8.8 a). In this configuration, the distance between sites 1 and 3 varies with γ. The effective coupling, and hence the Peierls phase, is then different for each link: the direct hoppings are $t_{12} = t_{23}$ and $t_{13} = \kappa t_{12}$ with $\kappa = 1/(2\cos[\gamma/2])^3$; the virtual coupling are $\kappa w^2 e^{i\gamma}/\mu$ for the $1 \to 2$ and $2 \to 3$ couplings and $w^2 e^{-2i\gamma}/\mu$ for the $3 \to 1$ coupling. The variation of the gauge flux through the triangle, which is the sum of the three Peierls phases, is represented in Figure 8.8 b) as a function of the angle γ. It exhibits an almost linear dependence for $\gamma \in [0°, 90°]$.

We show that we accurately control the gauge flux by observing the dynamics of an initially prepared state $|0-0\rangle$ for various angles γ, see Figure 8.8 c). For $\gamma = 0°$, the hopping is real and the propagation is symmetric, as performed in our very first implementation of the coherent transfer of an excitation in a chain of three atoms [Barredo *et al.*, 2015]. Interestingly enough, the gauge flux also cancels for an angle $\gamma \simeq 75°$, which we observe experimentally. Depending on the value of γ, we can force the excitation to propagate clockwise ($\gamma = 45°$) or preferentially towards atom 1 ($\gamma = 90°$).

In order to grasp these results under a single observable which characterizes the preferential direction of the excitation, we compute the population imbalance between site 1 and site 3, $\mathcal{I} = (P_{|100\rangle} - P_{|001\rangle})/(P_{|001\rangle} + P_{|100\rangle})$, at time $t_{\text{int}} = 0.4\,\mu$s for various angles γ, see Figure 8.8 d). We choose $t_{\text{int}} = 0.4\,\mu$s as it corresponds to the excitation mainly located on sites 1 and 3 for $\gamma = 0°$. For a negative flux (modulo 2π) the
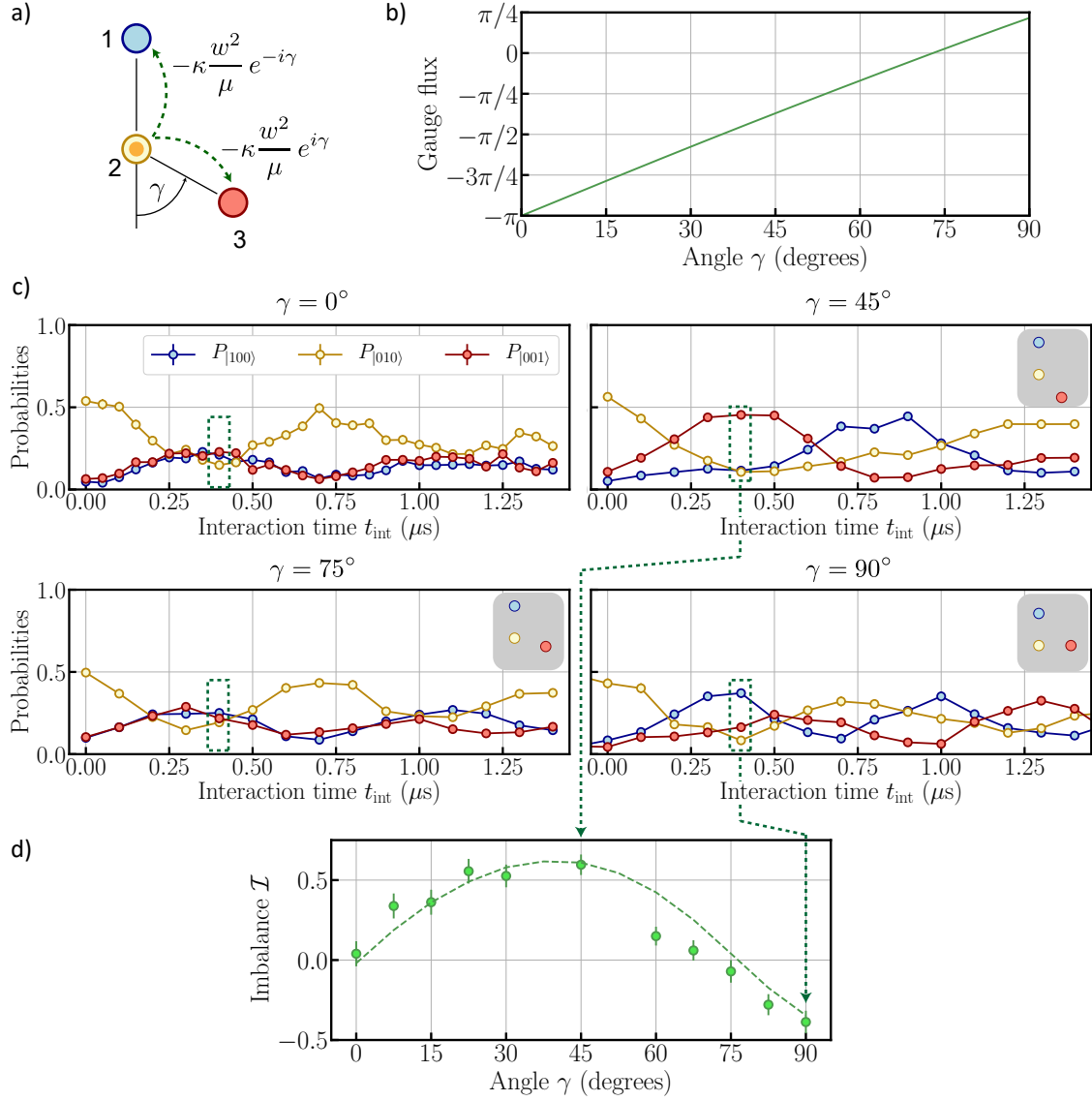
Figure 8.8: Tunability of the Peierls phase. a) Tunable geometry used for this experiment based on an isosceles triangle with $r_{12} = r_{23} = 11\,\mu$m. b) Calculated evolution of the magnetic flux threading through the isosceles triangle as a function of γ. c) Evolution of the system after preparing the state $|0{-}0\rangle$ for various angles γ. We can tune the system to observe (i) a symmetric propagation ($\gamma = 0°$ and $\gamma \simeq 75°$), (ii) a clockwise propagation ($\gamma = 45°$) or propagation preferentially towards atom 1 ($\gamma = 90°$). d) We record the imbalance $\mathcal{I}$ between the preferential propagation towards atom 1 ($\mathcal{I} > 0$) or 3 ($\mathcal{I} < 0$) after $t_{\text{int}} = 0.4\,\mu$s as a function of γ. The dashed line is the simulation.

excitation propagates towards site 1, while it propagates towards site 3 for a positive flux, as expected. The data are in good agreement with the simulation of the dynamics of the system (dashed line).

8.3.4 The two excitation case

Now that we have described the dynamics of single-particle systems and shown a good understanding and control over the Peierls phase, we move on to the study of the dynamics of two excitations. For ensembles of two-level atoms in resonant interaction, the excitations can be mapped onto hard-core bosons. A natural question to ask in our present multi-level situation is the consequence of the hard-core constraint on the dynamics of the $|-\rangle$ excitations.

In order to explore this experimentally, we arrange the atoms in a equilateral triangle and initialize the three-atom system with two $|-\rangle$ excitations on sites 2 and 3, while site 1 is in state $|0\rangle$, thus preparing the three atom state $|0--\rangle$ (see Figure 8.9 a)). To do so we again use the addressing laser on site 1, but tune the π microwave pulse on resonance with the *free space* $|0\rangle \rightarrow |-\rangle$ transition. As we drive the microwaves on two interacting atoms, the transition is harder to achieve as we need to fulfill the condition $\Omega_{\mathrm{MW}} \gg t_{\mathrm{b}}$ in order to efficiently populate the $|\uparrow\uparrow\rangle$ state. We perform the π rotation in 200 ns and light shift atom 1 by $\sim 35\,\mathrm{MHz}$.

In the case of hard-core bosons evolving with the Hamiltonian in Equation (8.10), one would expect the hole (state $|0\rangle$) to propagate in the opposite direction to the single $|-\rangle$ excitation case, as observed using superconducting circuits [Roushan *et al.*, 2017]. The result of our experiment is presented in Figure 8.9 b), where we use the same parameters as for the single excitation experiment, i.e., a Peierls phase $\varphi = \pi/6$. Remarkably, here we do not observe any chiral motion: the hole state $|0\rangle$ propagates almost symmetrically towards sites 2 and 3, suggesting that the hopping amplitude between sites is now real, and that the description of the dynamics by the Hamiltonian (8.10) is no longer valid. The simulations (solid lines) validate this observation. This indicates that the hard-core constraint between the excitations $|-\rangle$ influences the induced Peierls phases.

Density-dependent hopping. To understand this, we come back to the hard-core constraint in our system. Two particles, irrespective of their internal state $|+\rangle$ or $|-\rangle$, can not reside on the same site. As a consequence, the effective hopping from site 1 to 2 is modified if an excitation is already present on site 3: this suppresses the

a)

b)

c)

Energy
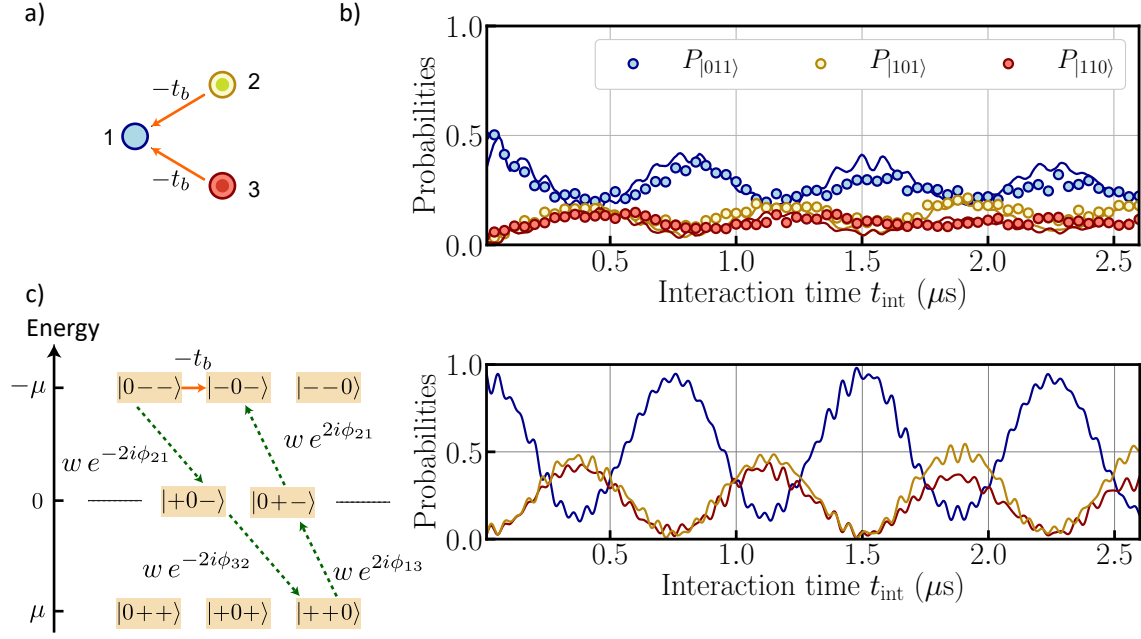
Figure 8.9: Density-dependent hopping. a) The presence of a $|-\rangle$ excitation on site 3 prevents the internal state-flipping process responsible for the complex hopping of the $|-\rangle$ excitation from 2 to 1: only the real coupling remains. b) Probability to be in the doubly excited three-site states $|011\rangle$ (targeted initial state), $|101\rangle$ or $|110\rangle$ as a function of t_{int}. The solid line is the simulation which takes into account experimental parameters, including state preparation. c) Simulations in an ideal case including the three levels of the V-structure. As displayed on the data, we observe a slow chiral motion towards populating the $|101\rangle$ state. This feature results from a fourth-order process via $|0++\rangle$.

off-resonant process, which is at the origin of the complex hopping amplitude in the single excitation case, leaving only the direct hopping described by $-t_b$. Therefore, the hard-core constraint generates a density-dependent hopping, where the phase of the hopping amplitude, as well as its strength, depends on the occupation of the third lattice site. The effective Hamiltonian describing this situation generalizes the one of Equation (8.10) to the case of more than one $|-\rangle$ excitation:

$$H_{\text{eff}}^{\text{many}} = -t \sum_{i=1}^{3} \left[e^{i\varphi(1-n_{i+2})} b_{i+1}^{\dagger} b_i + \Delta b_{i+1}^{\dagger} b_i n_{i+2} + \text{h.c.} \right] \qquad (8.11)$$

with $n_{i+2} = b_{i+2}^{\dagger} b_{i+2}$ the occupation of the third site and $\Delta = (t_b - t)/t$. The first term in the effective Hamiltonian shows that the Peierls phase is now density-dependent. The second term describes a conventional correlated hopping, which does not modify

the real or complex nature of the couplings between sites [Lienhard *et al.*, 2020]. In addition, the adiabatic elimination leads to two-body interactions terms $\propto (w^2/\mu)n_i n_j$, that do not play a role in an equilateral triangle and that we therefore drop.

Interpretation in terms of anyonic statistics. The influence of the density-dependent Peierls phases on the hopping amplitudes has a simple interpretation in terms of abelian anyonic particles in one-dimension in the absence of a magnetic field [Fradkin, 1991; Zhu and Wang, 1996; Kundu, 1999; Keilmann *et al.*, 2011; Greschner and Santos, 2015]. Here, we obtain anyonic particles with a hard-core constraint and a statistical angle 3φ. For this mapping, we use a particle-hole transformation and interpret a single hole as an anyonic particle. In the absence of a gauge field, a single anyon (a hole) exhibits a symmetric dynamics in a triangle, which is the result observed in Figure 8.9 b). Now placing two anyons (two holes) in the triangle, we are back to the case studied in Section 8.3.2, where we observe a chiral motion (see Figure 8.7 b) and c)): in the anyon interpretation, this is due to the statistical phase under exchange of the two anyonic particles or equivalently to the fact that one of the two anyonic particles carries a magnetic flux for the other one. The value of this magnetic flux through the triangle is the statistical phase of these anyons. The mapping onto anyons can be made rigorous and is presented in the supplemental material of Lienhard *et al.* [2020].

Fourth-order process. We still observe a residual asymmetry in the dynamics, see Figure 8.9 b), which is also present in the simulation. This indicates that the complex-valued hopping is not fully suppressed. Following the same effective Hamiltonian approach as the one outlined in Section 8.3.1, the internal state-flipping hopping is now a fourth-order process, see Figure 8.9 c). Considering the hopping from site 1 to site 2, the hole can directly hop with an amplitude $-t_b$, or virtually go through $|++0\rangle$, leading to a total amplitude $te^{i\varphi} = t_b + w^4/\mu^3 e^{-4i\pi/3}$. As $w \ll \mu$, the complex part of this hopping is extremely small compared to the single particle case, thus leading to the observed quasi-symmetric dynamics.

Extension towards larger number of atoms. I presented in this section our experimental implementation of a complex, density-dependent hopping amplitude on the minimal setup of three Rydberg atoms. These results are the first step towards its implementation on large 2D arrays, in views of studying the topological properties of such systems. As the hopping strongly depends on the actual system's geometry

(as demonstrated in Section 8.3.3), the extension of this work to large arrays is not straightforward. However, the team of H.P. Büchler numerically showed that on a honeycomb lattice, the chiral motion of an excitation along the system's edges is reachable using our platform [Weber *et al.*, 2018]. The honeycomb lattice and its connection to the Haldane model is discussed in detail in the Thesis of Vincent Lienhard [2019].

8.4 Conclusion

In this chapter, I presented the implementation of two models using the dipole-dipole interaction between Rydberg atoms. I started with the XX model on two atoms using the resonant term of the dipole-dipole interaction. I presented two main features of the model we will study in many-body systems in Chapter 9: the oscillation of the system's magnetization and the hopping of an excitation. I then presented the implementation of a density-dependent, complex hopping using the spin-orbit coupling naturally present in dipole-dipole interaction, by observing the characteristic chiral motion of an excitation in a minimal setup of three Rydberg atoms. A simple explanation of this chiral motion is achieved in the perturbative regime, where the spin-orbit coupling gives rise to Peierls phases describing a homogenous magnetic field through the triangle. Notably, the Peierls phase depends on the occupation of neighboring sites and therefore naturally gives rise to a dynamical gauge field. Especially, we have demonstrated in our minimal setup that this density-dependent Peierls phases can be interpreted as particles with an anyonic exchange statistics. This leads to an intriguing open question, whether the combination of such topological band structures with the strong interactions between the bosonic particles can lead to the experimental observation of integer or fractional Chern insulators.

Quantum simulation of programmable XXZ Hamiltonians

Contents

In this chapter, I present our engineering of XXZ Hamiltonians with tunable anisotropies using the dipole-dipole interaction between Rydberg atoms. The XXZ Hamiltonians model the behavior of a wide variety of systems: from the description of quantum magnetism in various situations [Manousakis, 1991], to superfluidity [Hauke et al., 2010], supersolidity [Ng and Lee, 2006; Heydarinasab and Abouie, 2018], or valance-bond solids [Isakov et al., 2006]. In particular, the models exhibit the "spin-liquid" phase [Anderson, 1987], which might play a role in high-Tc superconducting materials [Barnes, 1991]. The model has been analytically solved 50 years ago [Yang and Yang, 1966] in 1D and for nearest-neighbor interactions. However, its extension to long-range interactions [Sandvik, 2010; Gong et al., 2016; Maghrebi, Gong, and Gorshkov, 2017; Frerot, Naldesi, and Roscilde, 2017] and to higher dimensions [Yunoki, 2002; Yamamoto et al., 2017] is only known through approximate calculations. It is thus interesting to study these models on synthetic quantum platforms.

XXZ Hamiltonians have been implemented on various synthetic platforms, such as polar molecules [Yan *et al.*, 2013; Hazzard *et al.*, 2014], ultracold atoms in optical lattices [Jepsen *et al.*, 2020], and superconducting circuits [Kounalakis *et al.*, 2018]. Using the dipole-dipole interaction between Rydberg atoms, its implementation has been demonstrated using Rydberg states with the same parity, with an anisotropy fixed by the choice of the principal quantum number [Signoles *et al.*, 2021]. Circular Rydberg atoms also offer the promise of realizing the XXZ model with anisotropy tunable by external electric and magnetic fields [Nguyen *et al.*, 2018]. Here, we show that, starting from the resonant dipole-dipole interaction which implements the XX model (see Section 8.1), we can engineer XXZ Hamiltonians with tunable anisotropies using a sequence of four microwave pulses. I first explain how the engineering implements XXZ Hamiltonians, and benchmark the procedure on the simplest case of two atoms. We then study various XXZ Hamiltonians by performing two different experiments: the depolarization of an initially magnetized array, and the dynamics of 1D domain wall systems in periodic and open boundary conditions. We compare our data with numerical simulations and assess the residual limitations of the technique. Part of the results presented here are submitted in Scholl *et al.* [2021b].

9.1 Microwave engineering of programmable XXZ Hamiltonians

The engineering is based on the combination of the resonant dipole-dipole interaction between Rydberg atoms and a periodic driving of the system using microwave pulses, which can be seen as a Floquet driving. Floquet engineering techniques [Goldman and Dalibard, 2014], initially introduced in the context of NMR [Shirley, 1965; Vandersypen and Chuang, 2005], has been used to explore new physical phenomena such as dynamical phase transitions [Jurcevic *et al.*, 2017], Floquet-prethermalization [Rubio-Abadal *et al.*, 2020; Peng *et al.*, 2021], novel phases of matter [Kyprianidis *et al.*, 2021] and topological configurations [Aidelsburger *et al.*, 2013; Meinert *et al.*, 2016; Fläschner *et al.*, 2016; Eckardt, 2017; Schweizer *et al.*, 2019; Wintersperger *et al.*, 2020]. Here, we apply those techniques to Rydberg atoms in tweezers arrays. I first derive the analytical expression of the engineered XXZ Hamiltonians, then show its implementation on the simplest case of two interacting atoms. I then discuss and quantify the current technical limitations of the engineering on a single atom.
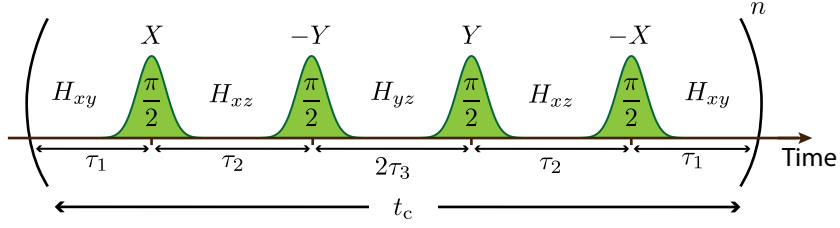
Figure 9.1: Pulse sequence. Sketch of the pulse sequence, composed of four $\pi/2$ pulses with rotation axis $(X, -Y, Y, -X)$ and delays τ_1, τ_2 and $2\tau_3$ between the pulses. The total sequence duration is $t_c = 2(\tau_1 + \tau_2 + \tau_3)$.

9.1.1 Pulse sequence

We consider an array of Rydberg atoms, each described as a two-level system with states of opposite parity mapped onto pseudo-spin states: $|nS\rangle = |\downarrow\rangle$ and $|nP\rangle = |\uparrow\rangle$. As described in Section 8.1, the resonant dipole-dipole interaction gives rise to the XX Hamiltonian:

$$H_{\mathrm{XX}} = \frac{1}{2} \sum_{i<j} J_{ij}(\sigma_i^x \sigma_j^x + \sigma_i^y \sigma_j^y). \tag{9.1}$$

Here, $J_{ij} = C_3(1 - 3\cos^2\theta_{ij})/(2r_{ij}^3)$, with r_{ij} the distance between atoms i and j, θ_{ij} their angle compared to the quantization axis, and $\sigma_i^{x,y}$ the Pauli matrices for atom i. Adding a resonant microwave field to couple the $|\downarrow\rangle$ and $|\uparrow\rangle$ states, the Hamiltonian becomes, in the rotating-wave approximation:

$$H_{\mathrm{driven}} = H_{\mathrm{XX}} + \frac{\hbar\Omega(t)}{2} \sum_i \cos\phi(t)\,\sigma_i^x + \sin\phi(t)\,\sigma_i^y, \tag{9.2}$$

where $\Omega(t)$ and $\phi(t)$ are the Rabi frequency and phase of the microwave field. We use a sequence consisting of four $\pi/2$-pulses with constant phases $\phi = (0, -\pi/2, \pi/2, \pi)$ separated by durations τ_1, τ_2 and $2\tau_3$, shown in Figure 9.1. This $(X, -Y, Y, -X)$ sequence alternates between clockwise and counter-clockwise rotations in order to limit the effect of imperfections in the engineering [Vandersypen and Chuang, 2005]. We define $t_c = 2(\tau_1 + \tau_2 + \tau_3)$ the total duration of the sequence, and consider in the following that the duration of the pulses is negligible compared to t_c. We repeat n times this sequence to access timescales longer than t_c in the dynamics.

The effect of this pulse sequence on the system can be intuitively understood as follows. Before the first $\pi/2$-pulse, the atoms interact under the XX Hamiltonian

for a duration τ_1: $H(t < \tau_1) = H_{\mathrm{XX}}$. Then, the first $\pi/2$-pulse in the x-direction rotates the spin frame: $U_x^\dagger \sigma^y U_x = \sigma^z$, and $U_x^\dagger \sigma^x U_x = \sigma^x$. This means that for a duration τ_2, the system evolves under the Hamiltonian: $H(\tau_1 < t < \tau_1 + \tau_2) = H_{\mathrm{XZ}} = \frac{1}{2} \sum_{i<j} J_{ij} (\sigma_i^x \sigma_j^x + \sigma_i^z \sigma_j^z)$. Then, the $\pi/2$-pulse in the y direction again transforms the spin frame: $U_x^\dagger U_y^\dagger \sigma^y U_y U_x = \sigma^z$ and $U_x^\dagger U_y^\dagger \sigma^x U_y U_x = \sigma^y$. The system thus evolves under H_{YZ}. Due to this rotation of the spin frame, the Hamiltonian changes after each rotation (see the successive Hamiltonians in Figure 9.1), and eventually comes back to H_{XY} after the four pulses. The system thus evolves under a periodic, *time-dependent* Hamiltonian. However, we can derive an effective time-independent Hamiltonian for the system's evolution using *Average Hamiltonian Theory* (AHT).

Average Hamiltonian theory. The AHT states that the system's evolution operator U during the pulse sequence can be written as $U(t_{\mathrm{c}}) = e^{-iH_{\mathrm{av}}t_{\mathrm{c}}/\hbar}$, where H_{av} is the time-average Hamiltonian over one sequence. The system thus appears to evolve under a time-independent Hamiltonian. We obtain H_{av} using a Magnus expansion of the form $H_{\mathrm{av}} = H^0 + H^1 + O(h^2/(J_{\mathrm{m}}t_{\mathrm{c}})^2)$, where we introduced the averaged interaction energy $J_m = 1/N \sum_{i<j} J_{ij}$, with N the total number of spins. The first two terms of the Magnus expansion are:

$$H^0 = \frac{1}{t_{\mathrm{c}}} \int_0^{t_{\mathrm{c}}} H(t)\mathrm{d}t, \tag{9.3}$$

$$H^1 = \frac{-i}{2t_{\mathrm{c}}} \int_0^{t_{\mathrm{c}}} \int_0^{t'} [H(t'), H(t)]\mathrm{d}t'\mathrm{d}t. \tag{9.4}$$

As the performed pulse sequence is symmetric, all the odd orders of the expansion (including H^1) are zero. Under the assumption $J_{\mathrm{m}}t_{\mathrm{c}}/h \ll 1$, we neglect the high order terms of the Magnus expansion and the average Hamiltonian reduces to $H_{\mathrm{av}} = H^0$. We will experimentally probe this condition on a many-body system in Section 9.2. The expression of H_{av} is given by the time average of the successive Hamiltonians during the sequence:

$$H_{\mathrm{av}} = \frac{1}{2} \sum_{i<j} \frac{2J_{ij}}{t_c} [(\tau_1 + \tau_2)\, \sigma_i^x \sigma_j^x + (\tau_1 + \tau_3)\, \sigma_i^y \sigma_j^y + (\tau_2 + \tau_3)\, \sigma_i^z \sigma_j^z]. \tag{9.5}$$

XXZ Hamiltonians. H_{av} is an XYZ Hamiltonian, whose coefficients are tunable by simply varying the delays between the pulses. In this work, we restrict ourselves to the case of the XXZ Hamiltonian which conserves the number of spin excitations by

setting $\tau_2 = \tau_3$. The corresponding Hamiltonian is:

$$H_{\text{XXZ}} = \frac{1}{2} \sum_{i<j} J_{ij}^x(\sigma_i^x \sigma_j^x + \sigma_i^y \sigma_j^y) + J_{ij}^z \sigma_i^z \sigma_j^z \ , \tag{9.6}$$

where $J_{ij}^x = J_{ij}^y = 2J_{ij}(\tau_1 + \tau_2)/t_c$ and $J_{ij}^z = 4J_{ij}\tau_2/t_c,$. The anisotropy of the Hamiltonian $\delta = J_{ij}^z/J_{ij}^x = 2\tau_2/(\tau_1 + \tau_2)$ is thus tunable in the range $0 < \delta < 2$. The nearest-neighbor interaction energies J_x, J_z in the engineered XXZ model are related to the natural nearest-neighbor interaction energy J:

$$J_x(\delta) = \frac{2J}{2+\delta} \text{ and } J_z(\delta) = \frac{2J\,\delta}{(2+\delta)}. \tag{9.7}$$

9.1.2 Benchmark on two atoms

We now demonstrate the implementation of the XXZ Hamiltonian of Equation (9.6) in the case of two interacting atoms. We observed on simulations that the high order terms of the Magnus expansion are always zero for this specific case of two atoms, which means that we do not need to fulfill the condition $J_{\text{m}}t_{\text{c}}/h \ll 1$. We use this asset to perform a single cycle, and vary the total duration t_{c} of the sequence to observe the system's evolution. The extension to multiple cycles and their limits are discussed in the next subsection.

We use the pseudo-spin states $|\downarrow\rangle = \left|90S_{1/2}, m_J = 1/2\right\rangle$ and $|\uparrow\rangle = \left|90P_{3/2}, m_J = 3/2\right\rangle$ separated by $f_{\text{MW}}/2\pi = 5.1\,\text{GHz}$. The microwave field couples these states with a Rabi frequency $\Omega/(2\pi) = 7.2\,\text{MHz}$. The atoms are separated by $30\,\mu\text{m}$, leading to a natural interaction energy of $J/h \simeq 930\,\text{kHz}$. We first check that we can faithfully implement XXZ Hamiltonians by measuring the oscillation of the y magnetization (see Section 8.2.2).

Benchmarking of the implementation on the magnetization oscillation. The spectrum of the XXZ Hamiltonian for two atoms, sketched in Figure 9.2 a), consists of two degenerate eigenstates $|\downarrow\downarrow\rangle$ and $|\uparrow\uparrow\rangle$ with energy J_z and two other eigenstates $|\pm\rangle = (|\uparrow\downarrow\rangle \pm |\downarrow\uparrow\rangle)/\sqrt{2}$ with energy $-J_z/2 \pm J_x$. To characterize the engineering of the XXZ Hamiltonians using microwave pulses, we prepare the atoms in the state $|\rightarrow\rightarrow\rangle_y = (|\uparrow\uparrow\rangle - |\downarrow\downarrow\rangle + i\sqrt{2}\,|+\rangle)/2$ following the procedure described in Figure 9.2 b) and detailed in Section 8.2.2. We then apply the pulse sequence for a variable duration $t_{\text{int}} = t_{\text{c}}$. This state evolves with time, and the total y-magnetization $\langle\sigma^y\rangle$ oscillates at
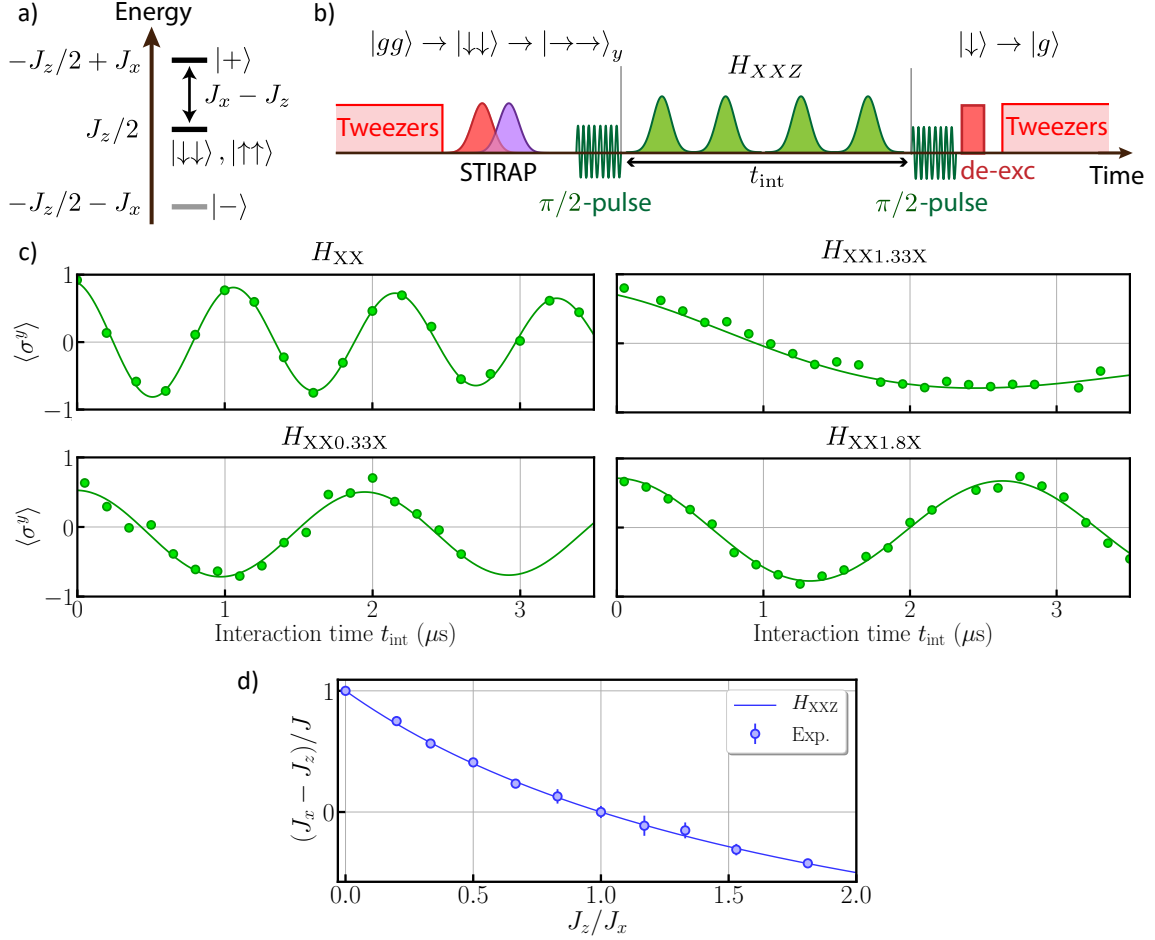
Figure 9.2: Oscillation of the magnetization under XXZ Hamiltonians. a) Sketch of the two-atom levels. b) Experimental procedure. We prepare the $|\rightarrow\rightarrow\rangle_y$ state (see Section 8.2.2), then let the system evolve whilst applying the pulse sequence with duration t_{int} to engineer various XXZ Hamiltonians. c) Oscillation of the y magnetization $\langle\sigma^y\rangle$ for various XXZ Hamiltonians. We observe a slow-down of the frequency for $\delta \sim 1$. The solid lines are fit to the data using damped sine functions. d) Oscillation frequency normalized to the natural interaction energy $(J_x - J_z)/J$ as a function of δ. The solid line is the expected behavior for XXZ Hamiltonians.
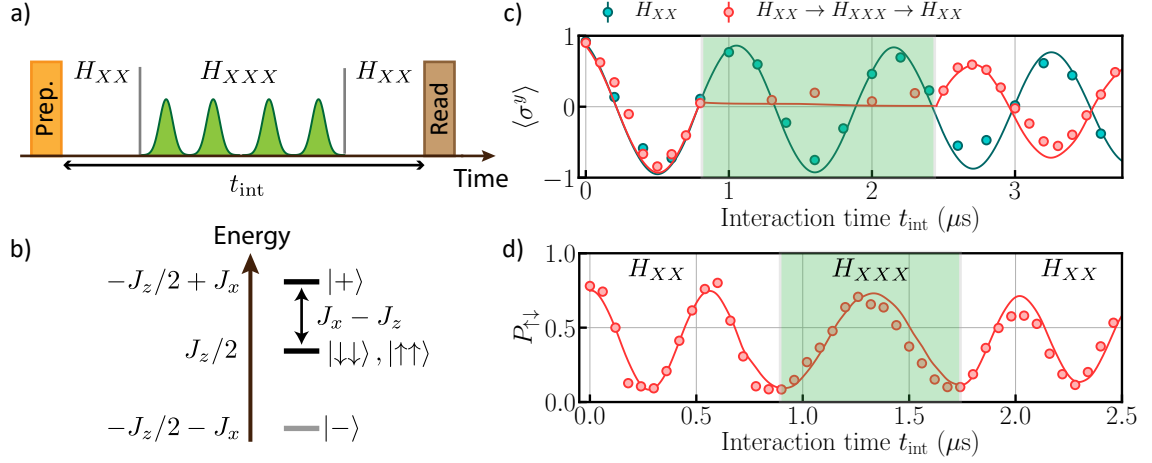
Figure 9.3: Dynamical tuning of the Hamiltonian and comparison to simulations.
a) Experimental sequence. We let the system evolve under the natural H_{XX}, then switch on the microwave engineering of H_{XXX}. We then let the system again freely evolve under H_{XX}. b) Sketch of the two-atom levels. c) Magnetization oscillation without (green) and with (red) microwave engineering of H_{XXX} during the dynamics. d) Spin-exchange experiment with microwave engineering of H_{XXX} during the dynamics. We observe a slow down of the oscillation frequency by a factor $2/3$. The solid lines are simulations of the Schrödinger equation, taking into account the microwave engineering.

a frequency $|J_x - J_z|$. We show the results of the experiment for various anisotropies $\delta = 0, 0.33, 1.33, 1.8$, see Figure 9.2 c). We observe a slow-down of the oscillation frequency compared to the XX Hamiltonian. We measure the oscillation frequency by fitting the data with damped sine functions, and plot them as a function of the corresponding anisotropy δ, see Figure 9.2 d). We normalize the obtained frequencies to the natural interaction energy J, measured by performing this experiment on the XX Hamiltonian, without the pulse sequence. The solid line is the theoretical prediction for XXZ Hamiltonians (derived from Equation (9.6)) without any fitting parameter. We find an excellent agreement with the data, showing that the pulse sequence faithfully implements the target XXZ Hamiltonian.

Dynamical tuning of the Hamiltonian. An asset of this engineering is the possibility to dynamically change the engineered Hamiltonian during the system's evolution. To demonstrate this, we perform two experiments in which we change the Hamiltonian during the evolution of the system, see Figure 9.3 a).

In a first experiment, we initialize the atoms in $|\rightarrow\rightarrow\rangle_y$, let them evolve under H_{XX} and apply the microwave pulse sequence between $0.8 - 2.4$ μs to engineer H_{XXX}. As

shown in Figure 9.3 b), $\langle \sigma^y \rangle$ is frozen during the application of the microwave pulses. This is expected, as $|\downarrow\downarrow\rangle$, $|\uparrow\uparrow\rangle$ and $|+\rangle$ are degenerate eigenstates of H_{XXX}. After 2.4 μs, $\langle \sigma^y \rangle$ oscillates again, with no appreciable loss of contrast in the magnetization oscillation compared to the case without any microwave pulses (green dots in Figure 9.3 b)). In order to show that we control the exact time at which the system switches from one Hamiltonian to the other, we chose the duration of H_{XXX} such that the magnetization now oscillates out-of-phase as compared to the case without any microwave pulses.

The second experiment we perform is the coherent exchange of an $\uparrow$ excitation between the two atoms, described in Section 8.2.3. The hopping amplitude is given by the difference in energy between the $|+\rangle$ and $|-\rangle$ states, equals to $2J_x$ (see Figure 9.3 c)). This hopping strength does not depend on J_z, hence does not depend on the anisotropy of the Hamiltonian. However, as the value of J_x depends on δ (see Equation (9.7)), the hopping strength depends on the XXZ Hamiltonian in our implementation using this microwave engineering. We perform the experiment by initializing the atoms in $|\uparrow\downarrow\rangle$, and measure the probability $P_{\uparrow\downarrow}$ as a function of the interaction time t_{int}, see Figure 9.3 d). As done above, we first let the system evolve under H_{XX} and we observe an oscillation between $|\uparrow\downarrow\rangle$ and $|\downarrow\uparrow\rangle$ at a frequency $2J$. We then engineer H_{XXX} and observe a reduction by a factor 0.65(2) of the oscillation frequency, in good agreement with the expected factor of 2/3 for $\delta = 1$ (see Equation (9.7)).

Comparison with simulations. Finally, we compare the results of the experiments described above with the solution of the Schrödinger equation using the Hamiltonian described in Equation (9.6). We include the imperfections measured on the experiment: state preparation and measurement errors (SPAM) (see Section 8.2.3), and shot-to-shot fluctuations of the interatomic distance (see Section 6.2.2). The results of the simulations are shown as solid lines in Figure 9.3 c) and d), and are in good agreement with the data. From this we conclude that the experimental imperfections are well understood, and that in the case of two atoms, the engineered pulse sequence faithfully implement the target Hamiltonian.

9.1.3 Current limitations

The above results were obtained using a single sequence of four pulses. However, when moving to the many-body experiments, the $J_{\mathrm{m}} t_{\mathrm{c}}/h \ll 1$ condition needs to be fulfilled, and to access dynamics over timescales longer than t_{c} we need to perform n

times the pulse sequence. We will typically aim for $J_\mathrm{m} t_\mathrm{c}/h \sim 0.1$ in order to fulfill this condition. As the relevant timescales is $t_\mathrm{int} \sim h/J_\mathrm{m}$ to observe the system's dynamics, the required number of cycles is $n \sim 10$. This means that we need to apply ~ 40 pulses on the atoms. Any single-pulse imperfection (such as a mismatch with respect to a $\pi/2$-pulse, or a residual detuning with the $|\downarrow\rangle \to |\uparrow\rangle$ transition) will thus strongly impact the system. In this subsection, I briefly present the microwave setup we use, then explain how we calibrate the pulses and benchmark their quality.

Microwave setup. We use a Tabor Electronics Arbitrary Waveform Generator (AWG) to generate the microwave pulses. The AWG has a sampling rate of $5\,\mathrm{GS/s}$, which allows us to design pulse sequences with a precision of $\sim 200\,\mathrm{ps}$, which is much smaller than the typical duration of the $\pi/2$-pulses, and the delay between the pulses ($\sim 20\,\mathrm{ns}$). The pulses synthesized by the AWG have a frequency of $\sim 200\,\mathrm{MHz}$. In order to reach the typical frequencies required to drive the $|\downarrow\rangle \to |\uparrow\rangle$ transition ($\sim 5 - 10\,\mathrm{GHz}$), we mix the AWG output with a Rhode and Schwartz microwave synthesizer outputting a continuous wave in the range $\sim 5 - 10\,\mathrm{GHz}$. The signal is then sent to a microwave antenna placed on top of the experimental chamber.

Single atom calibrations. We calibrate the pulses parameters by considering a single atom initially prepared in the $|\downarrow\rangle$ state, and perform the $(X, -Y, Y, -X)$ sequence. We set an equal delay between the pulses $t_\mathrm{c}/4$, see Figure 9.4 a). If the pulses were perfect, we should recover the atom in the $|\downarrow\rangle$ state at the end of each cycle, see Figure 9.4 b). We use this observable to calibrate the pulses: keeping constant the pulse width, we vary the peak amplitude of the pulses and the microwave frequency in order to maximize the probability $P_\downarrow$ to recover the atom in the $|\downarrow\rangle$ state at the end of each cycle. After optimization, we obtain the typical data presented in Figure 9.4 c) for $t_\mathrm{c} = 300\,\mathrm{ns}$. We observe that the pulses do not perfectly drive the system, which we now discuss.

Calibration of the pulse error. In order to understand where this pulse error comes from, we first compare the results of the above experiment for square pulses (purple) and Gaussian pulses (red). We observe that the pulse error is stronger for square pulses, which would indicate that the fast switch on/off of the pulses might be an issue. This observation motivated the use of Gaussian pulses in all the many-body experiment presented below. To further investigate this issue, we now fix the number of cycles to $n = 8$ and measure $P_\downarrow$ as a function of t_c, see Figure 9.4 d). The $1/e^2$ width
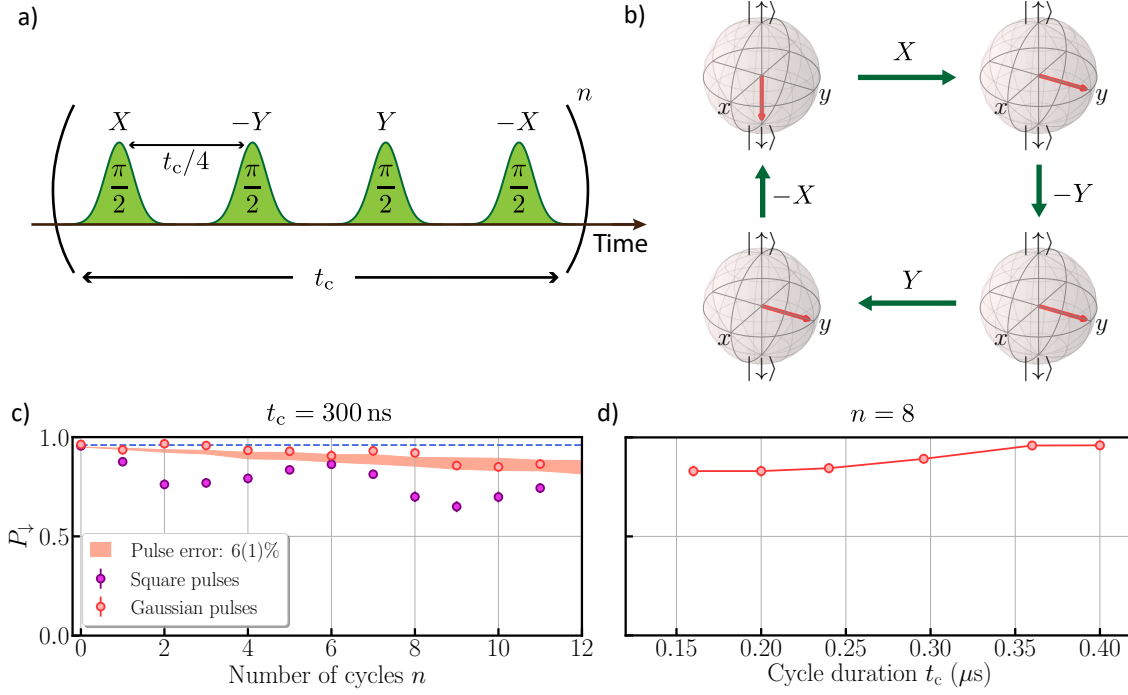
Figure 9.4: Microwave pulse error on a single atom. a) Pulse sequence used for this experiment. We set an equal delay between the pulses $\tau = t_c/4$. b) Bloch sphere representation of the pulse sequence on the atom. The atom should be in $|\downarrow\rangle$ at the end of each cycle if the sequence is perfect. c) Probability to find the atom in $|\downarrow\rangle$ as a function of the number of cycles n for $t_c = 300$ ns using square pulses (purple) and Gaussian pulses (orange). The shaded region is a simulation taking into account an uncertainty in the pulses $\theta = 6(1)\%$ (see text). d) Probability to find the atom in $|\downarrow\rangle$ after $n = 8$ cycles as a function of the cycle duration t_c. We obtain better results for longer t_c. The solid line is a guide to the eye.

of the pulses is set to be 16.8 ns. We observe that the results are better for longer t_c, which indicates that having pulses too close from each other affects the pulse error. For the rest of the chapter, we set $t_c = 300$ ns, which is a suitable trade-off between (i) fast enough cycles to fulfill the $J_m t_c/h \ll 1$ condition (studied in Section 9.2) and (ii) long enough cycles to limit the pulse errors. Further investigations would be required to understand the origin of the phenomenon, such as directly measuring the microwave field shone by the antenna.

To encompass these effects, we phenomenologically include an uncertainty in the angle of rotation of the microwave pulse: for each pulse, we assign two values n_1 and n_2 from a normal distribution centered around zero with a standard deviation $\Delta\theta$. We then use these values to describe the rotation operator: if the desired rotation axis is

x, the actual rotation is performed around the axis x' such that

$$\sigma^{x'} = (1 - n_1^2 - n_2^2)^{1/2}\sigma^x + n_1\sigma^y + n_2\sigma^z. \tag{9.8}$$

The shaded area in Figure 9.4 c) is a simulation taking into account a pulse uncertainty $\Delta\theta = 0.06 \pm 0.01$, which closely matches the experimental results. We include this pulse error in the following when comparing the results to simulations.

Conclusions. In this section, I showed that we are able to implement XXZ Hamiltonians with tunable anisotropies on two atoms, and dynamically change the engineered Hamiltonian during the system's evolution. I also showed on a single atom that the implementation is not perfect due to microwave pulse errors. We will see next that this imperfection is enough to closely match the data, indicating that solving this technical issue would be enough to faithfully implement XXZ Hamiltonians on many-body systems.

9.2 Freezing of the magnetization under the XXX Heisenberg Hamiltonian

In this section, we focus on the evolution of a magnetized state, as performed above for two atoms. For this purpose, as was done in Geier *et al.* [2021] for a gas of cold atoms, we engineer the XXX Heisenberg model for which the total magnetization is a conserved quantity. The ability to freeze the magnetization of a system for a controllable time provides a potential route towards dynamical decoupling and quantum sensing [Choi *et al.*, 2020]. We perform this experiment in 1D and 2D systems, and show that in both cases we are able to engineer the XXX model and freeze the magnetization. We also probe the effect of the $J_\mathrm{m}t_\mathrm{c}/h \ll 1$ condition on the freezing of the magnetization.

Freeze of the magnetization on a 1D chain. We first consider a system consisting of 10 atoms arranged in a circle (see Figure 9.5 a)) with a distance of $a = 19\,\mu\mathrm{m}$ between the atoms. For this experiment and for the rest of the chapter, we use the Rydberg states $|\downarrow\rangle = |75S_{1/2}, m_J = 1/2\rangle$ and $|\uparrow\rangle = |75P_{3/2}, m_J = -1/2\rangle$, separated by $f_\mathrm{MW} = 8.5\,\mathrm{GHz}$. In these conditions, the nearest neighbor interaction energy is $J/h \simeq 270\,\mathrm{kHz}$ and the mean interaction energy is $J_\mathrm{m}/h \simeq 0.6\,\mathrm{MHz}$. We initialize the system in the $|\rightarrow\rightarrow \cdots \rightarrow\rangle_y$ state following the protocol described in Section 8.2.2. We apply the driven Hamiltonian H_XXX for $2\,\mu\mathrm{s}$, then switch off the drive and let the

system evolve under H_{XX}. We use $t_c = 200\,\text{ns}$, such that $J_m t_c/h \simeq 0.15$. We measure the three magnetization components $\langle \sigma^{x,y,z} \rangle$ (orange, green, purple, respectively) after various evolution times t_{int}, see Figure 9.5 a). We observe two behaviors depending on the Hamiltonian:

- During the first $2\,\mu\text{s}$, the three magnetization components $\langle \sigma^{x,y,z} \rangle$ are approximatively constant. This is expected from the XXX Heisenberg Hamiltonian: as the model exhibits a $SU(2)$ symmetry, *each* magnetization component $\langle \sigma^{x,y,z} \rangle$ is conserved, hence the total magnetization. This shows that we faithfully implement H_{XXX} on this few-body system.

- After switching off the driving, we observe a decay of the y-magnetization towards zero. This behavior is different from the two atom case, in which we observed an oscillation of the magnetization (see Section 8.2.2). This demagnetization results from the beating of all the eigenfrequencies of H_{XX} for this many-atom system.

The fact that we accurately implement H_{XXX} shows that setting $J_m t_c/h \simeq 0.15$ is enough to consider that the higher orders of the Magnus expansion (see Section 9.1.1) have a negligible impact on the system.

Freeze of the magnetization on 2D arrays and probe of the $J_m t_c/h \ll 1$ condition. We now consider 2D arrays, and perform the same experiment as above. As the number of neighbors is higher than in 1D, the value of J_m is higher for the same nearest neighbor distance a, meaning that the $J_m t_c/h \ll 1$ condition is harder to achieve. Here, we use $t_c = 300\,\text{ns}$ and Gaussian microwave pulses with a $1/e^2$ width of $16.8\,\text{ns}$. We apply the driven Hamiltonian H_{XXX} for $3\,\mu\text{s}$, then switch off the drive and let the system evolve under H_{XX}. We measure $\langle \sigma^y \rangle$ for various t_{int} and perform the experiment with two different geometries: (i) a 32-atom array in a "diamond" configuration (green) with $a \simeq 27\,\mu\text{m}$ leading to $J/h \simeq 120\,\text{kHz}$ and $J_m t_c/h \simeq 0.2$, and (ii) a 36-atom square array (red) with $a \simeq 20\,\mu\text{m}$, leading to $J/(2\pi) \simeq 270\,\text{kHz}$ and $J_m t_c/h \simeq 0.5$. The dynamics is close to the one observed above for the 1D system. The freezing is less efficient for the square array, which shows that the high order terms of the Magnus expansion are not negligible and thus demagnetize the system, as the implemented Hamiltonian is not completely H_{XXX}. This latter experiment shows the importance of the $J_m t_c/h \ll 1$ condition on the engineered Hamiltonian.

In order to check the validity of our results, we compare the data of the "diamond" configuration ($J_m t_c/h \simeq 0.2$) with simulations using the Moving-Average-Cluster-Expansion (MACE) method [Hazzard *et al.*, 2014], which we now briefly discuss. The
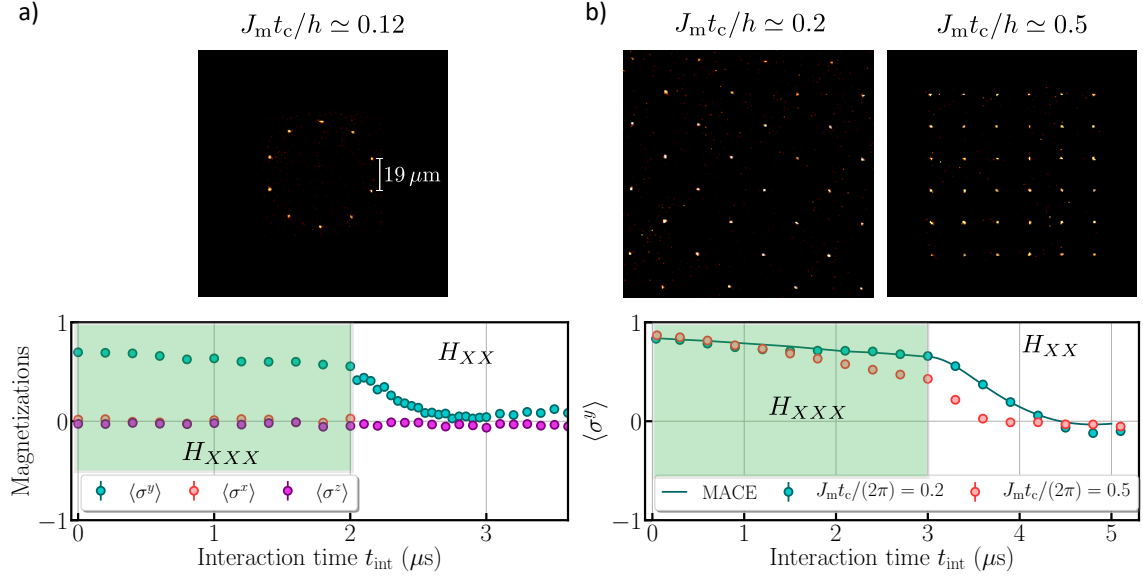
Figure 9.5: Freeze of the magnetization in the XXX Heisenberg model. After initializing the system in the $\left|\rightarrow\rightarrow\cdots\rightarrow\right\rangle_y$ state following the protocol described in Section 8.2.2, we engineer H_{XXX} for a few microseconds, then let the system evolve under the natural H_{XX} Hamiltonian. We perform the experiment for various geometries with different values of $J_{\text{m}}t_{\text{c}}/h$: a) a 10-atom circle, and b) 2D arrays with two different values of J_{m}. The solid line in b) is the results of MACE simulations, which agrees closely to the experimental results.

simulations were performed by the team of M. Weidemüller.

Comparison of the results in the "diamond" configuration to MACE simulations.
As the ab-initio calculation of the dynamics is challenging for a 32-atom array, we use a MACE method to simulate the system. This method consists of diagonalizing clusters, here of 12 atoms, using the Schrödinger equation and averaging the results over all 12-atom cluster configurations possible with 32 atoms. We include in the simulation the various state preparation and detection errors (see Section 8.2.3) and imperfections in the microwave pulses (see Section 9.1.3). The simulation, without adjustable parameters, is in good agreement with the observed dynamics at all times.

Furthermore, we find that not taking into account the imperfections of the microwave in the simulation would lead to a perfect freezing of the magnetization during the application of the pulses: the observed residual decay of the magnetization during their application is thus a consequence of the microwave imperfections. This indicates that $J_{\text{m}}t_{\text{c}}/h \simeq 0.2$ is enough to neglect the higher-order terms in the Magnus expansion. We thus set $J_{\text{m}}t_{\text{c}}/h < 0.2$ in the following in order to safely neglect the higher order of

the Magnus expansion. Previously, the MACE method was only validated against experiments using disordered ensembles with large numbers of atoms [Hazzard *et al.*, 2014; Signoles *et al.*, 2021]. Here, the good agreement between data and simulation observed in Figure 9.5 b) indicates that it is valid for ordered systems of mesoscopic size as well.

Conclusions. In this section, I demonstrated our implementation of the XXX Heisenberg Hamiltonian on 1D and 2D geometries by observing the freezing of the system's magnetization. I showed that (i) the magnetization along each spin component is frozen, (ii) used this observable to probe the $J_\mathrm{m} t_\mathrm{c}/h \ll 1$ condition and found suitable parameters to neglect the higher orders of the Magnus expansion, and (iii) showed a good agreement between the data and numerical simulations using a method which had never been performed on ordered systems. These results are the first step towards a more complete study of the dynamics of magnetized systems under XXZ Hamiltonians.

9.3 Dynamics of domain wall states in 1D systems

We now focus on the exploration of transport properties of spin excitations in 1D systems governed by spin-1/2 XXZ Hamiltonians. These properties are actively studied, both experimentally and theoretically [Gobert *et al.*, 2005; Sirker, Pereira, and Affleck, 2009; Barmettler *et al.*, 2009; Bertini *et al.*, 2021]. For 1D systems, the behavior is known to be highly dependent on the parameters of the Hamiltonians [Giamarchi, 2003]. Several experimental methods, involving the relaxation of spin-spiral states [Hild *et al.*, 2014; Jepsen *et al.*, 2020] or the melting of initially prepared domain walls [Wei *et al.*, 2021; Joshi *et al.*, 2021], enable the extraction of global transport behaviors ranging from ballistic to localized ones as a function of the Hamiltonian parameters. The study of transport dynamics in many-body system using single-atom resolution techniques has been demonstrated with trapped ions [Richerme *et al.*, 2014; Jurcevic *et al.*, 2014; Tan *et al.*, 2021], or ultra-cold atoms in optical lattices [Fukuhara *et al.*, 2013].

Here, I describe our experimental investigations on the dynamics of Domain Wall (DW) states. A DW is a state for which the spin-up atoms are bunched, such that a *wall* separates spin-up atoms from spin-down ones. The evolution of such systems depends on the anisotropy δ due to two competing effects: (i) a melting of the DW caused by spin-flips with a rate $2J_x$, and (ii) its maintaining due to an energy cost $2J_z$

to break the DW. In the case of a pure initial state, which is the relevant situation for our experiment, for $\delta < 1$, the DW should melt, with a magnetization profile expanding ballistically in time [Collura, De Luca, and Viti, 2018; Misguich, Pavloff, and Pasquier, 2019]. At the isotropic point ($\delta = 1$), one expects a diffusive behaviour with logarithmic corrections [Misguich, Mallick, and Krapivsky, 2017]. For $\delta > 1$, the magnetization profile is predicted to be frozen at long times [Gobert *et al.*, 2005; Mossel and Caux, 2010; Misguich, Pavloff, and Pasquier, 2019].

Here, we probe the emergence of these properties with few-body systems of 10 atoms. We will consider two cases: (i) a 1D chain with Periodic Boundary Conditions (PBC), and (ii) a 1D chain with Open Boundary Conditions (OBC). We will show that the system's dynamics strongly depends on the geometry. I start by briefly explaining the preparation of a DW state, then study the system's evolution under various XXZ Hamiltonians. I first describe the OBC case, then finally study the system's evolution in PBC.

9.3.1 Preparation of a domain wall state

We consider a 10-atom array arranged in a circle (OBC) and in a spiral (PBC) (see Figure 9.6) with nearest-neighbor distance $a = 19\,\mu$m. We consider again the Rydberg states $|\downarrow\rangle = \left|75S_{1/2}, m_J = 1/2\right\rangle$ and $|\uparrow\rangle = \left|75P_{3/2}, m_J = -1/2\right\rangle$, such that $J/h = 270\,$kHz and $J_\mathrm{m}/h = 0.6\,$MHz. We set $t_\mathrm{c} = 300\,$ns leading to $J_\mathrm{m}t_\mathrm{c}/h \simeq 0.18$, which is low enough to neglect the high order terms of the Magnus expansion (see Section 9.2).

Experimental sequence.   The experimental sequence used in this section is sketched in Figure 9.6 a). After initializing the atoms in $|\downarrow ... \downarrow\rangle$ using the STImulated Raman Adiabatic Passage (STIRAP) technique described in Section 2.3.1, we apply a first microwave π-pulse with Rabi frequency $\Omega_\mathrm{MW}/(2\pi) \simeq 7\,$MHz to bring the atoms in $|\uparrow ... \uparrow\rangle$. We then light-shift the $|\uparrow\rangle \rightarrow |\downarrow\rangle$ transition frequency by $\sim 15\,$MHz using an addressing beam close to resonance with the $6P_{3/2} \rightarrow |\downarrow\rangle$ transition. The addressing beam is focused on five adjacent atoms using a spatial light modulator (see Section 2.3.3). We combine this addressing technique with a second microwave π-pulse on resonance with the *free-space* transition. The non-addressed atoms are transferred to $|\downarrow\rangle$, thus preparing the $|$DW$\rangle$ state.

After the preparation, we let the system evolve under H_XXZ for a duration $t_\mathrm{int} = nt_\mathrm{c}$ by performing the microwave sequence n times. We then read the system's state by
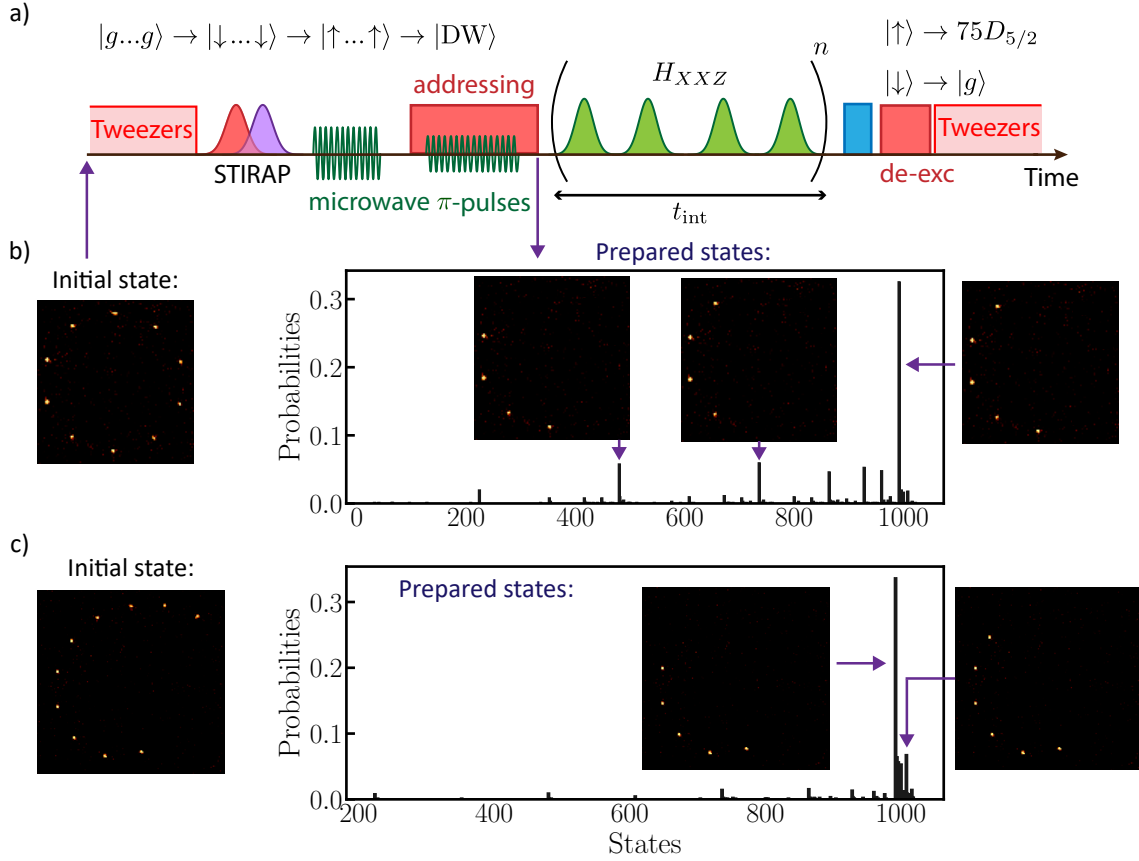
Figure 9.6: Preparation of the domain wall state. a) Sketch of the experimental sequences. After preparing the domain wall state $|DW\rangle$ following the protocol described in Section 8.2.3, we apply n times the pulse sequence to engineer H_{XXZ}. We then lift the system's dynamics by applying a strong microwave pulse on resonance with the $|\uparrow\rangle \rightarrow 75D_{5/2}$ transition, and detect the atoms in $|\downarrow\rangle$ by de-exciting them back to the ground state. b-c) State histograms at the end of the preparation for the PBC (b) and OBC (c). Due to state preparation and detection errors, the probability P_{DW} to obtain the $|DW\rangle$ state in both geometries is $\sim 33\%$. Other highly probable states ($\sim 5\%$) are domain wall states with lower (or higher) number of spin-up atoms.

de-exciting the atoms in the $|\downarrow\rangle$ state back to the ground state (see Section 2.3.1). The duration of the de-excitation process is typically $\sim 400\,\text{ns}$. In order to avoid any interactions during this time, we freeze the system's dynamics by applying a strong, short microwave pulse of $\sim 40\,\text{ns}$ on resonance with the $|\uparrow\rangle \rightarrow 75D_{5/2}$ transition. The $|\downarrow\rangle$ state and the $75D_{5/2}$ manifold are not coupled at first order via the dipole-dipole interaction. We can thus consider the system as not evolving during the $400\,\text{ns}$ de-excitation pulse.

Dowain wall state preparation efficiency. We measure the atoms state at the end of the preparation, and obtain the typical state histograms presented in Figure 9.6 b) for the circle and c) for the spiral. In both cases, we obtain a probability to prepare the perfect domain wall state of $\sim 33\%$. This value is explained by the finite efficiencies of the various processes. First, the STIRAP efficiency is $\sim 95\%$ per atom, leading to a probability to correctly initalize the system in the Rydberg manifold $P_{\downarrow\ldots\downarrow} = 60\%$. Second, the microwave pulse combined with the addressing beam has an efficiency of $\sim 95\%$ per atom. Third, the detection errors with values $\varepsilon \sim 2.5\%$ and $\varepsilon' \sim 2.5\%$ (see Section 3.3.1) also reduces the DW probability. By adding all these errors, we obtain the preparation efficiency presented above. We include the finite efficiency of these operations in the numerical simulations. We observe on the histograms that other prepared states with $\sim 5\%$ probability are DW states with a higher (or lower) number of spin-up atoms, and thus still contribute to the physics we wish to explore.

9.3.2 Dynamics in open boundary conditions

We now study the evolution of the system in OBC under H_{XXZ} for various δ. As discussed above, we expect to observe a melting of the domain wall for $\delta < 1$, and its freezing for $\delta > 1$. We study these behaviors on three observables: (i) the single-site z-magnetization $\langle \sigma^z \rangle$, (ii) the domain wall probability P_{DW} and (iii) the nearest-neighbor spin-spin correlations.

z-magnetization maps. We first look at the evolution of the single-site z-magnetization $\langle \sigma^z \rangle$. Due to our engineering of H_{XXZ}, the hopping strength, hence the rate at which the DW state might melt or be frozen, depends on the value of δ (see Equations (9.7)). In order to accurately compare the various Hamiltonians, we therefore normalize the time with respect to the hopping strength. As the hopping strength is $2J_x$, we set
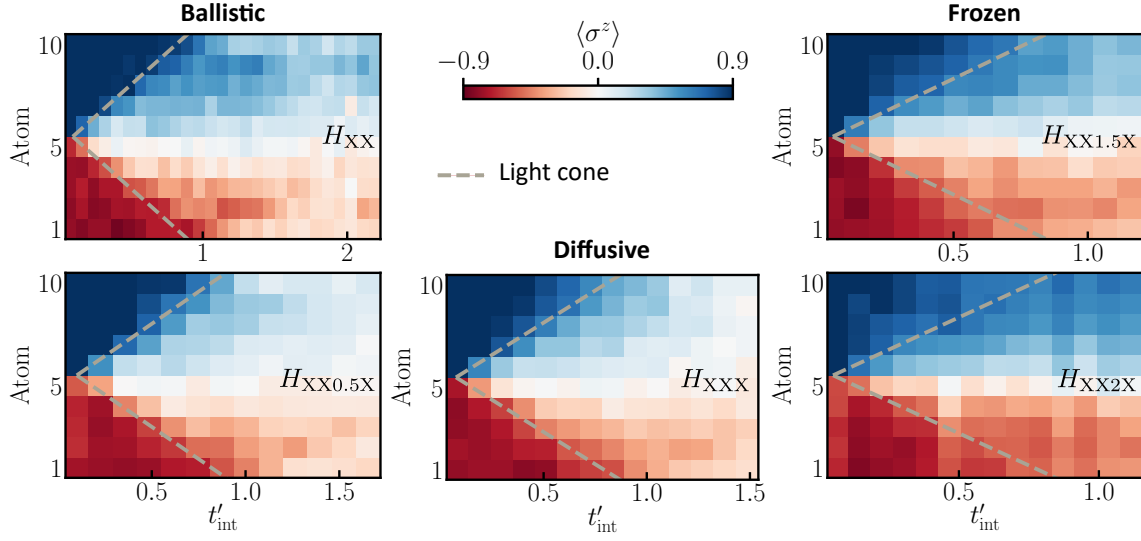
Figure 9.7: Evolution of the z-magnetization per atom for various XXZ Hamiltonians in OBC. We show $\langle \sigma^z \rangle$ per atom as a function of the time normalized to the hopping strength: $t'_{\text{int}} = (2J_{\text{x}}(\delta))t_{\text{int}}$. The dashed line shows the light-cone $\xi = \pm t'_{\text{int}}$. We qualitatively observe different system's behaviors depending on the anisotropy δ: a "ballistic" expansion of the DW following the light-cone for $\delta < 1$ (left plots), a "freeze" of the DW for $\delta > 1$ (right plots). In the case $\delta = 1$, we expect a "diffusive" behavior [Misguich, Mallick, and Krapivsky, 2017].

$t'_{\text{int}} = (2J_{\text{x}}(\delta))t_{\text{int}}$. The results are shown in Figure 9.7 with $\delta = 0, 0.5, 1, 1.5, 2$ [1]. In order to qualitatively appreciate the melting (and the freezing) of the domain wall, we show the *light-cone* of the dynamics $\xi = \pm t'$ [Collura, De Luca, and Viti, 2018; Misguich, Pavloff, and Pasquier, 2019] (dashed grey lines). This light-cone indicates the maximum rate at which the excitations can propagate, and thus the maximum rate at which the DW spreads. This maximum rate is $2J_x$ and is achieved when the system is governed by the XX model. We observe qualitatively different behaviors depending on δ:

- For $\delta \leq 1$ (left plots), we observe the melting of the domain wall, resulting in an approximately uniform magnetization profile at long times. The magnetization profile grows ballistically in time by following the light-cone, as expected numerically. The agreement between the light-cone which is valid for nearest-neighbor interactions and the data indicates that the $1/r^3$ range of the interactions has little effect in our few-body 1D system.

---

[1]Implementing H_{XX2X} requires $\tau_1 = 0$. We therefore remove the X and $-X$ pulses from the sequence, with the exception of the first and final pulses.

- For $\delta > 1$ (right plots), we observe a retention of the domain wall at all times: the magnetization profile does not evolve after $t'_{\text{int}} \sim 0.5$, indicating a freezing of the system dynamics.

- At the isotropic point $\delta = 1$ (central plot), the domain wall also melts as predicted by numerical investigations [Misguich, Mallick, and Krapivsky, 2017]. The exact nature of the melting, supposed to exhibit a "diffusive" behavior, would require a detailed study and is out of the scope of this manuscript.

The observation of these different transport behaviors for various δ, consistent with numerical investigations, indicates that the Hamiltonian engineering provides a reliable method to explore spin-transport physics in a versatile manner. We now confirm these qualitative behaviors by looking at other observables.

Domain wall probability.　We compute the probability $P_{\text{DW}}^{\text{ini}}$ to measure the initial domain wall state as a function of t'_{int} for various anisotropies δ. In order to partially take into account the finite efficiency of the various processes, and reduce the effect of the microwave pulse errors detailed in Section 9.1.3, we also include in $P_{\text{DW}}^{\text{ini}}$ the probability to measure DW states with four and six spins-up atoms. The results are presented in Figure 9.8 a) for $\delta = 0.5, 1, 1.5, 2$. For all anisotropies, we observe a decay of $P_{\text{DW}}^{\text{ini}}$ with t'_{int}. $P_{\text{DW}}^{\text{ini}}$ vanishes for $\delta < 1$, whereas for $\delta > 1$ there is a finite probability to obtain DW states at long times, which is $P_{\text{DW}}^{\text{ini}} \sim 10\%$ for $\delta = 2$. This once again shows the melting of the DW for $\delta < 1$, and its retention for $\delta > 1$.

Number of spin-flips.　The last observable we compute is the number of spin-flips N_{flip}, where a flip is defined as two neighboring atoms in opposite spin states. This quantity is related to the nearest-neighbor spin correlation function $\langle \sigma_i^z \sigma_{i+1}^z \rangle$ by:

$$N_{\text{flip}} = \sum_i \frac{1 - \langle \sigma_i^z \sigma_{i+1}^z \rangle}{2}. \tag{9.9}$$

Three examples of this observable are provided in Figure 9.8 b). Its minimum value is $N_{\text{flip}} = 1$, and corresponds to the initial DW state. The highest value is $N_{\text{flip}} = 9$, and corresponds to the antiferromagnetic state. An example of an uncorrelated state is provided with $N_{\text{flip}} = N/2 = 5$. This observable thus characterizes the system's ordering: if $N_{\text{flip}} \sim 1$, the system is close to a DW state as expected for $\delta > 1$, whilst if $N_{\text{flip}} \sim 5$, the system is uncorrelated as expected for $\delta < 1$.
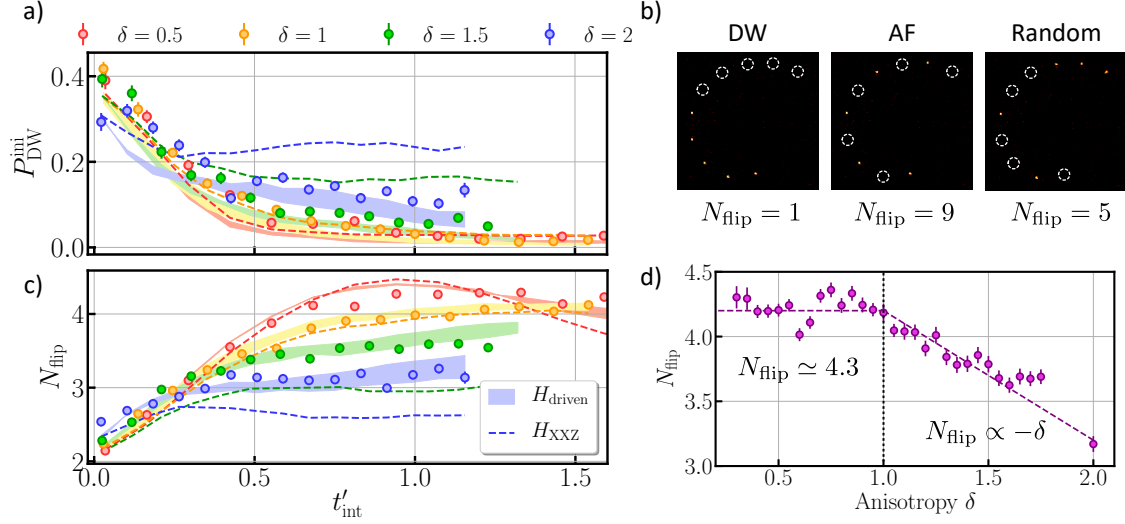
Figure 9.8: Evolution of the DW probability and the number of spin-flips for various XXZ Hamiltonians in OBC. a) Evolution of the initial DW probability $P_{\mathrm{DW}}^{\mathrm{ini}}$ for various anisotropies. $P_{\mathrm{DW}}^{\mathrm{ini}}$ does not vanish at long times for $\delta > 1$. b) Number of spin flips N_{flip} along the spiral for three examples: the initial DW with $N_{\mathrm{flip}} = 1$, the antiferromagnetic (AF) state with $N_{\mathrm{flip}} = 9$ and an uncorrelated state with $N_{\mathrm{flip}} = 5$. c) Evolution of N_{flip} for various anisotropies. Shaded regions: results of the simulation using H_{driven}, including the $6 \pm 1\%$ fluctuations on the microwave rotation axis (see Section 9.1.3). Dashed lines: results of the simulations using H_{XXZ}. d) N_{flip} as a function of δ measured after $n = 13$ cycles. The value of N_{flip} is constant for $\delta < 1$, then linearly decreases for $\delta > 1$. The dashed line is a guide to the eye.

We show the evolution of N_{flip} as a function of t'_{int} in Figure 9.8 c). For all anisotropies, we observe an increase of N_{flip} with time, which is expected considering that $P_{\mathrm{DW}}^{\mathrm{ini}}$ decreases. For $\delta \leq 1$, N_{flip} approaches $N/2$, confirming the fact that the system becomes fully uncorrelated. The value is not exactly $N/2$ due to the finite preparation efficiency, which leads to fluctuations of the number of excitations. If the number of excitations is different than $N/2$, the nearest-neighbor correlations are not zero (even for an uncorrelated system) and $N_{\mathrm{flip}} < 5$. The value of N_{flip} at long times is lower as δ increases, meaning that the $|\uparrow\rangle$ excitations tend to remain bunched.

In order to assess in detail the system's behavior at long times, we extract the value of N_{flip} after $n = 13$ cycles as a function of δ, see Figure 9.8 d). We qualitatively observe two behaviors. For $\delta \leq 1$, the value of N_{flip} is roughly constant, whereas for $\delta > 1$, its value decreases linearly with δ. In a perfect, infinite system, we would expect a sharp cut at $\delta = 1$, with $N_{\mathrm{flip}} = 1$ for $\delta > 1$. Here, we observe the emergence of this behavior. These data thus show that we are able to almost continuously vary δ (up to

the microwave generator time resolution) by varying the delay between the pulses, a strong asset of this microwave engineering of XXZ Hamiltonians.

Comparison to simulations. We finally compare the experimental data of Figure 9.8 a) and c) with numerical simulations using both the time-dependent engineered Hamiltonian H_{driven} (shaded regions) and the target H_{XXZ} Hamiltonian (dashed lines). The simulations were performed by Hannah Williams and Loïc Henriet. In both simulations, we include the finite efficiencies of the various processes described above, the residual shot-to-shot fluctuations of the interatomic distances, and the microwave imperfections discussed in Section 9.1.3. The data are well reproduced by the H_{driven} simulation, indicating that we reasonably understand the errors within the experiment. However, the engineered Hamiltonian implements the target Hamiltonian less well as δ increases. We numerically find that this mismatch between H_{driven} and H_{XXZ} is explained by the microwave imperfections (see Section 9.1.3), as for the freezing of the magnetization in Section 9.2. Further improvements to our microwave setup should hence lead to a faithful implementation of the XXZ Hamiltonian.

Conclusions. In this subsection, I presented our study of the dynamics of domain wall states under H_{XXZ} in a 1D open chain of 10 atoms. By computing various observables, we showed that (i) the domain wall melts for $\delta < 1$ and (ii) is retained for $\delta > 1$, as expected from numerical investigations. In particular, the matching of our results with numerical simulations including all the known errors shows that we accurately understand the system's evolution.

9.3.3 Dynamics in periodic boundary conditions

In this final subsection, we repeat the experiments presented above considering a 10-atom circle exhibiting periodic boundary conditions. The system's dynamics behaves in a different way. For $\delta > 1$, the initial DW is not retained, but *delocalizes* over the circle. We first show this feature experimentally, and finally gives a simple interpretation in a toy model.

Experimental observation of the delocalization. We use the same experimental protocol as above and observe the dynamics of the DW state, now in PBC. We first look at the z-magnetization $\langle \sigma^z \rangle$ per atom for $\delta = 0.5, 1, 1.5, 2$, see Figure 9.9 a). For $\delta \leq 1$, the results look similar to the OBC case, with a fast vanishing of the domain
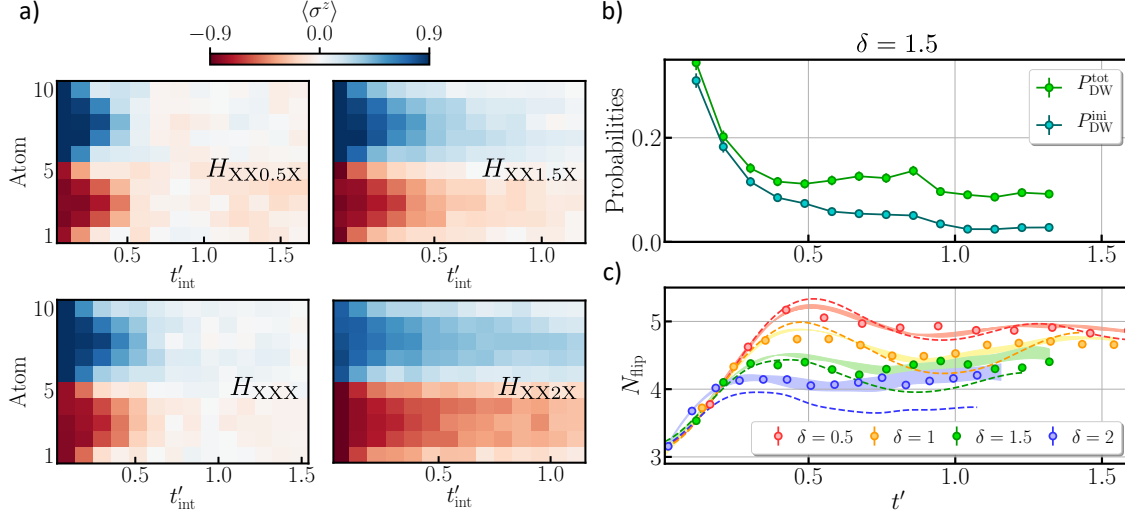
Figure 9.9: Delocalization of the domain wall in periodic boundary conditions. a) z-magnetization $\langle \sigma^z \rangle$ per atom for various H_{XXZ}. As opposed to the OBC case (see Figure 9.7), the initial DW breaks even for $\delta > 1$. b) Evolution of the initial DW probability $P_{\mathrm{DW}}^{\mathrm{ini}}$ and the total DW probability $P_{\mathrm{DW}}^{\mathrm{tot}}$ for $\delta = 1.5$. At long times, $P_{\mathrm{DW}}^{\mathrm{ini}}$ points towards low values whereas $P_{\mathrm{DW}}^{\mathrm{tot}} \simeq 0.1$: the DW delocalizes over the circle. c) Evolution of N_{flip} for various anisotropies. Shaded regions: results of the simulation using H_{driven}, including the $6 \pm 1\%$ fluctuations on the microwave rotation axis (see Section 9.1.3). Dashed lines: results of the simulations using H_{XXZ}.

wall. However, the results are different than in OBC: for $\delta > 1$, we qualitatively observe that the z-magnetization points towards $\langle \sigma^z \rangle \sim 0.5$ for every atom. This would indicate a melting of the DW.

In order to assess this, we focus on $\delta = 1.5$ and compute domain wall probabilities, see Figure 9.9 b). We compare the evolution of (i) the initial domain wall probability $P_{\mathrm{DW}}^{\mathrm{ini}}$ (dark green) and (ii) the total domain wall probability $P_{\mathrm{DW}}^{\mathrm{tot}}$ (light green), irrespective of its position. At short times, both probabilities matches as the prepared DW states are mainly the initial one. We then observe at long times that $P_{\mathrm{DW}}^{\mathrm{ini}}$ decays close zero, as expected considering the z-magnetization plots. However, we observe that the *total* domain wall probability $P_{\mathrm{DW}}^{\mathrm{tot}}$ does not vanish with time and reaches $P_{\mathrm{DW}}^{\mathrm{tot}} \simeq 0.1$. This value is close to the one obtained in OBC for the *initial* domain wall probability $P_{\mathrm{DW}}^{\mathrm{ini}}$. These results show that the DW still exists in the system, but delocalizes around the circle.

This observation is confirmed by the evolution of N_{flip} for the various anisotropies, see Figure 9.9 c). As observed for the OBC case, the value of N_{flip} decreases with δ, which once again indicates that the DW is preserved, even though it is delocalized
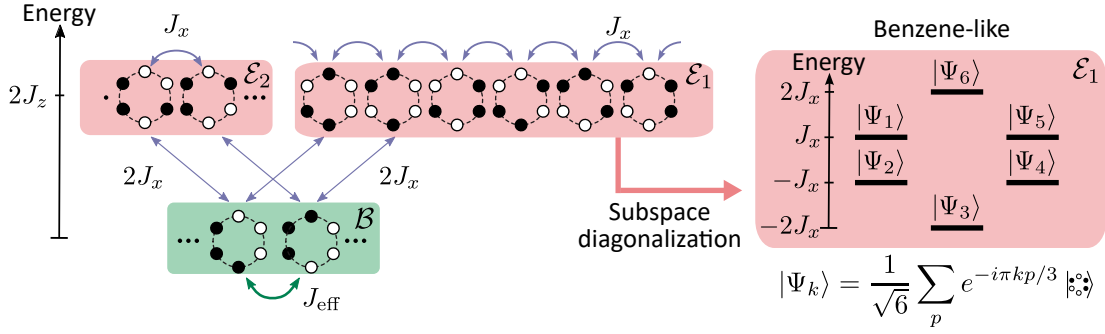
Figure 9.10: Delocalization of the domain wall in periodic boundary conditions. Sketch of the lowest energy levels for six atoms. When considering $\delta \gg 1$, two nearby DW states in $\mathcal{B}$ are coupled via excitations hoppings through $\mathcal{E}_1$ and $\mathcal{E}_2$, which are ensembles at an energy $2J_z$ where one excitation is detached from the DW. $\mathcal{E}_1$ and $\mathcal{E}_2$ are composed of six coupled states in the same way as a free electron hopping on a benzene. The subspace diagonalization is analytical and allows us to extract the coupling strength between $\mathcal{B}$ and $(\mathcal{E}_1, \mathcal{E}_2)$.

along the circle. We also compare these data to simulations as performed above. We again obtain the same conclusions: the data agree well with the simulation of H_{driven}, and the discrepancy with H_{XXZ} increases as δ increases. We numerically find that the mismatch is due to the microwave pulse errors.

This delocalization of the DW in the PBC case can be understood in a perturbative approach, which we now illustrate on a toy model of six atoms.

A toy-model for the delocalization of the domain wall. We consider the case $\delta \gg 1$ and limit the interactions to nearest-neighbors. For N atoms arranged in a circle, all N DW states obtained by rotation are degenerate. They are coupled together by a re-arrangement of excitations, requiring $N/2$ spin-flips. Due to this coupling the initial DW state is progressively transformed into a coherent superposition of all the different domain-walls. This process is illustrated in Figure 9.10 for $N = 6$ atoms: each DW state in $\mathcal{B}$ is coupled via spin-exchange to two states with a single detached atom, one in each of the two subspaces $\mathcal{E}_1$ and $\mathcal{E}_2$ with energy $2J_z$. These subspaces are composed of six coupled states $|p\rangle$ via spin-exchange in a cyclic fashion, which is reminiscent of a free electron hopping on a benzene. The diagonalization of the subspaces is analytical and gives the eigenstates:

$$|\Psi_k\rangle = \frac{1}{\sqrt{6}} \sum_p e^{-i\pi kp/3} |p\rangle , \qquad (9.10)$$

223

with eigenenergies $E_k = 2J_x \cos(k\pi/3)$. We treat perturbatively the coupling from $\mathcal{B}$ to these subspaces. The coupling J_{eff} between two nearby DW states $|\text{DW}_1\rangle$ and $|\text{DW}_2\rangle$ is:

$$J_{\text{eff}} = \sum_k \frac{\langle \text{DW}_1| H_{\text{XXZ}} |\Psi_k\rangle \langle \Psi_k| H_{\text{XXZ}} |\text{DW}_2\rangle}{2J_z - E_k}. \tag{9.11}$$

By combining the two above equations, we obtain:

$$J_{\text{eff}} = \frac{J_x^2}{6} \sum_k \frac{e^{ik\pi/3}}{2J_z - E_k}. \tag{9.12}$$

The development of this expression to the first order in J_x/J_z gives $J_{\text{eff}} \sim J_x^3/\delta^2$, and its extension to N atoms is $J_{\text{eff}} = 4J_x(2\delta)^{1-N/2}$. This exchange term vanishes with N due to the number of spin-flips necessary for the propagation of the domain-wall by one lattice site. However, at moderate system sizes as used here, the domain wall delocalization is still expected, which we observe experimentally. As this DW delocalization vanishes with N, this feature would not show up at the thermodynamic limit. It would be thus interesting to repeat this experiment for various N, and observe the localization of the DW also for periodic boundary conditions.

9.4 Conclusion

In this chapter, I presented our engineering of XXZ Hamiltonians with anisotropies $0 \leq \delta \leq 2$ using the resonant dipole-dipole interaction between Rydberg atoms in arrays coupled to a resonant microwave field. We have studied two situations: the Heisenberg model in 2D square arrays, where we demonstrated the ability to dynamically freeze the evolution of a state with a given magnetization, and the evolution of a domain wall in a 1D chain with open and periodic boundary conditions. By comparing our results to numerical simulations, we infer the current limitations as being due to the imperfections in the microwave pulses. Despite this limitation, which we hopefully can solve by improving the microwave hardware, we were able to observe all the qualitative features of the situations we explored. This highlights the versatility of our platform, beyond the implementation of the natural Ising-like or XX Hamiltonians. Future work could include the study of frustration in various arrays governed by the Heisenberg model [Richter, Schulenburg, and Honecker, 2004], or the study of domain wall dynamics for larger system size to confirm the various delocalization scalings beyond the emergent behaviors studied here.

Conclusion

In this manuscript, I have presented the development of a quantum simulator of spin systems based on assembled arrays of single Rydberg atoms. During the course of my PhD, we have bridged the gap between proof-of-principle experiments with tens of Rydberg atoms, and large-scale studies with hundreds of particles. We also extended the class of models we can simulate.

Quantum Ising model. We demonstrated this large-scale quantum simulation on the transverse field Ising model, a model which has been extensively studied theoretically, but with very few experimental realizations in a pristine setting. The model can be studied on the platform using the van der Waals interaction. Its demonstration was the first project of the platform: it was implemented for the first time in 2013 with two atoms [Béguin *et al.*, 2013], and with three atoms the following year [Barredo *et al.*, 2014]. With experience gained on the van der Waals interaction, the team studied the transverse field Ising model (for the first time with Rydberg atoms in tweezers arrays) in 2016 with ~ 10 atoms [Labuhn *et al.*, 2016]. The team could observe the emergence of anti-correlations, characteristic of antiferromagnetism. In this first study however (i) the model was not implemented in a clean two-level system due to the use of D states, and (ii) the geometrical configuration of the atoms was not fixed as the assembler had not yet been implemented. These two issues were solved by a proper tuning of the electric and magnetic fields [de Léséleuc *et al.*, 2018b], and the atom-by-atom assembler technique [Barredo *et al.*, 2016]. These allowed the group to revisit the model with up to 36 atoms in square and triangular geometries, by trying to adiabatically prepare the ground states of the model's various phases [Lienhard *et al.*, 2018]. They could observe the emergence of the phases features, but two critical drawbacks were limiting the observations: (i) the relatively small number of atoms which could be manipulated, and (ii) the restricted system's coherence [de Léséleuc *et al.*, 2018a].

These two issues were addressed during my PhD (i) by improving the capabilities of our machine to reach 200 atoms (Chapter 4), and (ii) by changing the Rydberg

excitation scheme (Chapter 3). Many small improvements of the various manipulations we perform on the atoms (Chapter 2) allowed us to obtain single-atom Rydberg excitation with $\sim 99\%$ efficiency, and two-atom entanglement fidelities above 90% (Chapter 5). Benefiting from the experience of the group in the implementation of the transverse field Ising model combined with these improvements, we were able to adiabatically prepare the antiferromagnetic ground states of the model with 100 atoms in a square geometry, and to observe long-range ordering on system sizes as large as 196 atoms (Chapter 6). This observation motivated various studies of the model. First, we assessed the new limitations of the system by comparing the data with numerical simulations involving up to 100 atoms, and concluded that the limiting factors are now (i) the residual disorder of the atom position in the tweezers, (ii) the detection errors and (iii) the driving field inhomogeneities. These insights help us devising the next steps for improving the quantum simulation of the Ising model. Second, we compared our results to numerical predictions relying on thermal equilibrium and found that they cannot be explained by a thermal driving of the system, thus providing a strong indication of its quantum nature. Third, we studied various quantum phase transitions, and showed that depending on the parameters, the system could follow (or not) the quantum Kibble-Zurek mechanism. Fourth, we probed a highly-frustrated phase (Chapter 7), and could observe the emergence of its features for the first time in a clean quantum system with hundreds of particles.

These experiments prove that quantum simulation with Rydberg atoms is now at a level which is comparable to state-of-the-art numerical simulations.

Increasing the range of Hamiltonians.   In parallel to the implementation of the quantum Ising model, the group also studied the resonant dipole-dipole interaction between Rydberg atoms, and demonstrated its implementation with three atoms in 2015 [Barredo *et al.*, 2015]. This interaction gives rise to the XX model, and was used to study a Symmetry Protected Topological (SPT) phase in 1D, which was the first project I worked on when I arrived on the setup [de Léséleuc *et al.*, 2019]. This work demonstrated that we could perform quantum simulation in the frame of the XX model, but also that good surprises could emerge from the experiment as the preparation of the SPT phase was not anticipated when we started the project. In the spirit of what have been performed by the group about the quantum Ising model, and having demonstrated its successful large-scale and accurate implementation, we then wanted to demonstrate the implementation of a wide variety of Hamiltonians. Here, the implementations are proof-of-principle with few-body systems, but will lead in the

near future to their large-scale implementation, as performed for the Ising model.

We first engineered a density-dependent, complex-valued interaction using the intrinsic spin-orbit coupling of the dipole-dipole interaction (Chapter 8). In particular, this Hamiltonian (which can be connected to the Haldane model) is expected to feature topological properties, in views of studying the quantum Hall effect. We then showed the implementation of tunable XXZ Hamiltonians by combining the XX interaction with an external microwave field (Chapter 9). These models feature various phenomena, such as superconductivity, superfluidity, or supersolidity [Manousakis, 1991; Ng and Lee, 2006; Hauke et al., 2010]. In both projects, we compared the results to numerical simulations, and showed that we understand the current limitations. These indicate the next improvements we need to perform towards the large-scale quantum simulation of these models.

Prospective and new directions.   Once the limiting factors in the implementation of transverse field Ising model listed above are solved, the team will revisit the model's features for which we could observe a first signal: (i) the quantum Kibble-Zurek mechanism in square lattices and especially its range of validity, (ii) the nature of the various phase transitions in triangular lattices and (iii) a complete characterization of the order-by-disorder phase. By combining our ability to study ground state physics in large systems and our implementation of the XX model, the team will explore its phase diagram and in particular the new types of liquid crystals the model exhibits. They will also study topological properties of 2D systems using the intrinsic spin-orbit coupling of the dipole-dipole interaction. The dynamics of out-of-equilibrium systems governed by XXZ models will also be explored, beyond the emergent features of few-body systems reported in this manuscript.

Beyond the exploration of fundamental many-body physics, the platform recently became interesting at an industrial level, in views of developing quantum computing [Henriet et al., 2020], and solving optimization problems [Henriet, 2020].

The wide tunability of the implemented Hamiltonians combined with the geometrical versatility of the platform allows us to study a large variety of many-body phenomena. The demonstration of the large-scale quantum simulation of the Ising model shows that the performances of the platform are now comparable to numerical simulations, bringing Rydberg quantum simulators one step closer to the original purpose of quantum simulation imagined by Richard Feynman.

Résumé en Français

Maintenant que la physique quantique est une théorie bien établie, le domaine évolue vers une utilisation pratique de ces lois pour des études appliquées. Cette évolution est possible grâce aux avancées techniques qui ont permis d'isoler et de contrôler de manière individuelle des particules quantiques. Grâce à ces avancées, des scientifiques ont pu vérifier de manière expérimentale les concepts fondamentaux énoncés par les fondateurs de la physique quantique, comme la superposition d'états ou l'intrication de deux particules quantiques.

Ces expériences ont déclenché un grand intérêt dans l'utilisation de ces lois fondamentales pour des applications pratiques. Par exemple, la manipulation cohérente de particules uniques permet de mesurer avec grande précision des champs électriques et magnétiques, ce qui a permis le développement de senseurs quantiques. En particulier, l'utilisation d'horloges atomiques a permis d'améliorer la précision de la géo-localisation par satellite. Dans le domaine des calculs quantiques, la superposition d'états et l'intrication peuvent être utilisés pour réaliser des opérations inaccessibles aux ordinateurs classiques. Durant ces dernières années, un effort considérable a été porté pour démontrer un avantage des calculs quantiques par rapports aux calculs classiques.

Bien que les lois fondamentales de la physique soient établies, il reste beaucoup de questions quant à leur impact sur une grande variété de systèmes fortements corrélés, dans des domaines allant de la physique des hautes énergies aux matériaux magnétiques. Dans ce dernier cas, ces lois jouent un rôle important dans la supraconductivité à haute température, ou bien dans les isolants topologiques gouvernés par l'effet Hall quantique. L'étude numérique de ces phénomènes est difficile à réaliser due à la présence de fortes interactions entre les particules quantiques, ce qui induit de fortes corrélations dans ces systèmes. En pratique, le nombre de paramètres qu'il faut prendre en compte pour réaliser une simulation exacte du système évolue de manière exponentielle avec le nombre de particules, ce qui rend les simulations exactes irréalisables pour plus de 50 particules.

Une autre approche pour étudier ces phénomènes est d'utiliser un simulateur quantique. Ce concept, originellement introduit par Richard Feynman, consiste à utiliser un système quantique artificiel pour comprendre le comportement de matériaux réels. Cette approche est récemment devenue possible grâce à des techniques expérimentales de pointe. Leur niveau de contrôle et la versatilité dans le type d'interactions implémentées permettent aujourd'hui aux physiciens d'utiliser ces simulateurs "comme si" ils réalisaient des simulations sur un ordinateur classique.

Dans ce manuscrit, je décris notre simulateur quantique, et expose les expériences de simulation quantique que nous avons réalisé pendant ma thèse. Il existe plusieurs manières de réaliser un simulateur quantique. Notre approche est basée sur des atomes de rubidium piégés individuellements dans des matrices de pinces optiques à géométrie variable, et excités vers des états de Rydberg pour permettre leur interaction. De nos jours, les simulateurs quantique font face à trois enjeux clés. Premièrement, la simulation quantique devient intéressante dès lors que le nombre de particules en interaction dépasse ce qui peut être calculé classiquement. Cette limite est de l'ordre d'une centaine de particules. Deuxièmement, les résultats du simulateur quantique doivent être verifiables et sûrs, ce qui signifie que les diverses imperfections de ces simulateurs doivent être calibrées avec précision. Troisièmement, les simulateurs doivent être capables de simuler différents phénomènes de la physique, ce qui veut dire qu'ils doivent être capables d'implémenter une grande variété de modèles.

Nous avons travaillé sur ces trois points pendant ma thèse, et cela constitue le plan de mon manuscrit de thèse. En Partie I, j'explique comment nous pouvons manipuler une centaine d'atomes avec grande précision. En Partie II, je réalise la simulation quantique à large échelle du modèle d'Ising, et vérifie les résulats du simulateur sur un système comprenant 100 particules. En Partie III, je présente de quelle manière nous avons pu accroître le nombre de modèles de spins que nous pouvons simuler avec notre plateforme.

Partie I: Amélioration du dispositif expérimental

Chapitre 2 Ce chapitre décrit l'ensemble du dispositif expériemental composé d'atomes individuels de rubidium, piégés dans leur état fondamental dans des matrices de pinces optiques, et excités vers des états de Rydberg. Tout d'abord, je présente la brique élémentaire de notre dispositif, à savoir le piégeage et l'imagerie d'un atome unique dans une pince optique. J'explique ensuite de manière globale comment nous produisons des matrices de pinces optique à géométrie variable, un point sur lequel je

reviens dans le Chapitre 4. Je détaille ensuite les méthodes expérimentales que nous utilisons de manière quotidienne, permettant de refroidir, manipuler et exciter les atomes vers leurs états de Rydberg. Ce dernier point est traité en particulier dans le Chapitre 4. Je termine par expliquer de quelle manière nous contrôlons précisément l'environnement électromagnétique entourant les atomes.

Chapitre 3 Ce chapitre détaille la manière dont nous excitons les atomes vers les états de Rydberg. Nous utilisons une transitions à deux photons avec un large désaccord avec le niveau intermédiaire pour limiter la décohérence du système. Durant ma thèse, nous avons remplacé le système laser pour obtenir de meilleurs résultats. Nous utilisons à présent l'état $6P_{3/2}$ comme état intermédiaire plutôt que le $5P_{1/2}$, car celui-ci a deux avantages: (i) un temps de vie quatre fois plus long, et (ii) les longueurs d'onde qui lui sont associées sont plus favorables en terme de puissance laser. Nous avons également changé de technologie laser, et utilisons maintenant des lasers à Titane Saphire. Ces changements nous ont permis d'obtenir une cohérence au moins dix fois supérieure au précédent système. J'explique également comment nous avons amélioré l'efficacité de l'excitation vers les états de Rydberg pour atteindre 97%. Je termine ce chapitre en comparant nos résultats expérimentaux avec des simulations incluant les divers facteurs limitants. Nous obtenons un bon accord expérience/simulations, ce qui indique que nous avons un bon contrôle sur les imperfections du système.

Chapitre 4 Ce chapitre présente une étude détaillée portant sur l'obtention de grandes matrices d'atomes. Dans un premier temps, j'explique brièvement la technologie utilisée pour générer des matrices de pinces optique. J'explique ensuite comment, durant ma thèse, nous avons augmenté le nombre de pinces optiques tout en gardant un bon contrôle sur leur qualité optique. Cet augmentation a été possible en particulier grâce à la mise en place de diagnostics *in situ* directement sur les atomes, permettant un contrôle amélioré de la qualité des pinces optiques. Dans un second temps, je présente la méthode d'assemblage d'atomes nous permettant de contrôler la géométrie des atomes, ici à deux dimensions. Je présente une étude détaillée des limites de cette technique d'assemblage, et motive les changements réalisés durant ma thèse qui ont permis d'augmenter d'un facteur quatre le nombre d'atomes qui nous pouvons manipuler: (i) la mise en place d'un algorithme d'assemblage optimisé et (ii) l'utilisation de deux cycles de réarrangement. Nous pouvons à présent contrôler environ deux cents atomes, ce qui nous place dans le régime intéressant pour la simulation quantique pour lequel les simulations classiques sont difficilement réalisables.

Partie II: Simulation quantique de l'antiferromagnétisme du modèle d'Ising

Chapitre 5 Ce chapitre est une introduction au modèle d'Ising. Je commence par présenter l'interaction de van der Waals entre deux atomes de Rydberg, et explique comment cette interaction permet de générer de l'intrication. Je présente des résultats expérimentaux montrant une fidélité d'intrication supérieure à 90%, plaçant notre plateforme à un niveau compétitif par rapport à ce qui a été démontré sur des plateformes similaires. Je détaille ensuite comment l'interaction de van der Waals implémente le modèle d'Ising en champ transverse. Je réalise ensuite une rapide étude théorique du modèle d'Ising à une dimension en m'appuyant sur des simulations. Je détaille les états fondamentaux du système en fonction des paramètres et présente l'émergence d'antiferromagnétisme dans le modèle d'Ising. Je termine le chapitre en présentant des résultats expérimentaux à 47 atomes montrant la préparation de cet ordre antiferromagnétique, en considérant diverses observables caractéristiques qui seront étudiées dans les deux prochains chapitres.

Chapitre 6 Ce chapitre détaille les travaux réalisés sur la simulation quantique à large échelle du modèle d'Ising sur des réseaux carrés. Ce modèle n'est pas résolu analytiquement, ce qui le rend intéressant à étudier avec notre simulateur quantique. Je commence par présenter le diagramme des phases du modèle, et de quelle manière nous explorons celui-ci sur des systèmes allant jusqu'à 196 atomes. J'étudie ensuite en détail l'effet de la taille finie de notre système sur ce diagramme des phases. Je montre que les propriétés du système dependent grandement de sa taille. En observant l'évolution de ces propriétés en fonction de la taille du système, j'extrait les propriétés à la limite thermodynamique et obtient des résultats cohérents avec ceux calculés par des méthodes numériques. Je compare ensuite les résultats des nos expériences avec des simulations réalisées par l'équipe de Andreas Laüchli, sur des systèmes comprenants jusqu'à cent atomes. Nous obtenons un bon accord, ce qui permet d'avoir confiance en les résultats donnés par le simulateur quantique. Ces résultats nous permettent aussi d'indentifier quels sont les points à améliorer sur notre dispositif expérimental dans le futur. Je compare ensuite nos résultats expérimentaux à des simulations classiques à l'équilibre thermodynamique. Le désaccord entre les résultats expérimentaux et les simulations montrent que nous n'obtenons pas un ensemble thermique, ce qui est une indication forte de la nature quantique de nos résultats. Je termine le chapitre

par une étude expérimentale d'une transition de phase quantique. En particulier, nous explorons le régime de Kibble-Zurek, et montrons qu'en fonction des paramètres choisis, nous obtenons des résultats en accord ou non avec ce régime.

Chapitre 7 Ce chapitre détaille les travaux réalisés sur la simulation quantique à large échelle du modèle d'Ising sur des réseaux triangulaires. Ce modèle présente un diagramme des phases plus riche que le réseau carré, avec notamment la présence d'une phase géométriquement frustrée. Je commence le chapitre par donner une image intuitive des différentes phases du modèle sur le cas le plus simple de trois atomes en interaction. Je présente ensuite le diagramme des phases dans le cas d'un système infini, et détaille de quelle manière nous explorons celui-ci. Je présente ensuite une étude expérimentale détaillée impliquant jusqu'à 147 atomes d'une des phases antiferromagnétique non frustrée du modèle, qui comprend: (i) une étude des effets de la taille finie du système, (ii) une comparaison de nos résultats avec des simulations classiques, et (iii) une étude d'une transition de phase. Ces résultats montrent que nous sommes capables d'étudier le modèle d'Ising sur des réseaux triangulaires, donc d'étudier la phase frustrée. Je termine le chapitre en présentant des premiers résultats expérimentaux ayant pour objectif de caractériser cette phase frustrée. Nous observons une transition de phase dont les caractéristiques mesurées sont cohérentes avec ce qui est attendu théoriquement. Ces premiers résultats tendent à montrer que nous pouvons étudier cette phase frustrée avec notre simulateur quantique.

Partie III: Ingénierie d'Hamiltoniens de spins en utilisant l'interaction dipôle-dipôle entre atomes de Rydberg

Chapitre 8 Ce chapitre présente l'utilisation de l'interaction dipôle-dipôle entre atomes de Rydberg pour implémenter deux modèles de spins: (i) le modèle XX et (ii) une phase de Peierls induite par une interaction à valeur complexe. Je commence par expliquer comment, à partir de l'expression générale de l'interaction dipôle-dipôle, nous pouvons choisir judicieusement les paramètres excpérimentaux pour implémenter l'un des deux modèles. Je détaille ensuite de manière expérimentale les caractéristiques du modèle XX sur le cas le plus simple de deux atomes en interaction, et compare nos résultats à des simulations pour identifier les facteurs limitants. Je présente ensuite nos résultats concernant l'ingénierie d'une interaction à valeur complexe sur un système comprenant trois atomes. Le terme complexe provient du couplage spin-orbite

intrinsèque à l'interaction dipôle-dipôle, et se manifeste par la prise en compte de trois états de Rydberg. La phase du couplage complexe est déterminée par la géométrie du système, par la différence d'énergie entre les trois niveaux et par la présence d'autres excitations dans le système. Je termine ce chapitre par l'implémentation et le contrôle de ce couplage complexe, et je montre également que le système peut être interprété en terme de particules anyoniques.

Chapitre 9   Ce chapitre présente l'ingénierie d'Hamiltoniens de Heisenberg à anisotropie variable. Je commence par expliquer comment nous pouvons réaliser cette ingénierie en combinant l'interaction dipole-dipôle résonante à un champ micro-onde externe. Je présente ensuite des résultats expérimentaux permettant de vérifier l'implémentation correcte de ces modèles sur le cas le plus simple de deux atomes. Je détaille ensuite l'implémentation de modèle de Heisenberg sur des sytèmes allant jusqu'à 64 atomes, et étudie expérimentalement les limites de l'ingénierie. Je finis par étudier un système unidimensionnel composé de 10 atomes, dans lequel nous étudions la propagation d'excitations de spins sous différents Hamiltoniens de Heisenberg. Nous varions également les conditions aux limites (périodiques et ouvertes) et observons leur impact sur la dynamique du système.

Bibliography

Aharonov, Y. and Bohm, D., *"Significance of electromagnetic potentials in the quantum theory,"* Phys. Rev. **115**, 485 (1959) [cited in page 188].

Aidelsburger, M., Atala, M., Lohse, M., Barreiro, J. T., Paredes, B., and Bloch, I., *"Realization of the Hofstadter Hamiltonian with ultracold atoms in optical lattices,"* Phys. Rev. Lett. **111**, 185301 (2013) [cited in page 202].

Aidelsburger, M., Atala, M., Nascimbène, S., Trotzky, S., Chen, Y.-A., and Bloch, I., *"Experimental realization of strong effective magnetic fields in an optical lattice,"* Phys. Rev. Lett. **107**, 255301 (2011) [cited in page 188].

Aidelsburger, M., Nascimbene, S., and Goldman, N., *"Artificial gauge fields in materials and engineered systems,"* Comptes Rendus Physique **19**, 394 (2018), quantum simulation / Simulation quantique [cited in page 178].

Anderson, P. W., *"The resonating valence bond state in La_2CuO_4 and superconductivity,"* Science **235**, 1196 (1987) [cited in page 201].

Anquez, M., Robbins, B. A., Bharath, H. M., Boguslawski, M., Hoang, T. M., and Chapman, M. S., *"Quantum Kibble-Zurek mechanism in a spin-1 Bose-Einstein condensate,"* Phys. Rev. Lett. **116**, 155301 (2016) [cited in page 141].

Arute *et al.*, ., *"Quantum supremacy using a programmable superconducting processor,"* Nature **574**, 505 (2019) [cited in pages 11 and 102].

Aspect, A., Grangier, P., and Roger, G., *"Experimental realization of Einstein-Podolsky-Rosen-Bohm gedankenexperiment: A new violation of Bell's inequalities,"* Physical Review Letters **49**, 91 (1982) [cited in page 11].

Atala, M., Aidelsburger, M., Barreiro, J. T., Abanin, D., Kitagawa, T., Demler, E., and Bloch, I., *"Direct measurement of the Zak phase in topological Bloch bands,"* Nature Physics **9**, 795 (2013) [cited in page 14].

Bakr, W. S., Peng, A., Tai, M. E., Ma, R., Simon, J., Gillen, J. I., Fölling, S., Pollet, L., and Greiner, M., *"Probing the superfluid–to–Mott insulator transition at the single-atom level,"* Science **329**, 547 (2010) [cited in page 14].

Balents, L., *"Spin liquids in frustrated magnets,"* Nature **464**, 199 (2010) [cited in pages 149 and 177].

Barmettler, P., Punk, M., Gritsev, V., Demler, E., and Altman, E., *"Relaxation of antiferromagnetic order in spin-1/2 chains following a quantum quench,"* Phys. Rev. Lett. **102**, 130603 (2009) [cited in page 214].

Barnes, T., *"The 2D Heisenberg antiferromagnet in high-Tc superconductivity: A review of numerical techniques and results,"* International Journal of Modern Physics C **02**, 659 (1991) [cited in page 201].

Barredo, D., Labuhn, H., Ravets, S., Lahaye, T., Browaeys, A., and Adams, C. S., *"Coherent excitation transfer in a spin chain of three Rydberg atoms,"* Physical Review Letters **114**, 113002 (2015) [cited in pages 195 and 226].

Barredo, D., de Léséleuc, S., Lienhard, V., Lahaye, T., and Browaeys, A., *"An atom-by-atom assembler of defect-free arbitrary two-dimensional atomic arrays,"* Science **354**, 1021 (2016) [cited in pages 16, 30, 86, and 225].

Barredo, D., Lienhard, V., de Léséleuc, S., Lahaye, T., and Browaeys, A., *"Synthetic three-dimensional atomic structures assembled atom by atom,"* Nature **561**, 79 (2018) [cited in page 85].

Barredo, D., Lienhard, V., Scholl, P., de Léséleuc, S., Boulier, T., Browaeys, A., and Lahaye, T., *"Three-dimensional trapping of individual Rydberg atoms in ponderomotive bottle beam traps,"* Phys. Rev. Lett. **124**, 023201 (2020) [cited in page 39].

Barredo, D., Ravets, S., Labuhn, H., Béguin, L., Vernier, A., Nogrette, F., Lahaye, T., and Browaeys, A., *"Demonstration of a strong Rydberg blockade in three-atom systems with anisotropic interactions,"* Physical Review Letters **112**, 183002 (2014) [cited in page 225].

Becker, C., Soltan-Panahi, P., Kronjäger, J., Dörscher, S., Bongs, K., and Sengstock, K., *"Ultracold quantum gases in triangular optical lattices,"* New Journal of Physics **12**, 065025 (2010) [cited in page 149].

Béguin, L., Measurement of the van der Waals interaction between two Rydberg atoms, Ph.D. thesis, Université Paris-Saclay (2013) [cited in pages 22, 23, 50, and 83].

Béguin, L., Vernier, A., Chicireanu, R., Lahaye, T., and Browaeys, A., *"Direct measurement of the van der Waals interaction between two Rydberg atoms,"* Physical Review Letters **110**, 263201 (2013) [cited in page 225].

Bergamini, S., Darquie, B., Jones, M., Lionel, J., Browaeys, A., and Grangier, P., *"Holographic generation of microtrap arrays for single atoms by use of a programmable phase modulator,"* Journal of the Optical Society of America B **21** (2004), 10.1364/JOSAB.21.001889 [cited in page 26].

Bergholtz, E. J. and Liu, Z., *"Topological flat band models and fractional Chern insulators,"* International Journal of Modern Physics B **27**, 1330017 (2013) [cited in page 187].

Bernien, H., Schwartz, S., Keesling, A., Levine, H., Omran, A., Pichler, H., Choi, S., Zibrov, A. S., Endres, M., Greiner, M., Vuletić, V., and Lukin, M. D., *"Probing many-body dynamics on a 51-atom quantum simulator,"* Nature **551**, 579 (2017) [cited in pages 28, 108, and 112].

Bertini, B., Heidrich-Meisner, F., Karrasch, C., Prosen, T., Steinigeweg, R., and Žnidarič, M., *"Finite-temperature transport in one-dimensional quantum lattice models,"* Rev. Mod. Phys. **93**, 025003 (2021) [cited in pages 178 and 214].

Beterov, I. I., Ryabtsev, I. I., Tretyakov, D. B., and Entin, V. M., *"Quasiclassical calculations of blackbody-radiation-induced depopulation rates and effective lifetimes of Rydberg ns, np, and nd alkali-metal atoms with $n \leq 80$,"* Phys. Rev. A **79**, 052504 (2009) [cited in page 42].

Beugnon, J., Contrôle de l'état interne d'un atome unique piégé et expériences d'interférences à deux photons : vers l'information quantique avec des atomes neutres, Ph.D. thesis (2007), Paris 11 [cited in page 81].

Binder, K., *"Finite size scaling analysis of Ising model block distribution functions,"* Zeitschrift für Physik B Condensed Matter **43**, 119 (1981) [cited in page 139].

Blatt, R. and Roos, C. F., *"Quantum simulations with trapped ions,"* Nature Physics **8**, 277 (2012) [cited in page 108].

Blatt, R. and Wineland, D., *"Entangled states of trapped atomic ions,"* Nature **453**, 1008 (2008) [cited in pages 14 and 102].

Bloch, I., *"Ultracold quantum gases in optical lattices,"* Nature Physics **1**, 23 (2005) [cited in page 14].

Blöte, H. W. J. and Deng, Y., *"Cluster Monte Carlo simulation of the transverse Ising model,"* Phys. Rev. E **66**, 066110 (2002) [cited in page 119].

Blöte, H. W. J. and Swendsen, R. H., *"First-order phase transitions and the three-state Potts model,"* Phys. Rev. Lett. **43**, 799 (1979) [cited in page 164].

Browaeys, A., Barredo, D., and Lahaye, T., *"Experimental investigations of dipole–dipole interactions between a few Rydberg atoms,"* Journal of Physics B **49**, 152001 (2016) [cited in pages 16 and 102].

Browaeys, A. and Lahaye, T., *"Many-body physics with individually controlled Rydberg atoms,"* Nature Physics **16**, 132 (2020) [cited in page 102].

Brown, M. O., Thiele, T., Kiehl, C., Hsu, T.-W., and Regal, C. A., *"Gray-molasses optical-tweezer loading: Controlling collisions for scaling atom-array assembly,"* Phys. Rev. X **9**, 011057 (2019) [cited in page 28].

del Campo, A. and Zurek, W., *"Universality of phase transition dynamics: Topological defects from symmetry breaking,"* International Journal of Modern Physics A **29** (2013) [cited in page 141].

Carusotto, I. and Ciuti, C., *"Quantum fluids of light,"* Rev. Mod. Phys. **85**, 299 (2013) [cited in page 15].

Chen, Y., Neill, C., Roushan, P., Leung, N., Fang, M., Barends, R., Kelly, J., Campbell, B., Chen, Z., Chiaro, B., Dunsworth, A., Jeffrey, E., Megrant, A., Mutus, J. Y., O'Malley, P. J. J., Quintana, C. M., Sank, D., Vainsencher, A., Wenner, J., White, T. C., Geller, M. R., Cleland, A. N., and Martinis, J. M., *"Qubit architecture with high coherence and fast tunable coupling,"* Phys. Rev. Lett. **113**, 220502 (2014) [cited in page 15].

Cheneau, M., Barmettler, P., Poletti, D., Endres, M., Schauß, P., Fukuhara, T., Gross, C., Bloch, I., Kollath, C., and Kuhr, S., *"Light-cone-like spreading of correlations in a quantum many-body system,"* Nature **481**, 484 (2012) [cited in page 178].

Choi, J., Zhou, H., Knowles, H. S., Landig, R., Choi, S., and Lukin, M. D., *"Robust dynamic Hamiltonian engineering of many-body spin systems,"* Phys. Rev. X **10**, 031002 (2020) [cited in page 211].

238

Cirac, J. I. and Zoller, P., *"Quantum computations with cold trapped ions,"* Phys. Rev. Lett. **74**, 4091 (1995) [cited in page 14].

Cline, R. A., Miller, J. D., Matthews, M. R., and Heinzen, D. J., *"Spin relaxation of optically trapped atoms by light scattering,"* Opt. Lett. **19**, 207 (1994) [cited in page 81].

Collini, E., *"Spectroscopic signatures of quantum-coherent energy transfer,"* Chem. Soc. Rev. **42**, 4932 (2013) [cited in page 178].

Collura, M., De Luca, A., and Viti, J., *"Analytic solution of the domain-wall nonequilibrium stationary state,"* Phys. Rev. B **97**, 081111 (2018) [cited in pages 215 and 218].

Cooper, N. R., Dalibard, J., and Spielman, I. B., *"Topological bands for ultracold atoms,"* Rev. Mod. Phys. **91**, 015005 (2019) [cited in page 187].

Cortiñas, R. G., Favier, M., Ravon, B., Méhaignerie, P., Machu, Y., Raimond, J. M., Sayrin, C., and Brune, M., *"Laser trapping of circular Rydberg atoms,"* Phys. Rev. Lett. **124**, 123201 (2020) [cited in page 42].

Crouse, D. F., *"On implementing 2D rectangular assignment algorithms,"* IEEE Transactions on Aerospace and Electronic Systems **52**, 1679 (2016) [cited in page 92].

Da Liao, Y., Li, H., Yan, Z., Wei, H.-T., Li, W., Qi, Y., and Meng, Z. Y., *"Phase diagram of the quantum Ising model on a triangular lattice under external field,"* Phys. Rev. B **103**, 104416 (2021) [cited in pages 164 and 171].

Dalibard, J., Gerbier, F., Juzeliūnas, G., and Öhberg, P., *"Colloquium: Artificial gauge potentials for neutral atoms,"* Rev. Mod. Phys. **83**, 1523 (2011) [cited in pages 178 and 188].

Darquié, B., Manipulation d'atomes dans des pièges dipolaires microscopiques et émission contrôlée de photons par une atome unique, Ph.D. thesis (2005), Paris 11 [cited in page 25].

Dehmelt, H., *"Experiments with an isolated subatomic particle at rest,"* Review of Modern Physics **62**, 525 (1990) [cited in page 11].

Devoret, M. H. and Schoelkopf, R. J., *"Superconducting circuits for quantum information: An outlook,"* Science **339**, 1169 (2013) [cited in page 15].

Dziarmaga, J., *"Dynamics of a quantum phase transition: Exact solution of the quantum Ising model,"* Phys. Rev. Lett. **95**, 245701 (2005) [cited in page 141].

Ebadi, S., Wang, T. T., Levine, H., Keesling, A., Semeghini, G., Omran, A., Bluvstein, D., Samajdar, R., Pichler, H., Ho, W. W., Choi, S., Sachdev, S., Greiner, M., Vuletić, V., and Lukin, M. D., *"Quantum phases of matter on a 256-atom programmable quantum simulator,"* Nature **595**, 227 (2021) [cited in pages 28, 108, 119, 141, and 147].

Eckardt, A., *"Colloquium: Atomic quantum gases in periodically driven optical lattices,"* Rev. Mod. Phys. **89**, 011004 (2017) [cited in page 202].

Endres, M., Bernien, H., Keesling, A., Levine, H., Anschuetz, E. R., Krajenbrink, A., Senko, C., Vuletic, V., Greiner, M., and Lukin, M. D., *"Atom-by-atom assembly of defect-free one-dimensional cold atom arrays,"* Science **354**, 1024 (2016) [cited in page 26].

Fey, S., Kapfer, S. C., and Schmidt, K. P., *"Quantum criticality of two-dimensional quantum magnets with long-range interactions,"* Phys. Rev. Lett. **122**, 017203 (2019) [cited in pages 119, 126, and 127].

Feynman, R. P., *"Simulating physics with computers,"* International Journal of Theoretical Physics **21**, 467 (1982) [cited in page 12].

Fläschner, N., Rem, B. S., Tarnowski, M., Vogel, D., Lühmann, D.-S., Sengstock, K., and Weitenberg, C., *"Experimental reconstruction of the Berry curvature in a Floquet Bloch band,"* Science **352**, 1091 (2016) [cited in page 202].

Fradkin, E., Field Theories of Condensed Matter Systems (Addison-Wesley, Redwood City, CA, 1991) [cited in page 199].

Frerot, I., Naldesi, P., and Roscilde, T., *"Entanglement and fluctuations in the XXZ model with power-law interactions,"* Physical Review B **95** (2017), 10.1103/Phys-RevB.95.245111 [cited in page 201].

Fukuhara, T., Schauß, P., Endres, M., Hild, S., Cheneau, M., Bloch, I., and Gross, C., *"Microscopic observation of magnon bound states and their dynamics,"* Nature **502**, 76 (2013) [cited in page 214].

Gaëtan, A., Miroshnychenko, Y., Wilk, T., Chotia, A., Viteau, M., Comparat, D., Pillet, P., Browaeys, A., and Grangier, P., *"Observation of collective excitation of*

two individual atoms in the Rydberg blockade regime," Nature Physics **5**, 115 (2009) [cited in page 15].

Galitski, V. and Spielman, I. B., *"Spin–orbit coupling in quantum gases,"* Nature **494**, 49 (2013) [cited in page 188].

Gallagher, T. F., *"Rydberg atoms,"* Reports on Progress in Physics **51**, 143 (1988) [cited in page 103].

Geier, S., Thaicharoen, N., Hainaut, C., Franz, T., Salzinger, A., Tebben, A., Grimshandl, D., Zürn, G., and Weidemüller, M., *"Floquet Hamiltonian engineering of an isolated many-body spin system,"* (2021), arXiv:2105.01597 [cond-mat.quant-gas] [cited in page 211].

Georgescu, I. M., Ashhab, S., and Nori, F., *"Quantum simulation,"* Review of Modern Physics **86**, 153 (2014) [cited in page 12].

Gerchberg, R. W. and Saxton, W. O., *"Practical algorithm for determination of phase from image and diffraction plane pictures,"* OPTIK **35**, 237 (1972) [cited in pages 27 and 76].

Giamarchi, T., Quantum physics in one dimension (Clarendon Press, 2003) [cited in page 214].

Glaser, C., Karlewski, F., Kluge, J., Grimmel, J., Kaiser, M., Günther, A., Hattermann, H., Krutzik, M., and Fortágh, J., *"Absolute frequency measurement of rubidium $5S-6P$ transitions,"* Phys. Rev. A **102**, 012804 (2020) [cited in page 61].

Gobert, D., Kollath, C., Schollwöck, U., and Schütz, G., *"Real-time dynamics in spin-1/2 chains with adaptive time-dependent density matrix renormalization group,"* Phys. Rev. E **71**, 036102 (2005) [cited in pages 214 and 215].

Goldman, N. and Dalibard, J., *"Periodically driven quantum systems: Effective Hamiltonians and engineered gauge fields,"* Phys. Rev. X **4**, 031027 (2014) [cited in pages 188 and 202].

Gong, Z.-X., Maghrebi, M. F., Hu, A., Foss-Feig, M., Richerme, P., Monroe, C., and Gorshkov, A. V., *"Kaleidoscope of quantum phases in a long-range interacting spin-1 chain,"* Phys. Rev. B **93**, 205115 (2016) [cited in page 201].

Graham, T. M., Kwon, M., Grinkemeyer, B., Marra, Z., Jiang, X., Lichtman, M. T., Sun, Y., Ebert, M., and Saffman, M., *"Rydberg-mediated entanglement in a two-dimensional neutral atom qubit array,"* Phys. Rev. Lett. **123**, 230501 (2019) [cited in page 107].

Greiner, M., Mandel, O., Esslinger, T., Hänsch, T. W., and Bloch, I., *"Quantum phase transition from a superfluid to a Mott insulator in a gas of ultracold atoms,"* Nature **415**, 39 (2012) [cited in page 14].

Greschner, S. and Santos, L., *"Anyon Hubbard Model in One-Dimensional Optical Lattices,"* Phys. Rev. Lett. **115**, 053002 (2015) [cited in page 199].

Grimm, R., Weidemüller, M., and Ovchinnikov, Y. B., *"Optical dipole traps for neutral atoms,"* (Academic Press, 2000) pp. 95–170 [cited in page 24].

Grünzweig, T., Hilliard, A., McGovern, M., and Andersen, M. F., *"Near-deterministic preparation of a single atom in an optical microtrap,"* Nature Physics **6**, 951 (2010) [cited in page 28].

Guardado-Sanchez, E., Brown, P. T., Mitra, D., Devakul, T., Huse, D. A., Schauß, P., and Bakr, W. S., *"Probing the quench dynamics of antiferromagnetic correlations in a 2D quantum Ising spin system,"* Phys. Rev. X **8**, 021069 (2018) [cited in page 108].

Haroche, S., *"Nobel lecture: Controlling photons in a box and exploring the quantum to classical boundary,"* Review of Modern Physics **85**, 1083 (2013) [cited in page 11].

Hauke, P., Cucchietti, F. M., Müller-Hermes, A., Bañuls, M.-C., Cirac, J. I., and Lewenstein, M., *"Complete devil's staircase and crystal-superfluid transitions in a dipolar xxz spin chain: a trapped ion quantum simulation,"* New Journal of Physics **12**, 113037 (2010) [cited in pages 201 and 227].

Hazzard, K. R. A., Gadway, B., Foss-Feig, M., Yan, B., Moses, S. A., Covey, J. P., Yao, N. Y., Lukin, M. D., Ye, J., Jin, D. S., and Rey, A. M., *"Many-body dynamics of dipolar molecules in an optical lattice,"* Phys. Rev. Lett. **113**, 195302 (2014) [cited in pages 202, 212, and 214].

Henelius, P. and Sandvik, A. W., *"Sign problem in Monte Carlo simulations of frustrated quantum spin systems,"* Phys. Rev. B **62**, 1102 (2000) [cited in page 149].

Henriet, L., *"Robustness to spontaneous emission of a variational quantum algorithm,"* Phys. Rev. A **101**, 012335 (2020) [cited in page 227].

Henriet, L., Beguin, L., Signoles, A., Lahaye, T., Browaeys, A., Reymond, G.-O., and Jurczak, C., *"Quantum computing with neutral atoms,"* Quantum **4**, 327 (2020) [cited in page 227].

Henry, C., *"Theory of the linewidth of semiconductor lasers,"* IEEE Journal of Quantum Electronics **18**, 259 (1982) [cited in page 59].

Heydarinasab, F. and Abouie, J., *"Spin supersolid phase in coupled alternating spin chains,"* Scientific Reports **8**, 7955 (2018) [cited in page 201].

Hild, S., Fukuhara, T., Schauß, P., Zeiher, J., Knap, M., Demler, E., Bloch, I., and Gross, C., *"Far-from-equilibrium spin transport in Heisenberg quantum magnets,"* Phys. Rev. Lett. **113**, 147205 (2014) [cited in page 214].

Hofstadter, D. R., *"Energy levels and wave functions of bloch electrons in rational and irrational magnetic fields,"* Phys. Rev. B **14**, 2239 (1976) [cited in page 188].

Hollerith, S., Zeiher, J., Rui, J., Rubio-Abadal, A., Walther, V., Pohl, T., Stamper-Kurn, D. M., Bloch, I., and Gross, C., *"Quantum gas microscopy of Rydberg macrodimers,"* Science **364**, 664 (2019) [cited in page 72].

Hubbard, J. and Flowers, B. H., *"Electron correlations in narrow energy bands,"* Proceedings of the Royal Society of London. Series A. Mathematical and Physical Sciences **276**, 238 (1963) [cited in page 12].

Šibalić, N., Pritchard, J., Adams, C., and Weatherill, K., *"ARC: An open-source library for calculating properties of alkali Rydberg atoms,"* Computer Physics Communications **220**, 319 (2017) [cited in page 104].

Isakov, S. V. and Moessner, R., *"Interplay of quantum and thermal fluctuations in a frustrated magnet,"* Phys. Rev. B **68**, 104409 (2003) [cited in pages 152, 153, and 155].

Isakov, S. V., Wessel, S., Melko, R. G., Sengupta, K., and Kim, Y. B., *"Hard-core bosons on the kagome lattice: Valence-bond solids and their quantum melting,"* Phys. Rev. Lett. **97**, 147202 (2006) [cited in page 201].

Isenhower, L., Urban, E., Zhang, X. L., Gill, A. T., Henage, T., Johnson, T. A., Walker, T. G., and Saffman, M., *"Demonstration of a Neutral Atom Controlled-NOT Quantum Gate,"* Physical Review Letters **104**, 010503 (2010) [cited in page 16].

Jaksch, D., Cirac, J. I., Zoller, P., Rolston, S. L., Côté, R., and Lukin, M. D., *"Fast quantum gates for neutral atoms,"* Phys. Rev. Lett. **85**, 2208 (2000) [cited in pages 15 and 101].

Jaksch, D. and Zoller, P., *"Creation of effective magnetic fields in optical lattices: the hofstadter butterfly for cold neutral atoms,"* New Journal of Physics **5**, 56 (2003) [cited in page 188].

Janke, W. and Villanova, R., *"Three-dimensional 3-state Potts model revisited with new techniques,"* Nuclear Physics B **489**, 679 (1997) [cited in pages 154 and 164].

Jau, Y.-Y., Hankin, A. M., Keating, T., Deutsch, I. H., and Biedermann, G. W., *"Entangling atomic spins with a Rydberg-dressed spin-flip blockade,"* Nature Physics **12**, 71 (2016) [cited in page 72].

Jepsen, P. N., Amato-Grill, J., Dimitrova, I., Ho, W. W., Demler, E., and Ketterle, W., *"Spin transport in a tunable Heisenberg model realized with ultracold atoms,"* Nature **588**, 403 (2020) [cited in pages 202 and 214].

Jo, G.-B., Guzman, J., Thomas, C. K., Hosur, P., Vishwanath, A., and Stamper-Kurn, D. M., *"Ultracold atoms in a tunable optical kagome lattice,"* Phys. Rev. Lett. **108**, 045305 (2012) [cited in page 149].

Joshi, M. K., Kranzl, F., Schuckert, A., Lovas, I., Maier, C., Blatt, R., Knap, M., and Roos, C. F., *"Observing emergent hydrodynamics in a long-range quantum magnet,"* (2021), arXiv:2107.00033 [cited in page 214].

Jotzu, G., Messer, M., Desbuquois, R., Lebrat, M., Uehlinger, T., Greif, D., and Esslinger, T., *"Experimental realization of the topological Haldane model with ultracold fermions,"* Nature **515**, 237 (2014) [cited in page 188].

Jurcevic, P., Lanyon, B. P., Hauke, P., Hempel, C., Zoller, P., Blatt, R., and Roos, C. F., *"Quasiparticle engineering and entanglement propagation in a quantum many-body system,"* Nature **511**, 202 (2014) [cited in page 214].

Jurcevic, P., Shen, H., Hauke, P., Maier, C., Brydges, T., Hempel, C., Lanyon, B. P., Heyl, M., Blatt, R., and Roos, C. F., *"Direct observation of dynamical quantum*

phase transitions in an interacting many-body system," Phys. Rev. Lett. **119**, 080501 (2017) [cited in page 202].

Kaufman, A., Laser cooling atoms to indistinguishability: Atomic Hong-Ou-Mandel interference and entanglement through spin exchange, Ph.D. thesis, Boulder, CO (2015) [cited in page 35].

Kaufman, A. M., Lester, B. J., and Regal, C. A., *"Cooling a single atom in an optical tweezer to its quantum ground state,"* Phys. Rev. X **2**, 041014 (2012) [cited in page 34].

Keesling, A., Omran, A., Levine, H., Bernien, H., Pichler, H., Choi, S., Samajdar, R., Schwartz, S., Silvi, P., Sachdev, S., Zoller, P., Endres, M., Greiner, M., Vuletić, V., and Lukin, M. D., *"Quantum kibble–zurek mechanism and critical dynamics on a programmable Rydberg simulator,"* Nature **568**, 207 (2019) [cited in pages 141 and 143].

Keilmann, T., Lanzmich, S., McCulloch, I., and Roncaglia, M., *"Statistically induced phase transitions and anyons in 1D optical lattices,"* Nature Communications **2**, 361 (2011) [cited in page 199].

Keimer, B., Kivelson, S. A., Norman, M. R., Uchida, S., and Zaanen, J., *"From quantum matter to high-temperature superconductivity in copper oxides,"* Nature **518**, 179 (2015) [cited in page 11].

Kiffner, M., O'Brien, E., and Jaksch, D., *"Topological spin models in Rydberg lattices,"* Applied Physics B **123**, 46 (2017) [cited in page 188].

Kim, K., Chang, M.-S., Korenblit, S., Islam, R., Edwards, E. E., Freericks, J. K., Lin, G.-D., Duan, L.-M., and Monroe, C., *"Quantum simulation of frustrated Ising spins with trapped ions,"* Nature **465**, 590 (2010) [cited in page 149].

King *et al.*, , *"Observation of topological phenomena in a programmable lattice of 1,800 qubits,"* Nature **560**, 460 (2018) [cited in page 108].

Kitching, J., Knappe, S., and Donley, E. A., *"Atomic sensors – a review,"* IEEE Sensors Journal **11**, 1749 (2011) [cited in page 11].

Klitzing, K. v., Dorda, G., and Pepper, M., *"New method for high-accuracy determination of the fine-structure constant based on quantized Hall resistance,"* Phys. Rev. Lett. **45**, 494 (1980) [cited in pages 11 and 178].

Knolle, J. and Moessner, R., *"A field guide to spin liquids,"* Annual Review of Condensed Matter Physics **10**, 451 (2019) [cited in page 178].

Kokail, C., Maier, C., van Bijnen, R., Brydges, T., Joshi, M. K., Jurcevic, P., Muschik, C. A., Silvi, P., Blatt, R., Roos, C. F., and Zoller, P., *"Self-verifying variational quantum simulation of lattice models,"* Nature **569**, 355 (2019) [cited in page 14].

Kolovsky, A. R., *"Creating artificial magnetic fields for cold atoms by photon-assisted tunneling,"* EPL (Europhysics Letters) **93**, 20003 (2011) [cited in page 188].

Kounalakis, M., Dickel, C., Bruno, A., Langford, N. K., and Steele, G. A., *"Tuneable hopping and nonlinear cross-Kerr interactions in a high-coherence superconducting circuit,"* npj Quantum Information **4**, 38 (2018) [cited in page 202].

Koziol, J., Fey, S., Kapfer, S. C., and Schmidt, K. P., *"Quantum criticality of the transverse-field Ising model with long-range interactions on triangular-lattice cylinders,"* Phys. Rev. B **100**, 144411 (2019) [cited in pages 153, 159, 160, and 171].

Kundu, A., *"Exact solution of double δ function Bose gas through an interacting anyon gas,"* Phys. Rev. Lett. **83**, 1275 (1999) [cited in page 199].

Kyprianidis, A., Machado, F., Morong, W., Becker, P., Collins, K. S., Else, D. V., Feng, L., Hess, P. W., Nayak, C., Pagano, G., Yao, N. Y., and Monroe, C., *"Observation of a prethermal discrete time crystal,"* Science **372**, 1192 (2021) [cited in page 202].

Labuhn, H., Rydberg excitation dynamics and correlations in arbitrary 2D arrays of single atoms, Ph.D. thesis, Université Paris-Saclay (2016) [cited in pages 76 and 85].

Labuhn, H., Barredo, D., Ravets, S., de Léséleuc, S., Macrì, T., Lahaye, T., and Browaeys, A., *"Tunable two-dimensional arrays of single Rydberg atoms for realizing quantum Ising models,"* Nature **534**, 667 (2016) [cited in page 225].

Lanyon, B. P., Hempel, C., Nigg, D., Müller, M., Gerritsma, R., Zähringer, F., Schindler, P., Barreiro, J. T., Rambach, M., Kirchmair, G., Hennrich, M., Zoller, P., Blatt, R., and Roos, C. F., *"Universal digital quantum simulation with trapped ions,"* Science **334**, 57 (2011) [cited in pages 14 and 102].

Laumann, C. R., Moessner, R., Scardicchio, A., and Sondhi, S. L., *"Quantum annealing: The fastest route to quantum computation?"* The European Physical Journal Special Topics **224**, 75 (2015) [cited in page 154].

Lee, S. A., Helmcke, J., Hall, J. L., and Stoicheff, B. P., *"Doppler-free two-photon transitions to Rydberg levels: convenient, useful, and precise reference wavelengths for dye lasers,"* Opt. Lett. **3**, 141 (1978) [cited in page 37].

de Léséleuc, S., Quantum simulation of spin models with assembled arrays of Rydberg atoms, Ph.D. thesis (2018), université Paris-Saclay [cited in pages 22, 38, 60, 76, 85, 86, 88, 92, and 186].

de Léséleuc, S., Barredo, D., Lienhard, V., Browaeys, A., and Lahaye, T., *"Optical control of the resonant dipole-dipole interaction between Rydberg atoms,"* Physical Review Letters **119**, 053202 (2017) [cited in page 44].

de Léséleuc, S., Barredo, D., Lienhard, V., Browaeys, A., and Lahaye, T., *"Analysis of imperfections in the coherent optical excitation of single atoms to Rydberg states,"* Physical Review A **97**, 053803 (2018a) [cited in pages 55, 59, 66, 68, 71, 131, and 225].

de Léséleuc, S., Lienhard, V., Scholl, P., Barredo, D., Weber, S., Lang, N., Büchler, H. P., Lahaye, T., and Browaeys, A., *"Observation of a symmetry-protected topological phase of interacting bosons with Rydberg atoms,"* Science **365**, 775 (2019) [cited in pages 178 and 226].

de Léséleuc, S., Weber, S., Lienhard, V., Barredo, D., Büchler, H. P., Lahaye, T., and Browaeys, A., *"Accurate mapping of multilevel Rydberg atoms on interacting spin-1/2 particles for the quantum simulation of Ising models,"* Physical Review Letters **120**, 113602 (2018b) [cited in pages 16, 75, and 225].

Levine, H., Keesling, A., Omran, A., Bernien, H., Schwartz, S., Zibrov, A. S., Endres, M., Greiner, M., Vuletić, V., and Lukin, M. D., *"High-fidelity control and entanglement of Rydberg-atom qubits,"* Physical Review Letters **121**, 123603 (2018) [cited in page 60].

Levine, H., Keesling, A., Semeghini, G., Omran, A., Wang, T. T., Ebadi, S., Bernien, H., Greiner, M., Vuletić, V., Pichler, H., and Lukin, M. D., *"Parallel implementation of high-fidelity multiqubit gates with neutral atoms,"* Phys. Rev. Lett. **123**, 170503 (2019) [cited in page 107].

Lieb, E., Schultz, T., and Mattis, D., *"Two soluble models of an antiferromagnetic chain,"* Annals of Physics **16**, 407 (1961) [cited in page 110].

Lienhard, V., Physique quantique expérimentale à N corps dans des matrices d'atomes de Rydberg. Des modèles de spins à la matière topologique., Ph.D. thesis (2019), université Paris-Saclay [cited in pages 42, 50, 183, 187, and 200].

Lienhard, V., de Léséleuc, S., Barredo, D., Lahaye, T., Browaeys, A., Schuler, M., Henry, L.-P., and Läuchli, A. M., *"Observing the space- and time-dependent growth of correlations in dynamically tuned synthetic Ising models with antiferromagnetic interactions,"* Physical Review X **8**, 021070 (2018) [cited in pages 16, 72, 108, 117, 119, 125, 159, and 225].

Lienhard, V., Scholl, P., Weber, S., Barredo, D., de Léséleuc, S., Bai, R., Lang, N., Fleischhauer, M., Büchler, H. P., Lahaye, T., and Browaeys, A., *"Realization of a density-dependent Peierls phase in a synthetic, spin-orbit coupled Rydberg system,"* Phys. Rev. X **10**, 021031 (2020) [cited in pages 187, 188, and 199].

Liu, Y., Chen, X., and Xu, Y., *"Topological phononics: From fundamental models to real materials,"* Advanced Functional Materials **30**, 1904784 (2020) [cited in page 188].

Love, G. D., *"Wave-front correction and production of Zernike modes with a liquid-crystal spatial light modulator,"* Appl. Opt. **36**, 1517 (1997) [cited in page 85].

Lukin, M. D., Fleischhauer, M., Cote, R., Duan, L. M., Jaksch, D., Cirac, J. I., and Zoller, P., *"Dipole blockade and quantum information processing in mesoscopic atomic ensembles,"* Phys. Rev. Lett. **87**, 037901 (2001) [cited in pages 15 and 101].

Löw, R., Weimer, H., Nipper, J., Balewski, J. B., Butscher, B., Büchler, H. P., and Pfau, T., *"An experimental and theoretical guide to strongly interacting Rydberg gases,"* Journal of Physics B: Atomic, Molecular and Optical Physics **45**, 113001 (2012) [cited in pages 15 and 67].

Madjarov, I. S., Covey, J. P., Shaw, A. L., Choi, J., Kale, A., Cooper, A., Pichler, H., Schkolnik, V., Williams, J. R., and Endres, M., *"High-fidelity entanglement and detection of alkaline-earth Rydberg atoms,"* Nature Physics **16**, 857 (2020) [cited in pages 60, 67, 72, 102, and 106].

Maghrebi, M. F., Gong, Z.-X., and Gorshkov, A. V., *"Continuous symmetry breaking in 1D long-range interacting quantum systems,"* Phys. Rev. Lett. **119**, 023001 (2017) [cited in page 201].

Mancini, M., Pagano, G., Cappellini, G., Livi, L., Rider, M., Catani, J., Sias, C., Zoller, P., Inguscio, M., Dalmonte, M., and Fallani, L., *"Observation of chiral edge states with neutral fermions in synthetic Hall ribbons,"* Science **349**, 1510 (2015) [cited in page 188].

Manousakis, E., *"The spin-1/2 Heisenberg antiferromagnet on a square lattice and its application to the cuprous oxides,"* Rev. Mod. Phys. **63**, 1 (1991) [cited in pages 201 and 227].

Marek, J. and Munster, P., *"Radiative lifetimes of excited states of rubidium up to quantum number n=12,"* Journal of Physics B: Atomic and Molecular Physics **13**, 1731 (1980) [cited in page 62].

Mazurenko, A., Chiu, C. S., Ji, G., Parsons, M. F., Kanász-Nagy, M., Schmidt, R., Grusdt, F., Demler, E., Greif, D., and Greiner, M., *"A cold-atom Fermi–Hubbard antiferromagnet,"* Nature **545**, 462 (2017) [cited in page 14].

Meinert, F., Mark, M. J., Kirilov, E., Lauber, K., Weinmann, P., Daley, A. J., and Nägerl, H.-C., *"Quantum quench in an atomic one-dimensional Ising chain,"* Phys. Rev. Lett. **111**, 053003 (2013) [cited in page 108].

Meinert, F., Mark, M. J., Lauber, K., Daley, A. J., and Nägerl, H.-C., *"Floquet engineering of correlated tunneling in the Bose-Hubbard model with ultracold atoms,"* Phys. Rev. Lett. **116**, 205301 (2016) [cited in page 202].

Menu, R., Gaussian-state approaches to quantum spin systems away from equilibrium, Ph.D. thesis (2020) [cited in page 170].

Misguich, G., Mallick, K., and Krapivsky, P. L., *"Dynamics of the spin-1/2 Heisenberg chain initialized in a domain-wall state,"* Phys. Rev. B **96**, 195151 (2017) [cited in pages 215, 218, and 219].

Misguich, G., Pavloff, N., and Pasquier, V., *"Domain wall problem in the quantum XXZ chain and semiclassical behavior close to the isotropic point,"* SciPost Physics **7**, 025 (2019) [cited in pages 215 and 218].

Moessner, R. and Sondhi, S. L., *"Ising models of quantum frustration,"* Phys. Rev. B **63**, 224401 (2001) [cited in pages 152 and 171].

Moessner, R., Sondhi, S. L., and Chandra, P., *"Two-dimensional periodic frustrated Ising models in a transverse field,"* Phys. Rev. Lett. **84**, 4457 (2000) [cited in pages 152 and 171].

Monroe, C., Campbell, W. C., Duan, L.-M., Gong, Z.-X., Gorshkov, A. V., Hess, P. W., Islam, R., Kim, K., Linke, N. M., Pagano, G., Richerme, P., Senko, C., and Yao, N. Y., *"Programmable quantum simulations of spin systems with trapped ions,"* Rev. Mod. Phys. **93**, 025001 (2021) [cited in page 108].

Moore, J. E., *"The birth of topological insulators,"* Nature **464**, 194 (2010) [cited in page 187].

Mossel, J. and Caux, J.-S., *"Relaxation dynamics in the gapped XXZ spin-1/2 chain,"* New J. Phys. **12**, 055028 (2010) [cited in page 215].

Nakamura, Y., Pashkin, Y. A., and Tsai, J. S., *"Coherent control of macroscopic quantum states in a single-cooper-pair box,"* Nature **398**, 786 (1999) [cited in page 15].

Ng, K.-K. and Lee, T. K., *"Supersolid phase in spin dimer XXZ systems under a magnetic field,"* Phys. Rev. Lett. **97**, 127204 (2006) [cited in pages 201 and 227].

Nguyen, T. L., Raimond, J. M., Sayrin, C., Cortiñas, R., Cantat-Moltrecht, T., Assemat, F., Dotsenko, I., Gleyzes, S., Haroche, S., Roux, G., Jolicoeur, T., and Brune, M., *"Towards quantum simulation with circular Rydberg atoms,"* Phys. Rev. X **8**, 011032 (2018) [cited in page 202].

Nogrette, F., Labuhn, H., Ravets, S., Barredo, D., Béguin, L., Vernier, A., Lahaye, T., and Browaeys, A., *"Single-atom trapping in holographic 2D arrays of microtraps with arbitrary geometries,"* Phys. Rev. X **4**, 021034 (2014) [cited in pages 16 and 27].

Omran, A., Levine, H., Keesling, A., Semeghini, G., Wang, T. T., Ebadi, S., Bernien, H., Zibrov, A. S., Pichler, H., Choi, S., Cui, J., Rossignolo, M., Rembold, P., Montangero, S., Calarco, T., Endres, M., Greiner, M., Vuletić, V., and Lukin, M. D., *"Generation and manipulation of Schrödinger cat states in Rydberg atom arrays,"* Science **365**, 570 (2019) [cited in pages 108 and 127].

Ozawa, T., Price, H. M., Amo, A., Goldman, N., Hafezi, M., Lu, L., Rechtsman, M. C., Schuster, D., Simon, J., Zilberberg, O., and Carusotto, I., *"Topological photonics,"* Rev. Mod. Phys. **91**, 015006 (2019) [cited in page 188].

Ozeri, R., Khaykovich, L., and Davidson, N., *"Long spin relaxation times in a single-beam blue-detuned optical trap,"* Phys. Rev. A **59**, R1750 (1999) [cited in page 40].

Paeckel, S., Köhler, T., Swoboda, A., Manmana, S. R., Schollwöck, U., and Hubig, C., *"Time-evolution methods for matrix-product states,"* Annals of Physics **411**, 167998 (2019) [cited in page 134].

Paul, W., *"Electromagnetic traps for charged and neutral particles,"* Review of Modern Physics **62**, 531 (1990) [cited in page 11].

Peng, P., Yin, C., Huang, X., Ramanathan, C., and Cappellaro, P., *"Floquet prethermalization in dipolar spin chains,"* Nature Physics **17**, 444 (2021) [cited in page 202].

Peter, D., Yao, N. Y., Lang, N., Huber, S. D., Lukin, M. D., and Büchler, H. P., *"Topological bands with a Chern number $C = 2$ by dipolar exchange interactions,"* Phys. Rev. A **91**, 053617 (2015) [cited in page 188].

Phillips, W. D., *"Nobel lecture: Laser cooling and trapping of neutral atoms,"* Review of Modern Physics **70**, 721 (1998) [cited in page 11].

Plumer, M. L. and Mailhot, A., *"Comment on "multiple-histogram Monte Carlo study of the Ising antiferromagnet on a stacked triangular lattice","* Phys. Rev. B **52**, 1411 (1995) [cited in page 171].

Polkovnikov, A., *"Universal adiabatic dynamics in the vicinity of a quantum critical point,"* Phys. Rev. B **72**, 161201 (2005) [cited in page 141].

Radgohar, R. and Montakhab, A., *"Global entanglement and quantum phase transitions in the transverse XY Heisenberg chain,"* Phys. Rev. B **97**, 024434 (2018) [cited in page 177].

Raizen, M. G., Gilligan, J. M., Bergquist, J. C., Itano, W. M., and Wineland, D. J., *"Ionic crystals in a linear paul trap,"* Phys. Rev. A **45**, 6493 (1992) [cited in page 14].

Ravets, S., Development of tools for quantum engineering using individual atoms : optical nanofibers and controlled Rydberg interactions, Ph.D. thesis (2014), institut d'optique théorique et appliquée [cited in pages 50 and 60].

Ravets, S., Labuhn, H., Barredo, D., Béguin, L., Lahaye, T., and Browaeys, A., *"Coherent dipole–dipole coupling between two single Rydberg atoms at an electrically-tuned Förster resonance,"* Nature Physics **10**, 914 (2014) [cited in page 103].

Richerme, P., Gong, Z.-X., Lee, A., Senko, C., Smith, J., Foss-Feig, M., Michalakis, S., Gorshkov, A. V., and Monroe, C., *"Non-local propagation of correlations in quantum systems with long-range interactions,"* Nature **511**, 198 (2014) [cited in page 214].

Richter, J., Schulenburg, J., and Honecker, A., *"Quantum magnetism in two dimensions: From semi-classical Néel order to magnetic disorder,"* in Quantum magnetism. Lecture Notes in Physics, edited by U. Schollwöck, J. Richter, D. Farnell, and R. Bishop (Springer, Berlin, 2004) pp. 85–153 [cited in page 224].

Roos, C. F., Lancaster, G. P. T., Riebe, M., Häffner, H., Hänsel, W., Gulde, S., Becher, C., Eschner, J., Schmidt-Kaler, F., and Blatt, R., *"Bell states of atoms with ultralong lifetimes and their tomographic state analysis,"* Phys. Rev. Lett. **92**, 220402 (2004) [cited in page 106].

Roushan, P., Neill, C., Megrant, A., Chen, Y., Babbush, R., Barends, R., Campbell, B., Chen, Z., Chiaro, B., Dunsworth, A., Fowler, A., Jeffrey, E., Kelly, J., Lucero, E., Mutus, J., O'Malley, P. J. J., Neeley, M., Quintana, C., Sank, D., Vainsencher, A., Wenner, J., White, T., Kapit, E., Neven, H., and Martinis, J., *"Chiral ground-state currents of interacting photons in a synthetic magnetic field,"* Nature Physics **13**, 146 (2017) [cited in pages 188, 192, and 197].

Rubio-Abadal, A., Ippoliti, M., Hollerith, S., Wei, D., Rui, J., Sondhi, S. L., Khemani, V., Gross, C., and Bloch, I., *"Floquet prethermalization in a Bose-Hubbard system,"* Phys. Rev. X **10**, 021044 (2020) [cited in page 202].

Sachdev, S., Quantum Phase Transitions, 2nd ed. (Cambridge University Press, 2011) [cited in page 143].

Saffman, M., Walker, T. G., and Mølmer, K., *"Quantum information with Rydberg atoms,"* Review of Modern Physics **82**, 2313 (2010) [cited in page 101].

Safronova, M. S., Williams, C. J., and Clark, C. W., *"Relativistic many-body calculations of electric-dipole matrix elements, lifetimes, and polarizabilities in rubidium,"* Phys. Rev. A **69**, 022509 (2004) [cited in page 62].

Salathé, Y., Mondal, M., Oppliger, M., Heinsoo, J., Kurpiers, P., Potočnik, A., Mezzacapo, A., Las Heras, U., Lamata, L., Solano, E., Filipp, S., and Wallraff, A., *"Digital quantum simulation of spin models with circuit quantum electrodynamics,"* Phys. Rev. X **5**, 021027 (2015) [cited in page 15].

Samajdar, R., Ho, W. W., Pichler, H., Lukin, M. D., and Sachdev, S., *"Complex density wave orders and quantum phase transitions in a model of square-lattice Rydberg atom arrays,"* Phys. Rev. Lett. **124**, 103601 (2020) [cited in pages 135 and 143].

Samajdar, R., Ho, W. W., Pichler, H., Lukin, M. D., and Sachdev, S., *"Quantum phases of Rydberg atoms on a kagome lattice,"* Proceedings of the National Academy of Sciences **118** (2021), 10.1073/pnas.2015785118 [cited in page 135].

Sandvik, A. W., *"Ground states of a frustrated quantum spin chain with long-range interactions,"* Phys. Rev. Lett. **104**, 137204 (2010) [cited in page 201].

Schäffner, D., Preuschoff, T., Ristok, S., Brozio, L., Schlosser, M., Giessen, H., and Birkl, G., *"Arrays of individually controllable optical tweezers based on 3D-printed microlens arrays,"* Opt. Express **28**, 8640 (2020) [cited in page 26].

Schauß, P., Cheneau, M., Endres, M., Fukuhara, T., Hild, S., Omran, A., Pohl, T., Gross, C., Kuhr, S., and Bloch, I., *"Observation of spatially ordered structures in a two-dimensional Rydberg gas,"* Nature **491**, 87 (2012) [cited in page 108].

Schlosser, N., Reymond, G., and Grangier, P., *"Collisional blockade in microscopic optical dipole traps,"* Phys. Rev. Lett. **89**, 023005 (2002) [cited in page 25].

Schlosser, N., Reymond, G., Protsenko, I., and Grangier, P., *"Sub-poissonian loading of single atoms in a microscopic dipole trap,"* Nature **411**, 1024 (2001) [cited in pages 15 and 25].

Schmidt-Kaler, F., Häffner, H., Riebe, M., Gulde, S., Lancaster, G. P. T., Deuschle, T., Becher, C., Roos, C. F., Eschner, J., and Blatt, R., *"Realization of the Cirac–Zoller controlled-NOT quantum gate,"* Nature **422**, 408 (2003) [cited in page 11].

Schmitt, M., Rams, M. M., Dziarmaga, J., Heyl, M., and Zurek, W. H., *"Quantum phase transition dynamics in the two-dimensional transverse-field Ising model,"* (2021), arXiv:2106.09046 [cond-mat.str-el] [cited in pages 141 and 147].

Scholl, P., Schuler, M., Williams, H. J., Eberharter, A. A., Barredo, D., Schymik, K.-N., Lienhard, V., Henry, L.-P., Lang, T. C., Lahaye, T., Läuchli, A. M., and Browaeys, A., *"Quantum simulation of 2D antiferromagnets with hundreds of Rydberg atoms,"* Nature **595**, 233 (2021a) [cited in pages 108, 118, 135, and 150].

Scholl, P., Williams, H. J., Bornet, G., Wallner, F., Barredo, D., Lahaye, T., Browaeys, A., Henriet, L., Signoles, A., Hainaut, C., Franz, T., Geier, S., Tebben, A., Salzinger, A., Zürn, G., and Weidemüller, M., *"Microwave-engineering of programmable XXZ Hamiltonians in arrays of Rydberg atoms,"* (2021b), arXiv:2107.14459 [quant-ph] [cited in page 202].

Schollwöck, U., *"The density-matrix renormalization group in the age of matrix product states,"* Annals of Physics **326**, 96 (2011), january 2011 Special Issue [cited in page 134].

Schuler, M., Whitsitt, S., Henry, L.-P., Sachdev, S., and Läuchli, A. M., *"Universal signatures of quantum critical points from finite-size torus spectra: A window into the operator content of higher-dimensional conformal field theories,"* Phys. Rev. Lett. **117**, 210401 (2016) [cited in page 120].

Schweizer, C., Grusdt, F., Berngruber, M., Barbiero, L., Demler, E., Goldman, N., Bloch, I., and Aidelsburger, M., *"Floquet approach to Z_2 lattice gauge theories with ultracold atoms in optical lattices,"* Nature Physics **15**, 1168 (2019) [cited in page 202].

Schymik, K.-N., Lienhard, V., Barredo, D., Scholl, P., Williams, H., Browaeys, A., and Lahaye, T., *"Enhanced atom-by-atom assembly of arbitrary tweezer arrays,"* Phys. Rev. A **102**, 063107 (2020) [cited in pages 91 and 92].

Schymik, K.-N., Pancaldi, S., Nogrette, F., Barredo, D., Paris, J., Browaeys, A., and Lahaye, T., *"Single atoms with 6000-second trapping lifetimes in optical-tweezer arrays at cryogenic temperatures,"* Phys. Rev. Applied **16**, 034013 (2021) [cited in pages 42 and 67].

Shirley, J. H., *"Solution of the Schrödinger equation with a Hamiltonian periodic in time,"* Phys. Rev. **138**, B979 (1965) [cited in page 202].

Signoles, A., Franz, T., Ferracini Alves, R., Gärttner, M., Whitlock, S., Zürn, G., and Weidemüller, M., *"Glassy dynamics in a disordered Heisenberg quantum spin system,"* Phys. Rev. X **11**, 011011 (2021) [cited in pages 202 and 214].

Simon, J., Bakr, W. S., Ma, R., Tai, M. E., Preiss, P. M., and Greiner, M., *"Quantum simulation of antiferromagnetic spin chains in an optical lattice,"* Nature **472**, 307 (2011) [cited in pages 14 and 107].

Sirker, J., Pereira, R. G., and Affleck, I., *"Diffusion and ballistic transport in one-dimensional quantum systems,"* Phys. Rev. Lett. **103**, 216602 (2009) [cited in page 214].

Sirko, L., Arndt, M., Koch, P., and Walther, H., *"Microwave ionization of Rb Rydberg atoms: Frequency dependence,"* Physical review. A **49**, 3831 (1994) [cited in page 67].

Smith, A., Kim, M. S., Pollmann, F., and Knolle, J., *"Simulating quantum many-body dynamics on a current digital quantum computer,"* npj Quantum Information **5**, 106 (2019) [cited in page 102].

Song, C., Xu, K., Liu, W., Yang, C.-p., Zheng, S.-B., Deng, H., Xie, Q., Huang, K., Guo, Q., Zhang, L., Zhang, P., Xu, D., Zheng, D., Zhu, X., Wang, H., Chen, Y.-A., Lu, C.-Y., Han, S., and Pan, J.-W., *"10-qubit entanglement and parallel logic operations with a superconducting circuit,"* Phys. Rev. Lett. **119**, 180511 (2017) [cited in page 108].

Song, Y., Kim, M., Hwang, H., Lee, W., and Ahn, J., *"Quantum simulation of cayley-tree Ising Hamiltonians with three-dimensional Rydberg atoms,"* Phys. Rev. Research **3**, 013286 (2021) [cited in pages 28 and 108].

Spalding, G. C., Courtial, J., and Leonardo, R. D., *"Holographic optical tweezers,"* (2008) [cited in page 77].

Stoli, E. and Domb, C., *"Shape and size of two-dimensional percolation clusters with and without correlations,"* Journal of Physics A: Mathematical and General **12**, 1843 (1979) [cited in page 140].

Stuhl, B. K., Lu, H.-I., Aycock, L. M., Genkina, D., and Spielman, I. B., *"Visualizing edge states with an atomic Bose gas in the quantum Hall regime,"* Science **349**, 1514 (2015) [cited in page 188].

Tan, W. L., Becker, P., Liu, F., Pagano, G., Collins, K. S., De, A., Feng, L., Kaplan, H. B., Kyprianidis, A., Lundgren, R., Morong, W., Whitsitt, S., Gorshkov, A. V., and Monroe, C., *"Domain-wall confinement and dynamics in a quantum simulator,"* Nature Physics **17**, 742 (2021) [cited in page 214].

Tarruell, L., Greif, D., Uehlinger, T., Jotzu, G., and Esslinger, T., *"Creating, moving and merging Dirac points with a Fermi gas in a tunable honeycomb lattice,"* Nature **483**, 302 (2012) [cited in page 14].

Thoumany, P., Hänsch, T., Stania, G., Urbonas, L., and Becker, T., *"Optical spectroscopy of rubidium Rydberg atoms with a 297 nm frequency-doubled dye laser,"* Opt. Lett. **34**, 1621 (2009) [cited in page 56].

Tuchendler, C., Lance, A. M., Browaeys, A., Sortais, Y. R. P., and Grangier, P., *"Energy distribution and cooling of a single atom in an optical tweezer,"* Phys. Rev. A **78**, 033425 (2008) [cited in page 33].

Urban, E., Johnson, T. A., Henage, T., Isenhower, L., Yavuz, D. D., Walker, T. G., and Saffman, M., *"Observation of Rydberg blockade between two atoms,"* Nature Physics **5**, 110 (2009) [cited in page 16].

Vandersypen, L. M. K., Bluhm, H., Clarke, J. S., Dzurak, A. S., Ishihara, R., Morello, A., Reilly, D. J., Schreiber, L. R., and Veldhorst, M., *"Interfacing spin qubits in quantum dots and donors—hot, dense, and coherent,"* npj Quantum Information **3**, 34 (2017) [cited in page 15].

Vandersypen, L. M. K. and Chuang, I. L., *"NMR techniques for quantum control and computation,"* Rev. Mod. Phys. **76**, 1037 (2005) [cited in pages 202 and 203].

Villain, J.,, Bidaux, R.,, Carton, J.-P.,, and Conte, R.,, *"Order as an effect of disorder,"* J. Phys. France **41**, 1263 (1980) [cited in pages 152 and 170].

Vitanov, N. V., Rangelov, A. A., Shore, B. W., and Bergmann, K., *"Stimulated Raman adiabatic passage in physics, chemistry, and beyond,"* Rev. Mod. Phys. **89**, 015006 (2017) [cited in page 37].

Walker, T. G. and Saffman, M., *"Zeros of Rydberg–Rydberg Föster interactions,"* Journal of Physics B **38**, S309 (2005) [cited in page 103].

Wallraff, A., Schuster, D. I., Blais, A., Frunzio, L., Huang, R.-. S., Majer, J., Kumar, S., Girvin, S. M., and Schoelkopf, R. J., *"Strong coupling of a single photon to a superconducting qubit using circuit quantum electrodynamics,"* Nature **431**, 162 (2004) [cited in page 15].

Wang, T., Hu, S., Eggert, S., Fleischhauer, M., Pelster, A., and Zhang, X.-F., *"Floquet-induced superfluidity with periodically modulated interactions of two-species hardcore bosons in a one-dimensional optical lattice,"* Phys. Rev. Research **2**, 013275 (2020) [cited in page 188].

Wang, X.-L., Dou, S. X., and Zhang, C., *"Zero-gap materials for future spintronics, electronics and optics,"* NPG Asia Materials **2**, 31 (2010) [cited in page 187].

Wannier, G. H., *"Antiferromagnetism. the triangular Ising net,"* Phys. Rev. **79**, 357 (1950) [cited in page 169].

Weber, S., de Léséleuc, S., Lienhard, V., Barredo, D., Lahaye, T., Browaeys, A., and Büchler, H. P., *"Topologically protected edge states in small Rydberg systems,"* Quantum Science and Technology **3**, 044001 (2018) [cited in pages 188 and 200].

Weber, S., Tresp, C., Menke, H., Urvoy, A., Firstenberg, O., Büchler, H. P., and Hofferberth, S., *"Calculation of Rydberg interaction potentials,"* Journal of Physics B: Atomic, Molecular and Optical Physics **50**, 133001 (2017) [cited in pages 182 and 190].

Wei, D., Rubio-Abadal, A., Ye, B., Machado, F., Kemp, J., Srakaew, K., Hollerith, S., Rui, J., Gopalakrishnan, S., Yao, N. Y., Bloch, I., and Zeiher, J., *"Quantum gas microscopy of Kardar-Parisi-Zhang superdiffusion,"* (2021), arXiv:2107.00038 [cited in page 214].

Weimer, H., Muller, M., Lesanovsky, I., Zoller, P., and Büchler, H. P., *"A Rydberg quantum simulator,"* Nature Phys. **6**, 382 (2010) [cited in page 16].

Wilk, T., Gaëtan, A., Evellin, C., Wolters, J., Miroshnychenko, Y., Grangier, P., and Browaeys, A., *"Entanglement of two individual neutral atoms using Rydberg blockade,"* Phys. Rev. Lett. **104**, 010502 (2010) [cited in pages 16, 105, and 107].

Wineland, D. J., Dalibard, J., and Cohen-Tannoudji, C., *"Sisyphus cooling of a bound atom,"* J. Opt. Soc. Am. B **9**, 32 (1992) [cited in page 33].

Wintersperger, K., Braun, C., Ünal, F. N., Eckardt, A., Liberto, M. D., Goldman, N., Bloch, I., and Aidelsburger, M., *"Realization of an anomalous Floquet topological system with ultracold atoms,"* Nature Physics **16**, 1058 (2020) [cited in page 202].

Xu, P., He, X., Wang, J., and Zhan, M., *"Trapping a single atom in a blue detuned optical bottle beam trap,"* Opt. Lett. **35**, 2164 (2010) [cited in page 40].

Yamamoto, D., Ueda, H., Danshita, I., Marmorini, G., Momoi, T., and Shimokawa, T., *"Exact diagonalization and cluster mean-field study of triangular-lattice XXZ antiferromagnets near saturation,"* Phys. Rev. B **96**, 014431 (2017) [cited in page 201].

Yan, B., Moses, S. A., Gadway, B., Covey, J. P., Hazzard, K. R. A., Rey, A. M., Jin, D. S., and Ye, J., *"Observation of dipolar spin-exchange interactions with lattice-confined polar molecules,"* Nature **501**, 521 (2013) [cited in pages 14 and 202].

Yang, C. N. and Yang, C. P., *"One-dimensional chain of anisotropic spin-spin interactions. I. proof of Bethe's hypothesis for ground state in a finite system,"* Phys. Rev. **150**, 321 (1966) [cited in page 201].

Younge, K. C., Knuffman, B., Anderson, S. E., and Raithel, G., *"State-dependent energy shifts of Rydberg atoms in a ponderomotive optical lattice,"* Phys. Rev. Lett. **104**, 173001 (2010) [cited in page 39].

Yunoki, S., *"Numerical study of the spin-flop transition in anisotropic spin-1/2 antiferromagnets,"* Phys. Rev. B **65**, 092402 (2002) [cited in page 201].

Zeiher, J., van Bijnen, R., Schauss, P., Hild, S., Choi, J.-Y., Pohl, T., Bloch, I., and Gross, C., *"Many-body interferometry of a Rydberg-dressed spin lattice,"* Nature Physics **12**, 1095 (2016) [cited in page 56].

Zhai, H., *"Degenerate quantum gases with spin–orbit coupling: a review,"* Reports on Progress in Physics **78**, 026001 (2015) [cited in page 188].

Zhou, Y. L., Ortner, M., and Rabl, P., *"Long-range and frustrated spin-spin interactions in crystals of cold polar molecules,"* Phys. Rev. A **84**, 052332 (2011) [cited in page 14].

Zhu, J.-X. and Wang, Z. D., *"Topological effects associated with fractional statistics in one-dimensional mesoscopic rings,"* Phys. Rev. A **53**, 600 (1996) [cited in page 199].

Zurek, W. H., Dorner, U., and Zoller, P., *"Dynamics of a quantum phase transition,"* Phys. Rev. Lett. **95**, 105701 (2005) [cited in page 141].

Titre : Simulation quantique de modèles de spins avec des grandes matrices d'atomes de Rydberg

Mots clés : pinces optique, modèles de spins, simulation quantique, problèmes à N corps

Résumé : Des atomes individuels piégés dans des matrices de pinces optiques et excités vers des états de Rydberg forment une plateforme expérimentale prometteuse pour la simulation quantique de modèles de spins. Lors de cette thèse, nous avons d'abord perfectionné la plateforme en augmentant le nombre d'atomes manipulables d'une quarantaine à environ deux cents, et en améliorant d'un facteur dix la cohérence quantique du système. Nous avons ensuite revisité le modèle d'Ising en excitant de manière cohérente plus d'une centaine d'atomes depuis leur état électronique fondamental vers un niveau de Rydberg. Nous avons exploré avec notre simulateur quantique des phénomènes comme les transitions de phase quantiques ou la recherche des états fondamentaux du système. Les simulations numériques de ces phénomènes sont difficiles à réaliser compte tenu du nombre de particules, ce qui rapproche la plateforme de son but originel : il s'agit d'un nouveau moyen d'étudier des systèmes complexes pour lesquels les simulations numériques sont limitées. Nous avons ensuite utilisé un autre régime d'interaction entre atomes de Rydberg pour implémenter de nouveaux modèles de spins permettant d'étudier une grande variété de phénomènes physiques. Nous nous sommes d'abord penchés sur la réalisation d'une interaction à valeur complexe en utilisant le couplage spin-orbite de l'interaction dipôle-dipôle. Cette interaction simule le mouvement d'une particule chargée dans un champ magnétique et permet d'étudier les propriétés topologiques de la matière comme l'effet Hall quantique. Nous avons ensuite implémenté le modèle d'Heisenberg avec une anisotropie variable en utilisant un champ micro-ondes externe. Ce modèle, très présent dans la description des matériaux magnétiques, permet aussi d'étudier des phénomènes comme la supraconductivité, la superfluidité ou la supersolidité.

Title : Quantum simulation of spin models with large arrays of Rydberg atoms

Keywords : optical tweezers, spin models, quantum simulation, many body problems

Abstract : Single atoms trapped in optical tweezers arrays and excited to Rydberg states are a promising experimental platform for the quantum simulation of spin models. In this thesis, we first improved the platform by increasing the number of atoms from around forty to two hundred, and by improving the system's coherence by a factor ten. We then revisited the Ising model by exciting coherently more than a hundred atoms from their ground state towards a Rydberg state. We explore with our quantum simulator the model's features such as quantum phase transitions or the system's ground states. The numerical simulations of these features are difficult to perform considering the high number of particles, bringing the platform one step closer from its original purpose: a new way to explore complex systems for which numerical simulations are hard to perform. We then used another type of interaction between Rydberg atoms to implement new types of spin models. We first implemented a complex-value interaction using the intrinsic spin-orbit coupling of the dipole-dipole interaction. This interaction models the movement of a charged particle in a magnetic field, and allows to study topological properties such as the quantum Hall effect. We then implemented the Heisenberg model with tunable anisotropy using an external microwave field. This model describes magnetic materials, but also allows to study phenomena like superconductivity, superfluidity or supersolidity.